Terahertz spectroscopy to explore the role of vibrational dynamics in systems with varying structural order and disorder

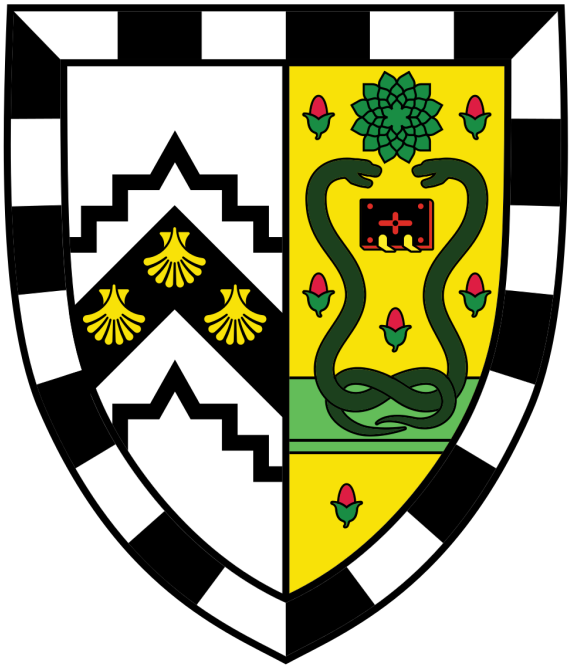

Johanna Kölbel

Gonville and Caius College

University of Cambridge

This thesis is submitted for the degree of

Doctor of Philosophy.

June 2022

Declaration

This thesis, entitled "Terahertz spectroscopy to explore the role of vibrational dynamics in systems with varying structural order and disorder", is the result of my own work and includes nothing which is the outcome of work done in collaboration except as declared in the preface and specified in the text. It is not substantially the same as any work that has already been submitted before for any degree or other qualification except as declared in the preface and specified in the text. It does not exceed the prescribed word limit for the Engineering Degree Committee.

Johanna Kölbel
Gonville and Caius College
Cambridge CB2 1TA
June 2022

Acknowledgements

This thesis is the result of four years that I will never forget. I am grateful for being given the chance to come to Cambridge and spend time with so many wonderful people who helped me along immensely. The first in that long list is Prof. Axel Zeitler, an amazing supervisor. He supported me through the years and always offered solutions to smaller and bigger problems. His guidance, knowledge, and patience often saved the day and I have learnt a lot from him.

I am extremely grateful for the support from Dr. Christopher Van der Walle (MedImmune) and Dr. Sajal Patel (AstraZeneca), my industrial supervisors. I would also like to thank Dr. Jonathan Evans, my College tutor, and Prof. Mick Mantle, my advisor. Being part of the Terahertz Applications Group has been wonderful. A big thank you to Adam, Amy, Dabwan, Daniel, Haseeb, Jongmin, Mike, Prince, Qi, Runqiao, Ruohan, Solomon, and Talia, as well as to the visitors. Thank you for helping with experiments, trouble shooting, and answering many stupid questions but also for numerous fun breaks and amazing conference trips. A special thank goes to Mike and Daniel who, amongst many other things, first taught me how not to break the lab equipment.

The work presented in this thesis would not have been possible without the support of many great scientists. I am very grateful to Dr. Evgenyi Shalaev who initiated the glycerol work and supported it ever since and Prof. Walter Schirmacher for extremely helpful discussions about theoretical concepts. It was a pleasure collaborating with Prof. Wolfgang Frieß, Moritz Anuschek, and Dr. Ivonne Stelzl on the lyophilised protein project. I would also like to thank Dr. Amberley Stephens and Prof. Gabi Kaminski for their help and many explanations about the behaviour of proteins in solution. The crystallisation project was improved immensely by the extensive knowledge of Prof. Terry Threlfall, the X-ray measurements of Dr. Andrew Bond, and the simulations of Margaret Davis and Prof. Tim Korter.

I am also grateful for funding from MediImmune/Astra Zeneca and the UKRI as well as the collaboration with Abbvie that allowed to extend it – thank you so much Adam for setting this up!

I would further like to thank Mark Scudder and Chris Bawden for their professional support and the admin team of the Sensor CDT for their many efforts and Axel and Qi for proofreading this thesis.

This thesis would not have seen the light of day without the help of family and friends. I would like to thank all past and present residents of 3 Harvey Road as well as Francesca, Luca, and Raphaël for being great friends. Qi and Dabwan, I could not have undertaken this journey without you. I am also very grateful for the encouragement of my family. You were always there for me and supported my choices.

Abstract

Understanding the processes occurring in materials with varying structural order and disorder, such as pharmaceutical mixtures, has profound implications for drug formulation and delivery. Pharmaceutically active biological molecules such as peptides, proteins, and antibodies need to be formulated and processed into dry powder form that can be reconstituted quickly in order to achieve long-term storage stability. The biomolecules retain their functional properties by embedding them into an amorphous matrix of suitable small organic molecular glass formers. Degradation mechanisms catalysed by water clusters, the influence of the solvation shell in solution upon reconstitution, and crystallisation processes are important aspects to consider in this context, and this thesis investigates these points using terahertz time-domain spectroscopy (THz-TDS).

Glycerol is commonly used to protect proteins during cryo-preservation and its interactions with small amounts of water are important to understand. The onset of molecular mobility, as measured by the infrared active dipoles in glycerol-water mixtures, resulted in increased anharmonic effects, obscured the boson peak, and influenced the vibrational density of states. The effect of the relative water content in aqueous mixtures of glycerol at room temperature was also explored.

By utilising four different model biopharmaceuticals, the effect of size on the dynamics of one-component lyophilised products was studied with THz-TDS and differential scanning calorimetry. Anharmonic effects were identified in the spectra and linked to protein jamming in high molecular-weight samples, hindering the increase in molecular mobility with temperature. Two-component lyophilisates of varying sucrose to monoclonal antibody ratio were assessed with terahertz spectroscopy and it was shown that protein jamming at a critical temperature must be associated with the macromolecular structure of the protein itself, that it is not dependent on the presence of any excipient, and that it is not dependent on the presence of water molecules.

Even if proteins are stored in dry form, they have to be rehydrated before use without losing their functionality due to misfolding or aggregation. Using terahertz spectroscopy and structural techniques, an increased aggregation rate of α-synuclein (aSyn), a protein associated with Parkinson's disease, in the presence of NaCl compared to CsI was found to be not due to a change in the structural conformations of aSyn, but due to a reduction in both the water mobility and subsequently the protein mobility. The same method was applied to two other proteins, namely β-lactoglobulin and bovine serum albumin, and the interactions with the surrounding salt solution were found to strongly depend on the protein characteristics.

Crystallisation dynamics in aqueous solution were studied using THz-TDS in a transmission geometry on the example of magnesium sulfate heptahydrate. A novel method was developed to perform temperature and concentration calibrations of liquid samples at terahertz frequencies, enabling the studies of local concentration of semicrystalline systems.

Publications and Conference Presentations

Publications in Peer-Reviewed Journals

- Li, Q.#, **Kölbel, J.**#, Threlfall, T, and Zeitler, J. A. Flow cell to study crystallization processes in situ using terahertz time-domain Spectroscopy. IEEE Transactions on Terahertz Science and Technology, 12, 2, 193-198, 2022 (# are co-first authors).

- **Kölbel, J.**#, Li, Q.#, Threlfall, T., and Zeitler, J. A. Measuring solute concentration with terahertz time-domain spectroscopy in single and multiphase systems, # are shared first-authors. Analytical Chemistry, 2022, 94, 3, 1713-1716 (# are co-first authors).

- Li, Q.#, **Kölbel, J.**#, Davis, M. P., Korter, T. M., Bond, A. D., Threlfall, T., and Zeitler, J. A. (2022). In situ observation of the structure of crystallizing magnesium sulfate heptahydrate solutions with terahertz transmission spectroscopy. Crystal Growth and Design, in press (# are co-first authors).

- Stephens, A. D., **Kölbel, J.**, Moons, R., Ruggerio, M. T., Mahmoudi, N., Shmool, T. A., ... and Schierle, G. S. K. The role of water mobility in protein misfolding. Under review. Preprint available on BioRxiv, doi: 10.1101/2021.01.06.425575.

- **Kölbel, J.**, Schirmacher, W., Shalaev, E., Zeitler, J. A. Terahertz dynamics in the glycerol-water system. In preparation.

- **Kölbel, J.**, Anuschek, M. L., Stelzl, I., Frieß, W., Zeitler, J. A. The role of terahertz dynamics in solid-state protein formulations. In preparation.

Conference Presentations

- **Kölbel, J.**, Li, Q., Threlfall, T., Zeitler, J. A. (2021). Crystallising magnesium sulfate solutions: observing structure with terahertz spectroscopy. Sensors Day 2021, Cambridge, UK.

- **Kölbel, J.**, Li, Q., Threlfall, T., Zeitler, J. A. (2021). Crystallising magnesium sulfate solutions: observing structure with terahertz spectroscopy. PSSRC 2021, online.

- Li, Q., **Kölbel, J.**, Threlfall, T., Zeitler, J. A. (2021). Crystallising magnesium sulfate solutions: observing structure with terahertz spectroscopy. 46th International Conference on Infrared, Millimeter, and Terahertz Waves (IRMMW-THz) 2021, online.

- **Kölbel, J.**, Li, Q., Threlfall, T., Zeitler, J. A. (2021). In-situ observation of the structure of crystallising magnesium sulfate solutions. CEB Research Conference 2021, online.

- **Kölbel, J.**, Anuschek, M., Seifert, I., Frieß, W., and Zeitler, J. A. (2020). Stability of protein-sugar lyophilizates investigated with terahertz spectroscopy. 45th International Conference on Infrared, Millimeter, and Terahertz Waves (IRMMW-THz), online.

- **Kölbel, J.**, Anuschek, M. L., Seifert, I., Frieß, W., Zeitler, J. A. (2020). Stability of protein-sugar lyophilisates investigated with terahertz spectroscopy. Sensors Day 2020, Cambridge, UK.

- **Kölbel, J.**, Anuschek, M. L., Seifert, I., Frieß, W., Zeitler, J. A. (2020). Terahertz spectroscopy for protein lyophilizates. PSSRC 2020, online.

- **Kölbel, J.** and Zeitler, J. A. (2019). Is there a water content threshold for cluster formation in glycerol?, 44th International Conference on Infrared, Millimeter, and Terahertz Waves (IRMMW-THz) (poster).

- **Kölbel, J.**, Zeitler, J. A. (2019). Is there a water content threshold for cluster formation in glycerol? PSSRC 2019, Düsseldorf, Germany.

- **Kölbel, J.**, Shalaev, E., Zeitler, J. A. (2019) Is there a water content threshold for cluster formation in glycerol? Sensors Day 2019 (Student Showcase), Cambridge, UK.

- **Kölbel, J.**, Shalaev, E., Zeitler, J. A. (2018) Is there a water content threshold for cluster formation in glycerol? PSSRC 2018, Leuven, Belgium.

List of Figures

1.1 Schematic representation of entropy as function of temperature and change of specific heat with temperature for the crystalline, liquid, undercooled, and glassy state. . . . 4
1.2 Dielectric response of disordered materials. . . . 5
1.3 Potential energy landscape topology. . . . 7
1.4 Placement of terahertz radiation in the electromagnetic spectrum. . . . 9
1.5 Schematic diagram of PCA emitter and detector. . . . 11
1.6 Principle of a terahertz time-domain spectrometer. . . . 13
1.7 Dove prism for ATR. . . . 14
1.8 Absorbance spectra of binary mixtures of amorphous and crystalline forms of indomethacin. . . . 16
1.9 Dielectric losses for supercooled sorbitol. . . . 17
1.10 Dielectric losses at 1 THz for different polyols. . . . 20
1.11 Illustration of different possible pathways for the behaviour of lyophilised protein molecules with increasing temperature and activation energy. . . . 22
1.12 Mean square displacement of glycerol reported in various publications. . . . 23
2.1 Left: Utensils to make pellets. Right: Manual press in the glove bag. . . . 27
2.2 Rendering of the crystallisation cell. . . . 28
2.3 Liquid cells used for room temperature measurements. . . . 28
2.4 Diagram of the liquid cell. . . . 28
2.5 Sample holder for transmission measurements 29
2.6 The Terapulse 4000, cold finger, and cryostat. . . . 30
2.7 The setup for performing variable-temperature measurements. . . . 30
2.8 Screenshot of Terapulse software. . . . 32
2.9 Screenshot of motor control software. . . . 33
2.10 Analysis procedure. . . . 35
2.11 Optical path of the terahertz beam. . . . 36
2.12 Absorption coefficient of pure glycerol with possible offset. . . . 43
2.13 Multiple measurements of glycerol at room temperature. . . . 44

3.1 Terahertz absorption spectra change with temperature. Comparison to neutron, nuclear inelastic scattering, and Raman data. 53
3.2 The boson peak and absorption depend on temperature. 54
3.3 Maximum boson peak frequencies plotted against temperature. 54
3.4 Terahertz spectra change with temperature and water content. 55
3.5 Absorption coefficient at 1 THz extracted for different temperatures. 57
3.6 Absorption spectra for glycerol-water mixtures. 60
3.7 Boson peak extrapolated to 0 K. 61
3.8 Comparison of transition temperatures and rate of absorption change characterising different regimes. 63
3.9 Room temperature spectra and absorption coefficient at 1 THz. 66
3.10 Measured spectra (up to 2.5 THz) and extrapolated VDOS at higher frequencies as well as VDOS parameters. 67
3.11 Example for a high-temperature transition and overview T_x for different water concentrations. 70
3.12 Small variations in water content were visible between single measurements. . . 75
3.13 Setup to measure water uptake/loss of glycerol over time. 75
3.14 Change of water content over time. 76
3.15 Change of water content over time (long experiment). 76
3.16 Rate of change of water gain/loss. 77
3.17 Setup for reflection (i.e. surface) measurement. 77
3.18 Amplitude of reflected peak changes with time. 78
4.1 Visualisation of the different molecules. 83
4.2 DSC curves for binary mixtures. 86
4.3 DSC curves for different samples. 87
4.4 Terahertz spectra for different samples. 88
4.5 Absorption at 1 THz for different samples. 89
4.6 Possible potential energy landscape topology. 91
4.7 Boson peak visualisation with quadratic fit for lysozyme. 92
4.8 Boson peak visualisation for different samples. 93
4.9 Anharmonic absorption at 1 THz for different samples. 93

4.10 Extrapolated VDOS for different samples. 95
4.11 Extrapolated centre frequency and maximum absorption for different samples. . 97
4.12 Absorption coefficient of pure sucrose and mAb measured at 1 THz. 100
4.13 Transition temperatures and rate of absorption change with temperature. 101
4.14 Anharmonic absorption coefficient for mixtures of mAb and sucrose. 103
5.1 Spectra of NaCl and CsI solutions and absorption coefficient at various frequencies. 110
5.2 Molar absorption coefficient for salt solution and solutions with different proteins. 111
5.3 Absolute and relative change in the molar absorption coefficient when introducing proteins into salt solutions. 112
5.4 Snapshot of the AIMD simulations of the solvated $aSyn_{72-78}$ peptide and extracted radial pair distribution functions. 114
5.5 Absorption coefficient of aSyn at 1 THz with 1.5 M salt in the solid state. 115
5.6 Absorption of water in the solvation shell excluding the protein itself compared to bulk water absorption at 1 THz. 116
5.7 Absorption of protein and shell combined compared in solutions with NaCl and CsI for different thicknesses of the solvation shell. 117
5.8 Syn aggregation kinetics. 120
5.9 aSyn binds more Cs^+ than Na^+ which does not grossly affect aSyn conformation. 121
5.10 E. coli treated with NaCl have a higher content of aSyn aggregates compared to E.coli treated with CsI. 121
6.1 Schematic setup. 126
6.2 Three-view drawing of the cuvette. 127
6.3 Renderings of the metal sample holder with cuvette inserted. 127
6.4 Schematic of the path of the terahertz beam in the sample chamber. 131
6.5 Reference and sample waveforms and power spectra. 132
6.6 Spectra recorded at different times throughout the process. 133
6.7 Absorption coefficient of water and different sample holders measured without sample to quantify possible beam clipping. 134
6.8 Solid-state terahertz spectra of crystalline $MgSO_4 \cdot 7H_2O$. 139
6.9 Linear fit of temperature (°C) and absorption. 140
6.10 Calibration curve of $MgSO_4 \cdot 7H_2O$ at 5 °C. 141

6.11 Absorption and calculated concentration of the solute in the liquid phase c_l at 0.5 THz. 142
6.12 PXRD pattern of various $MgSO_4$ hydrates. 151
6.13 Crystalline $MgSO_4$ hydrates measured at different temperatures. 153
6.14 Comparison of simulated and measured spectra of $MgSO_4$ heptahydrate. 154
6.15 Visual analysis of crystal growth. 156
6.16 Absorption extracted at 0.5, 1, and 1.6 THz. 157
6.17 Analysis parameters during crystal growth plotted against concentration, time, and temperature. 159
6.18 Illustration of using the calibration method to calculate liquid phase solute concentration based on measured absorption at various frequencies. 160
6.19 Relative absorption calculated and plotted against molar concentration of $MgSO_4$. 161
6.20 Relative changes in α when comparing the measured to the calculated purely liquid absorption before, during, and after crystallisation. 163
6.21 Crystal dissolution analysis. 165
7.1 Anharmonic absorption coefficient of HSA-sucrose mixtures. 168
7.2 Nitrogen flow measured during various measurements. 170

List of Tables

3.1 Temperatures where a change of mobility or in the contribution of anharmonic effects are observed in glycerol. 59
3.2 Parameters describing the change of the boson peak in glycerol water mixtures with temperature for selected concentrations. 62
4.1 Samples used. 84
4.2 Lyophilisation protocol. 84
4.3 Rate of absorption change with temperature. 89
5.1 Fit parameters for NaCl solutions (top) and CsI solutions (bottom). 112
6.1 Concentration overview for different solid-state samples. 146

Contents

Declaration i

Acknowledgements ii

Abstract iii

Publications and Conference Presentations iv

List of Figures vi

List of Tables ix

1 Introduction 1

1.1 Thesis Overview . . . 1

1.2 Background . . . 1

1.2.1 Structural Order and Disorder, the Glass Transition . . . 1

1.2.2 Rotational and Vibrational Spectroscopy . . . 8

1.3 Introduction to Terahertz Time-Domain Spectroscopy . . . 9

1.3.1 Terahertz Radiation . . . 9

1.3.2 Terahertz Time-Domain Spectroscopy . . . 12

1.4 THz-TDS Studies of Disordered Systems . . . 18

2 Experimental Methods 26

2.1 Sample Preparation . . . 26

2.1.1 Solid Samples . . . 26

2.1.2 Liquid Samples . . . 27

2.2 Experimental Setup . . . 28

2.3 Data Acquisition . . . 31

2.4 Data Analysis . . . 34

2.4.1 Determination of Complex Optical Constants . . . 34

2.4.2 Determination of Glass Transition Temperatures and Estimation of their Errors . . . 38

2.4.3 Discussion of Possible Errors . . . 41

3 Glycerol-Water System: Structural Dynamics and Water Clustering 46

3.1 Structural Dynamics in the Glycerol-Water System 46

3.1.1 Introduction 46

3.1.2 Materials and Methods 50

3.1.3 Results and Discussion: Pure Glycerol 51

3.1.4 Results and Discussion: Glycerol-Water Mixtures 59

3.1.5 Conclusions 68

3.2 High-Temperature Transition 69

3.3 The Influence of Water Content on Hygroscopy 71

4 The Role of Terahertz Dynamics in Solid-State Protein Formulations 79

4.1 The Effect of Size on the Terahertz Dynamics of One-Component Lyophilisates . 80

4.1.1 Introduction 80

4.1.2 Materials and Methods 82

4.1.3 Results and Discussion 85

4.1.4 Conclusions 96

4.2 Sucrose-Antibody Lyophilisates 98

4.2.1 Introduction 98

4.2.2 Materials and Methods 99

4.2.3 Results and Discussion 99

4.2.4 Conclusions 105

5 The Influence of Salts on Protein Mobility in Solution 106

5.1 Introduction 106

5.2 Materials and Methods 108

5.3 Results and Discussion 109

5.4 Conclusions 118

5.5 Outlook: Complementary Techniques 119

6 In-situ Observation of the Structure of Crystallising Magnesium Sulphate Solutions 123

6.1 Flow Cell to Study Crystallisation Processes In-Situ 123

6.1.1 Introduction 123

6.1.2 Methods 126
6.1.3 Results and Discussion 130
6.1.4 Conclusions 135
6.2 Measuring Solute Concentration in Single and Multiphase Systems 135
6.2.1 Introduction 135
6.2.2 Experimental Section 137
6.2.3 Results and Discussion 138
6.2.4 Conclusions 142
6.3 In-Situ Observation of the Structure of Crystallising Magnesium Sulphate Heptahydrate Solutions 143
6.3.1 Introduction 143
6.3.2 Materials and Methods 145
6.3.3 Results and Discussion 149
6.3.4 Conclusion 166

7 Conclusion and Future Work **167**

8 References **171**

1 Introduction

1.1 Thesis Overview

The aim of this thesis is to explore and extend the ability of terahertz spectroscopy to study of systems with varying degrees of disorder. Temperature and concentration affect molecular mobility and thereby the spectral shape.

Chapter 1 introduces concepts and gives a brief overview of existing literature. Chapter 2 focuses on the experimental methods and techniques for data acquisition as well as for data analysis. In Chapter 3.1, terahertz time-domain spectroscopy (THz-TDS) is applied to study structural dynamics in liquid and supercooled glycerol. The same methodology is used in chapter 3.2 to investigate the effect of water clustering in glycerol-water mixtures. Chapter 3.3 focuses on a suspected high-temperature transition in glycerol-water mixtures and Chapter 3.4 on quantifying hydrophobicity.

Solid-state protein formulations are the focus of Chapter 4, especially the effect of size (Chapter 4.1) and the role of sucrose in sucrose-antibody lyophilisates (Chapter 4.2). The influence of salts on protein mobility in solution is studied in Chapter 5.

These chapters cover a range of disordered systems. Chapter 6 instead focuses on the transition from a disordered to an ordered system, i.e. crystallisation, utilising the example of $MgSO_4 \cdot 7H_2O$. Chapter 6.1 describes a flow cell setup that allows to study crystallisation processes in situ. In Chapter 6.2 a method to measure solute concentration in single and multiphase systems is introduced, and Chapter 6.3 combines the setup and the methodology to investigate the crystallisation process in detail utilising THz-TDS. In Chapter 7, the findings are briefly summarised and some directions for future work are presented.

1.2 Background

1.2.1 Structural Order and Disorder, the Glass Transition

An atomic or molecular motif composed of a few atoms that is reproduced periodically in space is called the unit cell of a crystal. Upon adding lattice vectors to a point in space, the same structural situation is recovered, thereby achieving long range order by translational invariance. If X-ray diffraction is performed on a perfectly crystalline sample to determine the time-averaged

atomic positions, the diffracted intensity can be written as

$$I(\vec{Q}) = |F(\vec{Q})|^{\,2} \cdot \vec{I}(\vec{Q}) \tag{1.1}$$

where $\vec{Q}$ is the scattering vector, $\vec{F}$ is the structure factor that reflects the distribution of molecular positions in the unit cell relative to the lattice points, and $\vec{I}$ is the interference function that reflects the lattice geometry. In large crystals, $\vec{I}$ determines the positions of the Bragg peaks.[1]

However, in reality crystals contain defects, for example local displacements of atoms or a chemical substitution. Two kinds of crystalline imperfections are distinguished: imperfections of the first kind preserve the long range positional order of the lattice, i.e. fluctuations of the interatomic distances do not increase with the distance between motifs. An example for this is thermal agitation: the centres of mass of molecules are perfectly ordered, but single atoms and molecules are constantly vibrating and librating. Imperfections of the second kind do not preserve strict long range order, the fluctuations of the inter-motif distances increase with the distance between motifs or unit cells.[1]

The extreme case of a material containing imperfections of the second kind is an amorphous material which can only be described statistically because no lattice can be identified. The so-called pair distribution function (PDF) $g(r)$ gives the probability of finding an atom at the distance r from another one. An experimentally determined $g(r)$ describes the short range order of a material. Liquids and glasses do not exhibit long range order and are therefore classified as amorphous.[2]

Utilising amorphous materials is beneficial for example for the pharmaceutical industry. Often, active pharmaceutical ingredients (API) have a low solubility in water and hence a decreased bioavailability. In their amorphous state, they have a higher apparent aqueous solubility than in their crystalline form. However, it is important to control and predict the rate of recrystallisation and short and long-term stability.[1]

If a crystal is melted at temperature T_{m}, and the temperature is then decreased, the sample can either re-crystallise or undercool, i.e. it can stay amorphous. These two states have a different stability, measured by the Gibbs free energy G:

$$G = H - TS \tag{1.2}$$

and

$$\mathrm{d}G = -S\mathrm{d}T + V\mathrm{d}p \tag{1.3}$$

with the enthalpy H, temperature T, entropy S, volume V, and pressure p. Below T_m, the amorphous state has a higher free energy than the crystalline state and is hence only metastable.

Three main factors determine the the kinetics of recrystallisation of an undercooled liquid: the thermodynamic driving force (the decrease in free energy), molecular mobility, and structural similarity between liquid and crystal.

A simple description predicts a decrease in the recrystallisation rate close to T_m because the thermodynamic driving force is small. At much lower temperatures, decreased mobility also decreases the recrystallisation rate. However, crystallisation is a far more complex phenomenon based on the interplay of nucleation and crystal growth.

In classical nucleation theory, a nucleation event is the random appearance of a crystalline cluster with a minimum critical size. Sometimes, these clusters grow into crystalline domains. Nucleation and growth processes are not necessarily maximal at the same temperature. The nucleation rate $N(T)$ can be written as:

$$N(T) = f(T)\exp(-g/RT) \tag{1.4}$$

where the mobility term $f(T)$ describes the addition of molecules from the melt to the crystal, g is the nucleation barrier, and R is the universal gas constant. A similar semi-phenomenological expression for the growth rate $V(T)$ is:

$$V(T) \propto v(T) \cdot \Omega(\Delta G) \cdot [1 - \exp(-\Delta G/RT)] \tag{1.5}$$

with the mobility term $v(T)$. $\Omega(\Delta G)$ depends on the growth mechanism. Oswald's rule of stages states that the first form to crystallise is not that of the highest thermodynamics driving force but that of the highest entropy due to the change in disorder between the crystalline and amorphous phases. Crystallisation can be avoided if a sample is cooled very rapidly (quench-cooled) to decrease molecular mobility.[1]

A so-called undercooled liquid has a higher specific heat ($C_p = \frac{\partial H}{\partial T}$) than a crystal until the calorimetric glass transition temperature $T_{\mathrm{g},\alpha}$ is reached. At this temperature, the specific heat and expansion coefficient drop abruptly and the sample forms an amorphous glass with

reduced mobility, it vitrifies. Angell classified strong and fragile glass formers by the change of the viscosity of a material with temperature as it approaches the glass transition temperature from above and the corresponding change in heat capacity at $T_{g,\alpha}$ as shown in Figure 1.1.[3]

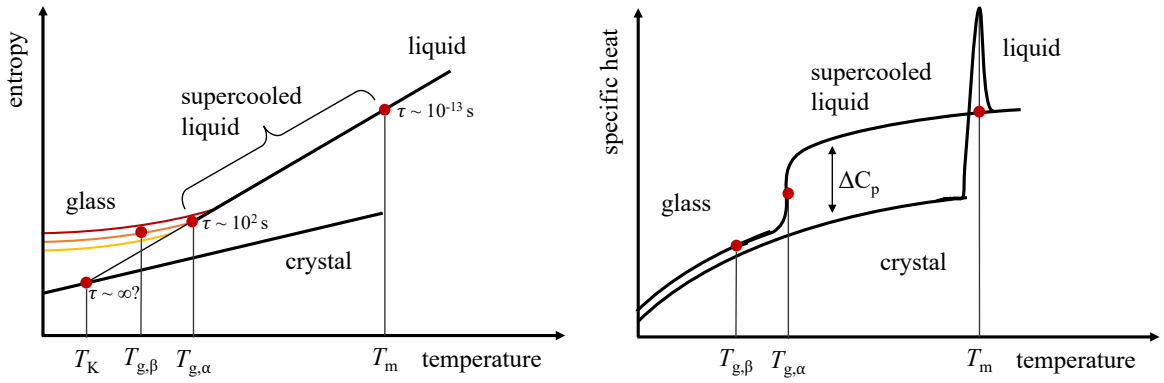

Figure 1.1. Left: Schematic representation of entropy as function of temperature in a liquid (high temperature, above melting point T_m) down to the supercooled liquid (below T_m) and further down into the glassy regime (below $T_{g,\alpha}$, eventually reaching $T_{g,\beta}$). The exact value of $T_{g,\alpha}$ depends on the cooling rate, slower cooling results in a lower $T_{g,\alpha}$ (different colours). Also shown are typical relaxation times, most notably $\tau \approx 100\,\mathrm{s}$ at $T_{g,\alpha}$. T_K is the Kauzmann's entropy crisis temperature, where the extrapolated liquid entropy hits the crystal entropy and where according to some theories there is a thermodynamic phase transition. Experimentally, this hypothesis could not yet be proven because a glass forms before that temperature is reached. Right: Change of specific heat with temperature for the crystalline, liquid, undercooled, and glassy state. At $T_{g,\alpha}$, the specific heat drops to a value close to that of the crystal. For clarity, only one cooling rate is shown. Adapted from Cavagna et al.[4]

The glass transition however is not a first-order phase transition and does not involve structural change. The structure factor of a glass is still that of a liquid. Furthermore, the exact value of the glass transition depends on the sample history, for example the cooling rate. A higher cooling rate results in a higher value of $T_{g,\alpha}$. Changing the cooling rate by one order of magnitude often changes $T_{g,\alpha}$ by about 3 K to 5 K.[1]

Below $T_{g,\alpha}$, the molecular mobility is reduced and molecules rearrange so slowly that they cannot explore all possible configurations within experimental time scales ($\approx 100\,\mathrm{s}$). The only motions still contributing to the specific heat are local motions, the local mobility, e.g. vibrations. Equivalently, according to the Maxwell relation (shear viscosity is proportional to the structural relaxation time), glass formers have a viscosity of about 10^{13} poises at $T_{g,\alpha}$.[1]

Between T_m and $T_{g,\alpha}$, the sample is in a metastable equilibrium and ergodic, i.e. the system can explore all possible configurations. Below $T_{g,\alpha}$, the system is no longer ergodic and ensemble averaging becomes restricted. It is no longer in an equilibrium state and tends to a stable state during ageing. The potential energy landscape (or surface, PES) instead describes potential energy minima corresponding to specific molecular configurations of the system. When an

experiment is performed on a glass, the outcome results from averaging over a limited number of domains of the PES which have been accessible to the system.[1]

Spectroscopic studies have been very useful to sample the PES and thereby explain different properties of ordered and disordered materials.[2] Dielectric spectroscopy measures the dielectric response of disordered materials that is due to a variety of different absorption mechanisms over a wide frequency range (see Figure 1.2).

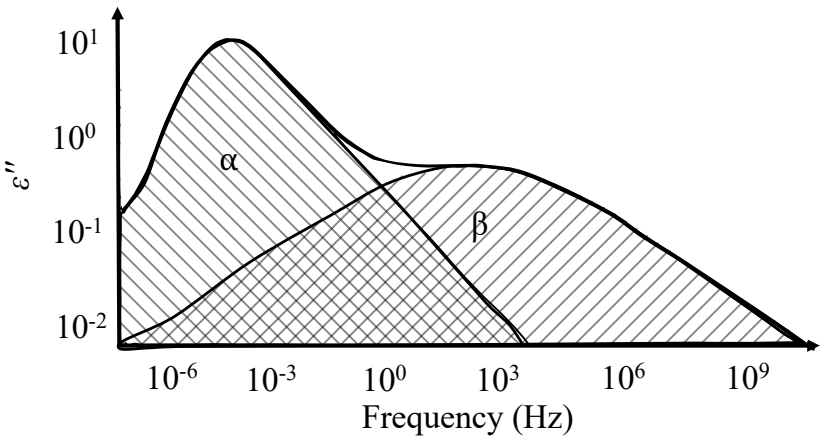

Figure 1.2. Dielectric response of disordered materials: α and β processes. Origins of the α and β-relaxation are discussed in the text. Chapter 1.3 focusses on absorption processes at higher (terahertz) frequencies. Adapted from Descamps et al.[1]

Dielectric spectra generally contain primary and secondary relaxation features. In statistical mechanics, "relaxation" denotes an irreversible process: the time-dependent change of a system or of a sub-system from one physical or thermodynamic state to another, involving the dissipation of energy.[1]

The primary (or α-) relaxation (global mobility) takes place in a temperature dependent frequency window of approximately 10^{-6} to 10^{3} Hz and vanishes below $T_{\mathrm{g},\alpha}$ when molecular mobility is decreased but not arrested. Aging of the glass occurs, as well as small-scale molecular motions. While some of these motions are due to internal degrees of freedom of molecules, another type of relaxations have first been identified by Johari and Goldstein. The Johari-Goldstein (JG) β processes are intrinsic to amorphous materials (even completely rigid molecules) and generally involve localised molecular motions. In low molecular weight compounds they may consist of translational and rotational motions of individual molecules but the exact nature of these motions is still debated. These motions however have a lower activation energy than the α-relaxation and therefore emerge at lower temperatures, and the associated transition tempera-

ture that characterises their onset, $T_{g,\beta}$, is thus lower than $T_{g,\alpha}$.[5] Johari introduced the concept of islands of mobility in a structurally nonuniform glass: translational and/or orientational motions of molecules in loosely packed regions form the origin of the JG-process and molecular motions in high-density regions are observed as the α-process.[6,7] Ngai developed a coupling model[8–11] and proposed that this primitive relaxation is located close to the most probable relaxation time of the JG β-relaxation.

According to the coupling model, which aims to link experimental observations in the mid-infrared and terahertz range to collective translational and/or rotational motions by means of a coupling process, the JG-relaxation (which Ngai considers a subset of the so-called primitive α-relaxation) is inherently coupled with the α-relaxation. The model also states that at low temperatures, molecules are trapped in cages formed by their neighbours, resulting in a nearly constant loss in susceptibility. This regime is terminated by the primitive relaxation involving rotation and/or translation of individual molecules, and the transition temperature is identified with $T_{g,\beta}$, thereby coupling the caged molecule dynamics with the JG-relaxation, and hence also the α-relaxation.[8–11]

However, both $T_{g,\alpha}$ and $T_{g,\beta}$ can be detected with a range of experimental techniques that probe different time-scales. For example, dielectric spectroscopy,[12] dynamic mechanical analysis (DMA),[13] differential scanning calorimetry (DSC),[14] and terahertz spectroscopy.[15] Time-scales probed experimentally with infrared and terahertz spectroscopy, for example, lie in the range of femto- to picoseconds, whereas the relaxation processes associated with α- and β-relaxation take place in milliseconds to seconds. This indicates that a more fundamental origin exists that links experimental data with the α-relaxation and results in the observed temperature behaviour.[16] There are several other theories that try to describe the origins of transition temperatures, including configurational entropy,[17] caged dynamics,[11] as well as the already mentioned islands of mobility[18] and Goldstein's energy landscape.[19]

Goldstein introduced the concept of large basins in the PES that are separated by high energy barriers that can be overcome by thermally activated hopping processes: moving from one basin to the next requires a high activation energy and cooperative rearrangement of molecules. At decreased temperature, the configurational entropy, i.e. the number of available minima, decreases. β-relaxations instead are linked to many smaller minima within the large basins with a much smaller activation energy (Figure 1.3).[20] This would explain why $T_{g,\alpha}$ and $T_{g,\beta}$ can be

detected with a multitude of analytical techniques as they are linked to the underlying structure of the PES that can be investigated with a range of different methods.

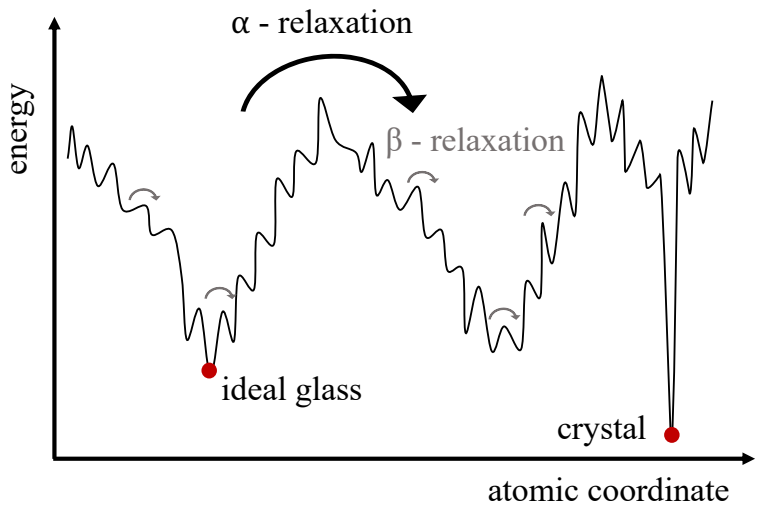

Figure 1.3. Potential energy landscape topology. With sufficient thermal energy, a sample can explore different configurations on the hypersurface. Schematic adapted from Descamps et al.[1]

Another theoretical framework that tries to describe glass phenomena is mode-coupling theory (MCT)[21] that is based on first principles. The aim of MCT is to describe the microscopic relaxation dynamics of glass-formers relying only on the knowledge of time-independent parameters such as the structure factor that can easily be obtained from scattering experiments. There is a strong bias to consider static properties and not explicitly account for molecular properties. In order to be able to compare results obtained from MCT with experiments over a wide range of temperatures, i.e. to describe the vitrification process from liquid to glass, the structure factor is usually measured for several temperatures and a separate MCT calculation focussing on density fluctuations is performed for each temperature. The theory has been shown to accurately predict the existence of a glass transition[22] at a critical temperature T_c, although this usually overestimates the experimentally found $T_{g,\alpha}$.

MCT also predicts another relaxation, the "fast β-relaxation", which is argued to arise from "rattling motions" of molecules in cages formed by their neighbours and therefore not necessarily of the same origin as the β-relaxation defined earlier.[23]

Spectroscopic measurements are very useful to gain insights into molecular excitations and can be used to confirm or disprove theories. A study by Wuttke et al. for example investigated supercooled glycerol with both neutron and light scattering.[24] Glycerol is a material where

mode coupling dynamics are competing with bond formation and breaking and deviations of experimental results from the theory are observed.[24] Wuttke's experiments resulted in qualitatively similar spectra, but showed pronounced deviations from the predictions made with MCT. It was concluded that MCT only provided a partial description of the system and a more detailed treatment of microscopic dynamics was necessary. This conclusion was later confirmed experimentally by more spectroscopic studies.[25,26]

1.2.2 Rotational and Vibrational Spectroscopy

Infrared spectra contain information about vibrational and rotational motions of molecules. Depending on the frequency range, this can be for example rotational motions (mostly in the microwave region), librations, torsions, or vibrations (mostly in the IR region). Intermolecular interactions usually fall into the "fingerprint region" below approximately $500\,\mathrm{cm}^{-1}$.[27]

From quantum mechanics it follows that those motions are quantised, i.e. only certain frequencies and therefore energies are allowed. For the example of a rigid diatomic molecule in the harmonic approximation, possible **rotational** energies are:

$$E_{\mathrm{rot}} = \frac{J(J+1)\hbar^2}{2MR^2} \tag{1.6}$$

Where J is the quantised angular momentum and the selection rule $\Delta J = \pm 1$ applies, with M the reduced mass, R the distance between the two atoms, and $\hbar$ the reduced Planck constant.[28]

Vibrational energy levels for a similarly simple example, the quantum mechanical harmonic oscillator, are given by:

$$E_{\mathrm{vib}} = \hbar\omega(n + \frac{1}{2}), (n = 0, 1, 2, ...) \tag{1.7}$$

Where ω is the angular frequency of the oscillator and n is the energy state. The frequency of that system is then given by:

$$\omega = \sqrt{\frac{k}{M}} \tag{1.8}$$

Where k is the force constant.[29]

These relations illustrate that energy levels resonant with terahertz radiation (in the frequency range of approximately $10^{12}\,\mathrm{Hz}$) correspond to systems with either small force constants or a large reduced mass. This is the case for example in the solid state where weak intermolecular

interactions between atoms and molecules often lead to vibrational motions that have small force constants, resulting in translations and external rotations of entire molecules. Larger molecules further exhibit internal torsional modes that also lie in the energy range probed with terahertz spectroscopy.

In practice, anharmonicity results in different shapes of the potentials, for example described by the Morse potential $V = D_e(1 - \exp(-\beta(r - r_0)^2))$, where D_e is the depth of the well, β is the level of curvature at the bottom of the well and $(r - r_0)$ is the internuclear distance. Anharmonic effects become more pronounced at higher energy levels when the shape of the potential differs more from that of the harmonic oscillator and the spacing of energy levels decreases.[28] The Boltzmann distribution describes how populated different energy levels are depending on temperature. At room temperature, excited states at terahertz frequencies are common. Hence in crystalline systems, a frequency shift and height change of peaks in the spectrum is often observed when the temperature is changed.[30] In disordered systems, where no peaks are present in the spectra, a temperature change still results in a different population of excited states as well as in changes in the mobility.

1.3 Introduction to Terahertz Time-Domain Spectroscopy

1.3.1 Terahertz Radiation

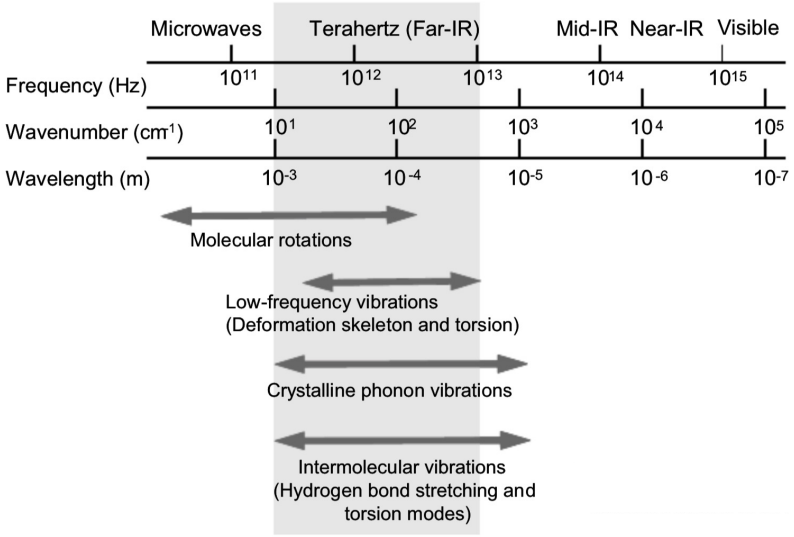

Figure 1.4. Placement of terahertz radiation in the electromagnetic spectrum. Adapted from Song et al.[31]

Terahertz radiation is non-invasive and non-destructive when investigating molecular solids due to the low photon energies, which lie in the loosely defined range between 0.4 and 40 meV (corresponding to frequencies between 0.1 and 10 THz). It is located between the microwave and far-infared region of the electromagnetic spectrum (Figure 1.4) and this spectral region has historically been to referred to as the "terahertz gap" due to the difficulties associated with the generation and detection of terahertz radiation, i.e. relatively weak incoherent sources, high intensity thermal background emission, and the requirement for cryogen cooled detectors.[31]

At gigahertz frequencies, electronic oscillating circuits can generate micrometer and millimeter waves but the transit time of carriers in semiconductors limits their applications at higher frequencies. Conversely, the lack waveguides for photonic devices hinders the use of optical techniques at those frequencies[32] although the development of beyond 5G-networks in sensing technologies and wireless communications is currently bridging that gap.[33]

Instead, a new experimental approach was used to to explore dynamics at terahertz frequencies. Maxwell's equations predict that a time-varying electric current radiates an electromagnetic pulse. Coherent terahertz radiation was first generated by Auston et al. in 1984 utilising photoconductive switches.[34] Free space propagation of terahertz pulses was successfully achieved in 1988/89 by Auston, Nuss, and Grischkowsky and this opened up new applications for spectroscopy.[35,36]

There are several types of emitters and detectors of terahertz radiation. What all emitters have in common is an ultrafast laser oscillator or amplifier that generates optical pulses with femtosecond pulse durations which are transformed into a picosecond terahertz pulse.[37] The most common emitters and detectors are photoconductive antennas (used for both generation and detection), and optical rectification (generation) and electro-optic sampling (detection). These are coherent detectors/emitters, which are a prerequisite for terahertz time-domain spectroscopy. Non-coherent, thermal detectors are for example bolometers and Golay cells.

Emitter: Photoconductive Antenna

When using a photoconductive antenna (PCA) as an emitter, a NIR femtosecond laser pulse generates carriers in the conduction band of a semiconductor between the two electrodes that form a Hertzian dipole oscillator antenna structure. A DC bias voltage is applied across the physical gap, forming a capacitor, which accelerates the carriers, thereby generating an electromagnetic pulse (shown schematically in Figure 1.5). If the geometry is chosen correctly, strong

electron scattering limits the photocurrent. The bandwidth of the emitted pulse is limited by the carrier lifetime in the semiconductor substrate. This combination results in sub-picosecond current pulses which then emit radiation at terahertz frequencies.[37,38] To decrease the beam divergence, silicon lenses collimate the beam directly after generation, for example by grafting them onto the PCA. Common emitter materials are semi-insulating GaAs (SI-GaAs) or low-temperature grown GaAs (LT-GaAs) and the photon energy of the laser needs to be larger than band gap of the material, e.g., GaAs is commonly paired with a Ti:sapphire laser (wavelength around 800 nm).

Detector: Photoconductive Antenna

A PCA used as a detector operates similarly to the emitter. However, instead of applying a DC voltage across the gap, the arrival of a terahertz pulse generates the electrical bias. If the NIR laser pulse arrives simultaneously with the terahertz pulse, free carriers are generated, the conductivity increases, and a photocurrent $J(t)$ directly proportional to the incoming terahertz electrical field is produced:

$$J(t) = \int_{-\infty}^{t} \vec{E}_{\mathrm{THz}}(t')\sigma(t-t')\mathrm{d}t' \tag{1.9}$$

The shorter the carrier lifetimes, the sharper the temporal response and hence the larger the achievable bandwidth. The generated current however is only on the scale of picoamperes to nanoamperes and this poses challenges for the detection. Due to thermal noise, the signal is of the same amplitude as the noise and selective signal amplification using a lock-in amplifier is needed. Because the NIR pulse has a much shorter duration than the terahertz pulse, it can "map" the electric field of the terahertz pulse in the time-domain by the use of a delay stage.[38]

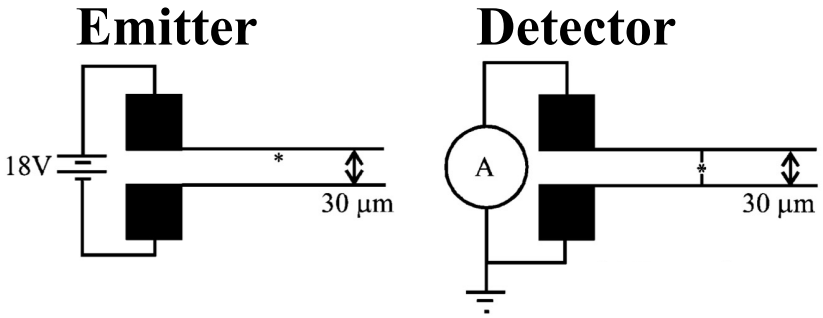

Figure 1.5. Schematic diagram of PCA emitter and detector. The asterisk represents the site at which the near-IR laser is focused. Adapted from Schmuttenmaer et al.[38]

Generation by Optical Rectification

Generation by optical rectification is primarily used in amplifier-based systems. If a nonlinear medium such as crystalline ZnTe is illuminated with fast optical laser pulses, intense electrical fields can be generated.[39] Optical rectification can be understood as mixing the high-frequency components of an optical pulse with the low-frequency components and thereby producing a pulse at the difference frequencies which fall into the terahertz range.[40] The bandwidth of the generated terahertz pulse is only limited by the optical laser pulse width and self-absorption of the used electrooptic material. Besides ZnTe, $LiNbO_3$, GaAs, and InP are also commonly used materials.[41,42]

Electro-Optic Sampling

Electro-optic sampling detects the terahertz radiation indirectly by use of a detection beam (optical sampling pulse). When the incident terahertz beam interacts with the detector crystal (often ZnTe), it introduces birefringence proportional to the amplitude of the pulse (Pockels effect).[39] When the sampling pulse hits the detector at the same time as the terahertz pulse, its polarisation is rotated proportionally to the amplitude of the incident terahertz pulse and the direction of rotation is proportional to the sign of the field. When the sampling pulse subsequently passes through a Wollaston prism and is split into two orthogonal linearly polarised beams, their difference signal can be recorded, again utilising a lock-in amplifier.[43] By varying when the detection pulse arrives at the crystal, the entire terahertz pulse is mapped, and this mapping in the time-domain is the principle behind terahertz time-domain spectroscopy.[43]

1.3.2 Terahertz Time-Domain Spectroscopy

In a typical terahertz time-domain spectrometer, a femtosecond (fs) near-infrared (NIR) laser pulse is divided by a beamsplitter into two pulses (see Figure 1.6). One (the "pump") reaches the terahertz emitter (often a photoconductive antenna) where a single cycle terahertz pulse is generated. This pulse, containing frequencies in the terahertz range, is directed by mirrors to pass through the sample. After interacting with the sample, the pulse is refocused onto the receiver.

The second part of the fs NIR pulse that has been split off at the beamsplitter (the "probe"), is also focused onto the receiver after passing through a variable time delay line that varies its

phase. A receiver signal is only present when both pulses are detected (i.e. the receiver is time-gated). The duration of the probe pulse is much shorter than that of the pump pulse and by varying the time delay, the electric field of the terahertz pulse at the detector is sampled and both its amplitude and phase are recorded. That provides the advantage that optical constants like the refractive index and absorption coefficient can be determined without the need to perform a Kramers-Kronig analysis.[38,44]

The detection scheme is coherent: constant background and incoherent signals are disregarded, resulting in a higher signal-to-noise ratio compared to other methods like Fourier-transform infrared (FTIR) spectroscopy. Because the measurement takes place in the time domain, this measurement technique is also called terahertz time-domain spectroscopy (THz-TDS).

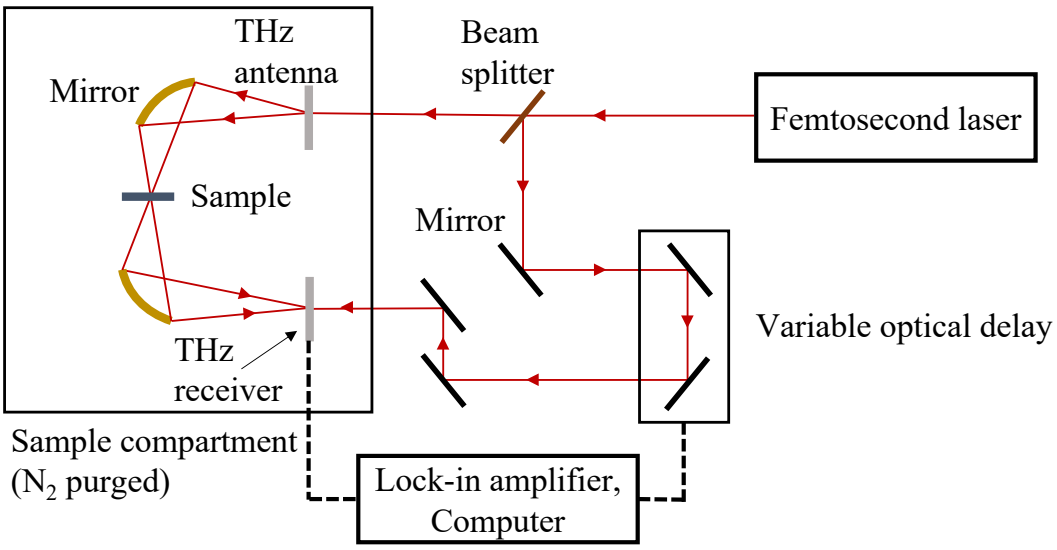

Figure 1.6. Principle of a terahertz time-domain spectrometer. Adapted from Schmuttenmaer et al.[38] and Bawuah et al.[45]

Different Geometries

Emitters and detector set up in different geometries allow to investigate samples for example in transmission, reflection, and attenuated total reflection.

In a transmission setup, the terahertz beam is transmitted at normal incidence to the sample from the emitter to the detector. The highest measurable absorbance (when the sample signal is at the same level as the noise) at a certain dynamic range (DR) is given by:

$$(\alpha d)_{\max} = 2 \ln \left(DR \frac{4n}{(n+1)^2} \right) \tag{1.10}$$

Where n is the refractive index of the sample with thickness d and absorption coefficient α.[46] The setup and data analysis are described in detail in Chapter 2.

Using the reflection mode instead is useful when investigating strongly absorbing samples by recording the field reflected from the sample. Contrary to transmission measurements, thickness and absorption do not influence the dynamic range and the maximum measurable absorption is defined by the reflectivity of the reference mirror and hence noise level.[46] This technique has been used for example for characterising polar liquids such as water or to track water ingress into pharmaceutical tablets.[47,48]

Another useful technique is attenuated total reflection (ATR). Utilising a Dove prism that can be inserted into a transmission-type THz-TDS system, the evanescent terahertz field generated by total internal reflection penetrates into the sample (shown in Figure 1.7) and by measuring the reflected signal, information about the sample surface region can be gained. ATR THz-TDS has for example been used to study surface plasmons in doped semiconductor materials.[49]

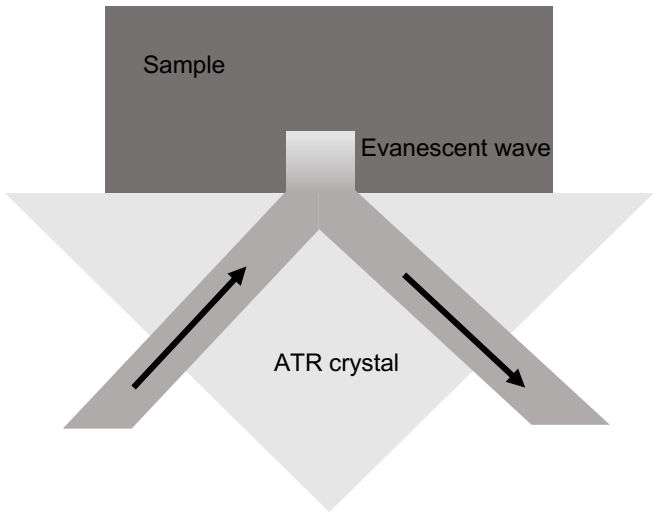

Figure 1.7. Dove prism for ATR. The evanescent terahertz field penetrates into the sample. Adapted from Mathanker et al.[50]

Terahertz radiation has been used in spectroscopy studies to characterise parameters like amorphous stability, molecular mobility, and intermolecular and intramolecular interaction strengths.[51,52] Many polymers that are opaque in the visible range are transparent at terahertz frequencies.

Terahertz Spectra of Crystalline and Disordered Systems

Different absorption mechanisms contribute to the observed absorption spectra at terahertz

frequencies. The already discussed dielectric relaxation processes (α and β-relaxation) dominate at gigahertz frequencies but penetrate into the frequency windows accessible with common THz-TD spectrometers (0.3 THz to 3 THz) when molecules have significant mobility.[27] Vibrational modes with energies of a few millielectronvolts also fall into the terahertz range and are populated at room temperature.

The long-range order exhibited by crystals allows the observation of discrete phonon modes with THz-TDS that are reflected in well-defined peaks in the spectra. These modes provide information about vibrational and rotational, as well as inter- and intramolecular motions. THz-TDS is particularly sensitive to hydrogen bonds and can measure a sample's "fingerprint" and thereby easily distinguish between different polymorphs.[53]

The overlap of inter- and intramolecular motions at terahertz frequencies however poses a challenge when interpreting the data. Individual atomic contributions to spectra can be hard to assign. Computational tools have been further advanced in the last decade and have led to insights into the origin of the terahertz response of crystalline solids by enabling a comparison of recorded spectra with simulations often based on density functional theory (DFT).[54,55]

The intensity of infrared (IR) active modes is proportional to the change in dipole moment μ upon displacement of molecules:

$$A_p \propto \left| \frac{\partial \mu}{\partial q_p} \right|^2 \tag{1.11}$$

where A_p and q_p are the intensity and displacement vectors of the pth mode, respectively, which can be shown utilising Fermi's golden rule.

In a material where the potential energy surface is perfectly harmonic, the vibrational energy spacing is constant and all of the vibrational transitions for a particular mode would be exactly the same energy. In this theoretical case, the measured intensities would be independent of temperature.[56,57]

However, in real materials, the PES is not completely harmonic and different transitions correspond to different energy levels, leading to peak broadening and shifting. In anharmonic potentials, mode coupling can also occur, opening up to further relaxation pathways and broadening the peaks. The peak shapes are hence determined by mode coupling and relaxations as well as vibrational lifetimes.[58,59]

Cooling of a sample reduces the effects of vibrational coupling and thereby decreases the

peak width and increases the peak intensity.[59] However, temperature variations also result in structural changes, namely thermal expansion, that also impact the intensity and frequency of IR-active modes.[60] In experiments, all these factors are combined and lead to complicated frequency and intensity shifts upon temperature changes. Even at very low cryogenic temperatures, anharmonicity in the PES leads to mode coupling, and thermal expansion influences the spectra.[57]

Accurately predicting the IR-intensity changes of a crystalline system is a field of active research.[59] Quasi-harmonic approximation (QHA) allows to determine the vibrational modes as a function of volume, mimicking thermal expansion. The intensity change predicted by QHA depends on the material and the behaviour of the vibrational modes depending on structural changes. QHA does not explicitly treat anharmonicity or mode coupling, all calculations are still performed under the harmonic approximation.[60,61]

In Figure 1.8 absorbance spectra of the amorphous and crystalline forms of indomethacin are shown, highlighting the difference between crystalline and amorphous terahertz spectra.

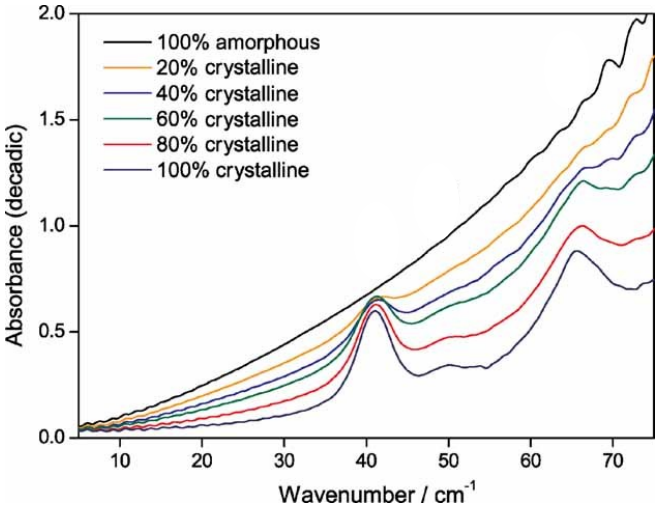

Figure 1.8. Absorbance spectra of binary mixtures of amorphous and crystalline forms of indomethacin at room temperature. Adapted from Strachan et al.[62]

In disordered materials, for example glasses, no discrete phonon modes can be sustained and the coupling of photons to the vibrational density of states (VDOS) forms the main absorption mechanism of amorphous samples in the terahertz range. It results in a broad "microscopical peak" that spans several THz and might have an underlying multi-peak structure.[63]

In disordered solids, modes are also coupling, and even to a greater degree than in crystalline samples.[63,64] As the spacing between molecules is no longer regular or periodic, this leads

to a series of narrow resonances. However, it is as yet unresolved whether the increase in absorption observed upon heating in amorphous samples[57] is due to vibrational modes that change in intensity or whether the entire VDOS shifting to lower frequencies as the temperature is increased.[65]

Indeed, it is not disputed that anharmonic effects increase with temperature when higher energy levels are populated. So while some amount of anharmonicity is present and influencing the spectra even at cryogenic temperatures, often a harmonic approximation leads to (very) good agreement between theoretical models and experimental results for crystalline systems.[56] In amorphous materials, the PES is also less harmonic at elevated temperatures when the system is more mobile.

A measurement of sorbitol on a broadband synchrotron THz-TD spectrometer provided dielectric loss measurements for frequencies in the range 1.5 THz to 13.5 THz, as shown in Figure 1.9. Due to high costs and beam time availability, this method is not usually applied to measure absorption in the terahertz range and benchtop spectrometers with a lower spectral range (ca. 0.3 THz to 3 THz) are more commonly used.

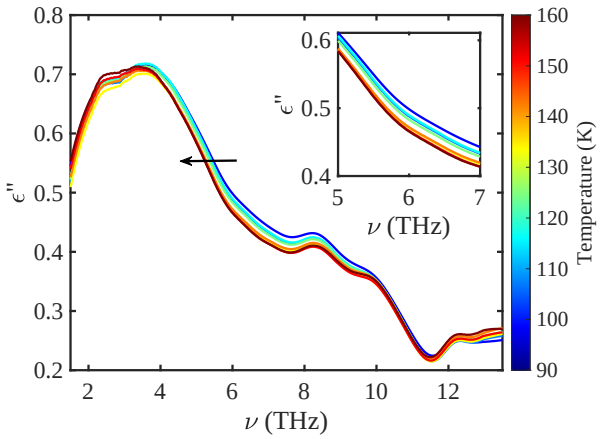

Figure 1.9. Dielectric losses for supercooled sorbitol for temperatures below 160 K and $T_{g,\beta}$ (178 K). Inset shows in more detail that the VDOS shifts towards lower frequencies with heating. Adapted from Ruggiero et al.[65]

The measurement of sorbitol shows some shifting of the entire VDOS to lower frequencies. It is probable that the observed increase in absorption in the spectrum of amorphous materials is due to a combination of different factors (i.e. VDOS shifting and intensity changes of modes).

Predicted by Debye theory and confirmed experimentally with far-infrared spectroscopy, the VDOS has a frequency-squared dependence. With increasing temperature, the total absorption

rises at the commonly measured frequencies (below 3 THz). At the glass transition temperatures, there is no apparent change in the spectra and one cannot distinguish the spectra of a glass, a supercooled liquid, and a liquid by eye. The excess density of states above the Debye level (i.e. an apparent peak at terahertz frequencies made visible when plotting the absorption coefficient divided by frequency-squared) is termed boson peak. It can be observed in experimental data when plotting the absorption coefficient by frequency squared, as well as when plotting the reduced density of states $g(\omega)/\omega^2$.[15]

There is evidence that boson-peak-related anomalies result from glass-specific structural quenched disorder.[2,66,67] The Ioffe-Regel limit denotes the frequency at which the mean-free path of transverse waves becomes equal to their wavelength, meaning that there is a crossover from wave-like to random-matrix-like physics.[67–69] Schirmacher et al.[69] and Marruzzo et al.[67] described the boson peak as a precursor for elastic instability. Due to this change of physical mechanisms, some models[68] are only valid above the boson peak and different parts of the spectra (and hence the VDOS) can be described separately.

At frequencies above the boson peak, an exponential decrease in the reduced density of states has been found experimentally[70] and explained for example by a model of Schirmacher et al. that is based on random spatial fluctuations (elastic heterogeneities) of dilatational-free (shear) stresses.[66,71,72]This model predicts a shape of $\omega^2 \exp(-\omega/\omega^2)$ for the VDOS at frequencies above the boson peak. Traditionally, a power law has also been used to describe the terahertz absorption spectra of glasses and amorphous solids.[73]

When investigating the model glass-former glycerol, Chumakov et al.[68] found that a significant part of the boson peak consists of collective modes by measuring the reduced density of states of collective motions with neutron scattering. They also found that it disappeared close to $T_{g,\alpha}$ due to increased sample mobility and further observed an exponential decrease in the reduced DOS at energies above the boson peak maximum. This will be discussed in detail in Chapter 3.1.

1.4 THz-TDS Studies of Disordered Systems

Previous experiments have used THz-TDS to investigate for example polymers,[74] disordered crystals,[75] and inorganic glasses.[76] Organic glasses have been studied even more extensively than inorganic because of their lower glass transition temperature that is often at or below

room temperature, and the liquid, supercooled, and glassy states are therefore easier to access experimentally.

Small Organic Molecules

THz-TDS is very sensitive to van-der-Waals forces and hydrogen bonds, which are prevalent in polar small organic molecules that form hydrogen-bonded chain structures (for example alcohols).[77–79] The loss spectrum of such a system is dominated by different types of relaxation that each occur on different time scales, characterised by their relaxation time τ, namely:

1. Cooperative rearrangement of the alcohol-alcohol chain structure ($\tau_1 \approx 100\,\mathrm{ps}$)
2. Reorientation of individual alcohol molecule situated at the end of the alcohol-alcohol chain ($\tau_2 \approx 10\,\mathrm{ps}$)
3. Relaxation of liquid molecules in the process of hydrogen-bond formation and breaking ($\tau_3 \approx 1\,\mathrm{ps}$)

These can be combined in an often used Debye model that can be fit to the complex dielectric loss spectra with the angular frequency ω:

$$\tilde{\epsilon} = \epsilon_\infty + \frac{\Delta\epsilon_1}{1 + i\omega\tau_1} + \frac{\Delta\epsilon_2}{1 + i\omega\tau_2} + \frac{\Delta\epsilon_3}{1 + i\omega\tau_3} \tag{1.12}$$

However, a point to consider is that by simply fitting more terms to the spectra, the fit quality can be improved but it can be unclear whether the data have been overfitted. If the model is restricted to two terms, the relaxation times for water become $\tau_1 = 8\,\mathrm{ps}$ and $\tau_2 = 170\,\mathrm{fs}$. Yada et al. included two further terms to describe intermolecular stretching vibrations and the formation and breaking of hydrogen bonds and studied their respective temperature dependence.[80] Models with two or three Debye terms have been applied to alcohols and their aqueous mixtures,[81,82] sugar-water mixtures,[83] and ionic liquids.[84,85]

Further studies on the (temperature dependence of) dielectric relaxation processes in water and its mixtures with other liquids provided for example information about hydration shells around solvated protons in water,[86] the structure of methanol/water mixtures and acetonitrile/water mixtures (complemented by MD and IR simulations),[87,88] the interaction between nonpolar and polar solvents,[89–91] as well as the complex interplay between reorientation motion and vibration dynamics in hydrogen-bonded liquids.[92–94]

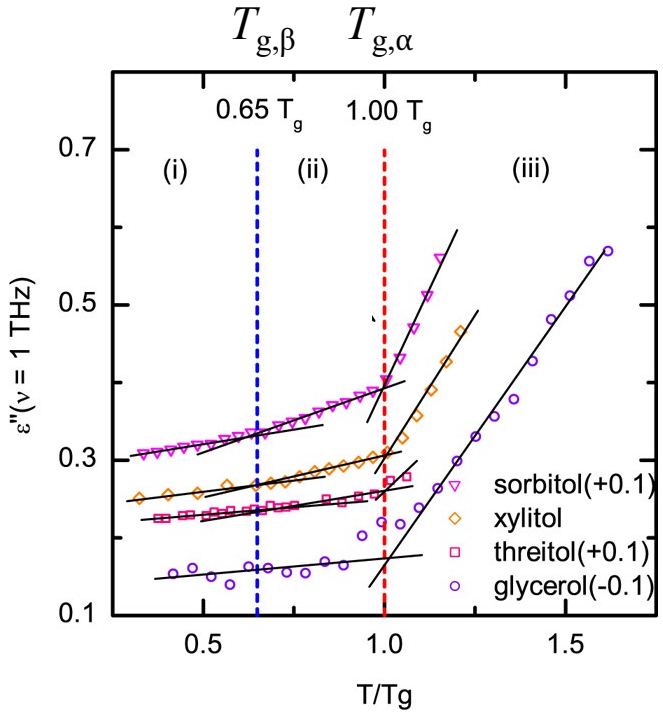

Figure 1.10. Dielectric losses at 1 THz for different polyols with glass transition temperatures highlighted. The respective offset is indicated in the legend. Adapted from Sibik et al.[95] T_g is 269, 253, 216, 194 K for sorbitol, xylitol, threitol, and glycerol, respectively.

Upon supercooling glasses, the losses decrease and the boson peak emerges. This was for example studied for the polyols glycerol, threitol, xylitol, and sorbitol.[95] When plotting the losses at 1 THz, Sibik et al. observed a linear decrease with temperature until $T_{g,\alpha}$, where a change of gradient occurred when the primary relaxation became too small to contribute to the molecular mobility and hence spectra. In the case of sorbitol, xylitol, and threitol, $T_{g,\beta}$ was observed approximately at a fraction of $0.65\,T_{g,\alpha}$. $T_{g,\alpha}$ and $T_{g,\beta}$ of glycerol are more similar in temperature and were only identified by a combined T_g, as shown in Figure 1.10.

By studying both normal and secondary alcohols, it was found that the position of the OH group had a strong effect on local structures in monohydric alcohols.[93]

Macromolecular Solid-State Systems

More complex amorphous systems may also show a glass transition behaviour. In polymers, the α-relaxation is usually associated with segmental motions of a few monomeric units whose onset defines $T_{g,\alpha}$. The temperature at which localised reorientational motion of smaller segments occurs characterises $T_{g,\beta}$.[96,97]

The biodegradable copolymer poly lactic-co-glycolic acid (PLGA) was investigated with THz-

TDS and its dynamics were correlated with temperature, lactide to glycolide ratio, and free volume. It was found that the widely used empirical Fox-Flory equation[98,99] predicting $T_{\mathrm{g},\alpha}$ as a function of molecular weight (M_{n}) can be applied:

$$T_{g,\alpha} = T_{g,\alpha,\infty} - K/M_{\mathrm{n}} \tag{1.13}$$

With the proportionality constant K and $T_{g,\alpha,\infty}$ the glass transition temperature for an ideal polymer chain of infinite length.[100] It was rationalised that the free volume of a polymer with a lower molecular weight is relatively high due to the increased number of chain ends. This and temperature effects lower the barrier heights of Goldstein's potential energy landscape.[101]

Polymer-peptide interactions were studied using the example of lyophilised (freeze-dried) PLGA microspheres and glass transition temperatures $T_{\mathrm{g},\beta}$ and $T_{\mathrm{g},\alpha}$ were found to depend on the interaction strength between the polymer and the peptide.[102] Increased polypeptide loading led to a higher $T_{\mathrm{g},\beta}$ due to a stronger hydrogen-bond network impacting the free volume and molecular mobility.[102]

Lyophilised protein formulations are even more complex. The onset of $T_{\mathrm{g},\beta}$ is associated with local dipole mobility and in proteins, individual parts or subunits of the molecule can become mobile upon heating if the respective potential energy barrier is overcome. This leads to a distribution of active motions in the entire sample. For example, the terahertz dielectric response of oxidised cytochrome c solutions was increased at 200 K, attributed to activated side chain motions.[57]

THz-TDS measurements of lyophilised proteins (globular bovine serum albumin and an antibody) and of spray-dried BSA have shown a plateauing of terahertz active modes above approximately 300 K which suggests a localised confinement of the protein/excipient matrix at high temperatures hindering a further mobility increase. It has been proposed that upon heating, protein molecules can either continuously explore new conformations (accompanied by high molecular mobility and an increase in the terahertz absorption) or reach an energy minimum, which introduces a plateau in the terahertz absorption, as schematically shown in Figure 1.11.[103,104]

These molecular jamming effects however occurred above storage temperature. It has been hypothesised that active motions below storage temperature can influence stability and thereby the storage time. An increase in molecular mobility has been correlated with reduced storage stability.[106] Subtle changes in formulation influenced the high-temperature behaviour of

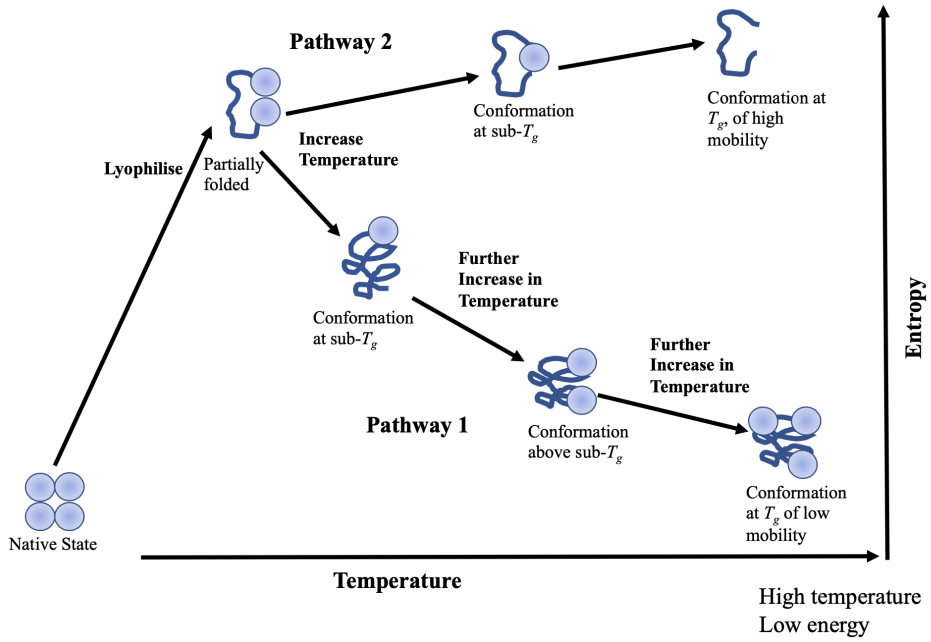

Figure 1.11. Illustration of different possible pathways for the behaviour of lyophilised protein molecules with increasing temperature and activation energy. Excipients are not included here for clarity. Adapted from Shmool et al.[105]

biomolecules as well as their stability. This could be because the excipient matrix slows down local protein conformation fluctuations.[107]

The onset temperature of internal protein mobility in the solid state is usually referred to as the protein dynamical transition temperature.[57,108] The exact nature of the motions and relaxation processes is still discussed, however, it is generally accepted that understanding protein dynamics is key to their biochemical activity and function.[109] Experiments have shown that the protein dynamical transition does not depend on a polypeptide, secondary, or tertiary structure.[110]

The value of the protein dynamical transition further depends on frequency and hydration, with some results indicating that the presence of solvent (often water molecules) is a necessary precursor for the dynamical transition, ensuring that the protein can access anharmonic motions.[111–113]

Historically, the dynamic transition was often detected in the mean square displacement (MSD) calculated from neutron scattering data which relies heavily on some models and assumptions. This can be visualised when comparing the reported mean square displacement of the relatively simple model system glycerol between different publications, as shown in Figure 1.12.

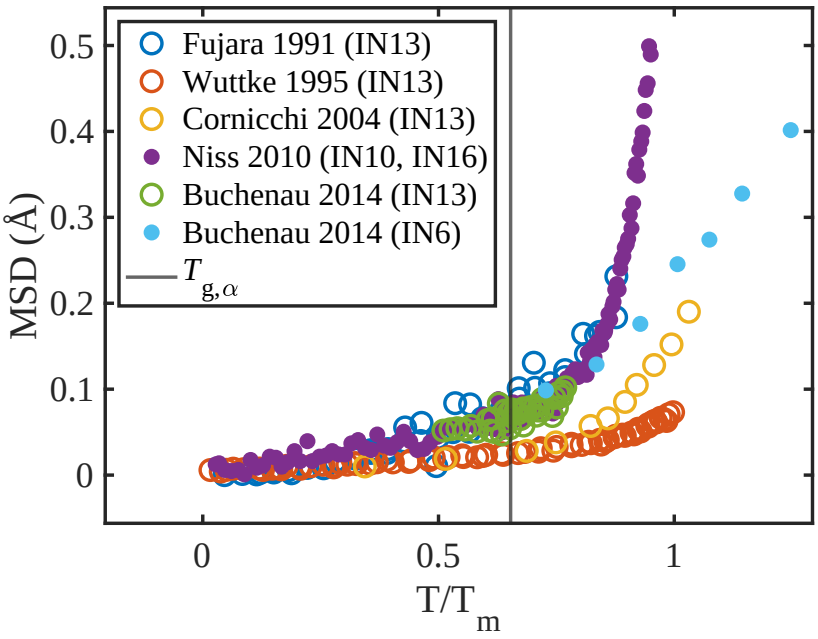

Figure 1.12. Mean square displacement of glycerol reported in various publications scaled by glyerol's melting temperature T_m (291 K) and the calorimetric glass transition temperature $T_{g,\alpha}$ (194 K) is also shown by the vertical line. Measurements were performed either on the IN6, IN13, or IN16 in Grenoble and should yield very similar values. The apparent differences can be attributed to the data processing. Data are taken from Fujara et al.,[114] Wuttke et al.,[70] Cornicchi et al.,[115] Niss et al.,[116] and Buchenau et al.[117]

Nonetheless, the hydration level and solvent strongly impact terahertz dynamics and small water clusters may play a role in the dynamic transition.[118] In solution, proteins exhibit a characteristic T_m above which unfolding events and denaturation can occur and some have linked the solution-state T_m to events occurring in the solid state by using it as a scaling parameter.[119] The importance of protein-solvent interactions for protein conformational changes, stability, and unfolding is commonly recognised.[109]

Macromolecules in Solution

The high absorption coefficient of liquid water limits the use of THz-TDS to study solvated biological samples in transmission geometry: an attenuated total reflection setup can yield information about a thin layer.[50] In transmission, the sample length is commonly limited to less than 200 µm.

Despite these experimental limitations, THz-TDS has been useful to probe changes in the fast water network dynamics or collective intermolecular vibrations. Biomolecular solutes like proteins, salts, or sugars interact with the surrounding water. Due to conformational fluctuations

and local confinement of water molecules the hydration shell of proteins exhibits dynamical inhomogeneities.[120] It has been shown that water activity in the hydration shell can be reduced[121,122] and that the solvent is influenced beyond the first hydration shell.[123] Reorientational water dynamics influence residue side chains which again induce changes to the protein core, resulting in longer time scale motion of protein backbone necessary for its function.[124,125]

Crystallisation

Of interest was also the phenomenon of recrystallisation and the following model can be fit both to the spectra of disordered as well as ordered samples:[73,126]

$$\sigma' = n(\nu)\alpha(\nu) = A + C(\nu - \nu_0)^q \tag{1.14}$$

where σ' is the real part of the conductivity, ν_0 and A the experimental low-frequency cut-off and absorption offset at that frequency, respectively, and the exponent q is about 2 for glasses, decreases upon heating to 1 for liquids, and approaches 2 again during crystallisation. THz-TDS has been used to study crystalline polymorphs,[62,127] hydrates,[128,129] or co-crystals[130,131] and Strachan et al. showed that it is possible to use THz-TDS and a least-squares analysis to determine the levels of crystallinity in a mixture of amorphous and crystalline drugs as low as 1 %.[62] Upon increasing the crystallinity, the intensity of vibrational modes increased while the featureless absorption decreased (see Figure 1.8). This has been applied to a range of systems, even to aqueous mixtures in attenuated total reflection geometry.[132]

Further crystallisation studies were performed at different temperatures. Above $T_{g,\alpha}$, the crystallisation and subsequent phase change into a different polymorph of paracetamol were studied for example.[126] However, crystallisation can also occur below $T_{g,\alpha}$, as demonstrated using the example of naproxen.[133] The thermodynamic driving force toward the crystalline state is its lower total energy and the local mobility at temperatures between $T_{g,\beta}$ and $T_{g,\alpha}$ enables nuclei formation and crystal growth. The higher the thermal gradient at those temperatures, the more local mobility contributes and results in a lowering of stability.[133]

Different models can be applied to monitor the progress of crystallisation, either by simple peak tracking,[134] or by fitting more complex functions, for example by the sum of a Lorentzian centred at a crystalline feature (frequency ν_c, half width at half maximum γ, height A) and a power law to describe the background:[135]

$$\alpha(\nu) = \frac{A}{1 + (\frac{\nu - \nu_c}{\gamma})^2} + B\nu^a + C \tag{1.15}$$

In the latter case, an Avrami-type kinetics was found to describe the progress of crystallisation well:

$$\Phi = 1 - \exp\left(-K(t - t_{\text{ind}})^n\right) \tag{1.16}$$

where K and n are the Avrami constants and t_{ind} the induction time.

The line shape of features in a crystalline terahertz spectra is often described by a Gaussian or Lorentzian due to the exponential vibrational population relaxation.[136] In infrared studies of disordered materials on the other hand, a power law ($\alpha(\nu) = B\nu^a + C$) showed a good fit for the low-THz frequency absorption with an exponent close to 2 in many reported cases. This fit was hence adopted for fitting THz-TDS spectra and is commonly used.[73,137]

These examples illustrate that terahertz spectroscopy is very useful to study the role of vibrational dynamics in systems with varying structural order and disorder. The next chapter introduces experimental methods in more detail.

2 Experimental Methods

2.1 Sample Preparation

2.1.1 Solid Samples

Solid samples were ground gently in an agate mortar with a pestle to a uniform powder, transferred into a pellet die and subsequently pressed into pellets with a manual hydraulic press (Specac Ltd., Kent, UK) at a load of $\approx 2\,\mathrm{t}$ (shown in Figure 2.1). The resulting cylindrical samples had a diameter of 13 mm. To preserve the dynamics in amorphous samples under measurement conditions, as well as the widest possible temperature range for measurements (polyethylene, a common dilutant, has a melting point of 400 K, for example, which can be too low when investigating lyophilised proteins), the samples were not mixed with a diluting material and the sample absorption hence limited the pellet thickness, which had implications for their physical stability. For highly absorbing samples about 50 mg to 80 mg of powder were used to make 300 µm to 800 µm thick samples that were put between two quartz windows during measurements for physical support. For less absorbing samples, about 250 mg to 300 mg powder were needed and the resulting pellets had a thickness of 2 mm to 3 mm and could be measured free-standing.

Polycrystalline samples were diluted with high density polyethylene (PE, Induchem, Volketwil, Switzerland) and also made into free-standing samples. In the case of diluted samples, a second pellet of pure PE was pressed, containing the same amount of PE as the sample, which was used as the reference subsequently.

The whole process was either performed under ambient conditions or in a glove bag (Atmos-Bag, Sigma-Aldrich Company Limited, Gillingham, Dorset, UK) purged with dry air to avoid water uptake from air by strongly hygroscopic samples. The pellets were then placed in a sample holder (either sandwiched between z-cut quartz windows or directly, as described above) for subsequent measurements.

Figure 2.1. Left: Utensils to make pellets. Right: Manual press in the glove bag.

2.1.2 Liquid Samples

For studying the crystallisation of magnesium sulfate heptahydrate, $MgSO_4 \cdot 7H_2O$ (Sigma-Aldrich, Gillingham, UK) was mixed with Milli-Q water (IQ 7000, Merck, Darmstadt, Germany, resistivity 18.2 MΩ cm) to the desired concentration in a beaker. The mixture was placed on a magnetic stirrer for constant stirring until the sample was fully dissolved.

Other liquid samples were mixed to desired concentrations and, if needed, de-gassed by placing them inside a desiccator and reducing the pressure with an attached vacuum pump.

For measurements performed close to room temperature, the liquid was either injected into a crystallisation cell (described in detail in Chapter 6, shown in Figure 2.2) or a custom-built liquid cell (shown in Figure 2.3). The former consisted of a microfluidic channel between two quartz windows with an inlet and an outlet that could be fit into a hollow metal block through which a cooling/heating medium was circulated to control the temperature. The custom-built liquid cell consisted of two z-cut quartz windows (diameter 32 mm), a PTFE spacer, a metal top, inlets and outlets, and a metal jacket. The spacer determined the thickness of the sample.

Prior to any measurement, the cell was taken apart and all parts cleaned thoroughly. Sample was injected once the cell had been assembled and any air bubbles were purged. The sample holders for the liquid cells fit directly into the sample compartment of the spectrometer.

For measurements at cryogenic temperatures, the liquid samples were sealed tight to avoid sublimation when the pressure was reduced during measurements. A drop of liquid was hence placed onto the centre of one quartz window, loctite super glue (Henkel Adhesives, UK) and cyanolube adhesive (Electrolube, UK) were applied to both sides of a spacer and used to create

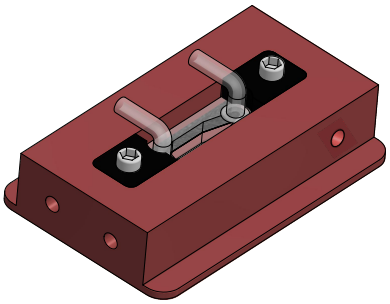

Figure 2.2. Rendering of the crystallisation cell. The set-up is described in detail in Chapter 6.

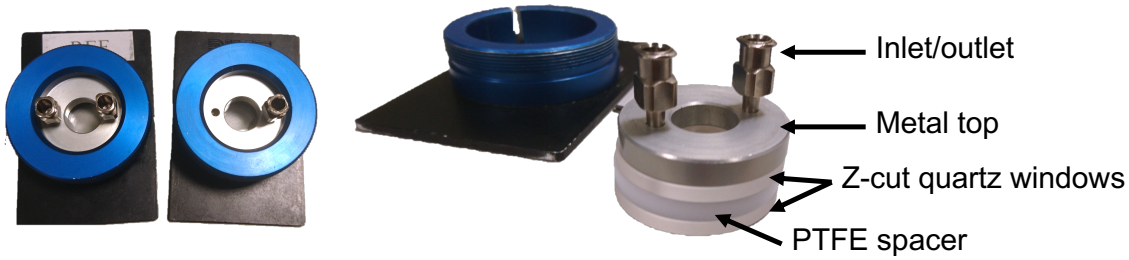

Figure 2.3. Liquid cells used for room temperature measurements. A spacer is inserted between two windows and the sample is injected from the top.

an airtight seal around the liquid, as shown in Figure 2.4. After the glue had dried, the cell edges were further wrapped in parafilm. An existing sample holder that fit onto the coldfinger was widened by 0.5 mm to encompass the liquid cell.

2.2 Experimental Setup

Solid samples were either sandwiched between two z-cut quartz windows (diameter 13 mm, width 2.05 mm) or directly placed in the sample holder (see for example Figure 2.5). Reference measurements were either performed of an empty sample chamber (for free-standing samples), of two z-cut quartz windows (for pure, sandwiched samples), or of the sample chamber containing

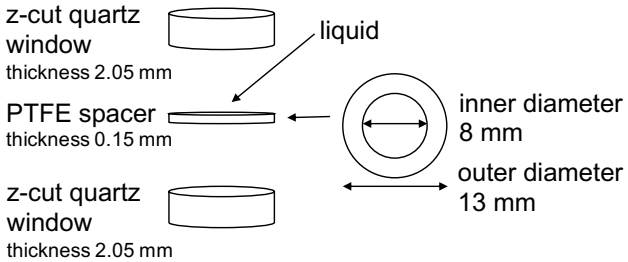

Figure 2.4. Diagram of the liquid cell. The spacer in the form of a hollow cylinder is first glued onto the bottom window, the sample is loaded between the spacers and then the upper window is glued on top.

the PE pellet (for diluted samples).

For both liquid and solid samples, the sample holder was fit into the sample compartment of the spectrometer so that it was situated at the waist of the beam. For room temperature measurements, no further preparation was needed and reference and sample spectra were acquired once the measurement chamber was completely purged with dry air.

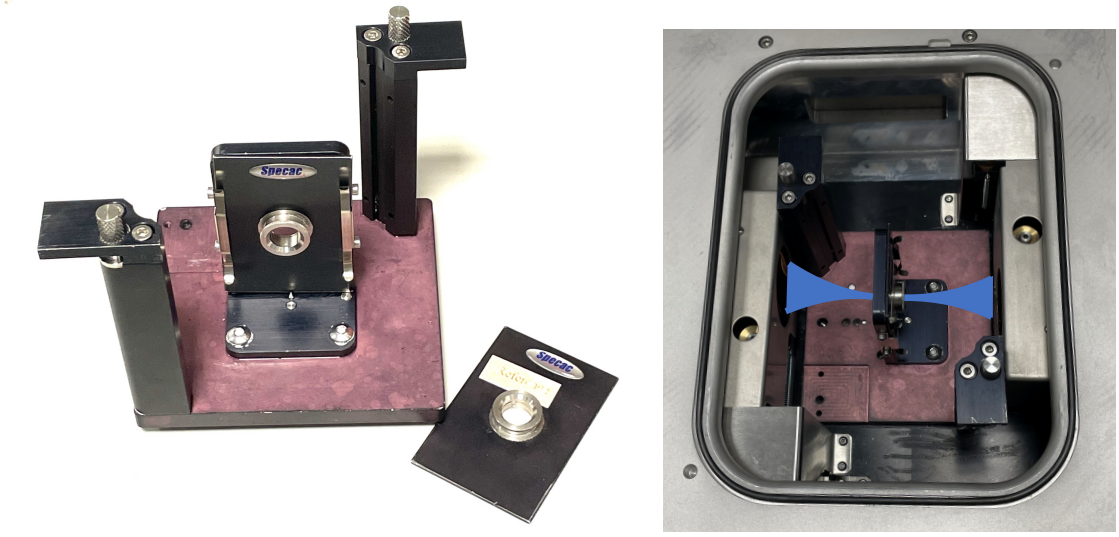

Figure 2.5. Left: Sample holder for transmission measurements of solid pellets at room temperature. Right: Inserted into sample chamber. The location of the beam is highlighted in blue.

To study both solid and liquid samples at variable temperatures, a modified Janis ST-100 cryostat system (Janis, Wilmington, USA) was used. Both a sample and a reference were screwed onto the end of the coldfinger, as shown in Figure 2.6. The transmission chamber was set up for temperature-variable measurements by inserting a vacuum chamber into which the cryostat was placed vertically so that the coldfinger was situated at the beam waist. By moving it up and down with an electrical motor, reference and sample were moved in and out of the beam centre.

The vacuum chamber was evacuated with a vacuum pump (Turbolab 90/250 i, Leybold GmbH, Germany) to a pressure of 4 mbar during measurements to facilitate cooling with liquid nitrogen. The rest of the measurement chamber was further purged with dry air to remove highly absorbing water vapour from the beam path. A thermocouple and silicon diode were situated close to the end of the coldfinger to monitor the temperature. Heating was achieved with a cartridge heater and a Lakeshore 331 temperature controller (Lakeshore, Westerville, USA) was used to control the temperature via an internal PID-controller.

The amount of liquid nitrogen flow needed to keep the system at a stable temperature

varied depending on temperature. The flow was therefore roughly regulated by hand and the PID-controller achieved temperature stabilisation by varying the heating power. The usable temperature range was 80 K to 500 K for solid samples, and 80 K to 305 K for liquid samples.

Before starting a measurement, the assembled system (shown in Figure 2.7) was cooled down to the minimum desired temperature (often 80 K) and left to equilibrate for at least 20 min.

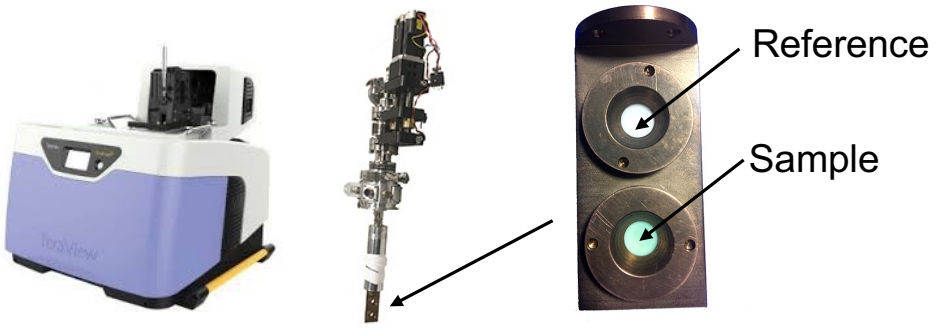

Figure 2.6. The Terapulse 4000 (left) was used for all measurements. For variable-temperature measurements, both reference and sample were screwed onto a cold finger (right) which was situated at the end of a Janis cryostat (middle).

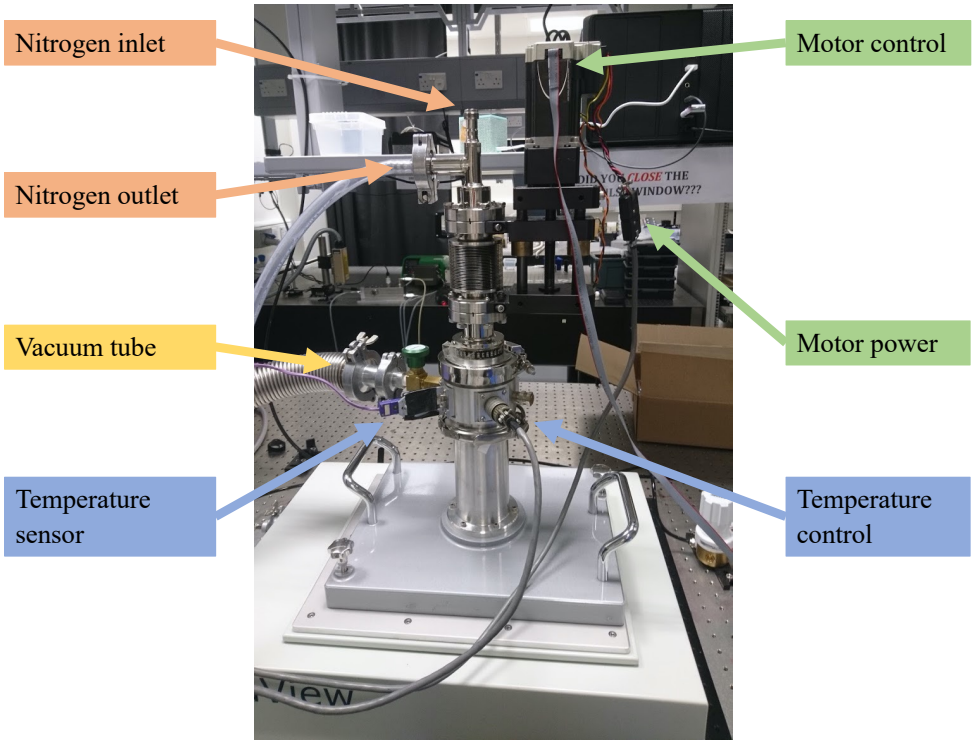

Figure 2.7. The setup for performing variable-temperature measurements.

2.3 Data Acquisition

The software "Terapulse" of Teraview Ltd. (Cambridge, UK) was used to acquire the measurements and "SEM Terminal" (Schneider Electric Motion, USA) was used to control the motor and switch between sample and reference during variable-temperature experiments. The interface is shown in Figure 2.9.

Utilising standard settings for the "Spectra Series" measurement type, each measurement consisted of an average of 1,000 waveforms, with a waveform rate of 15 Hz, and the resolution was set to 0.94 cm^{-1}. The optical delay offset was varied depending on whether quartz windows were used and resulted in a shift of the recorded waveform in the time-domain. These settings were used for all measurements except when crystallisation was investigated.

In crystallisation measurements, air was used as the reference while the sample was located between quartz windows, introducing a larger time delay between the reference and sample waveforms. Therefore, the so-called "Hi-res" mode was used in which a longer optical delay was probed and each measurement was formed of the average of only 15 waveforms. This introduced necessary changes to the data analysis procedures which are described in detail in Chapter 6.

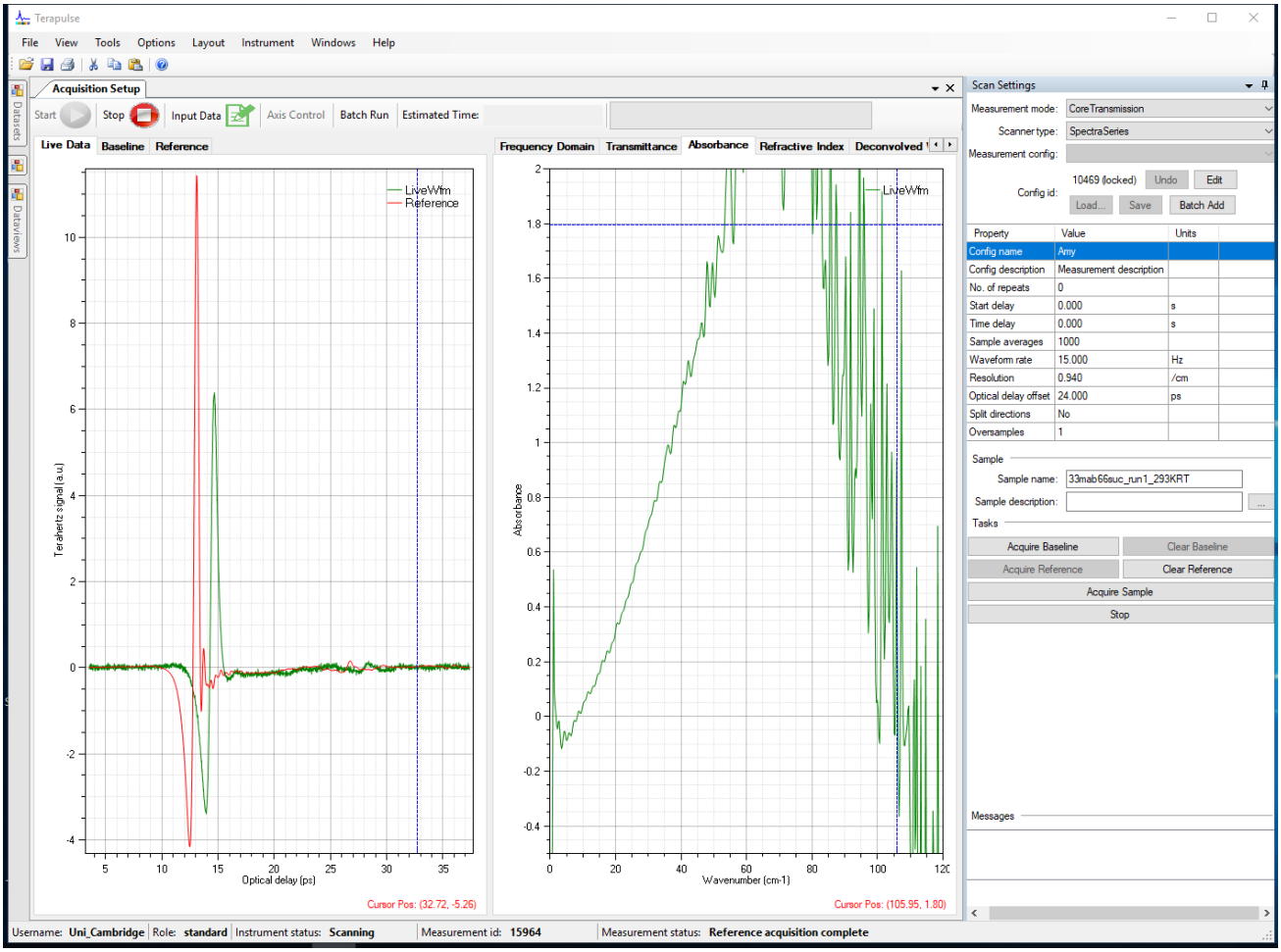

Figure 2.8. Screenshot of typical measurement settings.

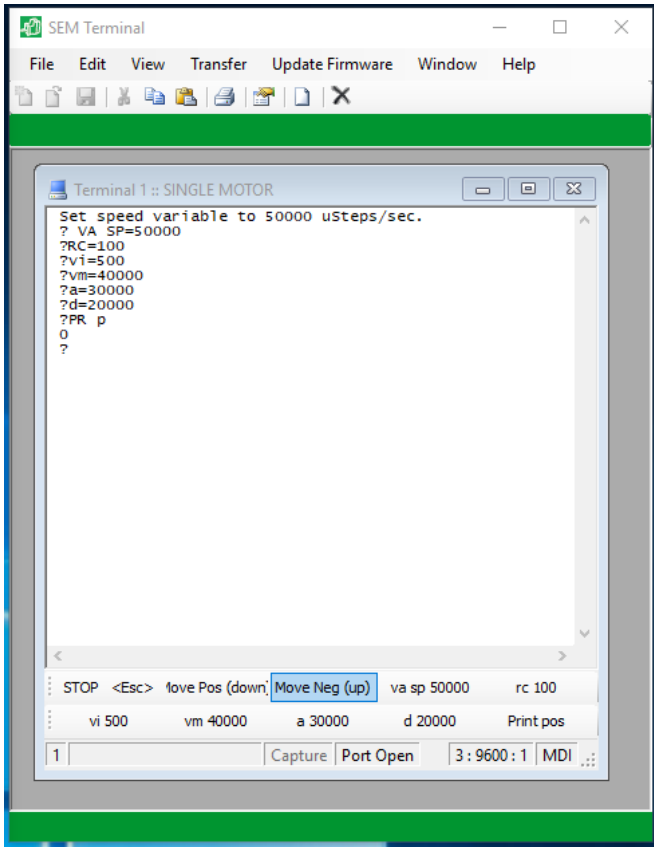

Figure 2.9. Screenshot of motor control software.

In all cases, the reference and sample waveforms were acquired alternatively. Variable-temperature measurements can be quite time consuming and to partly automate the process, the existing programme "TPA" (designed by Mario Gaimann, DAAD RISE Worldwide Summer Research Intern) was altered and used. It controlled the mouse and keyboard and was interfaced with the heater and motor so that the temperature change could be initiated automatically after a fixed amount of time and the motor could switch between reference and sample when needed. The only part not yet automated is the liquid nitrogen flow.

Utilising the programme, each temperature step of 10 K took approximately 10 min, so that the average heating rate for all samples was $1\,\mathrm{K\,min^{-1}}$.

Algorithm 1 Terapulse Automation programme (TPA)

```
initialise motor, heater, screen settings, remote control of mouse and keyboard
waitForUserInput sample position, temperature range and steps, TemperatureTolerance

for T = temperature(1) to temperature(end) do
    adjustTemperature and wait for fixed time

    while ΔTemperature > TemperatureTolerance do
        wait
    end while

    moveToReference

    while acquireReference do
        if ΔTemperature > TemperatureTolerance then
            soundAlarm
            wait, continue measurement once ΔTemperature < TemperatureTolerance
        end if
    end while

    moveToSample

    while acquireSample do
        if ΔTemperature > TemperatureTolerance then
            soundAlarm
            wait, continue measurement once ΔTemperature < TemperatureTolerance
        end if
    end while

    save

end for

exit programme
```

2.4 Data Analysis

2.4.1 Determination of Complex Optical Constants

Generally, data analysis is performed in two steps, as shown in Figure 2.10. First, the power spectra are calculated by applying a fast-Fourier-transform (FFT) to the measured reference and sample waveforms. Secondly, the complex-valued optical constants are calculated, which are then used for further analysis and extraction of information about the samples, for example

the glass transition temperature.

The Fourier-transform of the function $f(t)$ is defined as

$$F(\omega) = \mathcal{F}(f(t)) = \frac{1}{\sqrt{2\pi}} \int_{-\infty}^{\infty} f(t) \cdot \exp(-i\omega t) \mathrm{d}t \tag{2.1}$$

Measured waveforms contain a finite number of discrete data points, and the FFT hence computes the discrete Fourier-transform and converts the data from the time domain into the frequency domain. An electric field in the frequency domain is described by a complex variable, $\tilde{E}(\omega) = E(\omega) \cdot \exp(-i\phi(\omega))$, where ω denotes the angular frequency and ϕ the phase. An advantage of THz-TDS is that both amplitude and phase are measured directly.

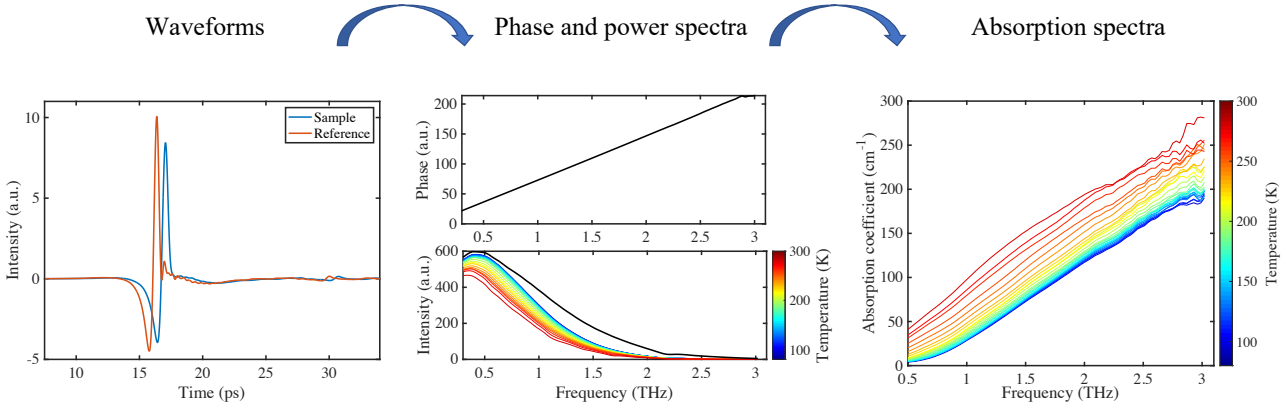

Figure 2.10. Analysis procedure: First, reference and sample waveforms are acquired (left, shown for only one temperature for clarity), then transformed into the frequency domain; the phase information for the reference is shown on the top, and the amplitude is shown on the bottom (reference in black, sample measurements blue to red), and finally the absorption coefficient (right) from which other optical parameters are calculated.

The data analysis is performed in matlab and the optical constants are extracted using either the Beer-Lambert-law (for weakly absorbing samples) or the method developed by Duvillaret et al.[138] (general case). Both methods agree very well for weakly absorbing samples and allow to extract the complex refractive index ($\tilde{n}_2$) and absorption coefficient (α).

The following is assumed:[138]

- Samples and windows are magnetically isotropic
- There are no free surface charges
- The sample, reference, and windows are homogeneous and the interfaces are flat and parallel

- The electromagnetic response of sample, reference, and window is linear
- The terahertz beam is approximated by a plane wave impinging on the sample at normal incindence
- The polarisation is linear and parallel to the optical axis
- The samples are optically thick, i.e. Fabry-Pérot reflections are temporally well separated

Utilising these assumptions, light passing through media is described by the propagation coefficient $P_a(\omega, d)$ in medium a over distance d with refractive index of the medium $\tilde{n_a}$:

$$P_a(\omega, d) = \exp\left(-i\frac{\tilde{n}_a \omega d}{c}\right) \tag{2.2}$$

where c denotes the speed of light in vacuum. At interface changes, light is reflected, as described by the Fresnel coefficients. The reflection coefficient at an interface between medium a and b is given by:

$$R_{ab}(\omega) = \frac{\tilde{n}_a - \tilde{n}_b}{\tilde{n}_a + \tilde{n}_b} \tag{2.3}$$

where $\tilde{n}_a$ and $\tilde{n}_b$ are the complex-valued refractive indices of medium a and b, respectively. Furthermore, the transmission coefficient from medium a to medium b is:

$$T_{ab}(\omega) = \frac{2\tilde{n}_a}{\tilde{n}_a + \tilde{n}_b} \tag{2.4}$$

Figure 2.11 illustrates the specific case for different media and interfaces for sample (medium 2) and reference (medium 1) measurements.

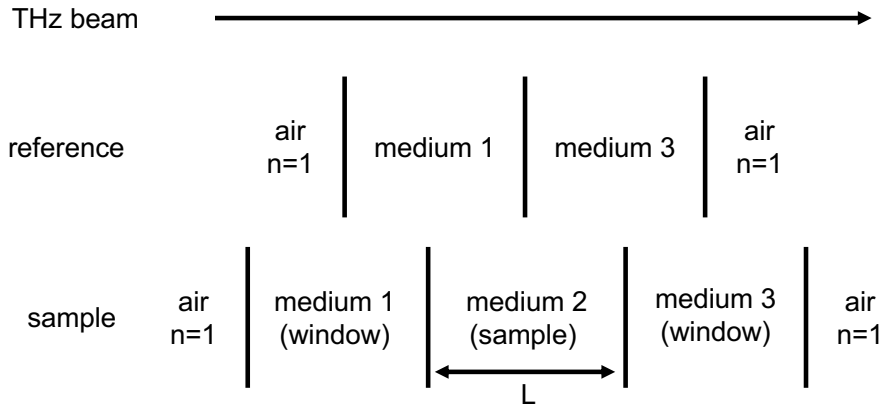

Figure 2.11. Optical path of the terahertz beam for the reference (upper) and sample (lower) case.

The electric field transmitted through a sample of width L can therefore be written as:

$$S_{\text{Sample}} = \eta(\omega) \cdot T_{12}(\omega) \cdot P_2(\omega, L) \cdot T_{23}(\omega) \cdot \text{FP}(\omega) \cdot E(\omega) \tag{2.5}$$

Where $E(\omega)$ is the incident electric field. As medium 1 and medium 3 are the same for both reference and sample, all their reflection, transmission, and propagation coefficients are included in the term $\eta(\omega)$. The Fabry-Pérot effect results in multiple reflections in the sample, these are summarised in $\text{FP}(\omega)$.

In the case of the terahertz beam passing through the reference, the transmitted wave is written as:

$$S_{\text{Reference}} = \eta(\omega) \cdot T_{13}(\omega) \cdot P_{\text{air}}(\omega, L) \cdot E(\omega) \tag{2.6}$$

The complex transmission coefficient $T(\omega)$ is obtained by dividing the transmitted sample signal $S_{\text{Sample}}(\omega)$ by the transmitted reference signal $S_{\text{Reference}}(\omega)$:

$$T(\omega) = \frac{S_{\text{Sample}}}{S_{\text{Reference}}} = \frac{2\tilde{n}_2(\tilde{n}_1 + \tilde{n}_3)}{(\tilde{n}_2 + \tilde{n}_1)(\tilde{n}_2 + \tilde{n}_3)} \cdot \exp(-i(\tilde{n}_2 - \tilde{n}_{\text{air}})\frac{\omega L}{c}) \cdot \text{FP}(\omega) \tag{2.7}$$

For the case of using two z-cut quartz windows as medium 1 and 3 (with refractive index $\tilde{n}_{\text{w}}$) and air with a refractive index of $n_{\text{air}} = 1$, this simplifies to:

$$T(\omega) = \frac{4\tilde{n}_2\tilde{n}_{\text{w}}}{(\tilde{n}_2 + \tilde{n}_{\text{w}})^2} \cdot \exp(-i(\tilde{n}_2 - 1)\frac{\omega L}{c}) \cdot \text{FP}(\omega) \tag{2.8}$$

In optically thick samples, optical windowing can be applied and $\text{FP}(\omega)$ can be removed from Equation 2.8. This can now be solved numerically with the method developed by Duvillaret et al.[138] Beginning from an initial guess for $\tilde{n}_2 = n + i\kappa$, the complex refractive index is changed iteratively to minimise the error between the measured transmission coefficient and the calculated $T(\omega)$. Once the algorithm has converged and the complex refractive index of the sample is found, the absorption coefficient α is given by:

$$\alpha(\omega) = \frac{2\omega\kappa}{c} \tag{2.9}$$

The problem can also, alternatively, be analytically solved using the Beer-Lambert law, if the sample is only weakly absorbing:

$$\frac{I_{\text{Sample}}}{I_{\text{Reference}}} = T^2 = \exp(-\alpha L) \tag{2.10}$$

In this case:

$$n(\omega) = 1 + \frac{\phi c}{\omega d} \tag{2.11}$$

$$\alpha(\omega) = -\frac{2}{L} \ln \left[\frac{(n + n_{\text{w}})^2}{4 n n_{\text{w}}} \Re(T(\omega)) \right] \tag{2.12}$$

Where n_{w} denotes the real part of the refractive index of the window.

2.4.2 Determination of Glass Transition Temperatures and Estimation of their Errors

In small molecular systems, the glass transition temperatures are easily identifiable with THz-TDS because the sample response to a small increase in temperature depends on the mobility of the system. An increased mobility above a glass transition temperature hence results in an increased change in absorption coefficient. A good visualisation of that concept is to extract the absorption at a specific frequency and plot it over temperature for further analysis, frequently performed at the frequency with the highest signal to noise ratio. A change in sample mobility at certain temperatures results in a change of the gradient (i.e. the rate of absorption change with temperature) and $T_{\text{g},\alpha}$ and $T_{\text{g},\beta}$ can be extracted.

An algorithm is used to identify the temperatures at which the sample behaviour changes. It is shown in pseudocode in Algorithm 2. Its underlying aim is to find two transition points (termed a and b) that form the boundaries of three regions while minimising the error of linear regressions in each region. From the linear regressions, the two transition temperatures $T_{\text{g},\alpha}$ and $T_{\text{g},\beta}$ are computed. The algorithm can easily be expanded to include more regions and transition temperatures (not shown here).

The choice of 1 THz as the analysis frequency is somehow arbitrary, and the effects of glass transitions should affect all parts of the spectrum, so the analysis is expanded to include more frequencies while retaining the general fitting algorithm. The absorption coefficients are evaluated at frequencies between 0.7 THz to 1.4 THz and linear fitting procedures lead to the identification of $T_{\text{g},\alpha}$ and $T_{\text{g},\beta}$ and the rate of absorption change at each frequency.

This yields two methods to estimate the error of the transition temperatures. Firstly, only the data at 1 THz is considered and the fit boundaries between the different regions are noted:

Algorithm 2 Calculation of transition temperatures

load *data*
$maxi = \text{length}(data)$
$minerror$=100 *% large number*

for $a = 3$ **to** *maxi* - 6 **do** *% first transition point*
  for $b = a + 3$ **to** *maxi* - 3 **do** *% second transition point*
    $[fitresult1, rmse1] = \text{fit}(xData(1:a), yData(1:a))$ *% region 1*
    $[fitresult2, rmse2] = \text{fit}(xData(a:b), yData(a:b))$ *% region 2*
    $[fitresult3, rmse3] = \text{fit}(xData(b:maxi), yData(b:maxi))$ *% region 3*

    $error = rmse1 + rmse2 + rmse3$

    if $error < minerror$ **then**
      $minfit1 = fitresult1$
      $minfit2 = fitresult2$
      $minfit3 = fitresult3$
      $minerror = error$
    end if

  end for
end for

$T1 = \frac{minfit2.p2 - minfit1.p2}{minfit1.p1 - minfit2.p1}$ *% calculate transition temperatures from fit coefficients*

$T2 = \frac{minfit3.p2 - minfit2.p2}{minfit2.p1 - minfit3.p1}$

plot *data, minfit1, minfit2, minfit3, T1, T2*

Algorithm 3 Calculation of uncertainty of transition temperatures

load *data,* a_{min}*,* b_{min}*,* $T1$*,* $T2$ *% load optimal parameters*
$T_{min1} = T_{max1} = T1$
$T_{min2} = T_{max2} = T2$

for $a = a_{min} - 1$ **to** $a_{min} + 1$ **do** *% first transition point*
  for $b = b_{min} - 1$ **to** $b_{min} + 1$ **do** *% second transition point*
    $[fitresult1, rmse1] = \text{fit}(xData(1:a), yData(1:a))$ *% region 1*
    $[fitresult2, rmse2] = \text{fit}(xData(a:b), yData(a:b))$ *% region 2*
    $[fitresult3, rmse3] = \text{fit}(xData(b:maxi), yData(b:maxi))$ *% region 3*

    $T1 = \frac{minfit2.p2 - minfit1.p2}{minfit1.p1 - minfit2.p1}$ *% calculate transition temperatures*

    $T2 = \frac{minfit3.p2 - minfit2.p2}{minfit2.p1 - minfit3.p1}$

    if $T1 < T_{min1}$ **then**
      $T_{min1} = T2$
    end if

    if $T2 < T_{min2}$ **then**
      $T_{min2} = T2$
    end if

    if $T1 > T_{max1}$ **then**
      $T_{max1} = T2$
    end if

    if $T2 > T_{max2}$ **then**
      $T_{max2} = T2$
    end if
  end for
end for

error1 = $(T_{max1} - T1,\ T1 - T_{min1})$
error2 = $(T_{max2} - T2,\ T2 - T_{min2})$

the first fit covers the range from the first data point (often at 80 K) to a cut-off data point a' (determined when finding $T_{g,\beta}$), the second from a' to b' (determined when finding $T_{g,\alpha}$), and the third from b' to the last data point (highest considered temperature).

a' and b' are subsequently varied by ±10 K (i.e. the size of the temperature interval between two data points). This yields nine scenarios for each of which the crossover temperatures are determined. Their spread gives an estimate for how much the calculated glass transition temperatures depend on the exact cut-off temperatures between the linear regions. It is used to estimate the influence of random errors on the calculation of the original cut-off temperatures. This simultaneously yields errors for the gradients of those regions and is shown in pseudocode in Algorithm 3.

Secondly, the multiple-frequency analysis already provides eight sets of crossover temperatures and gradients which are averaged for each sample and their spread is used as an indicator for the error. The gradients of the linear fits are inherently frequency dependent so only the data extracted at 1 THz is used for further analysis of the rate of absorption change.

Both methods of estimating an error of the transition temperatures result in similar values. The first method is preferred because it yields both an estimate for the error of the transition temperatures as well as the gradients.

2.4.3 Discussion of Possible Errors

Errors that Influence the Absorption Coefficient

Depending on the type of sample and measurement, repeating experiments might not easily be possible many times, either because there is little sample available (e.g. purified protein), or because the experiments take very long (e.g., a full temperature scan from 80 K to 450 K can take 9 hours and longer including sample preparation, setting up, measuring, and dismantling). An error analysis helps to understand which factors impact a measurement and allows to estimate the accuracy of results for some of the measurements that were not repeated many times.

The sample preparation as well as the measurement technique can result in errors. The measurement error is reduced by averaging many waveforms. Nevertheless, temperature fluctuations during signal acqusition give rise to subtle changes in absorption. Also, it is not guaranteed that the measured temperature is accurate due to the fact that the temperature sensor sits approximately 6.5 cm away from the sample in the sample holder. Waiting a defined amount of time for

stabilisation at each temperature improves the precision of temperature measurements for the sample. The estimated standard error in temperature is therefore as low as 2 K.

The measured thickness of reference and sample influences the absolute calculated absorption coefficient, which depends on the difference between them, strongly. While this error can be minimised in solid samples by measuring the respective thicknesses carefully several times, further attention should be paid to initially liquid samples that are being cooled down while their surrounding is evacuated.

In the case of liquid glycerol-water samples, the measured sample thickness before and after a measurement differed by about 0.09 mm which could change the difference between sample and reference by up to 30 %. However, the thickness of the liquid sample was influenced by the pressure in the measurement chamber. While decreasing the pressure, the sample equilibrated. If bubbles formed during the depressurisation (i.e. the sample had not been sealed properly), it was clearly visible in the frequency spectrum and the measurement was aborted and a new sample was made. During the equilibration, it was also possible that the sample was not of uniform thickness due to the liquid settling at the bottom of the cell.

The pressure inside the measurement chamber is 4 mbar under optimum conditions using a dry diaphragm pump. It has not yet been investigated how the pressure inside the measurement chamber influences the pressure of the (sealed liquid) sample.

The measured thickness after the sample has been exposed to vacuum and equilibrated in the vertical position is therefore more reliable. However, an offset in thickness that is present throughout the whole measurement will translate directly into an offset of the absorption coefficient and will not influence the transition temperatures but only the absolute values of the absorption coefficient. This fact is important during temperature scans. Due to the large range of temperatures covered, the sample holder expands/contracts over the course of one measurement. This might introduce a change in measurement position which combined with a thickness variation could distort the result.

In the following, the influence of varying thickness is examined using the example of a measurement of pure glycerol. The thickness as measured after a full temperature scan was 4.467 mm with a standard error of 0.017 mm. After subtracting the reference (with a thickness of 4.135 mm $\pm$ 0.004 mm), the thickness of interest is 0.332 mm $\pm$ 0.017 mm. This standard error corresponds to 5.12 % error. The data is subsequently analysed 3 times, with thicknesses

of 0.332 mm, 0.349 mm, and 0.315 mm. This introduces deviations of up to 5.5 % from the mean absorption coefficient. The result for the absorption coefficient is shown in Figure 2.12, where the black markers correspond to the average thickness and the shaded area to the 5.5 % offset that is introduced by the thickness variations.

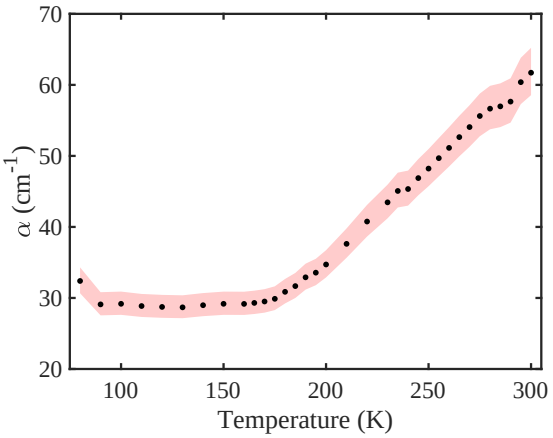

Figure 2.12. Black dots: Absorption coefficient of pure glycerol at 1 THz with varying temperature. Shaded area: Possible 5.5 % offset of the absorption coefficient that result from 5.1 % thickness variation.

If the temperature-dependent expansion of the sample holder leads to a change of the measurement position, the absorption coefficient is shifted. Such changes are, following the reasoning above, expected to be on the order of 5.5 % or less over the whole measurement. One temperature scan of a liquid sample usually includes temperatures between 80 K and 300 K. However, the thickness will vary smoothly, with an expected maximal rate of $\frac{5.5\,\%\cdot 10\,\mathrm{K}}{300\,\mathrm{K}-80\,\mathrm{K}} = 0.25\,\%$ per 10 K increment. This in turn will lead to a change in absorption coefficient of not more than 0.25 cm^{-1} at 300 K. This is of an order that can be neglected and does not noticeably affect the transition temperatures.

Summing up, thickness variations in the sample and changes of measurement positions are likely to introduce a change to the measured absorption coefficients as high as 5.5 %. This however does not influence possible transition temperatures.

Another source of error is the tilt of the sample in the sample holder when measuring liquid samples. Optimally, the sample surface is orthogonal to the incoming beam. A slight tilt is however not avoidable due to the way the sample is mounted in the holder which can be a tight fit due to the parafilm wrapped around the windows. To examine this further, the same sample was put in the sample holder 3 times, measured at different positions, and then taken

out again (which formed a so-called cycle). The results for 3 cycles are shown in Figure 2.13 when analysed with the same nominal thickness. Measurements within the same cycle deviate less than 6 % from the average value, which is close to the value that has been estimated above. If only frequencies between 0.7 THz and 1.4 THz are considered, measurements differ less than 5.1 %, with notably less deviations around 1 THz. Across all cycles, the standard error is about 2.1 % between 0.5 THz and 2.5 THz and about 1.9 % between 0.7 THz and 1.4 THz. This is the motivation for using frequencies between 0.7 THz and 1.4 THz for the calculation of transition temperatures.

The combination of errors stemming from sample preparation and sample mounting affect the total values of the absorption coefficient. Errors are estimated to be well below 10 % for liquid samples and even lower for solid samples.

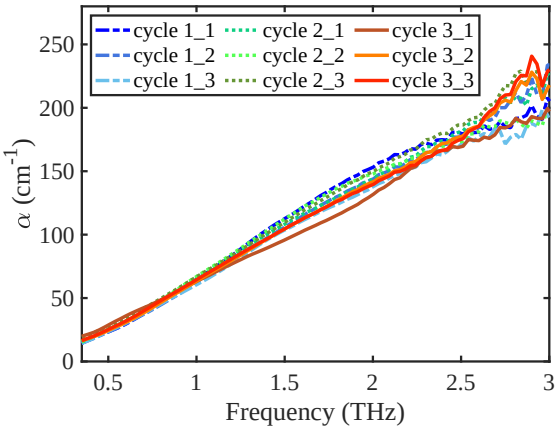

Figure 2.13. Absorption coefficient at 300 K of pure glycerol measured in 3 cycles at 3 positions each. The measurements deviate the least from each other at around 1 THz, which is the frequency where most subsequent analyses are performed.

A further error source is the fact that some sampels are highly hygroscopic, for example glycerol or freeze-dried proteins. Glycerol might absorb water during storage, as investigated in detail in Chapter 3.4. The closed bottle was therefore wrapped in parafilm. However, a measurement of pure glycerol after the flood in the Department of Chemical Engineering and Biotechnology in February 2019 clearly showed an increased water content and new glycerol was used subsequently.

Errors that Influence the Calculated Transition Temperatures

The transition temperatures depend strongly on the fits that are used to calculate them. Several

decisions influence the uncertainty in estimating the transition points:

- The choice whether some temperatures are excluded from the analysis, in particular at high temperatures where there might be another transition (in glycerol samples, see Chapter 3.3), or a crystallisation or denaturation event occurs (Chapter 4)
- The choice of how many linear functions to fit to the data sets
- The choice of the points a and b that separate the regions
- The choice of the fit function

The uncertainty of the calculated transition temperatures was estimated using Algorithm 3 by varying the transition points and calculating alternative transition temperatures. This approach was taken because the errors associated with different fits are often very similar and will result in transition temperatures in the same range.

It was chosen to fit linear functions to the data because of their simplicity. They do not yet represent a physical model and in other systems a different fit function might be used. However, in the temperature ranges measured, linear functions describe the observed changes well.

3 Glycerol-Water System: Structural Dynamics and Water Clustering

The dynamics of glasses are temperature-dependent. In the following chapter, the behaviour of the model glass glycerol and its aqueous mixtures is investigated in the harmonic (below the glass transition temperature T_g), anharmonic (above T_g), and liquid regime. The onset temperature of the molecular mobility as measured by the infrared active dipoles, T_g, is found to correlate with the onset of anharmonic effects, leading to an apparent shift of the boson peak and obscuring it at elevated temperatures.

The chapter is split into three parts. Section 3.1 focuses on the behaviour of pure glycerol and introduces the methodology. Temperature-induced changes in the dynamics and their effect on the measured absorption coefficient are examined and explained. The methodology is subsequently applied to mixtures of glycerol and water and the role of water clustering is investigated. Section 3.2 introduces a possible further transition at temperatures close to the eutectic point of glycerol-water mixtures. Section 3.3 focuses on the hygroscopicity of glycerol and how it can be measured both using THz-TDS and with a simple balance experiment.

I performed all described experimental work utilising THz-TDS as well as the balance experiments. The project originated from a collaboration with Evgenyi Shalaev (Abbvie), who has previously investigated glycerol-water mixtures with Raman spectroscopy, and Walter Schirmacher (University of Mainz), who is very interested in boson peak characteristics and linking the measured absorption with a theoretical model.

A manuscript corresponding to Chapter 3.1 is in preparation.

3.1 Structural Dynamics in the Glycerol-Water System

3.1.1 Introduction

Dynamics of Glass-Formers

Upon cooling an organic molecular liquid to temperatures below its melting point, it either forms a crystal or remains disordered, ultimately forming an amorphous solid. Initially, at temperatures just below its freezing temperature a liquid is referred to as supercooled. In such thermodynamically metastable systems the Stokes-Einstein relation breaks down, and diffusion and viscosity decouple.[139] The molecular arrangement remains similar to that of liquids and

long-range order is completely absent. Upon further cooling to temperatures below the glass transition temperature ($T_{g,\alpha}$), a sharp change in the thermal expansion coefficient and specific heat is observed and a glass is formed. In contrast to crystals, amorphous solids do not possess a well-defined melting point and a solid crystal lattice structure but rather exhibit an increase in viscosity while experiencing only minute structural changes.[140] Given the nature of the glass transition as a kinetic second-order transition rather than a first-order phase transition, the specific value of $T_{g,\alpha}$ depends on the experimental cooling and heating rate.[4,141]

Motions that occur at temperatures at and above $T_{g,\alpha}$ include translational, cooperative molecular motions. At temperatures below $T_{g,\alpha}$ the molecular motions are restricted to local or so-called secondary mobility which are frequently referred to by the relatively broad term 'beta-relaxation'. In low molecular weight compounds the hindered rearrangements of individual molecules are also called Johari-Goldstein (JG) beta-relaxation.[6] These motions have a lower activation energy compared to the motions associated with the alpha-relaxation and therefore the beta-relaxation prevails at lower temperatures, and the associated transition temperature, $T_{g,\beta}$, is thus lower than $T_{g,\alpha}$. Experimentally, the $T_{g,\alpha}$ can be measured by a range of techniques, such as differential scanning calorimetry (DSC), which detects the change in heat capacity at the glass transition temperature. The onset of localised motions at $T_{g,\beta}$ is typically too subtle to be detected in DSC measurements.[133]

Terahertz time-domain spectroscopy (THz-TDS) probes frequencies in the range of 0.35 THz to 3 THz by coupling to dipole moments at photon energies on the order of the hydrogen bond strength and picosecond relaxation time. It hence provides a sensitive probe of mobility in condense phase organic molecular materials. Past studies using THz-TDS have investigated the complex interplay between reorientation motion and vibration dynamics in hydrogen-bonded liquids.[92–94]

Due to the inherent disorder of glasses, no discrete phonon modes can be sustained and the coupling of photons to the vibrational density of states (VDOS) results in the relatively featureless so-called microscopical peak that constitutes the main absorption mechanism in the terahertz range[63] with a frequency-squared dependence as predicted by Debye theory.[15] With increasing temperature, an overall increase in absorption is measured within the accessible spectral bandwith of THz-TDS instruments (< 3 THz). In addition to the microscopical peak, THz-TDS also detects the excess density of states (DOS) above the Debye level. This excess DOS is termed

boson peak and becomes apparent when plotting the absorption coefficient divided by frequency squared.

While the exact origin of the boson peak is still not fully understood, it is generally accepted that the boson peak is a harmonic phenomenon due to inherent disorder, and should therefore be temperature independent.[66,67,69]

Chumakov et al.[68] embedded a probe molecule in a glass matrix and monitored its translational motions with nuclear inelastic scattering. Because the probe followed the collective motions of the glass with a correlation length larger than the probe size, the density of states of collective motions (CDOS) of the glass matrix was directly measured. Chumakov et al. found that a significant part of the boson peak in the model glass former glycerol is constituted of collective modes and that it disappears close to $T_{g,\alpha}$ due to increased sample mobility. They further observed an exponential decrease in both the reduced VDOS and CDOS at energies above the boson peak maximum.[68]

Goldstein proposed that properties of glasses can be explained by the characteristics of the potential energy surface (PES).[20] The atomic dynamics have been described as a consequence of the shape of the PES.[141] In this context, anharmonic effects only begin to dominate the spectra above a certain temperature. Below that temperature, the contributions to the spectra (and hence the boson peak) are mostly harmonic in nature.

Glycerol is a widely studied network material and model system for a glass former[142] as it is non toxic and easily supercools and has been investigated with experimental techniques like Raman scattering,[143,144] infrared spectroscopy,[145,146] dielectric spectroscopy,[147,148] neutron and light scattering,[142,149] DSC,[150] terahertz spectroscopy,[151] as well as theoretical work with molecular dynamics simulations.[145,152] Its $T_{g,\alpha}$ was found to lie between 185 K and 194 K.[95,150,153,154] In glycerol, the VDOS extends from approximately 0.5 THz to 7 THz.[153]

In THz-TDS measurements of glycerol, its $T_{g,\beta}$ was found to be more pronounced than the $T_{g,\alpha}$.[95,155] Glycerol is hence a promising model system to investigate whether anharmonic effects can be detected at temperatures even below $T_{g,\alpha}$. Here we study the impact of temperature changes on glycerol dynamics, especially anharmonic effects that can obscure the boson peak.

Glycerol-Water Mixtures

Modern biopharmaceutical drugs are often developed into complex amorphous formulations that are prepared by spray-drying or freeze-drying (lyophilisation). Given its resistance to crystallisa-

tion, glycerol is used widely as a cryoprotectant of cells and organs and also to stabilise lyophilised proteins.[107,156] Some pharmaceutical degradation mechanisms are catalysed by water clusters and the influence of water content on the stability of lyophilised products has been investigated previously.[157] In macromolecules, water can both serve to stabilise the native structure while simultaneously acting as a catalyst for destabilisation. It was suggested that unclustered water molecules (that are commonly found in products containing only a few wt. % water) are less catalytically active than water clusters.[158] Starciuc et al. hypothesised that proton transfer becomes possible only once a water clustering threshold is exceeded, thereby supporting pharmaceutical degradation reactions such as amide hydrolysis and deamidation.[158]

The model system of glycerol-water mixtures has been studied widely:[145,147,159–162] Towey et al. used a combination of neutron diffraction experiments and computational modelling to investigate the structure and hydrogen-bonding of pure glycerol,[161] dilute aqueous glycerol solution,[160] and glycerol-water mixtures for glycerol mole fractions of x_g = 0.05, 0.10, 0.25, 0.50, 0.80, and 1.00.[162] They found bipercolating clusters of both water and glycerol in samples containing a mole fraction between 0.75 and 0.5 water (i.e. between 16.4 and 37 wt % water). They further found that water maintained its full hydrogen-bonding capacity independently of the glycerol concentration.

Murata and Tanaka found evidence for a water liquid-liquid transition (LLT) without macroscopic phase separation in glycerol-water mixtures containing between approximately 45.5 wt % to 56 wt % water.[159]

Recently, Starciuc et al. investigated glycerol-water mixtures containing between 0 and 40 wt % water water with low- and high-wavenumber Raman spectroscopy, and three water-content regions were found.[158] This confirmed the existence of a threshold for water clustering in glycerol.[158] A transition from predominantly unclustered water molecules to small water clusters was reported at 6.1 ± 0.7 wt% water and a second threshold at 18.6 ± 4.4 wt% water, which was proposed to correspond to the formation of large water clusters associated with proton transfer and the onset of freezing.

And while glycerol and glycerol-water systems have been investigated thoroughly with a range of methods, there has not yet been a comprehensive study in the terahertz frequency range over a range of temperatures to investigate the role of water, especially the formation of water clusters, in glycerol-water mixtures with a water content below 30 wt % water. This water content range

represents typical specification limits for freeze-dried pharmaceuticals. By understanding the structural dynamics of the glycerol-water system, such water content specifications in the design of pharmaceutical products can be scientifically substantiated and their design can be optimised.

The dynamics of the model system of glycerol-water mixtures are investigated with THz-TDS by varying both the temperature and the water concentration. The aim is to extract as much information as possible about both the glass and the amorphous solid and to investigate the role of the boson peak and the shape of the VDOS and their relationship with the glass transition temperatures.

In addition to the THz-TDS data at various (cryogenic) temperatures, high-quality room temperature data of liquid glycerol-water mixtures with different water concentrations were also acquired to further understand how the water content influences the terahertz spectra of the liquids.

3.1.2 Materials and Methods

Variable-Temperature THz-TDS Measurements

Glycerol was obtained from Sigma Aldrich (Poole, UK) and was mixed with Milli-Q water (IQ 7000, Merck, Darmstadt, Germany, resistivity 18.2 MΩ cm) in various ratios (0 wt % water to 30 wt % water). The mixtures were de-gassed inside a desiccator attached to a vacuum pump. For subsequent measurements, a drop of liquid sample was sealed between two z-cut quartz windows (Crystran, UK) separated by a 100 µm thick PTFE spacer in a liquid cell which was then fit into the cryostat and placed under vacuum. The samples were analysed in transmission using a commercial Terapulse 4000 spectrometer (TeraView Ltd., Cambridge, UK) with a liquid nitrogen cryostat attached, as described by Sibik et al.[73] Two z-cut quartz windows (Crystran, UK) were used for reference measurements. The spectral range the instrument was able to access was in the range of 0.35 THz to 3 THz, depending on sample absorption.

Utilising the cryostat and liquid nitrogen cooling, a wide range of temperatures were studied (80 K to 305 K), as described by Sibik et al.[73] At each temperature, the co-average of 1000 waveforms was acquired for both reference and sample and used to calculate the optical constants.

To increase reproducibility and facilitate comparison between different water concentrations, the measurements were controlled with a computer program that kept the length of temperature steps and therefore the overall heating rate constant at about 1 K min^{-1}.

THz-TDS Measurements at Room Temperature

Glycerol and its mixtures were prepared following the same steps as described above. However, instead of sealing the sample into a liquid cell that fit into the cryostat, a room temperature liquid cell was utilised which was easier to assemble. This liquid cell also consisted of two z-cut quartz windows separated by a 100 µm thick PTFE spacer. This was subsequently placed into the measurement chamber which was purged with dry nitrogen and samples were analysed in transmission using the Terapulse 4000 spectrometer utilising the same settings as for measurements at variable temperatures.

3.1.3 Results and Discussion: Pure Glycerol

The Boson Peak in Glycerol

The featureless terahertz absorption spectra measured by THz-TDS of the investigated glycerol-water samples are part of the rising flank of the VDOS. An example spectrum is shown in Figure 3.1a. Without further analysis it is not possible to distinguish between the glass and the liquid states.

In Figure 3.1b, the reduced density of states is plotted for pure glycerol, i.e. the absorption coefficient divided by frequency squared. At low temperatures, the boson peak is clearly visible at around 1.4 THz and its amplitude and centre frequency are mostly constant. With increasing temperature, the maximum appears to shift to lower frequencies before features of the boson peak can no longer be detected at even higher temperatures.

Chumakov et al.[68] used nuclear inelastic scattering to measure delocalised collective motions in glycerol with a correlation length greater than 20 Å. In comparison to the measurements of the VDOS by neutron scattering by Wuttke et al.[142] the nuclear inelastic scattering data detects the boson peak at slightly lower frequency, while exhibiting a similar shape overall (Figure 3.1c). In pure glycerol Wuttke et al. found a pronounced boson peak at 170 K that disappeared at 210 K. This observation is confirmed by our THz-TDS measurements (Figure 3.1d). Even at very low temperatures (below 120 K), the boson peak, as measured with THz-TDS, increases in intensity while the maximum frequency stays constant. In the same temperature interval, the neutron data shows no temperature-dependent change. Because the rising flank of the boson peak in α/ν^2 measured with THz-TDS is steeper than in the neutron scattering experiments, it was instead plotted as α/ν^3 which resulted in a better agreement and a sharper peak. In

Figure 3.1e, the same α/ν^3 measured with THz-TDS is also directly compared to the CDOS. The agreement is better at 210 K than at 90 K and 170 K.

The boson peak was also measured with low-frequency Raman scattering by Uchino and Yoko.[163] The temperature range in their study was somewhat higher but the peak was found situated at frequencies very close to the ones measured by THz-TDS as shown in Figure 3.1f. At 170 K, the intensity at frequencies below the frequency of the maximum is very similar. At higher frequencies the reduced VDOS measured with THz-TDS decreases less in intensity than the one measured by Raman scattering. It is notable that while in the Raman data, a distinct peak with a well-defined maximum was observed at 260 K, no distinct peak shape is obvious in the terahertz data.

While the boson peak itself is temperature-independent,[66,67,69] additional anharmonic effects that contribute to the absorption give the impression of an apparent shift of the boson peak with temperature. Even though the underlying boson peak is constant, by tracking the changes of the apparent maximum we can observe when the anharmonic effects influence the absolute maximum intensity. This process ultimately results in the intensity of the boson peak being subsumed entirely by the anharmonic contributions to the absorption intensity.

To track the apparent change in the peak frequency and its intensity, the data is first smoothed with a moving average and then its numerical derivative is calculated. Figure 3.2a highlights the apparent position of the boson peak maximum for different temperatures. Its frequency is plotted against temperature in Figure 3.2b.

In pure glycerol, the change is very sudden while for some of the glycerol/water mixtures the change in centre frequency is more gradual (see Figure 3.3).

The behaviour of the boson peak is hence described by a set of three parameters: the centre frequency at 80 K, $\omega_{80\mathrm{K}}$, the temperature at which the centre frequency starts to decrease (T_1, in glycerol 180 K), and the highest temperature at which a peak is still apparent in the THz-TDS data (T_2, in glycerol 240 K, Figure 3.2b).

Below approximately 170 K, the apparent peak frequency does not shift, and the intensity of the peak only increases very little with temperature, in a linear manner at each frequency, as shown in Figure 3.2c. The absorption was hence extrapolated to 0 K at each frequency to calculate the temperature-independent boson peak, shown in Figure 3.2d. As the absorption shift with temperature is known for each frequency, a theoretical spectrum can be calculated for

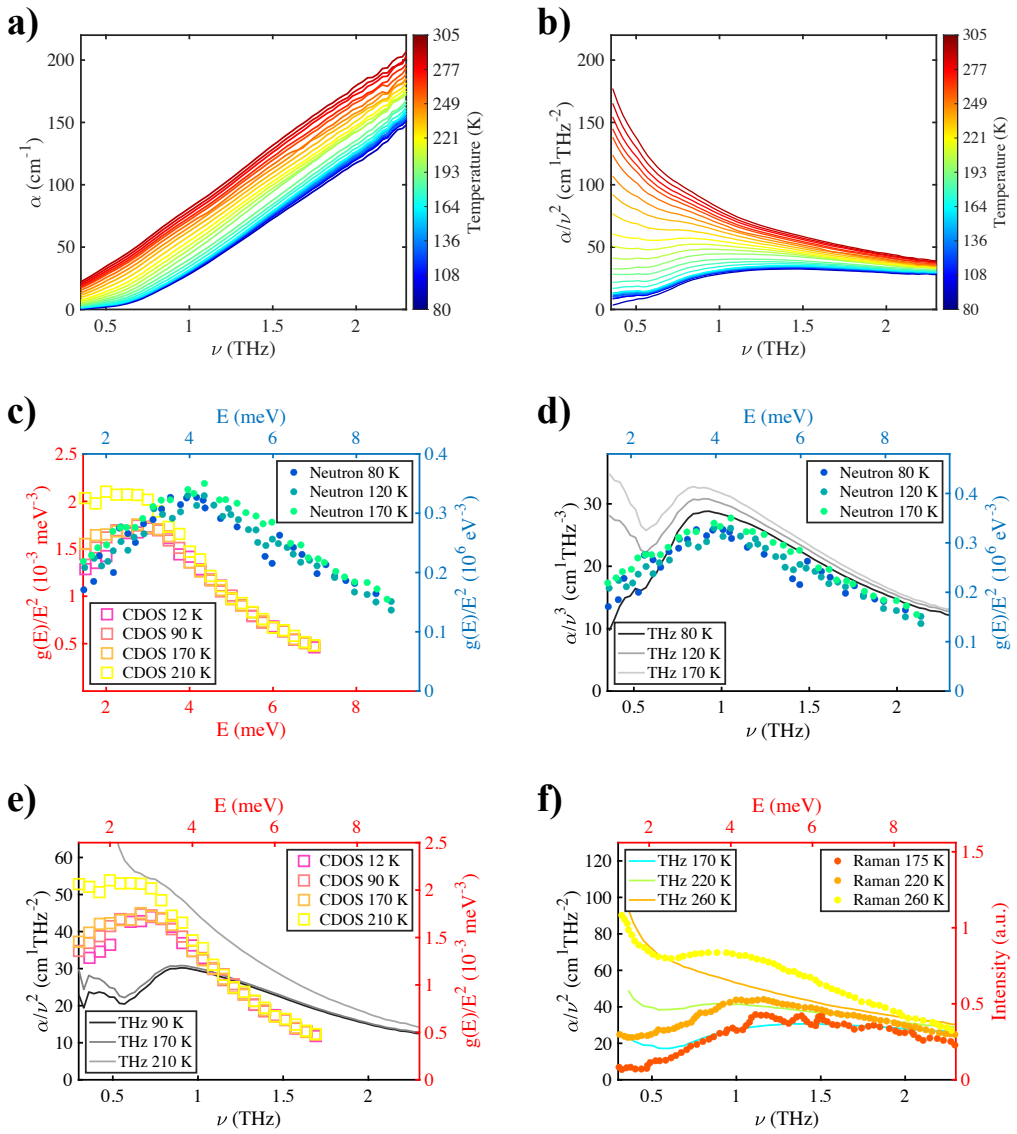

Figure 3.1. Terahertz absorption spectra change with temperature. Comparison to neutron, nuclear inelastic scattering, and Raman data.
(a) THz-TDS absorption spectrum of glycerol for temperature steps of 10 K from 80 K to 280 K and steps of 5 K above. The sample is amorphous over the range of temperatures measured and absorption increases with temperature at all frequencies. (b) Boson peak visualised for the same sample by plotting α/ν^2. A broad maximum is visible at around 1.3 THz at low temperatures that disappears upon heating.(c) Comparison of the boson peak in the VDOS measured with neutron scattering (dots)[164] and the boson peak in the CDOS measured with nuclear inelastic scattering[68] (squares). The maximum in the CDOS is located at slightly lower frequencies than in the VDOS.(d) Comparison of the boson peak in the VDOS measured with neutron scattering[164] and α/ν^3 measured with THz-TDS (lines). The maxima and shapes are very similar.(e) Comparison of the boson peak in the CDOS measured with nuclear inelastic scattering[68] and α/ν^2 measured with THz-TDS (lines). (f) Comparison of the α/ν^2 measured with THz-TDS (lines) and the VDOS measured with Raman scattering (Uchino 1996, dots).[163] The maxima below 260 K occur at similar frequencies and the shape is very similar.

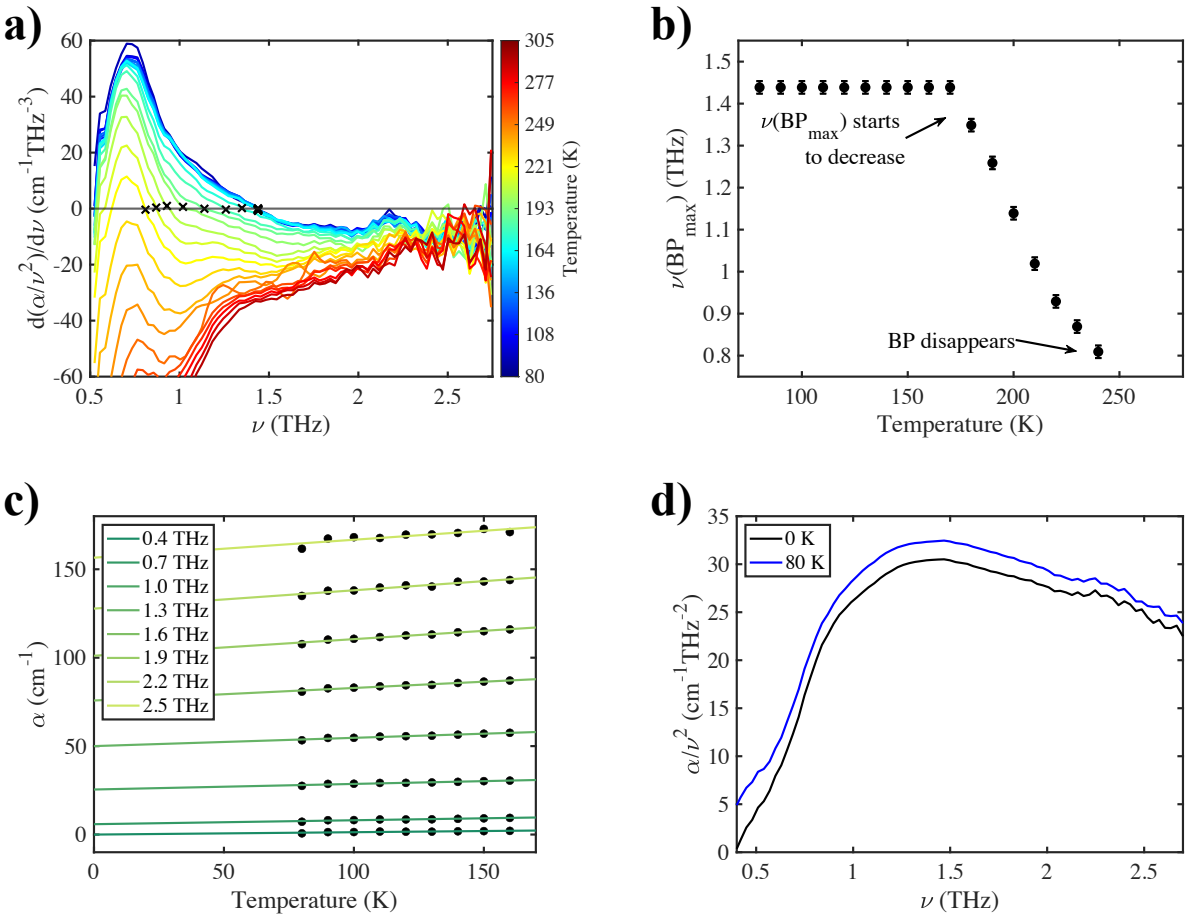

Figure 3.2. (a) Derivative $\frac{d\alpha/\nu^2}{d\nu}$. Crosses denote the frequencies where the derivative is closest to zero and the boson peak therefore maximal. (b) Maximum boson peak frequencies plotted against temperature for pure glycerol. Error bars are half the spacing between two frequencies in $\frac{d\alpha/\nu^2}{d\nu}(\nu)$. (c) Absorption coefficient at various frequencies for temperatures below 160 K and extrapolation to 0 K. (d) Boson peak measured at 80 K (blue) and extrapolated at 0 K (black).

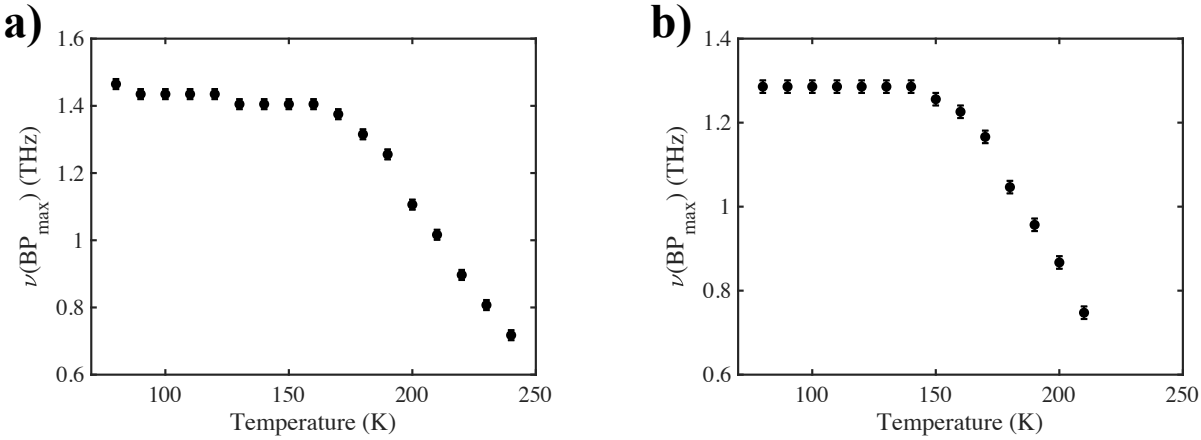

Figure 3.3. Maximum boson peak frequencies plotted against temperature for mixture containing 10 wt % water (a) and 30 wt % water (b). Error bars are half the spacing between two frequencies in $\frac{d\alpha/\nu^2}{d\nu}(\nu)$.

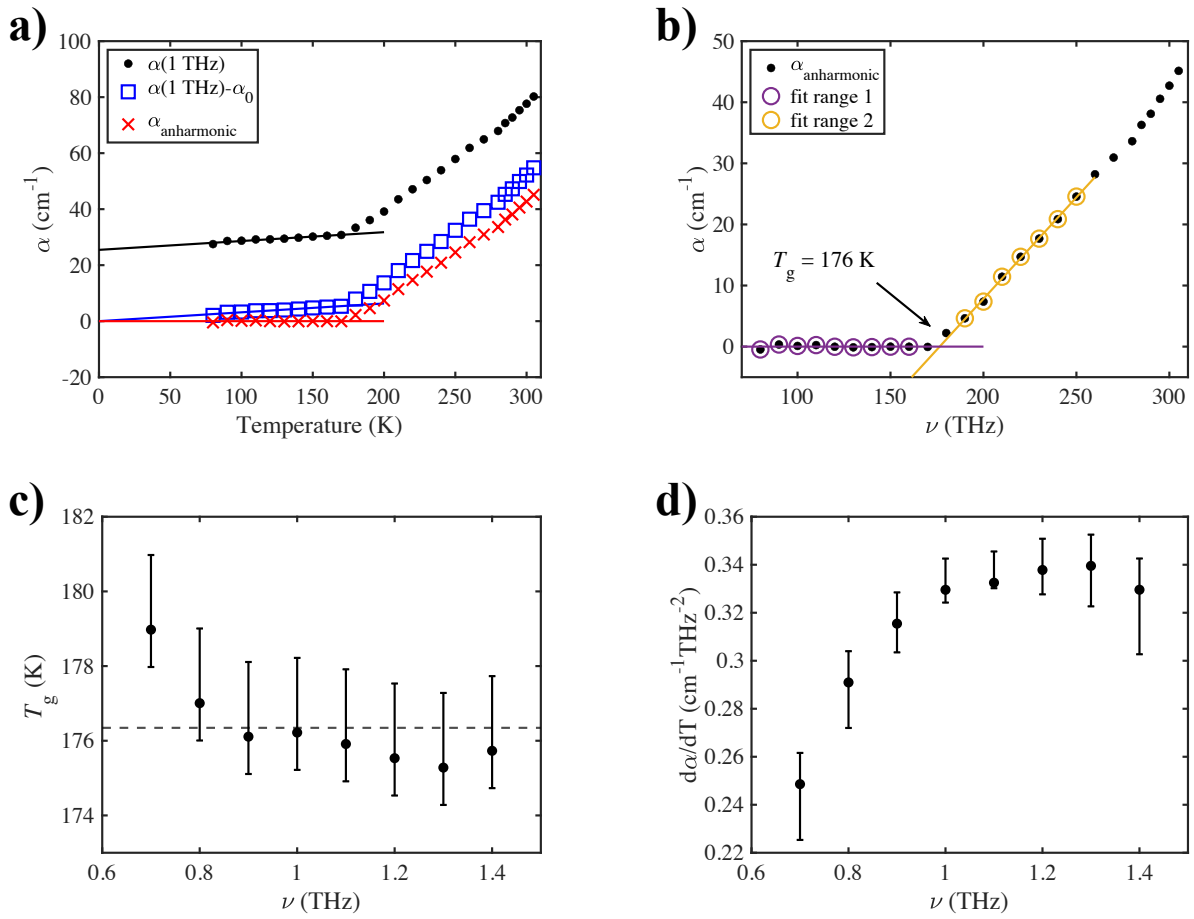

Figure 3.4. Terahertz spectra change with temperature and water content. (a) Fit to the absorption coefficient of glycerol at 1 THz for the raw data (black dots), the absorption coefficient minus the absorption at 0 K (blue squares), and with the harmonic contribution removed (red crosses). Lines are drawn through the low temperature data to guide the eye. (b) Anharmonic absorption at 1 THz (black dots) with the two best linear fits in the harmonic regime (purple) and anharmonic regime (yellow). The regimes are also highlighted by respective circles. (c) Transition temperatures of glycerol are weakly frequency-dependent. The average is shown as a horizontal line and it is very close to the value at 1 THz. (d) Gradients of linear fits in sample of pure glycerol once anharmonic effects dominated above 170 K. Gradients are frequency-dependent.

each temperature. After subtracting this mainly harmonic contribution from the experimental spectrum, the anharmonic contribution remains.

The Absorption Coefficient of Glycerol at Cryogenic Temperatures

While the absorption changes only very little at temperatures below approximately 170 K, a discontinuity at temperatures above 170 K is observed which corresponds to a change in mobility and the onset of anharmonic effects.

The temperature behaviour of glasses can be separated into 3 regimes: at low temperatures in the harmonic regime, any mobility (e.g. dihedral angle changes) is severely restricted and

molecules vibrate at their equilibrium position due to their thermal energy. An increase in thermal energy results in an approximately linear increase in absorption that can be measured throughout the accessible frequency range. This also affects the apparent intensity of the (itself temperature-independent) boson peak.

Within the concept of the PES, the system is trapped in a deep and steep minimum which can be approximated as harmonic. Anharmonic effects play only a small role at the low temperatures of the so-called harmonic regime. The measurable increase in absorption coefficient at single frequencies, however, is due to anharmonic effects.[57] At temperatures at which the apparent centre frequency of the boson peak is not affected by anharmonicity, we will call the temperature range the harmonic regime.

Once the temperature is increased sufficiently for the system to escape the deep minimum, it has access to shallower regions of the PES that are characterised by numerous local minima separated by smaller energy barriers. The temperature at which the system contains sufficient thermal energy to leave the deep minimum on the PES coincides with $T_{g,\beta}$, i.e. the onset of local mobility, observed by THz-TDS as an increase in the rate of absorption change with temperature. Anharmonic effects start to dominate the spectrum and result in an apparent change of the boson peak frequency as well as a stronger increase in the absorption coefficient with temperature.

A further temperature increase, ultimately resulting in $T_{g,\alpha}$, opens up more local minima on the PES while anharmonic effects continue to play an important role. The larger the amplitude of the possible motions, the higher the associated change in dipole moment and hence the measured absorption coefficient. The shallower the minima, the more anharmonicity influences the spectra.

The calorimetric glass transition temperature $T_{g,\alpha}$ of glycerol is harder to detect with THz-TDS, as has previously been reported by Sibik et al.[95] and Capaccioli et al.[155] Sibik et al.[95] found a mean T_g of 194 K because $T_{g,\beta}$ and $T_{g,\alpha}$ could not be separated. Capaccioli et al. argued that a $T_{g,\beta}$ at 161 K was consistent with the same $T_{g,\alpha}$. In glycerol, $T_{g,\alpha}$ and $T_{g,\beta}$ are only separated by approximately 30 K. In this "transition region", characterised by a mean transition temperature T_g, the onset of local and global mobility as well as anharmonic effects, increase the rate of change in absorption with temperature which results in the apparent decrease of the boson peak frequency as discussed above. The difficulties in accurately determining both $T_{g,\beta}$ and $T_{g,\alpha}$ in glycerol with THz-TDS indicate that for the small molecular system of glycerol and

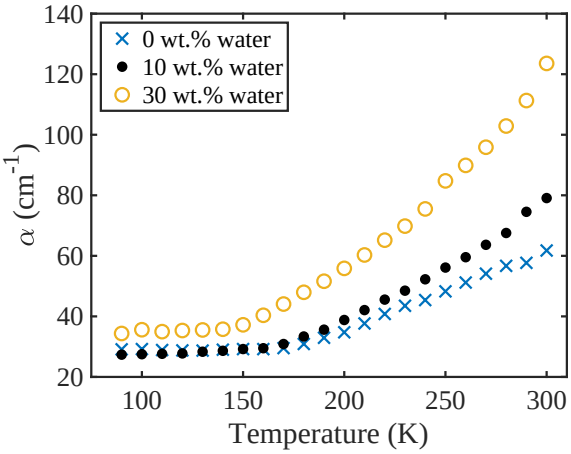

Figure 3.5. Absorption coefficient at 1 THz extracted for different temperatures for glycerol (blue crosses), a mixture containing 10 wt % water (black dots), and 30 wt % water (yellow circles).

water molecules, the PES is shaped relatively similar below and above $T_{g,\alpha}$.

Above $T_{g,\beta}$, anharmonic effects increase the absorption just below the centre frequency of the boson peak strongest, as shown in Figure 3.4d. This seems to shift the apparent centre frequency of the boson peak to lower frequencies and also screens the effect of $T_{g,\alpha}$ and could be another reason why it is harder to detect $T_{g,\alpha}$ at 1 THz than in other materials where the boson peak is located at different frequencies.

The temperature dependence of the absorption coefficient extracted at a chosen frequency is illustrated in Figure 3.4a for a frequency of 1 THz for a sample of pure glycerol. Other concentrations are shown in Figure 3.5.

By subtracting the harmonic effect from the spectrum following the method outlined above, the anharmonic contributions become visible, as shown in Figure 3.4a. At $T_{\text{anharmonic}}$ (approximately 180 K), $\alpha_{\text{anharmonic}}$ becomes larger than zero. By fitting two linear functions to $\alpha_{\text{anharmonic}}$ below and above the transition region, shown in Figure 3.4b, the transition temperature is detected more accurately. The exact algorithm that was used and the calculation of the error bars are described in the following. Complex optical constants were calculated from the acquired waveforms for all samples using the method of Duvillaret et al.[138]

Glass transition temperatures are commonly extracted from the absorption coefficient at 1 THz measured at variable temperatures, where the signal-to noise ratio is highest[101] by fitting linear functions to the data and minimising the sum of their sum-squared error. The crossover temperatures between the linear fits determine the glass transition temperatures.

In the glycerol-water system however, $T_{g,\beta}$ and $T_{g,\alpha}$ are quite close together with $T_{g,\beta}$ more pronounced that $T_{g,\alpha}$. Because of the large uncertainty when trying to determine both, only one T_g was extracted, which characterised the transition region between the harmonic (no mobility) and anharmonic (local and global mobility present) regimes.

First, the harmonic contribution was subtracted from the absorption coefficient. Then, the temperature data point a at which anharmonic effects first increased the anharmonic absorption coefficient, $T_{\text{anharmonic}}$, was found and a linear regression was performed from the lowest measured temperature up to the data point $a-2$. A second linear regression was performed from temperature data point $a+1$ up until the temperature at which the boson peak first disappeared. The crossover between these two regressions was used as a measure of T_g.

The choice of 1 THz as the analysis frequency is somehow arbitrary, and the effects of glass transitions should affect all parts of the spectrum,[27] so the analysis was expanded to include more frequencies while retaining the general fitting procedure. The absorption coefficients were evaluated at frequencies between 0.7 THz to 1.4 THz and linear fitting procedures led to the identification of T_g and the rate of absorption change. The choice of linear functions is based on using the simplest function that describes the data well but its physical relevance is as yet unknown.

Considering the data at a single frequency, the fit boundaries between the different regions were varied by ± 10 K (i.e. the size of the temperature interval between two data points) while keeping the transition region the same size. This yielded different scenarios for each of which the crossover temperatures were determined. Their spread gave an estimate for how much the calculated glass transition temperatures depended on the exact cut-off temperatures between the linear regions. It was used to estimate the influence of random errors on the calculation of the original cut-off temperatures. This simultaneously yielded errors for the gradients of those regions.

This procedure was repeated for different frequencies, as shown in Figure 3.4c and higher transition temperatures were found for lower frequencies. The change in $\mathrm{d}\alpha/\mathrm{d}T$ is also frequency dependent, as shown in Figure 3.4d. It is largest at frequencies just below the maximum of the boson peak, resulting in its apparent shift.

Some of the parameters shown in Table 3.1 are evaluated at certain frequencies (T_g, $T_{\text{anharmonic}}$) while others are found by evaluating the entire spectrum (T_1, T_2). At 0.7 THz for example, the

Table 3.1. Temperatures where a change of mobility or in the contribution of anharmonic effects are observed in glycerol.

Parameter	Temperature (K)
Calorimetric glass transition $T_{g,\alpha}$	190
T_g (1 THz)	176
T_g (0.7 THz)	179
$T_{anharmonic}$ (1 THz and 0.7 THz)	180
T_1	180
T_2	240

linear fits to the anharmonic absorption coefficient yield consistently higher transition temperatures than at 1 THz. This implies that higher frequencies are first affected by mobility changes and hence exhibit anharmonic effects first. Motions at higher frequencies often involve molecules with a smaller reduced mass or a higher force constant, i.e. with stronger bonds. Collective motions typically appear at lower frequencies. This means that smaller changes, for example of vibrations, occur first and agrees with the observations.

The mean transition temperature T_g hence does not coincide exactly with $T_{g,\beta}$ or $T_{g,\alpha}$ but is a good description of a temperature where anharmonic effects start to influence the spectrum. It can be compared with other parameters, e.g. the calorimetric glass transition $T_{g,\alpha}$ determined with DSC, the temperature where the boson peak appears to begin to shift to lower frequencies (T_1), or the temperature at which the anharmonic contribution is no longer negligible ($T_{anhamonic}$) and an overview is given in Table 3.1.

With increasing temperature, the VDOS is enhanced until the liquid state (the third regime) is reached where quasi-elastic scattering occurs and the boson peak is no longer defined.

These observations and explanations are now used to examine the influence of water content and temperature on the behaviour of glycerol-water mixtures.

3.1.4 Results and Discussion: Glycerol-Water Mixtures

When data at various concentration are reported, one has to keep in mind that Starciuc et al. showed that the transition from predominantly unclustered water molecules to clusters occurs at around 6.1 ± 0.7 wt % water. A second threshold was found at 18.6 ± 4.4 wt % water and linked to larger, percolating water clusters.[158] Below the first threshold, water molecules are predominantly unclustered, do not induce major structural changes, and form mostly water-glycerol hydrogen bonds. The LLT found by Murata and Tanaka occurs at higher water concentrations

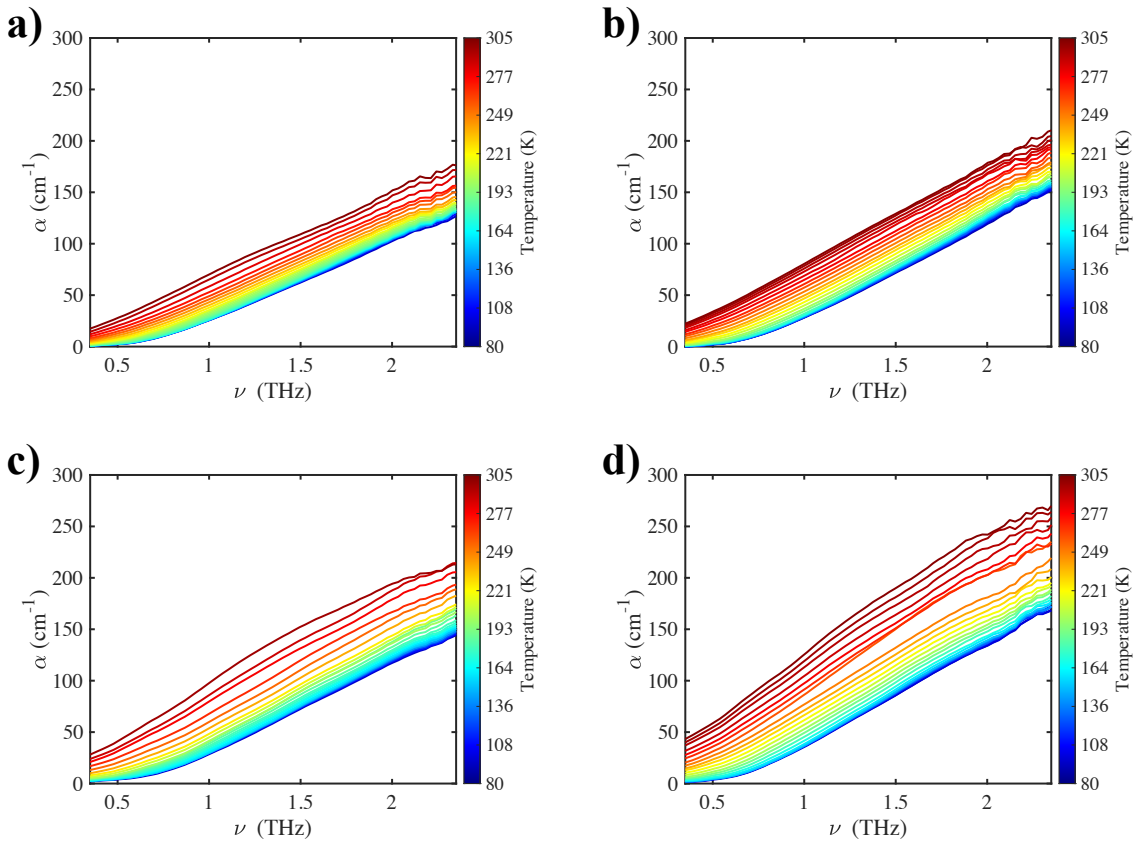

Figure 3.6. Absorption spectra for mixtures containing 5 wt % water water (a), 10 wt % water water (b), 20 wt % water water (c), and 30 wt % water water (d) at different temperatures.

than investigated here.[159] Any change in behaviour found at approximately 6 or 19 wt % water can therefore be attributed to the influence of water on the structural dynamics by increasing the cluster size and connectivity, as well as a strengthening of the hydrogen bonds between water molecules.

Harmonic Regime ($T \leq T_g$)

By extrapolating the harmonic contributions to the spectra of samples containing water (spectra shown for selected concentrations in Figure 3.6) to 0 K using the method outlined above, the boson peak is visualised and shown in Figure 3.7a. The dependence of its centre frequency and intensity on water content is shown in Figure 3.7b.

Most decrease in centre frequency only occurs above T_1. The correlation coefficient of $\omega_{80\mathrm{K}}$ with water content is only -0.21 and indicates that at these very low temperatures the centre frequency does not (at least linearly) depend on water content. In the harmonic regime, unclustered and clustered water molecules do not influence the centre frequency of the boson

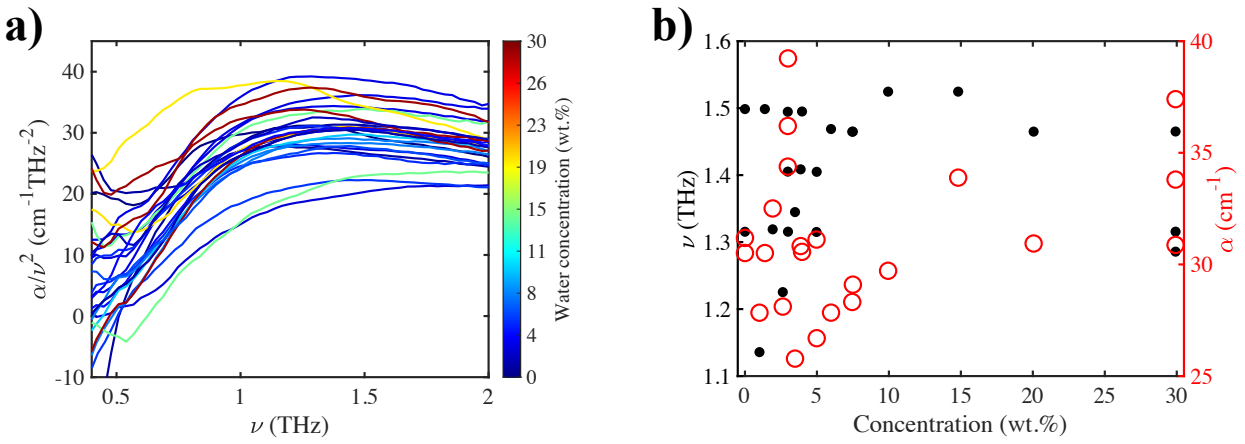

Figure 3.7. (a) Boson peak extrapolated to 0 K from measured data from 80 K to 140 K for all samples. (b) Centre frequency (black dots) and height (red open circles) of the extrapolated boson peak for all measured concentrations.

peak. The Ioffe-Regel crossover is linked to the centre frequency of the boson peak and denotes a crossover from wave-like to random-matrix-like physics as the mean free path of transverse waves becomes equal to their wavelength.[67–69] The results indicate that the Ioffe-Regel crossover is not influenced by the presence of clustered or unclustered water.

Clustered water may increase the intensity of the boson peak slightly, indicating a higher level of disorder. While the centre frequency is largely independent of water content, the peak intensity may exhibit a shallow minimum around a concentration of about 5 wt % water when water molecules are homogeneously distributed throughout the sample.

The absorption increases in an approximately linear manner at each frequency. This rate of increase does not clearly depend on water concentration (cf. Figure 3.7c). As discussed for the case of pure glycerol, the system is trapped in a minimum on the PES. The shape of the PES determines the rate of absorption change as well as the temperature at which the system contains sufficient thermal energy to overcome the energy barrier, enter the anharmonic regime, and experience mobility.

The deepest minimum of the PES is shaped similarly independent of water concentration or the presence of water clusters, otherwise the rate of absorption change would be different.

In Figure 3.8a, an overview of the different transition temperatures is given for all glycerol-water mixtures measured for transition temperatures based on data at 1 THz. Black crosses denote DSC measurements of $T_{g,\alpha}$. The temperatures at which the boson peak appeared to shift and dissolved were characterised for all samples and the results are also shown in Figure 3.8

Table 3.2. Parameters describing the change of the boson peak in glycerol water mixtures with temperature for selected concentrations.

	ω_{80K} (THz)	T_1 (K)	T_2 (K)
pure glycerol	1.44±0.03	180±5	240±5
10 wt % water	1.47±0.03	170±5	240±5
30 wt % water	1.29±0.03	150±5	210±5

together with the transition temperatures that are extracted from the absorption coefficient for some selected concentrations (Table 3.2).

The temperature at which the anharmonic absorption coefficient becomes larger than zero, $T_{\text{anharmonic}}$, changes very little below approximately 3 wt % water to 5 wt % water and decreases above 5 wt % water. At concentrations below 4 wt % water the temperature at which the boson peak appears to shift (T_1) also does not depend on water content. This means that unclustered water molecules do not change $T_{\text{anharmonic}}$, or the temperature at which anharmonic effects result in an apparent shift of the boson peak. $T_g(1\,\text{THz})$ is also not affected by unclustered water molecules. The height of the energy barrier separating the harmonic from the anharmonic regime is hence not influenced by unclustered water molecules embedded in the glycerol matrix.

$T_{\text{anharmonic}}$, T_1, and T_g are very similar over the entire concentration range. The T_g evaluated at 0.7 THz and 1.0 THz are compared in Figure 3.8b. As in the measurement of pure glycerol, the transition temperature is higher if evaluated at lower frequencies. Furthermore, the plateau at low water concentrations is not present in $T_g(0.7\,\text{THz})$. Conversely, while still being higher than $T_g(1\,\text{THz})$, the presence of water resulted in a reduction of $T_g(0.7\,\text{THz})$. The frequency of 0.7 THz lies well below the maximum of the boson peak. As the length scale of motions associated with certain frequencies increases with decreasing frequency, the decrease in $T_g(0.7\,\text{THz})$ could hence point to an overall weakening of the entire hydrogen-bonded network once a small number of water molecules are present.

At water concentrations above 5 wt % water, most parameters changed their behaviour: the maximum of the boson peak increased slightly with concentration, anharmonic effects decreased the temperature at which they influence the appearance of the boson peak, $T_{\text{anharmonic}}$ decreased, as well as $T_g(1\,\text{THz})$.

A neutron scattering study by Towey et al.[160–162] has shown that at a concentration of 5 wt % water, water monomers are distributed homogenously throughout the material. As the water concentration is increased, water clusters coexist with unclustered water molecules. Past

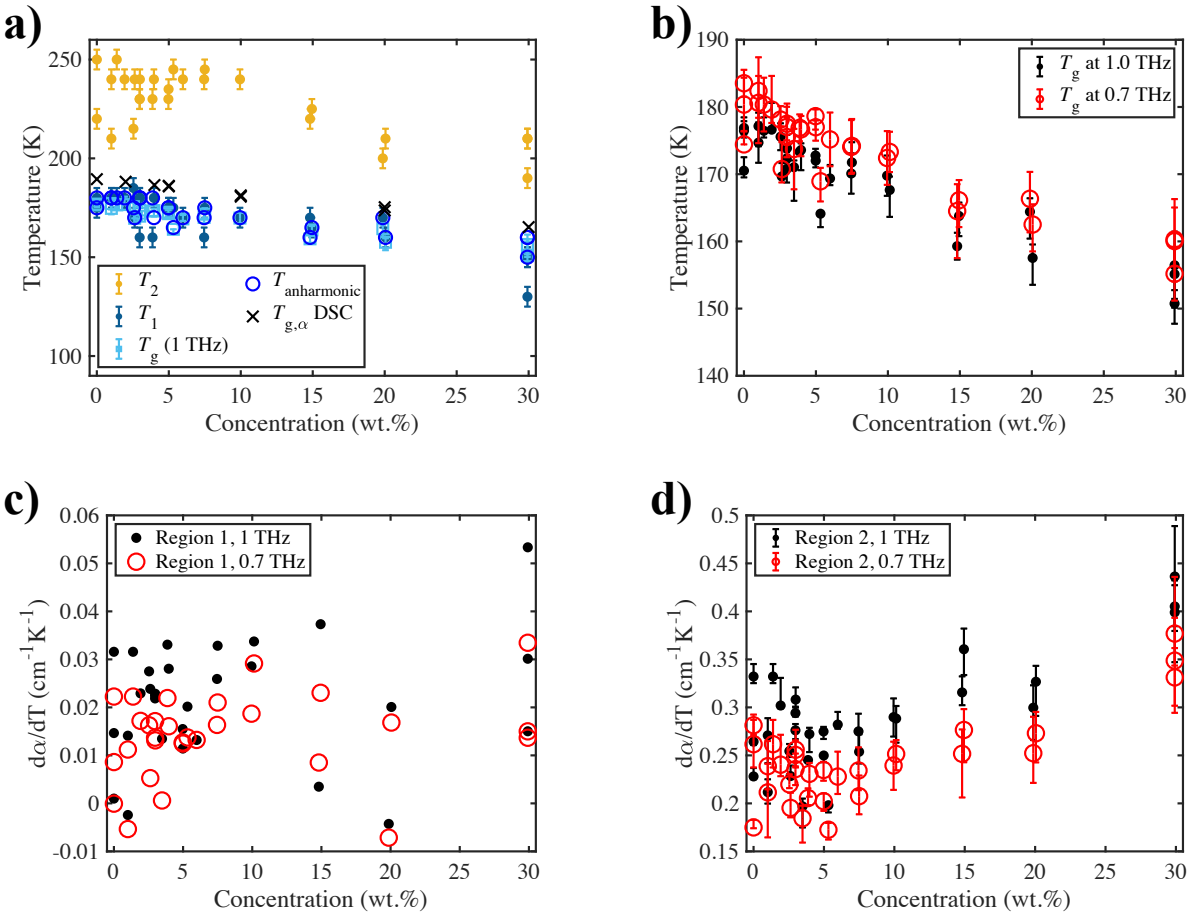

Figure 3.8. (a) Different transition temperatures characterising the onset of mobility and anharmonicity (blue), the calorimetric $T_{g,\alpha}$ (black crosses), and the temperature at which the boson peak dissolves (yellow). T_g was extracted at 1 THz. (b) Comparison of T_g extracted at 1 THz (black dots) and at 0.7 THz (red open circles). (c) and (d) Gradients of linear fits evaluated at 1 THz (black dots) and at 0.7 THz (red open circles) in regions 1 (harmonic contribution, left) and 2 (anharmonic contribution, right). Error bars are shown are calculated by varying the regions for the linear fit as described in Chapter 2.

studies suggest that the onset of mobility in amorphous water may lie in the range of 120 K to 150 K[165] and the PES of bulk-like water is hence expected to comprise shallower minima than that of glycerol where the onset of mobility lies at higher temperatures. The THz-TDS results indicate a shift in the structural dynamics once clusters form, accompanied by a reduced height of the potential energy barrier separating the harmonic from the anharmonic regime.

As the water concentration is increased up to 16.4 wt % water water, the percentage of water molecules that are part of clusters increases to 80 %.[160–162] Our THz-TDS measurements show that the temperature at which the boson peak appears to shift, T_1, is mostly constant for water concentrations between 7.5 wt % water to 20 wt % water. This indicates that while the presence of water-water hydrogen bonds lowers the barriers on the PES, their relative number does not.

Water-water cooperative domains[166,167] and percolating water clusters[158] have been found at even higher water content. In our THz-TDS measurements, the onset temerature of anharmonic effects was decreased noticeably in samples with a water concentration of 30 wt % water. We can hence infer that the mean size of clusters influences the PES and thereby structural dynamics stronger than their number and that the height of the lowest energy barrier is the limiting factor determining the onset temperature of anharmonicity. Regions with lower energy barriers first exhibit an increase in mobility which is measured by THz-TDS.

Anharmonic Regime ($T_g < T < T_m$)

Below T_g (i.e. in region 1), the rate of absorption change does not strongly depend on water content, as shown in Figure 3.8c. In the second region however (i.e. at $T > T_g$), the rate of absorption change starts to increase with water concentration above 5 wt % water (see Figure 3.8d). There is also evidence for a shallow minimum at around 5 wt % water which is more pronounced if the gradient is evaluated at 0.7 THz.

As discussed before, the onset of local mobility and anharmonic effects result in an apparent shift of the boson peak. The rate of absorption change (and therefore the shape of the PES) also started to depend on water concentration. At a concentration of about 5 wt % water, the anharmonic absorption coefficient depended least on temperature. This could be because the sample is most homogenous at this concentration.

Unclustered water reduced the rate of absorption change compared to pure glycerol. This "plasticiser effect" could be because the unclustered water molecules are surrounded by larger glycerol molecules, and any reorientation of the glycerol molecules first requires the breaking of

hydrogen bonds with water.

Once clusters are formed, however, the larger mobility of water molecules in a bulk-like environment increased the rate of absorption change again.

The higher the temperature and mobility, the more anharmonic effects obscure the boson peak until it can no longer be resolved at temperature T_2. This temperature does not depend on water content below 10 wt % water, it decreased for water concentrations up to 20 wt % water, and was constant at higher concentrations. This indicates that the presence of a number of larger water clusters increases anharmonic effects. Unclustered water and small isolated clusters had no effect. However, once percolating clusters were present, at approximately 20 wt % water, they did not further decrease T_2.

Raman scattering experiments have shown that an underlying boson peak continues to be present above T_2 which can no longer be resolved by THz-TDS because it is obscured by anharmonic effects.

At a temperature of approximately 30 K above T_2 lies the melting temperature of the crystalline system and by further heating the supercooled liquid, it enters the liquid regime.

Liquid Regime ($T = 293\,\mathrm{K}$)

A room temperature (293 K) set-up was utilised to measure glycerol-water mixtures in the same concentration range (0 wt % water to 30 wt % water) as discussed above. Measurements could be repeated easily and the spectra shown in Figure 3.9a are the average of 18 measurements each. The absolute error associated with the absorption coefficient measurement is hence decreased and the data quality and spectral range are better than for measurements performed at variable temperatures.

At room temperature, the mixtures are fully liquid and no boson peak is present. The absorption coefficient at 1 THz depends linearly on water concentration c, as can be seen in Figure 3.9b:

$$\alpha(c) = 1.47\,\mathrm{cm}^{-1}\,\%^{-1} \cdot c[\,wt\,\%\,water] + 65.6\,\mathrm{cm}^{-1} \tag{3.1}$$

and the presence or absence of water clusters does not seem to influence this relationship. To investigate how water clusters influence the THz-TDS spectra of liquid glycerol-water mixtures, the frequency-dependent absorption is hence evaluated. The high data quality allowed to extrapolate the absorption coefficient measured in the range 0.6 THz to 2.5 THz according to a

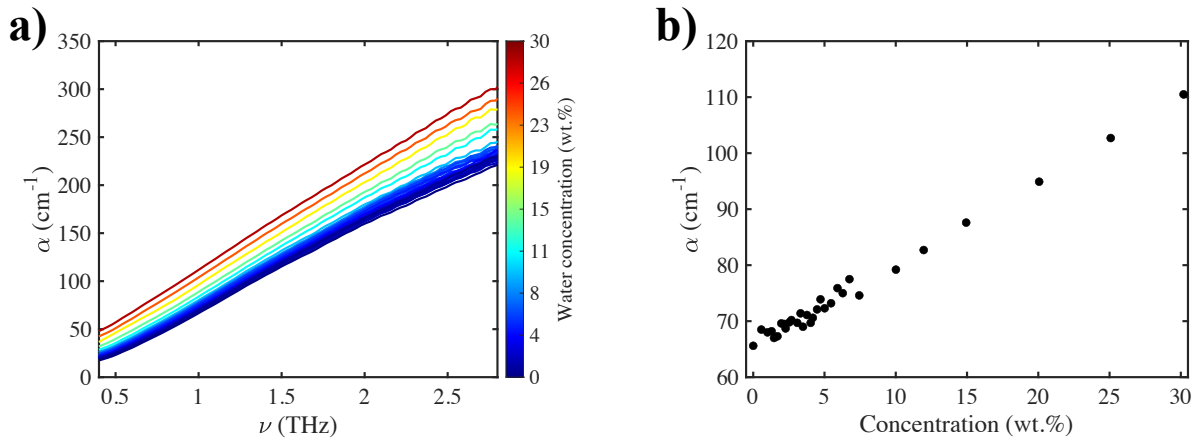

Figure 3.9. (a) Room temperature glycerol solution spectra for different water concentrations. (b) Absorption coefficient at 1 THz.

model developed by Schirmacher et al.[68] However, the model only makes predictions and in a future experiment, the VDOS could be measured on a THz-TDS system with a higher spectral bandwidth.

The better data quality allows to fit Schirmacher et al.'s model[68] to the data in the range 0.6 THz to 2.5 THz to extrapolate the spectra further and investigate the influence of concentration:

$$\alpha = A \cdot \nu^2 \cdot \exp\left(-\nu/(\nu_c/2)\right) + C \tag{3.2}$$

Which predicts a broad peak centred at ν_c. The model was fitted to experimental data restricted to frequencies below 2.5 THz because with increasing frequency the noise increased.[168] Measured spectral data are reduced to the fit parameters and the influence of water concentration is examined.

The parameters α_{max} (maximum absorption) and the full width at half maximum (FWHM) describing the VDOS are determined for different concentrations as shown in Figure 3.10 with the concentration range below 8.5 wt % water water shown in detail in the insets. As expected an increase in water content leads to an increase in absorption, as well as to a broadening of the peak. This also leads to the previously discussed increase in the absorption at 1 THz.

Unclustered water molecules are tightly integrated into the hydrogen-network, with most glycerol hydrogen bonds formed between water and glycerol molecules.[158] Above the glass transition temperature, these water molecules exhibit different degrees of freedom which broadens the VDOS. Increasing the amount of unclustered water led to the most noticeable change in

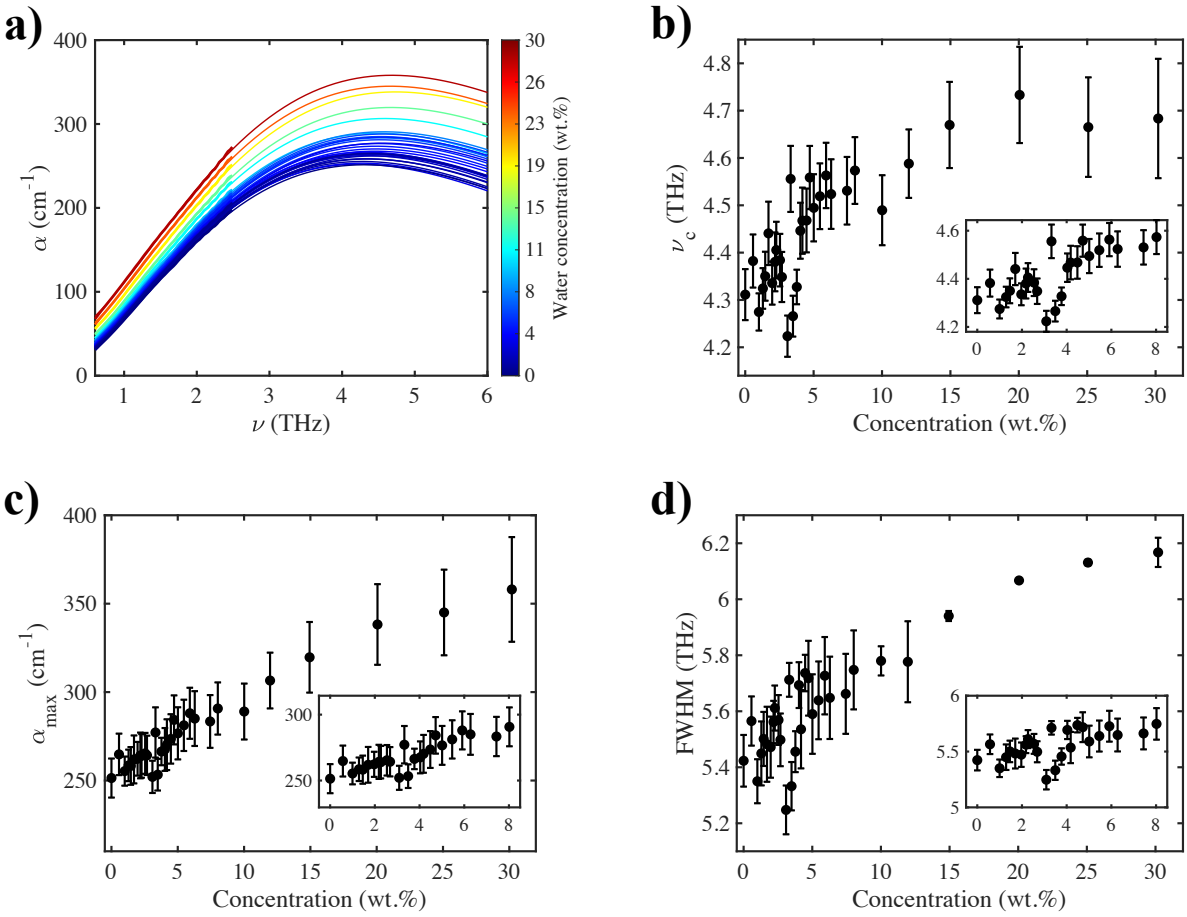

Figure 3.10. (a) Measured spectra (up to 2.5 THz) and extrapolated VDOS at higher frequencies. (b)-(d) Predicted centre frequency (a), maximum absorption (b), and FWHM of the VDOS for different water contents. Error bars are calculated from 95% confidence interval of the fit. The insets show the concentration range 0 wt % water to 8.5 wt % water in more detail.

those three parameters over the whole concentration range studied.

At 6 wt % water, the rate of change in maximum absorption with water content decreases slightly. Once water clusters form, the number of water-glycerol hydrogen bonds decreases and the number of water-water bonds increases. Once clusters are present, a higher water content changes the dynamics less because the water would only increase the cluster size and thereby disrupt the hydrogen-bonded network of glycerol molecules less. Within the clusters, the water dynamics are markedly different from unclustered water molecules that are hydrogen-bonded to glycerol.

While the second clustering threshold just below 20 wt % water was not clearly observed in the boson peak, it influences the behaviour of the system at higher frequencies. All three parameters describing the VDOS change less above a water content of 20 wt % water. Most notably, the centre frequency plateaus above 20 wt % water. At room temperature, bulk water has a higher absorption at 1 THz than glycerol (220 cm^{-1} compared to 66 cm^{-1}) and the larger the water clusters, the more they behave like bulk water. Once percolating water clusters form, they dominate the absorption of liquid glycerol-water mixtures at higher frequencies comprising the VDOS.

3.1.5 Conclusions

While the terahertz spectra of amorphous solids and liquids are featureless, they provide considerable information about glass transition temperatures and the related mobility changes. They also offer insight into the vibrational density of states and the boson peak.

The temperature behaviour is characterised by three regimes: below the glass transition temperature, the system is trapped in a deep minimum of the potential energy landscape and exhibits only harmonic vibrations. The onset of local (and, at slightly higher temperatures), global mobility is accompanied by anharmonic excitations, obscuring the boson peak and eventually leading to its dissolution. Once the system crosses over into the liquid regime, the absorption spectra are dominated by quasi-elastic scattering.

The implications of this model were examined in detail on the example of glycerol and the insights were applied to study the influence of clustered and unclustered water.

In the harmonic regime, the shape of the PES is unaltered in the presence of clustered and unclustered water molecules. Unclustered water molecules are embedded into the glycerol matrix

and do not decrease the onset temperature of anharmonicity. A change in structural dynamics is observed at a water concentration of approximately 5 wt % water, corresponding to a transition from isolated water molecules distributed homogeneously throughout the sample to the presence of small water clusters and an increased number of water-water hydrogen bonds which lower the barriers on the PES.

Interestingly, the intensity of anharmonic effects did not depend on the number of water clusters but on their mean size. It was further found that higher frequencies are first affected by mobility changes upon increasing the temperature.

Data acquired at room temperature were extrapolated according to a model by Schirmacher et al. which allows to investigate the shape of the VDOS for different concentrations for liquid glycerol-water mixtures and confirms a change of dynamics once percolating water clusters formed between 15 wt % water to 20 wt % water.

This methodology has great potential to be applied to other systems to investigate the change of mobility and dynamics.

3.2 High-Temperature Transition

A third transition, termed T_{x}, is found at increased temperatures closer to room temperature. An example is shown in Figure 3.11a. This transition depends on water content and is not a glass transition as it is situated well above the $T_{\mathrm{g},\alpha}$ as measured by THz-TDS and DSC.

In Figure 3.11a, one typical example of that transition is shown. Two linear regressions are performed above the previously determined $T_{\mathrm{g},\alpha}$ and the resulting crossover temperature is termed T_{x}. The fitting procedure is repeated for all measurements and the corresponding T_{x} are shown in Figure 3.11b.

Over the range of all measured concentrations, the third transition temperature coincides well with the onset temperatures of crystal growth of water-glycerol mixtures as observed by Lane,[169] which are shown as red squares in Figure 3.11b. The transition that was found with THz-TDS occurred during heating. Samples had previously been cooled down from room temperature to 80 K over a course of 30 min. Lane on the other hand had slowly cooled down seeded glycerol-water mixtures and reported the temperature at which crystals first appeared and continued to grow.[169]

Liquid glycerol-water mixtures become gradually more viscous upon cooling. In supercooled

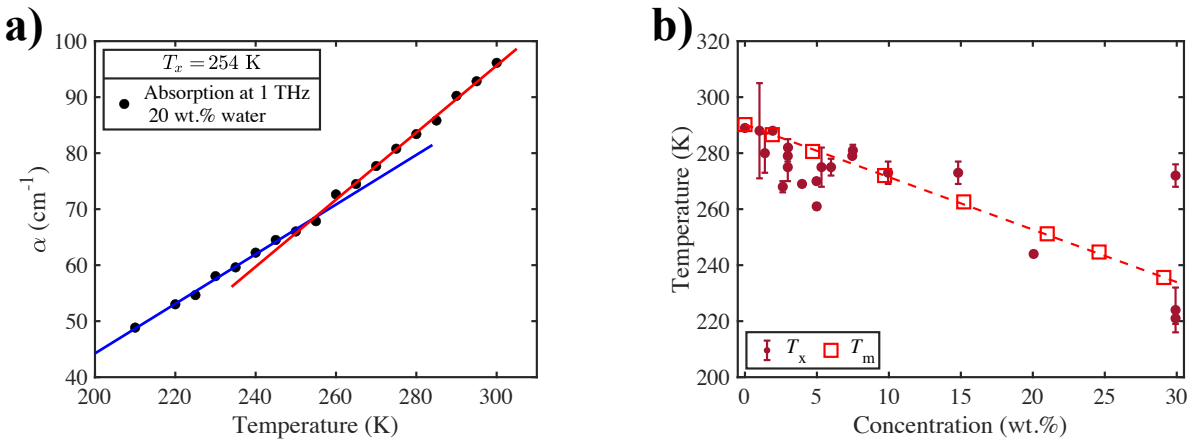

Figure 3.11. (a) Example for a high-temperature transition. Linear fits are shown below and above the transition. (b) Overview T_x for different water concentrations and comparison with data for the glycerol liquidus point from literature.[169] The error bars for T_x are calculated from its spread at different evaluated frequencies.

liquids, mobility fluctuations are relevant, relaxation and diffusion decouple, and the Stokes-Einstein (SE) relation, which connects diffusion coefficient, temperature, and viscosity, is no longer valid. This coincides with a change of the Vogel–Fulcher–Tammann (VFT) fit VFT parameters or other fitting parameters linking viscosity and temperature.[4]

This happened at the so-called "crossover" temperature T_x, where a crossover from nonactivated to activated dynamics (i.e. phonon-assisted hopping processes) takes place, which has been first described by Goldstein.[4,20]

Goldstein's potential energy landscape model is valid until the thermal energy becomes comparable to typical potential energy barriers. T_x therefore separates a low-temperature viscous regime where activation is the main mechanism of diffusion from a high-temperature regime where the SE relation holds. Remarkably, above T_x, dynamics are reasonably well described by mode coupling theory (MCT), which predicts a transition from free diffusion to a dynamically jammed state.[170] T_x could therefore conceptually be considered as coinciding with the critical temperature T_c predicted by MCT.

It is therefore hypothesised that the change in sample behaviour observed with THz-TDS, which is sensitive to intramolecular motions, corresponds to a change in transport mechanism and the T_x measured with THz-TDS indeed coincides with Goldstein's T_x.

Once diffusion is possible, crystals can continue to grow from the seeds, which was observed by Lane and a stronger temperature dependence is found with THz-TDS.

3.3 The Influence of Water Content on Hygroscopy

Glycerol is highly hygroscopic. Literature suggests that below approximately 15 wt % water, glycerol takes up water from air, and that some contained water evaporates at higher concentrations.[171] As it has been shown in the previous measurements that the absorption coefficient is dependent on water content, THz-TDS might also be useful to reliably quantify the water content of glycerol-water mixtures.

Especially in the samples measured only at room temperature, the influence of hygroscopy was seen in some measurements. At each concentration (between 0 wt % water to 30 wt % water as discussed in Section 3.2), the liquid was injected into the cell 6 times and each measured 3 times so that the presented absorption coefficient was calculated from the average of 18 measurements. Two different liquid cells were available that differed slightly in thickness and gave a slightly different absorption coefficient. Each of those liquid cells wqs used three times to ensure that measurements for different concentrations were comparable. The measurement of each concentration took between 40 and 55 min so that the measured absorption coefficient could be plotted against the time at which it was measured to visualise a possible trend. In between measurements, care was taken to seal the test tube in which the liquid had been prepared but due to the repeated opening and closing of the vials, the water content might have changed slightly between different measurements.

Depending on the initial water concentration in the samples, the absorption coefficient measured changed over time, as shown in Figure 3.12. Least change was observed in samples containing around 12 wt % water water. Figure 3.12 shows three different representative measurements where the absorption increased with time, stayed constant, or decreased, respectively.

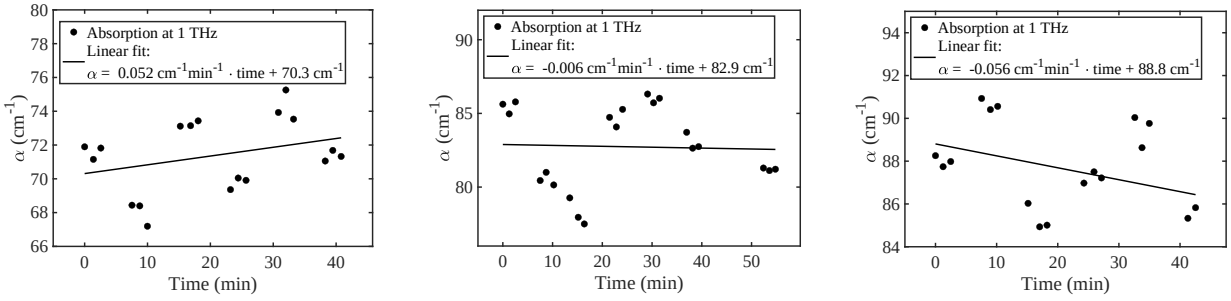

Figure 3.12. Small variations in water content were visible between single measurements. One liquid cell gave continuously higher absorption values than the other, however, this did not influence the time-dependent trend which is visualised by a linear regression (black line).

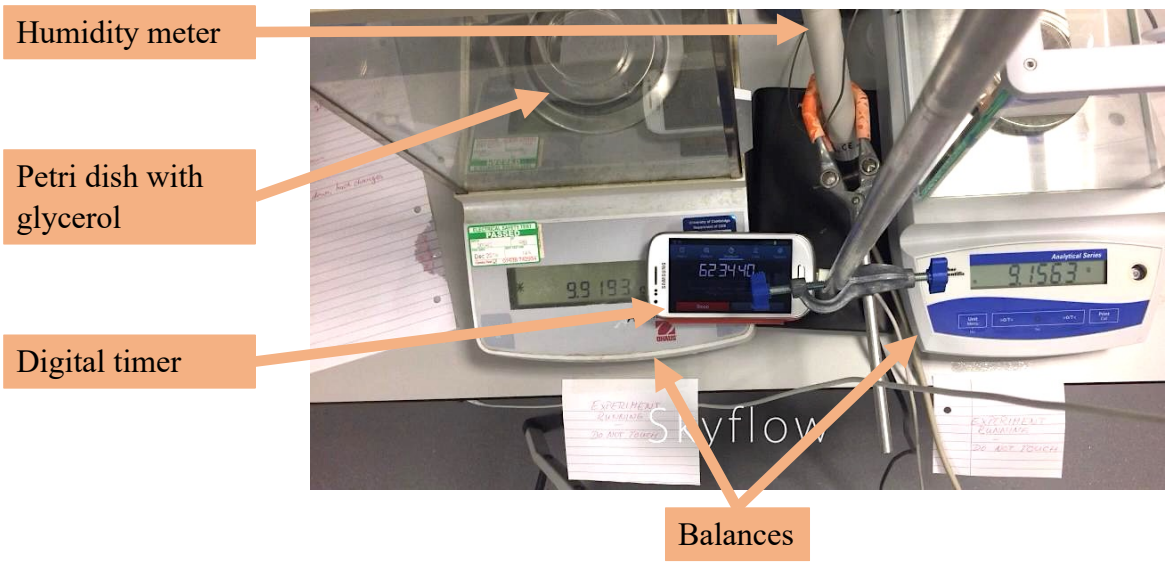

Figure 3.13. Setup to measure water uptake/loss of glycerol over time.

That the absorption would sometimes increase and sometimes decrease was peculiar, and it was investigated systematically. A very simple experiment was performed by measuring the weight gain/loss of a petri dish filled with glycerol-water mixtures over time. As the initial water concentration is known, the water content at any time can be calculated. The setup is shown in Figure 3.13.

Glycerol was filled in a petri dish in the desired concentration and the initial weight was noted. A digital timer was started and a camera took photos of both the balance display and the digital timer automatically in fixed intervals. As two balances were available, they were placed next to each other so the displays could be captured simultaneously. Weight fluctuations were then recorded over a period of approximately 6 hours for each initial concentration (0, 2, 3.5, 5, 8, 10, 15, 20, an 30 wt % water, shown in Figure 3.14). During one longer experiment, temperature and humidity were also recorded to investigate whether their fluctuations made an impact, as shown in Figure 3.15.

Subsequently, time and weight were extracted from the images and converted to water concentration. The results for different initial water concentrations are shown in Figure 3.14 and Figure 3.15.

As apparent in Figure 3.15, there might be a small correlation between a fast increase in humidity at around 250 $s^{1/2}$ and an increase in water content, especially in the sample containing 10 wt % water. However, both samples were placed in very close proximity and the other sample

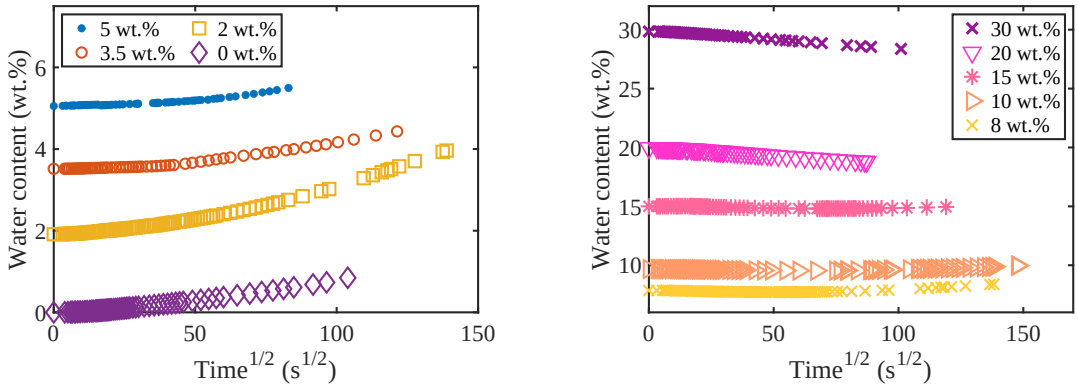

Figure 3.14. Change of water content over time for samples containing less than 5 wt % water (left) or more than 8 wt % water (right) at the beginning of the measurement.

should have been affected equally. As the effects are very weak, it is hard to be certain what the influence of humidity changes were. The temperature was very stable over the course of the measurement and small fluctuations seemed not to impact the water gain/loss measurably.

The shorter experiments showed that samples initially containing less than 8 wt % water gain weight over time. Intermediate initial concentrations (between 8 wt % water to 15 wt % water) lead to a fluctuation of the mass change over time between gain and loss. In agreement with literature[171] , samples initially containing more than 15 wt % water lost weight over time as water evaporated.

The weight loss at high water contents may be linked to percolating water clusters where water molecules close to the surface behave similarly to bulk water and easily evaporate. Pure glycerol is very hygroscopic, and it is hypothesised that the presence of at least small clusters is necessary for water to evaporate and that the fluctuations at intermediate concentrations hence indicate the presence of smaller clusters.

The rate at which water was gained or lost is plotted in Figure 3.16 depending on the initial concentration. The mixtures containing 20 wt % water and 30 wt % water behave very similarly. The initial decrease in concentration slows slightly, probably because the water molecules close to the surface are depleted first before an equilibrium with the surrounding is formed. In mixtures initially containing 8 wt % water to 15 wt % water, the gradient fluctuates initially before getting close to zero when an equilibrium is formed, which is probably located close to 15 wt % water, in agreement with literature.[171]

In mixtures containing even less water, the initial increase is stronger and an equilibrium

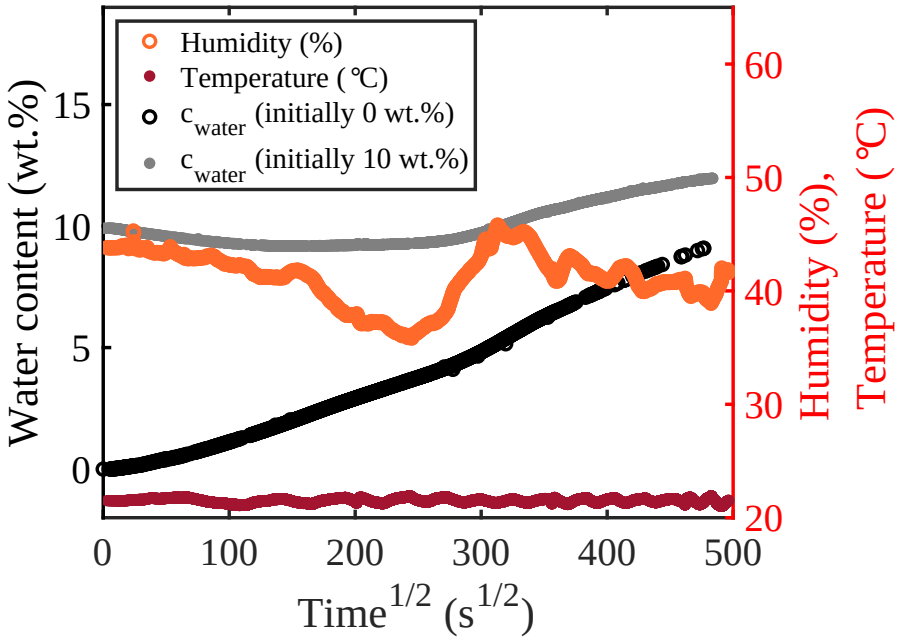

Figure 3.15. Change of water content over time for sample containing 0 wt % water (black) and 10 wt % water (grey) water at the beginning of the measurement. Temperature (red) and humidity (orange) are also shown. The entire experiment was running for approximately 70 hours.

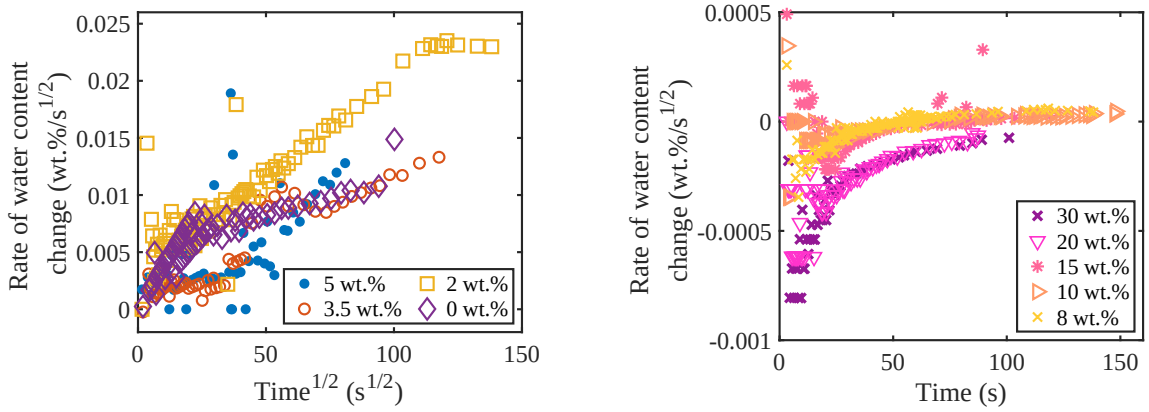

Figure 3.16. Rate of change of water gain/loss for samples containing less than 5 wt % water (left) or more than 8 wt % water (right) at the beginning of the measurement.

is not reached on experimental time scales. Interestingly, the rate of water content change in mixtures initially containing 0 wt % water and 2 wt % water is largest, probably because at the start of the experiment, almost no water molecules are present near the surface.

In all experiments, it was assumed that the water was distributed evenly throughout the sample and the concentration calculation was based on the entire sample volume and not just a volume close to the surface which should be higher.

The observations described in Chapter 3.1 have shown that samples containing water clusters might absorb differently compared to samples without clusters, explaining some of the observations made when repeating THz-TDS measurements at room temperature.

Samples with initial concentrations of 20 wt % water and 30 wt % water already contain clusters, and predominantly lose water due to evaporation, as water in percolating clusters is not tightly bound to glycerol. If less water is present in samples at the beginning, i.e. 8 wt % water to 15 wt % water, the clusters are smaller, and the water near the surface might get depleted. Once hygroscopic glycerol molecules dominate the surface, more water is absorbed, and the cycle starts again. At even lower water content, for example between 3.5 wt % water and 5 wt % water, the number of clusters is smaller and while some water evaporates from the clusters, more is absorbed. If no clusters are present, it is energetically favourable for water molecules to be embedded into the glycerol network and the water uptake is fastest.

The experiments described here are very simple and the results intriguing. In future work, this concept could be explored further. One possibility would be to use THz-TDS to quantify the amount of surface-near water utilising the reflection setup, as shown in Figure 3.17 for a sample of initially pure glycerol.

From balance experiments, the bulk water concentration is known, so ideally, the content of near-surface water can be compared to the entire water content of the sample, as illlustrated in Figure 3.18.

A limitation was the fact that it is unknown whether the balance experiment actually measured bulk concentration. Depending on how fast adsorbed water diffuses into the sample, the mixing might have not been ideal. Furthermore, due to necessary calibration of the reflection probe on the sample surface, the measurement could not reliably be started at a water concentration of 0 wt % water. Another limitation is the amount of data that has to be acquired due to the high noise level and which leads to glitches in the data acquisition programme.

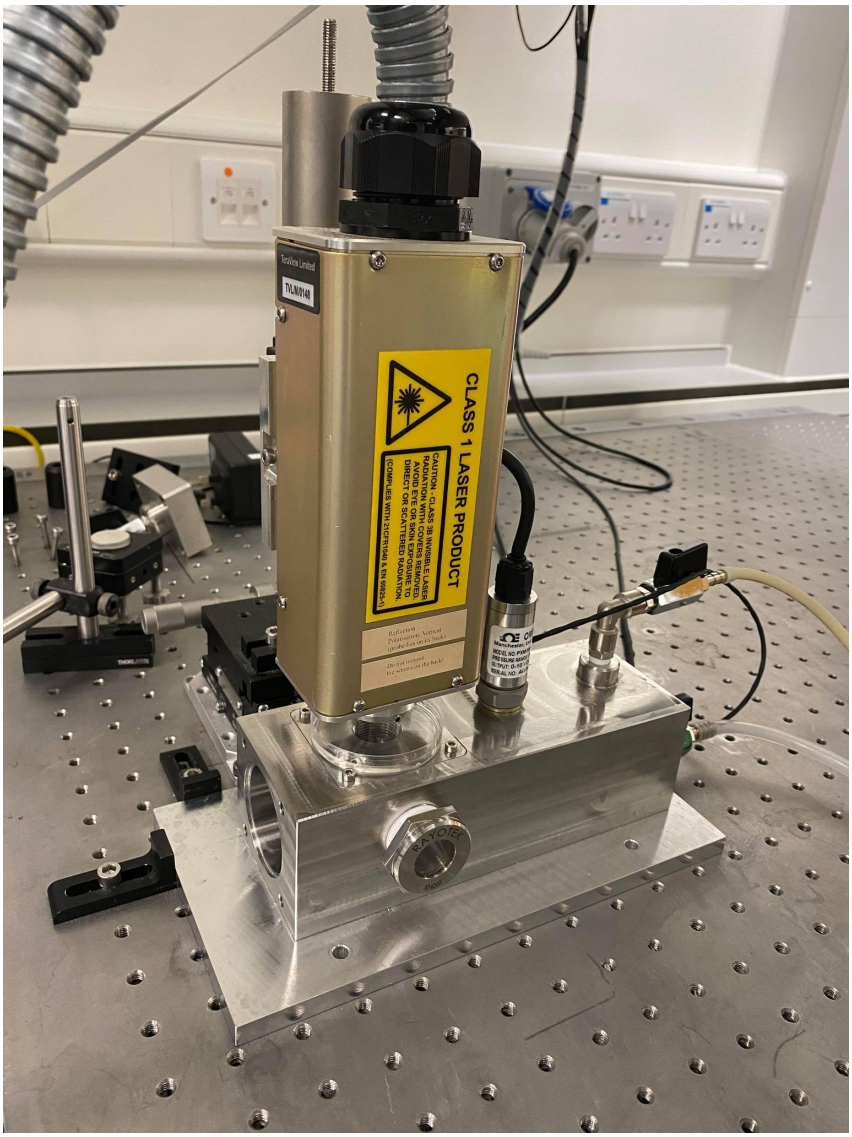

Figure 3.17. Setup for reflection (i.e. surface) measurement.

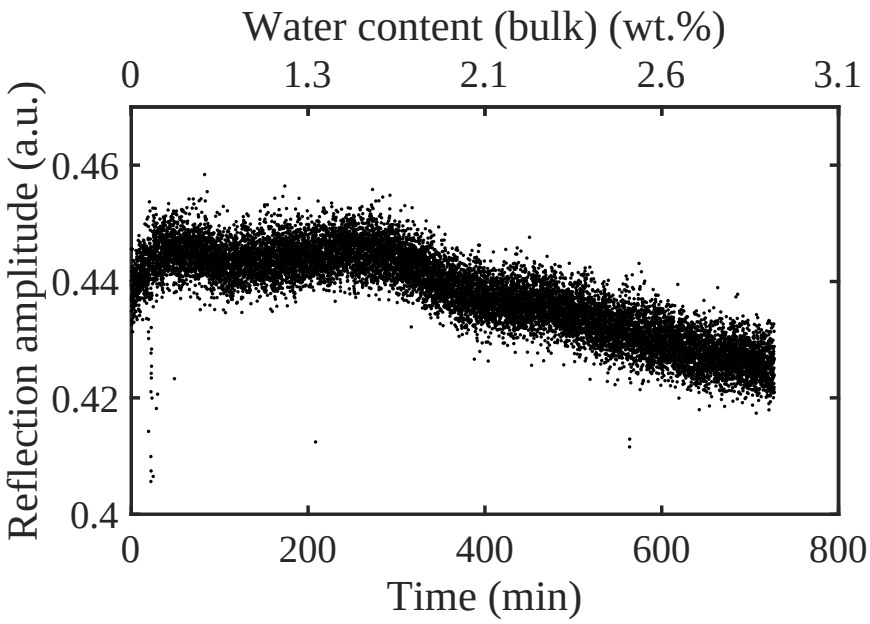

Figure 3.18. Amplitude of reflected peak changes with time. Expected bulk water concentration is also shown.

If the methodology utilising THz-TDS to quantify surface-water content is improved in the future, and complemented by other methods, the influence of water clusters on hygroscopicity can be further investigated.

4 The Role of Terahertz Dynamics in Solid-State Protein Formulations

Understanding of the molecular mobility in freeze-dried matrices is of high importance for the assessment and prediction of the stability of lyophilised protein and peptide drugs. Using terahertz spectroscopy it is possible to measure the molecular mobility in such lyophilisates.

In Chapter 4.1, the effect of size on the dynamics of four one-component lyophilised (freeze-dried) products, covering a range of molecular complexity from simple sugar to globular protein, is studied with terahertz time-domain spectroscopy and differential scanning calorimetry. While sucrose exhibits the well-known behaviour of increasing absorption with temperature observed in small organic molecular systems, the polypeptide bacitracin and the two globular proteins lysozyme and human serum albumin show a more complex temperature dependence. Further analysis is performed to extract additional information from the spectral signature of the boson peak. The analysis reveals evidence for the onset of anharmonic motions that can be extracted from the boson peak that also give evidence for partial unfolding and molecular jamming.

In Chapter 4.2, samples composed of different ratios of the excipient sucrose to monoclonal antibody (mAb) are discussed. Upon increasing the relative amount of mAb in the mixture, evidence for vibrational confinement which clearly originates from the protein molecules and not the excipient matrix or residual water molecules in the system was observed.

This chapter resulted from a collaboration with Wolfgang Friess and Ivonne Seifert from the Ludwig-Maximilias-University Munich who lyophilised the samples and performed the DSC measurements. I measured the samples with THz-TDS and applied the analysis methodology originally developed for the glycerol-water system.

The THz-TDS measurements for Chapter 4.2 were performed together with the visiting master's student Moritz Anuschek who wrote part of his master's thesis about the project. The results of Chapter 4.2 were published and presented in a talk at the 2020 45th International Conference on Infrared, Millimeter, and Terahertz Waves (IRMMW-THz) (doi: 10.1109/IRMMW-THz46771.2020.9370816.,[172] `youtu.be/Td4jrbKLCSw`[173]) and a manuscript relating to Chapter 4.1 is in preparation.

4.1 The Effect of Size on the Terahertz Dynamics of One-Component Lyophilisates

4.1.1 Introduction

Traditional small molecular active pharmaceutical ingredients (API) commonly exhibit low solubility in water that limits their bioavailability. By transforming the crystalline material into its amorphous state an increase in the apparent aqueous solubility can be achieved but the challenge shifts to controlling and predicting the rate of recrystallisation in order to achieve sufficient long-term stability to market such drug products. In contrast, for the administration and delivery of so-called biopharmaceutical drugs, i.e. more complex molecular structures such as peptide and protein structures, the solubility of the drug molecules may not be the primary concern. However, the fact that these structures typically need to be administered by injection combined with the poor stability of the molecules in aqueous solution means that they are typically freeze- or spray-dried into an amorphous solid matrix for storage. In either case, a better understanding of the fundamental limitations of amorphous organic molecular materials is critical for the successful development of modern medicines.[1]

Biopharmaceutical drugs need to be developed into complex amorphous formulations by adding a number of excipient molecules in order to preserve the functional structure of the protein during drying and subsequent reconstitution as well as to achieve the correct pH, ionicity and viscosity of the solution suitable for injection. In lyophilisation (freeze-drying) a solution of the formulation is prepared and then the solvent (water) is separated under reduced temperature and pressure during the so-called primary drying phase when the ice sublimates. Any residual moisture is removed during secondary drying at higher temperatures.[174] The aim of lyophilisation is to increase the stability of the formulation thus allowing for room temperature storage. The exact properties of lyophilised samples depend on their composition and common formulation components include buffers, bulking agents, tonicity modifiers, and surfactants, as well as the active biomolecule. The design of pharmaceutical products requires a good understanding of the underlying mechanisms of the formulation components as well as the process.[107,174]

Previous work utilising terahertz time-domain spectroscopy (THz-TDS) has shown that two glass transition processes, $T_{g,\alpha}$ and $T_{g,\beta}$, can be measured at terahertz frequencies.[15] Both of these are thought to influence the structural dynamics of complex lyophilised protein formu-

lations.[104] This oberservation is not unique to THz-TDS and $T_{g,\alpha}$ and $T_{g,\beta}$ can be detected using a wide range of experimental techniques that probe the dynamics on different time-scales, for example, dielectric spectroscopy,[175] dynamic mechanical analysis (DMA)[176] and differential scanning calorimetry (DSC).[177]

Terahertz dynamics play an important role in understanding solid-state protein dynamics. At storage temperature (room temperature), a considerable amount of motions in the terahertz frequency range is active and contributes to the formulation stability. Past experiments have further shown that vibrational confinement can strongly reduce the molecular mobility at temperatures above $T_{g,\alpha}$ (in many cases this is close to room temperature) and such behaviour was found to be heavily dependent on formulation.[104] Upon increasing the temperature, the molecular mobility in the sample increases, until the free volume is taken up completely and the molecule becomes "jammed". Any further increase in mobility, and hence measurable terahertz absorption, is no longer possible until a higher energy barrier is overcome that is associated with further degrees of freedom for the motions of the molecules.

In crystalline samples, Allen et al. have used a Bose-Einstein distribution approach to track the frequency changes of terahertz modes with temperature, assuming it was entirely mediated by phonons.[178] In contrast, in inherently disordered glasses, no discrete phonon modes can be sustained due to the lack of long-range order and hence the coupling of photons to the vibrational density of states (VDOS) forms the main absorption mechanism of amorphous samples in the terahertz range. This absorption results in a broad, so-called "microscopical peak" that spans in frequency from a few hundred gigahertz to several THz.[63] Typical THz-TDS instruments do not have sufficient spectral bandwidth to resolve the high frequency part of the peak and hence most spectra of amorphous organic molecular materials resemble a steadily rising flank of absorption that can be fitted, e.g. by a power law function.

According to Debye theory, and confirmed experimentally with far-infrared spectroscopy, the VDOS is expected to follow a frequency-squared dependence. At frequencies that are easily accessible with THz-TDS ($< 3\,\mathrm{THz}$) the total absorption rises with increasing temperature. Taraskin et al. showed that the coupling between photons and atomic vibrations below the Ioffe-Regel crossover has a quadratic dependence, and that the absorption in the terahertz range can be expressed as $\alpha(\nu) = C(\nu)g(\nu)$ with the coupling function $C(\nu) \propto \nu^2$ and the VDOS $g(\nu) \propto \nu^2$.[63]

The excess density of states above the Debye level is referred to as the boson peak. It can be observed in experimental data when plotting the absorption coefficient by frequency squared. The boson peak is a harmonic phenomenon due to inherent disorder that can be obscured by anharmonic effects.[66] Utilising THz-TDS, the onset temperature of molecular mobility was found to correlate with anharmonic effects in the model glass-former glycerol. These anharmonic effects resulted in an apparent shift of the boson peak centre frequency and could be separated from harmonic contributions as described in detail in Chapter 3.1. Chumakov et al. found that a significant part of the boson peak in glycerol is constituted of collective modes.[68] They also found that it disappeared close to $T_{g,\alpha}$ due to increased sample mobility and further observed an exponential decrease in the reduced density of states at energies above the boson peak maximum.

Markelz et al.[57] observed that in an amorphous sample an increase in absorption at a single frequency as measured with THz-TDS is due to anharmonic effects, even at very low temperatures. While no real PES is perfectly harmonic, these effects are comparatively small at low temperatures, e.g. the boson peak is not yet obscured or its apparent centre frequency affected. We will hence refer to the temperature region below $T_{g,\beta}$, i.e. at temperatures at which the boson peak is unaffected by anharmonic effects, as the harmonic regime, and to the temperature region at which the boson peak is affected as the anharmonic regime.

In the present work we investigated the effect of excipient size on terahertz dynamics in four different one-component lyophilized products, namely sucrose (a common bulking agent, molecular weight 0.34 kDa), bacitracin (a polypetide antibiotic, molecular weight 1.4 kDa), lysozyme (a globular protein, molecular weight 14.5 kDa), and human serum albumin (HSA, a globular protein and bulking agent, molecular weight 66.5 kDa), which are also shown in Figure 4.1.

4.1.2 Materials and Methods

Materials

Sucrose and HSA were purchased from Merck GmbH (Steinheim, Germany). Bacitracin and lysozyme were purchased from Carl Roth GmbH (Karlsruhe, Germany). The samples detailed in Table 4.1 were prepared with highly purified water (HPW; Sartorius Arium Pro, Sartorius, Göttingen, Germany) to reach a total solid content of 10 % prior to lyophilisation.

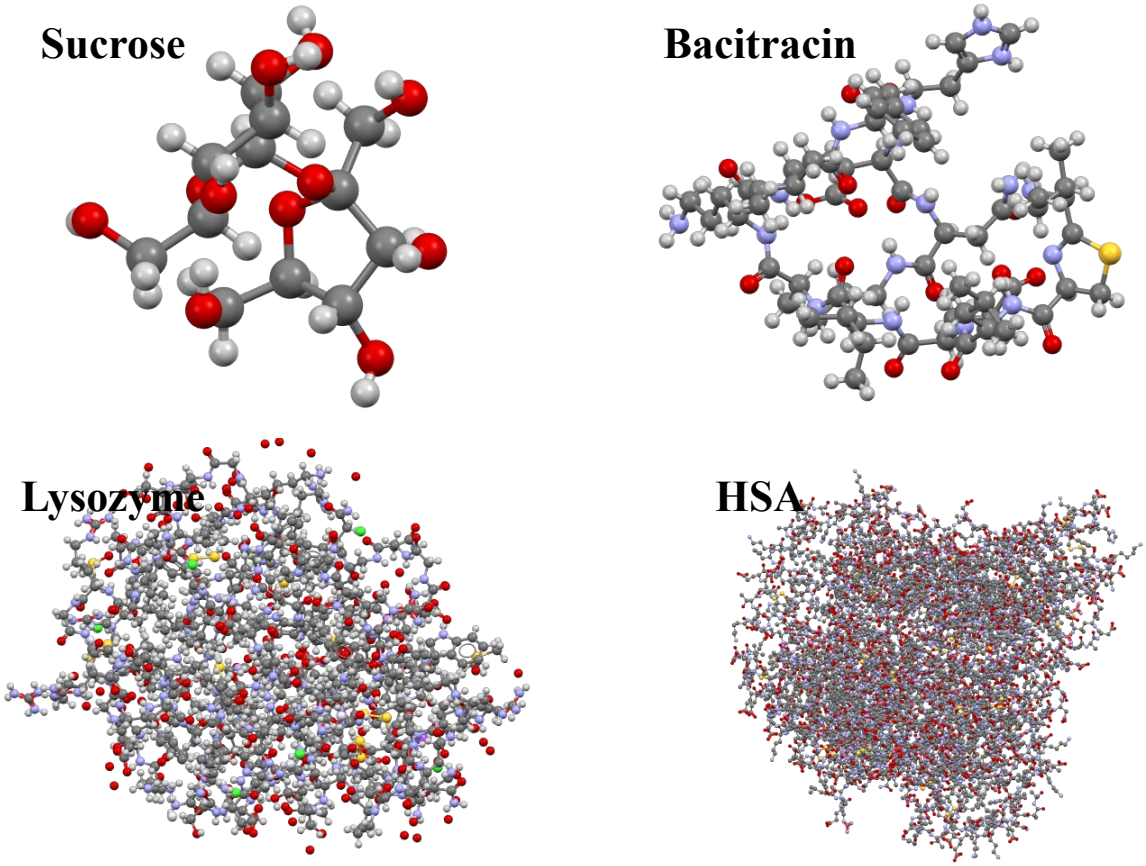

Figure 4.1. Visualisation of the different molecules.

Table 4.1. Samples used.

	Sucrose	Bacitracin	Lysozyme	HSA
Weight (kDa)	0.342	1.423	14.5	66.5

Lyophilisation

Lyophilisation stoppers (B2-TR coating, West) and DIN 10R vials (Fiolax®, Schott, Germany) were cleaned with highly purified water and dried at 333 K for 8 h. The vials were filled with 3 mL solution and subsequently semi-stoppered. The product temperature over the shelf area was recorded with a thermocouple. Formulations were freeze-dried according to the protocol shown in Table 4.2 using a FTS LyoStar™ 3 freeze dryer (SP Scientific, Warminster, Pennsylvania, USA). End of primary drying was controlled by comparative pressure measurement between a Pirani and MKS sensor. The vials were stoppered after secondary drying under nitrogen atmosphere at 800 mbar and crimped with flip-off seals.

Table 4.2. Lyophilisation protocol.

Step	Ramp (K/ min)	Shelf temperature (K)	Pressure (µbar)	Hold time (h)
Freezing	1.0	223	–	3
Primary drying	0.5	253	60	50
Secondary drying	0.4	323	60	5

Differential Scanning Calorimetry (DSC)

The glass transition temperature ($T_{g,\alpha}$) of the lyophilisates was determined with a DSC 821^e (Mettler Toledo, Gießen, Germany). 5 to 10 mg of crushed cake were filled into aluminium 40 µL crucibles (Mettler Toledo, Gießen, Germany) under controlled humidity conditions ($\leq$10 % rel. humidity) and sealed hermetically. The samples were heated from 280 K to 415 K at 2 K/min. $T_{g,\alpha}$ was determined as the midpoint of the phase transition.

Terahertz Time-Domain Spectroscopy (THz-TDS)

Lyophilised samples were stored in sealed vials to prevent water uptake. All further sample preparation was performed just prior to measurements under dry nitrogen atmosphere utilising a glove bag (AtmosBag, Merck UK, Gillingham, UK). The lyophilised cake was broken up and the powder was gently mixed using an agate mortar and pestle and then pressed into thin pellets (thickness less than 800 µm, diameter 13 mm) using a manual press (load 3 t, Specac

Ltd, Orpington, UK). The pellet was then sealed between two z-cut quartz windows of 2 mm thickness each and fixed to the coldfinger of a cryostat (ST-100, Janis, Wilmington, MA, USA).

Samples were analysed with a Terapulse 4000 (Teraview Ltd, Cambridge, UK) in transmission while the samples were kept under vacuum (pressure < 20 mbar). Each sample and reference spectrum was calculated from the co-average of 1000 waveforms which were acquired with a resolution of $0.94\,\mathrm{cm}^{-1}$ and transformed to the frequency domain by a FFT. The absorption coefficient was calculated following the method by Duvillaret et al.[138]

At the beginning of each measurement, the sample was cooled down from room temperature to 80 K and left to equilibrate for at least 30 min. The temperature was subsequently increased in steps of 10 K up to a maximum temperature of 440 K. The system was allowed to equilibrate again for 8 min at each temperature increment before both a reference (of two z-cut quartz windows with no sample in between) and the sample measurement were performed.

4.1.3 Results and Discussion

Thermal Analysis

DSC data were acquired for pure lyophilised samples as well as for mixtures with sucrose in different ratios with a heating rate of $2\,\mathrm{K\,min}^{-1}$ (shown in Figure 4.2) and the glass transition temperatures for sucrose and mixtures containing 33 % and less protein were evaluated. In samples containing more than 33 % protein, the heat flow did no longer show a clear step corresponding to the glass transition. Instead, a gradual decrease in heat flow was observed that is linked to protein unfolding at elevated temperatures. The time scales of unfolding are strongly temperature-dependent and it is possible that mobility was insufficient to maintain equilibrium between folded and unfolded states during the DSC measurements.[179] In each of the three pure protein samples, an inflection point was found, namely at 348 K (bacitracin), 330 K (lysozyme), and 337 K (HSA). In Figure 4.3, the curves for the neat formulations are shown in detail.

Molecular Mobility and Confinement Effects Depend on the Size of the Molecules

The absorption spectra of different samples are shown in Figure 4.4. It is apparent that while all spectra qualitatively look similar, the absorption coefficient of sucrose was most dependent on temperature.

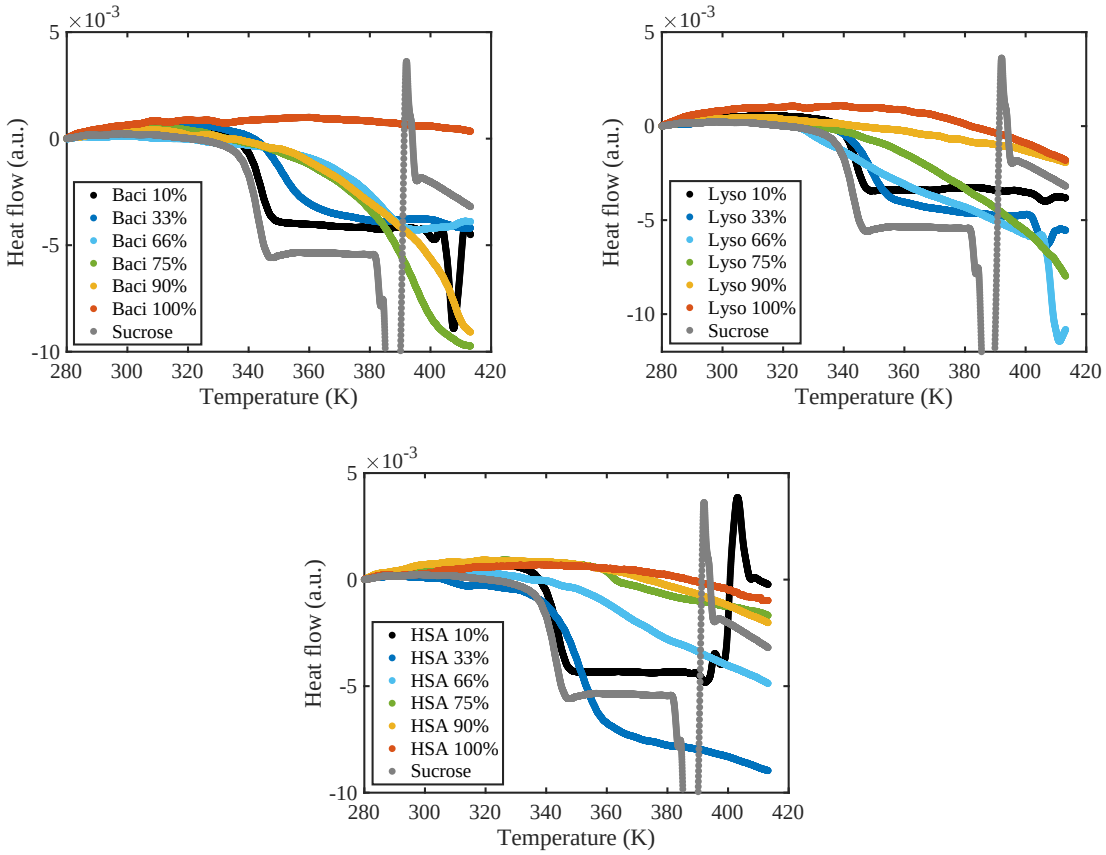

Figure 4.2. DSC curves for different samples. With decreasing sugar content, $T_{g,\alpha}$ gets less pronounced.

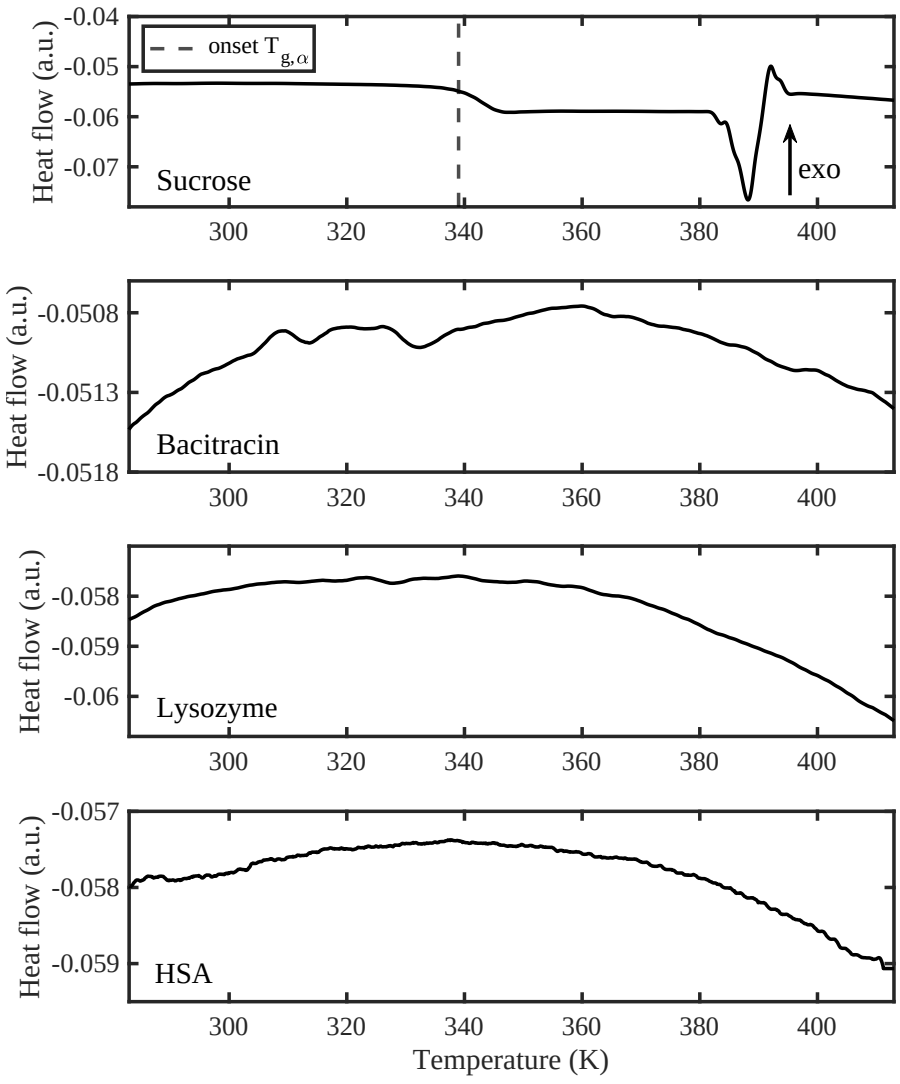

u

Figure 4.3. DSC curves for different samples. A clear $T_{g,\alpha}$ was only found for sucrose. The inflection points for the other curves were found at 348 K (bacitracin), 330 K (lysozyme), and 337 K (HSA).

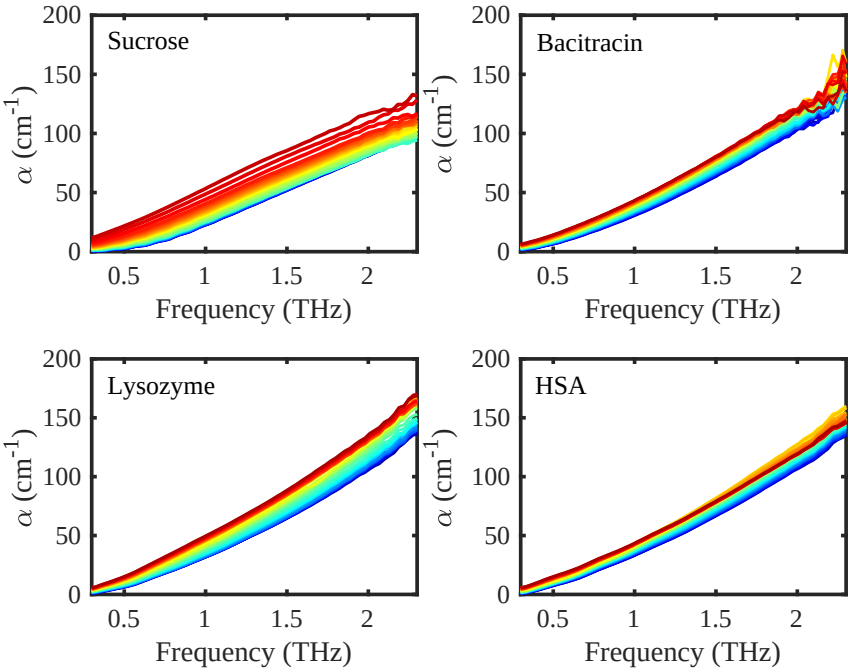

Figure 4.4. Terahertz spectra for different samples. Absorption mostly increases with temperature. Blue: 80 K, red: 420 K, spectra were acquired in temperature intervals of 10 K.

Sucrose is an example for a model small molecular system that, in the disordered state, exhibits two glass transition temperatures ($T_{g,\alpha}$ and $T_{g,\beta}$) upon heating before crystallising at around 380 K.[180] When plotting the absorption coefficient at a specific frequency (commonly the one with the highest signal-to-noise ratio, in our setup 1 THz), the rate of absorption change increased at both glass transition temperatures (see Figure 4.5). The exact temperatures were determined by fitting linear functions to the data and determining the temperature ranges that minimised the sum of the root-mean-square deviation of the fits.[101] $T_{g,\alpha}$ was found at 340 K which agreed very well with DSC and literature values[180] and $T_{g,\beta}$ was found at 230 K.

The larger systems, however, exhibited a different behaviour, as can be seen in Figure 4.5. The changes in gradient between different temperature regions were very subtle for the sample of bacitracin. In lysozyme, the absorption change below 220 K was the most gradual of the different samples. Generally, the rate of absorption change decreased at temperatures above 300 K in the larger molecular weight systems, which is also shown in Table 4.3.

This phenomenon was previously observed in other (more complex) lyophilised formulations and attributed to high-temperature macromolecular confinement.[104] We observe that the con-

Table 4.3. Rate of absorption change with temperature.

	Sucrose	Bacitracin	Lysozyme	HSA
Weight (kDa)	0.342	1.423	14.5	66.5
$\mathrm{d}\alpha/\mathrm{d}T$ for $T < 200\,\mathrm{K}$ ($\mathrm{cm}^{-1}\,\mathrm{K}^{-1}$)	0.03	0.03	0.04	0.03
$\mathrm{d}\alpha/\mathrm{d}T$ for $200\,\mathrm{K} < T < 300\,\mathrm{K}$ ($\mathrm{cm}^{-1}\,\mathrm{K}^{-1}$)	0.07	0.05	0.09	0.05
$\mathrm{d}\alpha/\mathrm{d}T$ for $T > 300\,\mathrm{K}$ ($\mathrm{cm}^{-1}\,\mathrm{K}^{-1}$)	0.11	0.03	0.05	0.02

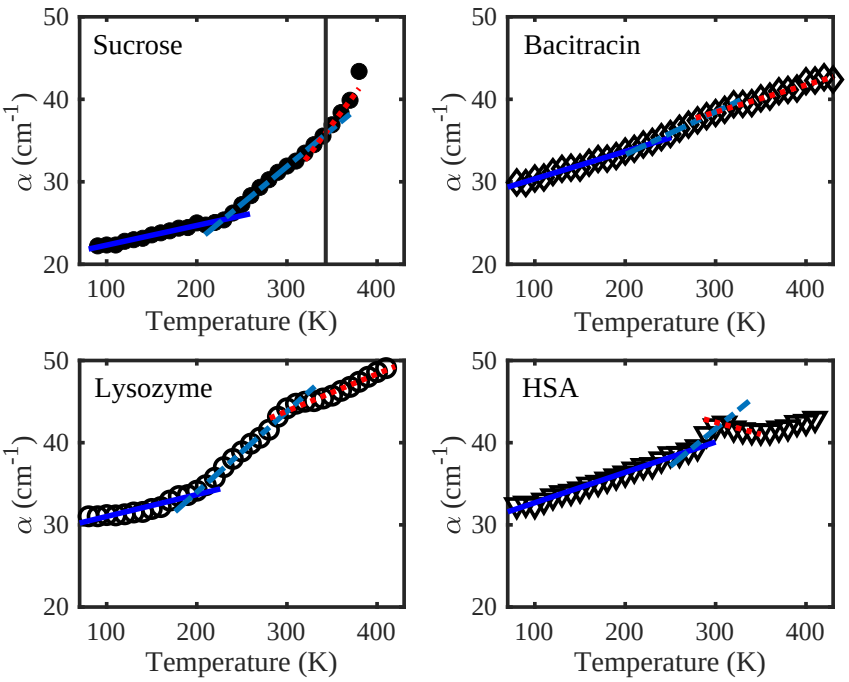

Figure 4.5. Absorption at 1 THz for different lyophilised samples. The vertical line in the plot of sucrose marks the $T_{\mathrm{g},\alpha}$ as determined with DSC.

finement effect depends clearly on the shape and size of the molecules. In small molecular systems (like sucrose) it cannot be observed: the molecules are too small and have too few degrees of freedom to reach a "jammed conformation". Both in bacitracin and lysozyme, a restriction of motions, i.e. a change of the PES, is observed similarly, however more pronounced in lysozyme as expected due to the increased size and hence higher number of internal degrees of freedom. Between 310 K to 330 K, the absorption coefficient in lysozyme does not increase and as shown in Table 4.3, the overall absorption change with temperature is decreased above 300 K compared to lower temperatures. Above 330 K, the absorption increases again with temperature, namely with a rate of $0.04\,\mathrm{cm^{-1}\,K^{-1}}$ in bacitracin, and $0.06\,\mathrm{cm^{-1}\,K^{-1}}$ in lysozyme. In BSA formulations, a similar increase was found at 325 K, corresponding to an energy barrier of 2.7 kJ/mol (equal to 0.65 kcal/mol).[105] The temperature where the increase was observed in bacitracin and lysozyme is very close to that value, indicating that the energy barrier to overcome the intermolecular jamming was of a similar height. This however is still lower than the energy barrier from the native to the denatured state, which lies in the tens of kcal/mol.[181]

The confinement was most pronounced in HSA, the sample with the largest macromolecule. Between 310 K to 360 K, the absorption coefficient even decreased, possibly because the molecules, once trapped in a steep minimum on the potential energy landscape, as shown schematically in Figure 4.6, lost some of the degrees of freedom as the conformational jamming increased. Even after the jammed conformation was overcome, $\mathrm{d}\alpha/\mathrm{d}T$ in HSA was lower compared to lysozyme by more than half.

While bacitracin and lysozyme are known to exhibit a protein dynamical transition (equivalent to $T_{\mathrm{g},\beta}$ in smaller systems) at around 200 K, it is not found in HSA at a similar temperature. Instead, the protein dynamical transition might occur just before the trapping is observed, at around 270 K, as a necessary precursor for molecular jamming.

Molecular jamming decreases anharmonicity

The boson peak was made visible by plotting the absorption coefficient α divided by the square of the frequency ν, as shown in Figure 4.8 on the left hand side. Due to the broad nature of the peak and noise in the spectrum, the maximum value of α/ν^2 had to be found from a fit of a second order polynomial to the data. This fit function uses the least number of parameters necessary to reproduce the shape and even though the exact physical meaning behind the parameters is unknown, Taraskin et al.[63] predicted a quadratic dependence for α/ν^2. An example for a

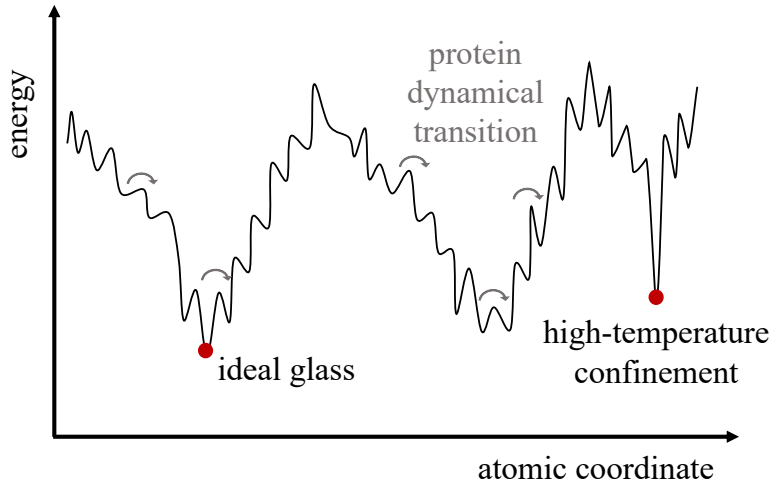

Figure 4.6. Possible potential energy landscape topology. With sufficient thermal energy, a sample can explore different configurations on the hypersurface and might become trapped in shallow minima.

quadratic fit to lysozyme data is shown in Figure 4.7.

If the peak was situated below the lower fit boundary, the fit function was not extrapolated and no maximum was reported to avoid too large extrapolation errors.

As previously observed in small molecular systems, for example in glycerol, the dynamics of glasses upon heating usually fall into two regimes. At very low temperatures, the terahertz spectra are dominated by harmonic excitations. The boson peak itself is harmonic in nature and therefore a temperature-independent phenomenon. Its centre frequency is constant. Below the glass transition temperatures, the intensity increases approximately linearly at each frequency and after extrapolating the intensity shift to 0 K, the harmonic contribution to the spectra can be calculated for each frequency, as shown in Chapter 3.1.

Upon heating above the glass transition temperature (in sucrose) or the protein dynamical transition temperature (in protein samples), the system leaves the harmonic minimum on the potential energy landscape. Shallower minima increase the amount of anharmonicity and absorption. Once anharmonic effects dominate at T_1, they lead to an apparent shift of the boson peak maximum frequency and obscure it completely at T_2.

We tracked the frequency shift of the boson peak maximum upon heating and the results are shown in Figure 4.8. A very similar behaviour was observed in the integrated BP, however, because the integral boundaries would have to be arbitrarily defined, we decided to base the following analysis on the maximum of the boson peak. The onset of anharmonicity led to an increase in the apparent boson peak intensity as well as a slight broadening. The boson peak

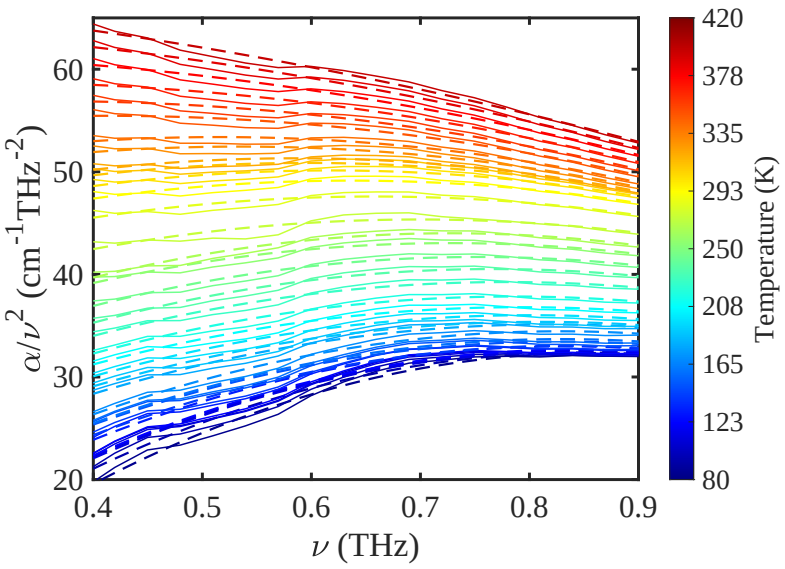

Figure 4.7. Boson peak visualisation with quadratic fit for lysozyme.

maximum frequency stayed mostly constant in the harmonic regime below approximately 150 K to 200 K and decreased in the anharmonic regime above before dissolving at around 300 K.

The experimentally observed absorption can hence be separated into a harmonic and anharmonic contribution. The anharmonic absorption coefficient is shown in Figure 4.9. Anharmonicity clearly increases in sucrose at $T_{\mathrm{g},\beta}$ and again at $T_{\mathrm{g},\alpha}$.

In bacitracin and lysozyme, anharmonicity also increases at the protein dynamical transition at around 200 K and this increase in anharmonicity continues to temperatures of about 300 K. In bacitracin, the anharmonic absorption $\alpha_{\mathrm{anharmonic}}$ then increases much less and remains almost constant. In lysozyme, $\alpha_{\mathrm{anharmonic}}$ reaches a plateau until a temperature of approximately 340 K, then increases again but with a lower gradient. It is very interesting to note that the anharmonic absorption of lysozyme at 300 K is almost five times as strong as that of bacitracin.

In HSA, the protein dynamical transition is less pronounced, and was not found in the total absorption coefficient as discussed above. However, there is a small increase in $\alpha_{\mathrm{anharmonic}}$ at around 170 K. Anharmonicity increases strongly between 270 K to 300 K, then decreases, and remains constant at zero at temperatures above 380 K. It is conceivable that there may even be two dynamical transitions in HSA: one at around 170 K, prompting the onset of anharmonic motions, and another one at 270 K which results in large-scale conformational changes.

Once the protein dynamical transition occurred, the proteins can access different parts of the

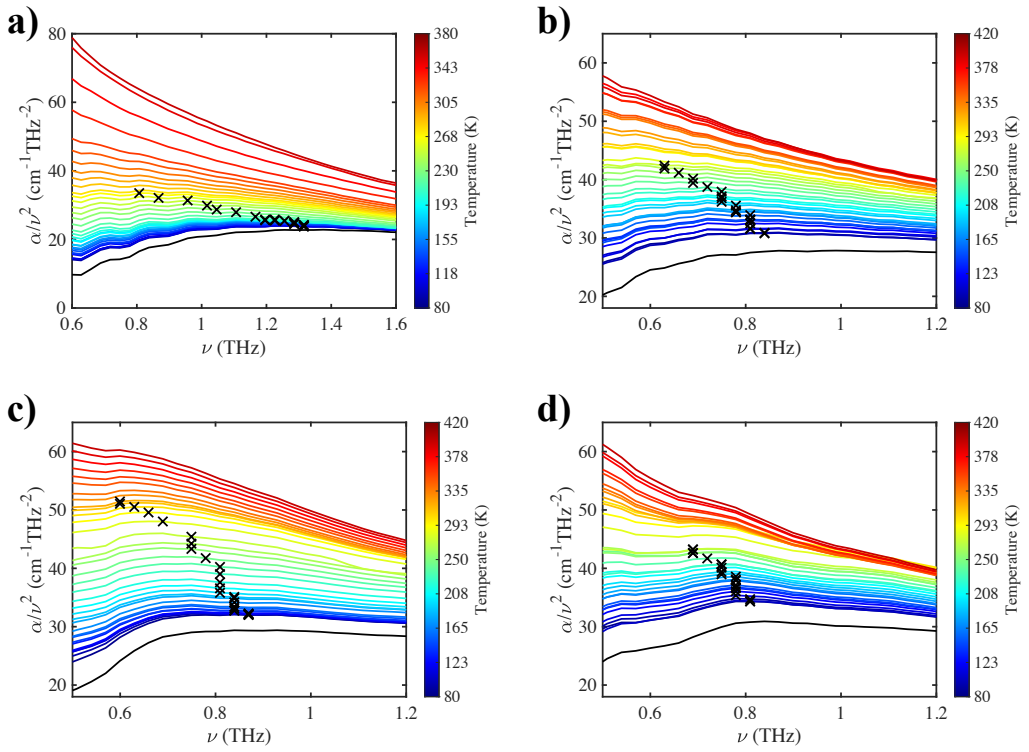

Figure 4.8. Boson peak visualisation for different samples (a) sucrose, b) bacitracin, c) lysozyme, d) HSA) and temperatures. Peaks have been determined from quadratic fits to the data (not shown for clarity) and peak positions are highlighted with crosses. Extrapolation to 0 K is shown in black.

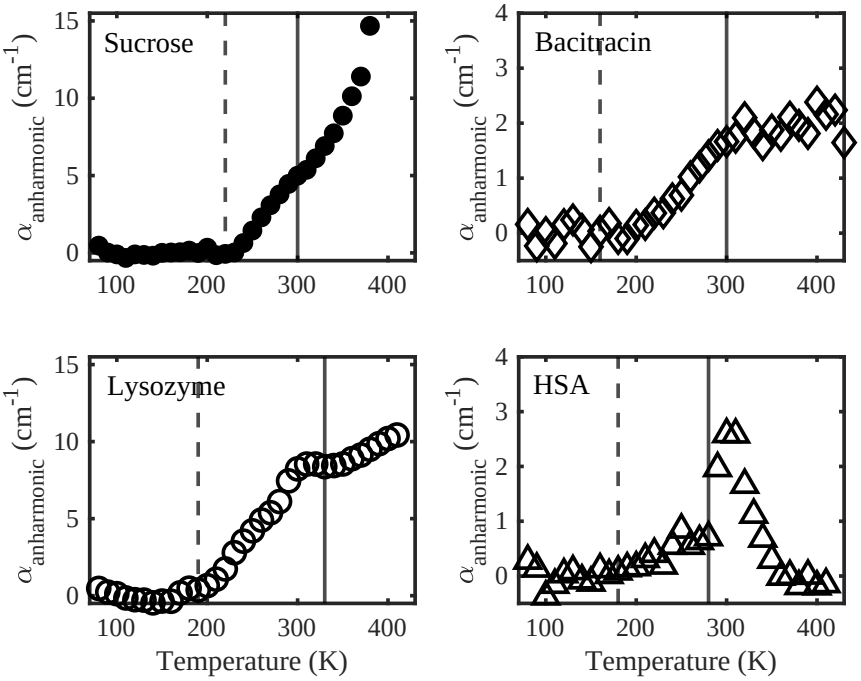

Figure 4.9. Anharmonic absorption at 1 THz for different samples. T_1 (anharmonic effects start to influence the spectra) are shown with a dashed line and T_2 (boson peak dissolves) with a black line.

potential energy landscape. The higher the temperature, the more anharmonicity and absorption (due to the molecular mobility) increased.

Molecular jamming at temperatures just above 300 K also influenced $\alpha_{\text{anharmonic}}$. As apparent from the data in Figure 4.9, once jamming occurs, the anharmonic absorption with temperature decreases (HSA), plateaus (lysozyme), or increases less (bacitracin).

This also coincides with the temperature at which the boson peak could no longer be resolved. The boson peak is located close to the Ioffe-Regel crossover at which the mean-free path of transverse waves becomes equal to their wavelength, meaning that there is a crossover from wave-like to random-matrix-like physics. Once global mobility set in above the glass transition temperature, anharmonicity and mobility increased with temperature until a "critical" mobility had been reached which completely obscured the boson peak.

At very similar temperatures, the proteins reconfigure and get trapped in a different conformation, which decreases overall the mobility. The deeper potential minimum was more harmonic, leading to the observed change in $\alpha_{\text{anharmonic}}$.

Interestingly, the inflection point observed in the DSC data coincides with the temperature regime just above the initial trapping. It can be hypothesised that the trapping and/or the conformational change inducing the trapping result in a subtle change in the change of heat capacity with temperature and the maximum in the DSC data corresponds to a partly unfolded state.

The exact consequence of the molecular jamming on $\alpha_{\text{anharmonic}}$ was sample dependent. In sucrose, no jamming was observed and $\alpha_{\text{anharmonic}}$ increased with temperature as expected. It is noticeable that the larger the molecules, the more pronounced the change in $\alpha_{\text{anharmonic}}$ was. While some jamming was observed in bacitracin, the anharmonicity still increased at temperatures above 300 K, albeit slower. In lysozyme, the system became trapped in a minimum until approximately 340 K, but then gained sufficient thermal energy to explore different conformations. $\alpha_{\text{anharmonic}}$ of lysozyme increased more than in bacitracin, indicating that the potential energy landscape of lysozyme is characterised by many shallow minima.

In HSA, the largest macromolecule, more thermal energy was needed to increase $\alpha_{\text{anharmonic}}$ noticeably. This substantiates the earlier hypothesis that a second protein dynamical transition in HSA may have occurred close to room temperature and just before the molecular jamming was observed. Only in a narrow temperature interval did the system have sufficient energy and

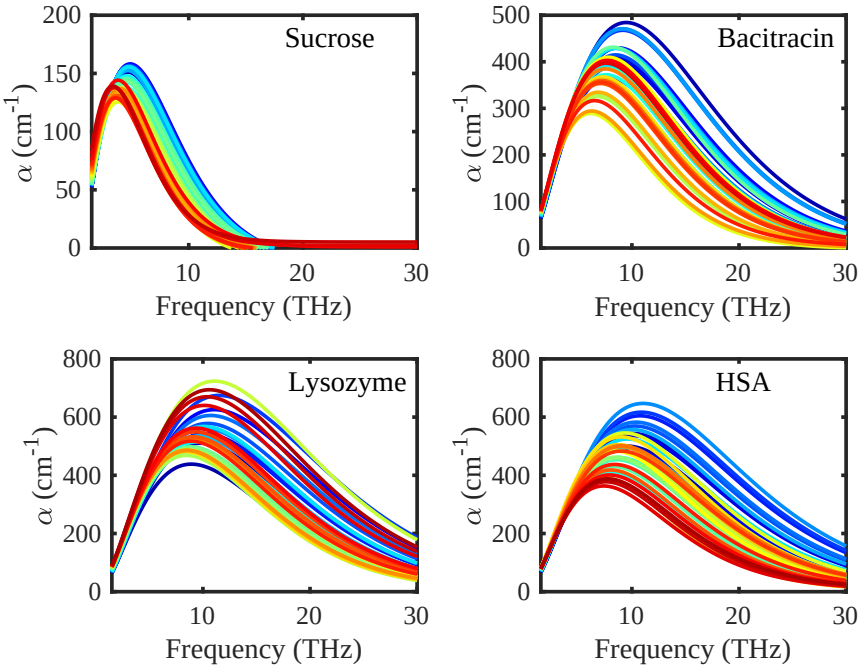

Figure 4.10. Extrapolated VDOS for different samples. Blue: 80 K, red: 420 K.

free volume, leading to increased mobility, before molecular jamming decreased the amount of anharmonicity to zero.

Molecular Confinement is Observed in the Spectrum at Increased Frequencies

While the absorption coefficient at 1 THz is located close to the boson peak and strongly influenced by anharmonic effects, at higher frequencies a different behaviour may be observed over the temperature range investigated.

By fitting and extrapolating an exponential function $\alpha = A \cdot \nu^2 \cdot \exp -\nu/\nu_c + C$ to the higher frequency part of the experimentally accessible spectrum allows to investigate what kind of effect the subtle spectral changes have on the extrapolated vibrational density of states (VDOS) with its maximum located at $2\nu_c$. It has to be noted that this is only an extrapolation based on the available data from the Ioffe-Regel crossover up to approximately 2.3 THz, while the actual VDOS may well be characterised by an underlying multi-peak structure[182] and might also show more features beyond the peak itself.[65]

The extrapolation is shown in Figure 4.10 for the different samples. The expected peak is narrowest and least intense in sucrose, and gets wider and more intense as the molecular weight

increases. Some temperature dependence of the centre frequency was also apparent is shown in Figure 4.11.

In all samples, the centre frequency of the VDOS decreased with increasing temperature, thereby shifting the VDOS to lower frequencies and increasing the absorption coefficient measured at the shoulder (e.g. at 1 THz). It is possible that the frequency shift may follow a Bose-Einstein distribution as previously observed for crystalline modes where thermal excitation was mediated by phonons populating an anharmonic potential. A redshift of a mode is observed when phonons are excited by sufficient thermal energy.[178] However, because the data is only extrapolated, we refrain from fitting a model to it and will simply discuss it in broader, qualitative, terms. In the future, it might be beneficial to measure similar samples on a spectrometer with a higher spectral bandwidth to be able to extract more accurate data.

In sucrose, the change in the centre frequency was most pronounced between $T_{g,\beta}$ and $T_{g,\alpha}$. Above $T_{g,\alpha}$, the centre frequency stayed constant until the sample recrystallised. In bacitracin, the decrease was continuous, while the data for lysozyme was noisier. In HSA, the centre frequency decreased until 250 K, stayed constant up to 310 K, and decreased again. This behaviour indicates that the VDOS did not shift at the temperatures at which confinement was observed. If the molecules were trapped in their respective confirmations, it is sensible to assume that the vibrations that did occur were not temperature-dependent.

In this respect, the choice of 1 THz as the analysis frequency was very beneficial as it allowed insight into anharmonic effects as well as the disappearance of the boson peak at low temperatures, and into the jamming at higher temperatures.

4.1.4 Conclusions

Terahertz time-domain spectroscopy was used to study the sample mobility of different lyophilised systems depending on temperature. In amorphous sucrose, the two glass transition temperatures $T_{g,\alpha}$ and $T_{g,\beta}$ were identified. DSC measurements on bacitracin, lysozyme, and HSA could not identify any glass transitions. Utilising THz-TDS, however, their respective protein dynamical transitions were found that correspond to an increase in mobility. Below this transition, the thermal energy is not sufficient to allow the system to leave the deep minimum on the potential energy landscape and the spectra are dominated by harmonic effects.

Anharmonicity began to influence the spectra in sucrose at $T_{g,\beta}$, and at the protein dynamical

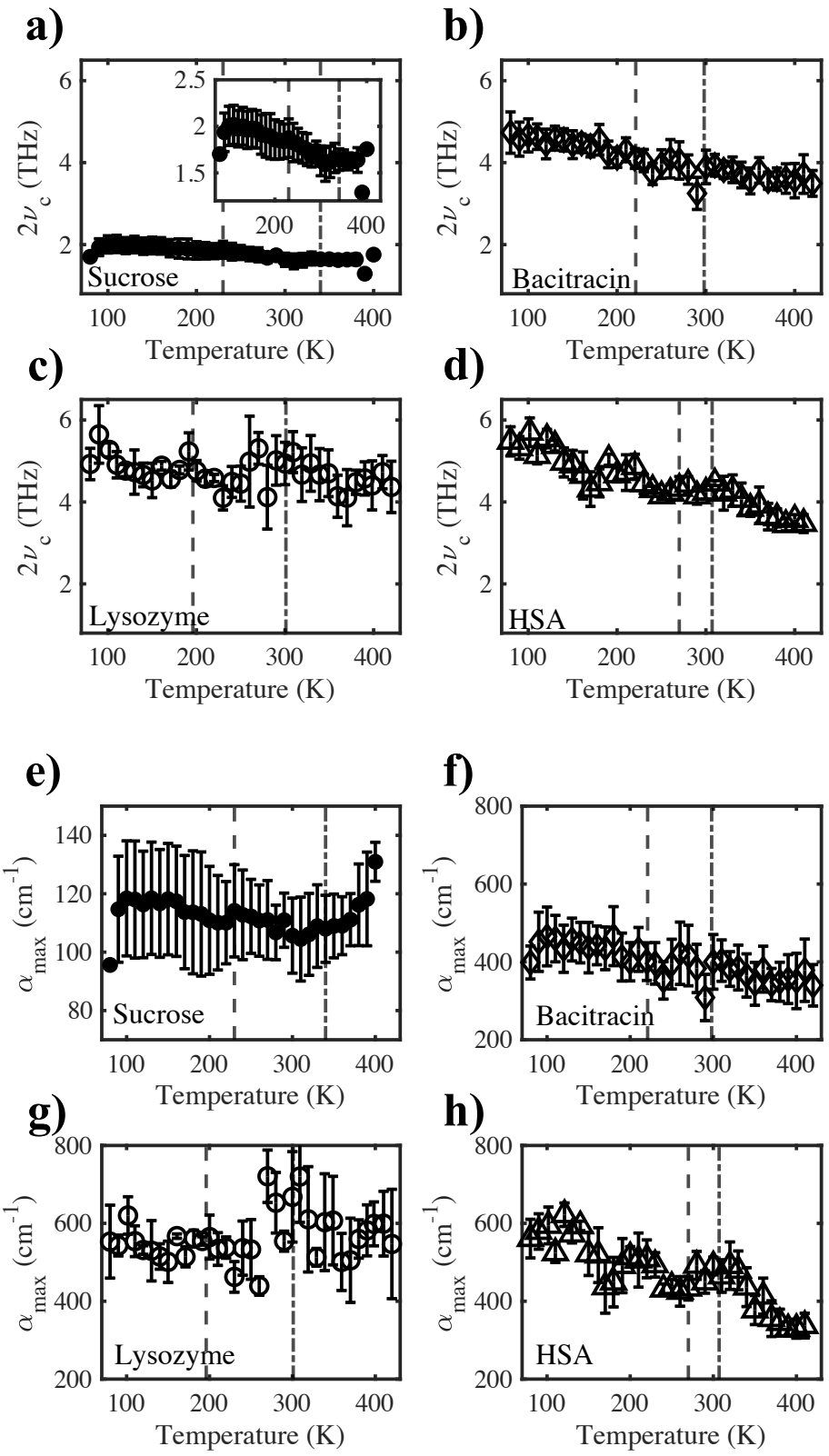

Figure 4.11. Extrapolated centre frequency (a-d) and extrapolated maximum absorption (e-h) for different lyophilised samples. Transitions that have been identified from the absorption coefficient at 1 THz are represented by vertical lines. Error bars are st. err. from 3 measurements for all samples except bacitracin (4).

transition in the other samples, and resulted in an apparent shift of the centre frequency of the boson peak.

A further increase of temperature and thereby mobility led to the dissolution of the boson peak. The anharmonic absorption increased continuously in sucrose. In the larger samples, molecular jamming was observed at increased temperatures after the dissolution of the boson peak, accompanied by a sample-specific change in the anharmonic absorption. As the free energy and mobility subsequently decreased, so did anharmonicity. The larger the molecule, the stronger this effect was.

In bacitracin and lysozyme, the molecular jamming could only be overcome by a further increase in temperature. HSA was still trapped in a very harmonic minimum at 420 K, the highest temperature measured. Molecular jamming also affected the higher frequencies of the VDOS. Future experiments making use of a higher-bandwidth spectrometer can investigate the impact of temperature change on the VDOS.

4.2 Sucrose-Antibody Lyophilisates

4.2.1 Introduction

To predict the stability of amorphous pharmaceuticals, including lyophilised (freeze-dried) drugs, an understanding of the molecular mobility in the sample is beneficial. Low mobility in the solid matrix, at the long-term storage temperature, is desirable as it is thought to result in slower physical and chemical degradation. It has been suggested that in protein formulations the internal protein dynamics are coupled to the dynamics of the surrounding excipient matrix, and that this coupling can be exploited to decrease the protein molecular mobility. Understanding the molecular mechanisms behind the stabilising effect of the matrix is crucial for optimising formulations suited to prevent degradation, denaturation, and aggregation of the protein.[183]

In simple small organic molecular systems terahertz time-domain spectroscopy (THz-TDS) is a useful tool to observe two transition temperatures, namely $T_{g,\beta}$ at low temperatures and $T_{g,\alpha}$ at higher temperatures, corresponding to the onset of local and global mobility, respectively. Previously, high-temperature macromolecular confinement was detected with THz-TDS in more complex systems of lyophilised protein formulations containing a range of excipients.[184] Here we use highly reproducible THz-TDS experiments on a well-controlled and simple two-component system containing different ratios of sucrose to monoclonal antibody (mAb) to measure the

molecular mobility in the samples and investigate the effect of the sucrose matrix.

4.2.2 Materials and Methods

A monoclonal IgG1 antibody in 15 mM histidine buffer pH 5.3 was used when 'mAb' was stated. Samples containing different ratios of sucrose to mAb in the lyophilised state (0, 2.8, 10, 25, 33, 66, 75, 90, 95, 100 % mAb) were prepared with highly purified water (HPW; Sartorius Arium Pro, Sartorius, Göttingen, Germany) to reach a total solid content of 10 % prior to lyophilisation. The same lyophilisation protocol as detailed in Chapter 4.1.2 was used for all samples. Secondary drying was also carried out at 50 °C (323 K). The main objective during lyophilisation was to achieve a lyophilisate with low residual moisture. No stability studies on the mAb were carried out and freeze drying cycle design was not considered important for thermal analysis.

Immediately before each THz-TDS measurement, the dry powder was pressed into a pellet under nitrogen atmosphere to avoid uptake of ambient water. The sample was analysed using a TeraPulse 4000 spectrometer (TeraView Ltd., Cambridge, UK) with a liquid nitrogen continuous flow cryostat attached. Terahertz spectra were acquired over a range of temperatures (80 K to 420 K, some samples up to 450 K) in steps of 10 K. Glass transition temperatures and associated errors were calculated for single THz-TDS measurements as introduced in Chapter 2. Complementary thermal characterisation using differential scanning calorimetry (DSC) was carried out at LMU Munich with the same instruments and experimental settings as described in Chapter 4.1.2.

4.2.3 Results and Discussion

The value of $T_{g,\alpha}$ measured for pure sucrose was found to be in good agreement with literature data.[185] In Fig. 4.12, the absorption coefficient of lyophilised pure sucrose is shown for different temperatures. For all samples containing $< 50\%$ mAb three relaxation regimes, separated by $T_{g,\beta}$ and $T_{g,\alpha}$, were observed and the change of absorption coefficient with temperature closely resembles that of sucrose as shown in Figure 4.12. The changes in absorption coefficient with temperature in these samples qualitatively resemble those observed in pure sucrose, i.e. the absorption coefficient increases strictly with temperature and $T_{g,\beta}$ and $T_{g,\alpha}$ indicate where the molecular mobility in the system changes. Crystallisation of sucrose occurs at 380 K (T_c), apparent in the spectrum (as shown in the appendix).

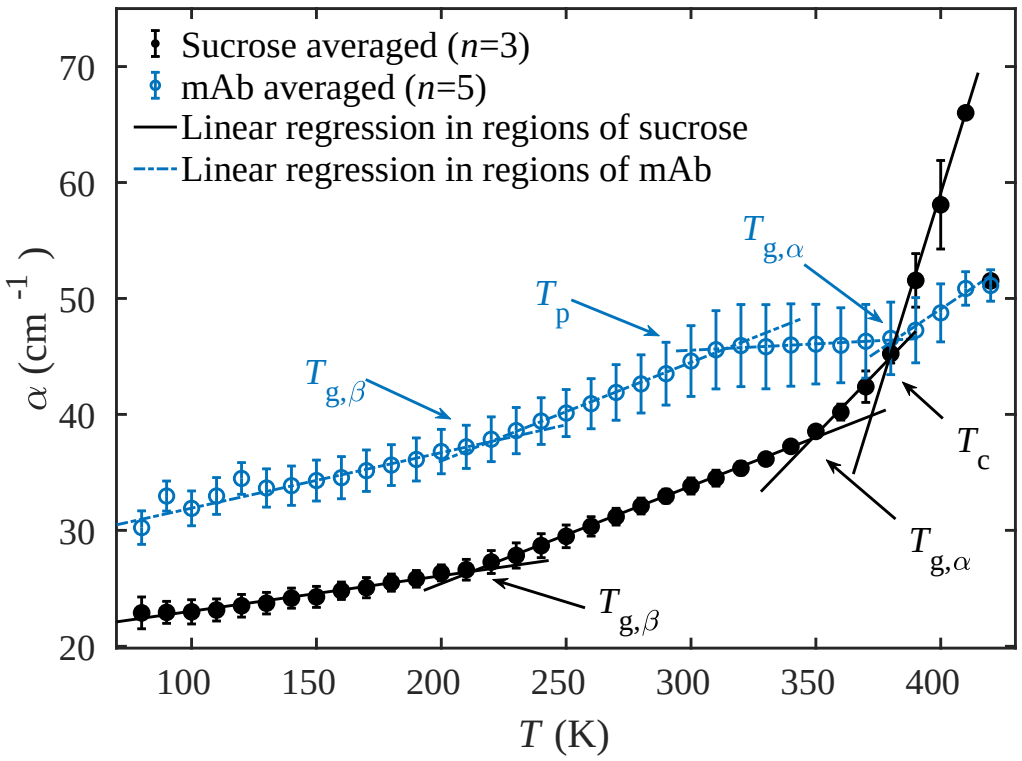

Figure 4.12. Absorption coefficient of pure sucrose (black) and mAb (blue) measured at 1 THz. The average of n measurements is shown and each error bar indicates their standard error. Lines are drawn to highlight different absorption regimes. Arrows point to glass transitions of sucrose and mAb, respectively, as well as to the temperature where the absorption of the antibody flattens, T_{p}.

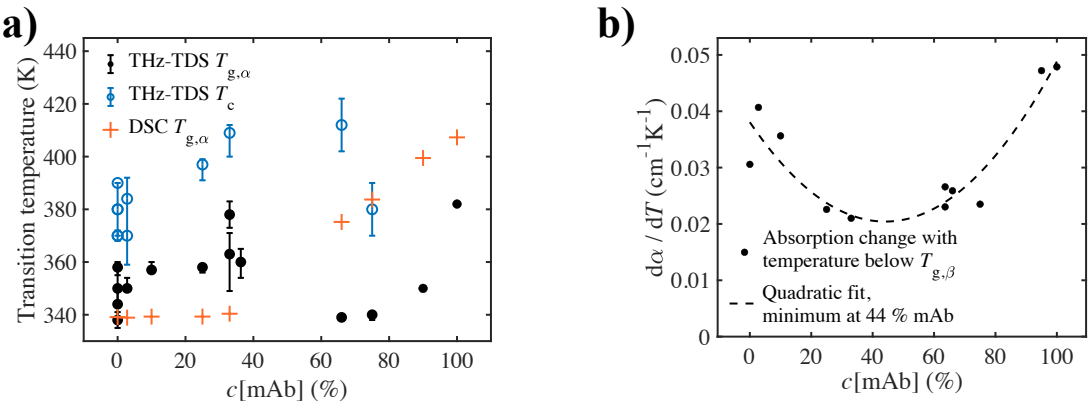

Figure 4.13. (a)Transition temperatures above room temperature extracted from the absorption coefficient at 1 THz (black and blue). Error bars are derived from the fitting algorithm. For comparison, the calorimetric $T_{g,\alpha}$ as measured with DSC is shown. (b) Change of absorption with temperature below $T_{g,\beta}$. A quadratic fit yields a minimum change at 44 % mAb.

Upon adding mAb to the sucrose matrix we observe an increase of $T_{g,\alpha}$ and crystallisation temperature of sucrose for concentrations up to 40% mAb as shown in Fig. 4.13. The DSC measurements result in lower values of $T_{g,\alpha}$ compared to THz-TDS for mAb concentrations between $2.8\% \leq c[\text{mAb}] < 66\%$.

The potential energy surface (PES) model links energy barriers that surround local energy minima on the PES to glass transition temperatures that are high enough to leave those local minima through thermal activation of the molecule. For certain motions to take place, a corresponding energy barrier must be overcome first. It has been proposed that not only the depth of those minima, but also the rate by which excess motions become available upon increasing the temperature account for protein stability.[186] If the slope of the PES is low, an increase in temperature will result in more motions becoming activated compared to the same temperature increase applied to a PES with very steep minima. Conversely, when investigating a system at different temperatures with THz-TDS, we can track how the absorption coefficient and hence the dipole moment change. It is therefore possible to link the amount of absorption change with temperature (gradient of linear regressions) to the steepness of the PES. The higher the gradient, the shallower the PES. A steep gradient indicates that the molecular mobility can be modified quite readily by a small change in temperature. For the mAb samples we observe that the change in absorption is lower at intermediary concentrations with a minimum at $c[\text{mAb}] \approx 44\%$ and hence propose that stability is increased at intermediate c[mAb].

The DSC measurements are in good agreement with the results from THz-TDS for pure

sucrose but diverge at intermediary concentrations (Figure 4.13). Above c[mAb] = 75%, the changes in heat flow as measured with DSC are very low, hindering an accurate determination of transition temperatures. Crystallisation of sucrose is no longer observed with THz-TDS. It is important to note that the DSC method can only determine $T_{g,\alpha}$ but not the other transition points.

For c[mAb] > 66% the response appears to be dominated by the mAb as the absorption coefficient does no longer strictly increase with temperature, as can be seen in Figure 4.12. Further, $T_{g,\alpha}$ and $T_{g,\beta}$ differ considerably from those found in samples containing less mAb, as apparent in Figure 4.13. In some samples, the absorption reaches a local maximum at 300 to 320 K, similar to what has been discussed in Chapter 4.1. This behaviour was pseudo irreversible behaviour: upon direct reheating the flattening of the gradient of the absorption coefficient with increasing temperature vanished and instead a continuous increase in absorption with temperature was observed. This is is consistent with previous observations in complex formulations of bovine serum albumin (BSA).[184]

However, the secondary drying temperature during the lyophilisation process was carried out at higher temperatures (323 K). Given that we still observed this flattening of the absorption coefficient in the first heating run the molecular mechanism behind this observation must be reversible on longer timescales. Water desorption as a potential origin of the peak can be excluded since i) at no point did the spectra indicate the presence or emergence of water vapour, which exhibits clear spectral features at terahertz frequencies; and, ii) so far this phenomenon has only been observed in samples containing proteins and not in e.g. pure sugar matrices or linear polymers.

Anharmonicity analysis as introduced in the previous section can complement these observations. As shown in Figure 4.14, anharmonicity steadily increases in samples containing 25 % mAb and less. Discontinuities at around 220 K and 350 K correspond to $T_{g,\beta}$ and $T_{g,\alpha}$, as expected.

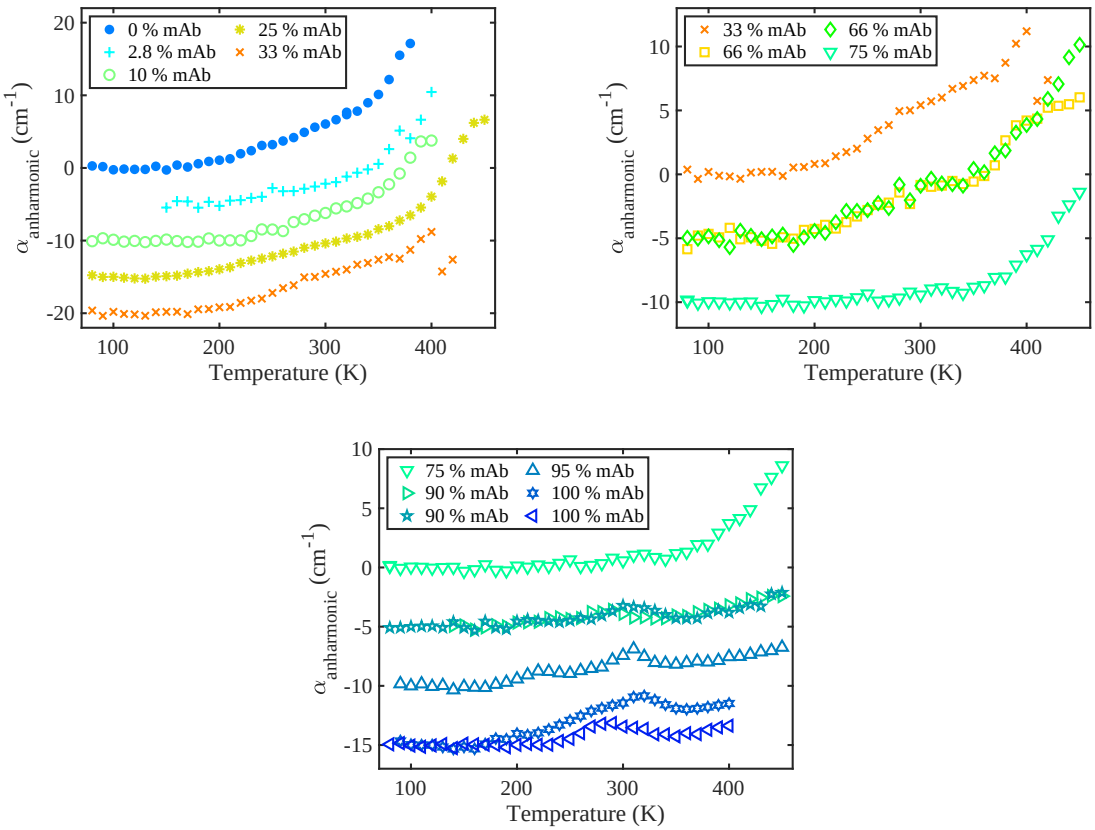

Figure 4.14. Anharmonic absorption coefficient for mixtures of mAb and sucrose in different ratios measured for individual samples. Subsequent concentrations are offset by $-5\,\mathrm{cm}^{-1}$ for clarity.

In samples containing 33 and 66 % mAb, $\alpha_{\mathrm{anharmonic}}$ behaves similarly at low temperatures but the increase in anharmonic absorption between 290 K and 370 K is slightly decreased, and $\alpha_{\mathrm{anharmonic}}$ plateaus between 300 K to 350 K in samples containing 66 % mAb.

The behaviour of $\alpha_{\mathrm{anharmonic}}$ below approximately 280 K is first affected by a mAb content of 75 %, when the discontinuity at around 220 K disappears and $\alpha_{\mathrm{anharmonic}}$ remains close to zero from 80 K until around 300 K where a small maximum in $\alpha_{\mathrm{anharmonic}}$ with temperature appears. $\alpha_{\mathrm{anharmonic}}$ then increases strongly at temperatures above 340 K.

An even higher amount of antibody increases the intensity and width of the maximum in $\alpha_{\mathrm{anharmonic}}$ with temperature at 300 K. At temperatures above approximately 350 K, the rate of change of $\alpha_{\mathrm{anharmonic}}$ with temperature is decreased in samples containing more than 90 % mAb compared to the sample containing only 75 % mAb. In samples containing 95 % and 100 % mAb, $\alpha_{\mathrm{anharmonic}}$ again starts to increase at temperatures at around 200 K.

These data provide further evidence that the protein molecules can be locked, or jammed, into specific conformations in the solid state. During the initial heating process the increase in

molecular mobility is hindered at a critical temperature due to the jamming until the temperature is high enough to overcome the associated potential energy barrier of the confinement and changes in dihedral angles become available again. This has also been hypothesised by Shmool et al.[184] Our new experiments clearly show that this process must be associated with the macromolecular structure of the protein itself and is not dependent on the presence of any excipient or the formation of a specific protein-excipient matrix. The experimental data furthermore highlight that this process is not dependent on the presence of water molecules. The thermal barrier for the mAb samples is similar to that previously measured for BSA ($\approx 2.67\,\mathrm{kJ\,mol^{-1}}$).[105] and bacitracin and lysozyme (Chapter 4.1). However, this barrier is much lower than the energy barrier from the native to the denatured state, which lies in the tens of kcal/mol[181] and closer to the energy of weak (hydrogen) bonds.

A transition below 300 K is detected by THz-TDS in all samples in the total absorption coefficient, implying that rotational and translational motions are present in the samples at and above room temperature. The confined state at 320 K is therefore likely to be related to intermolecular degrees of freedom.

This agrees with the observations in $\alpha_{\mathrm{anharmonic}}$, where samples containing 25 % mAb and less show the same behaviour as pure sucrose. In these samples, the dynamics are dominated by sucrose-sucrose interactions and no molecular jamming can be observed. The sample containing 33 % mAb shows an intermediary behaviour between that of sucrose-like samples and that of samples with a higher protein content.

A higher mAb content increases the protein-protein interactions and leads to molecular jamming. In the sample containing 75 % mAb, no anharmonic effects are apparent below 300 K. This protein concentration may be sufficient to suppress large-scale sucrose motions that would result in an increase in $\alpha_{\mathrm{anharmonic}}$ if sucrose was acting only as a void filler.

Only at even higher temperatures, above 340 K, anharmonic effects start to play a role. mAb concentrations above 90 % lead to a slower increase of $\alpha_{\mathrm{anharmonic}}$ at these temperatures, possibly because less sucrose molecules are present and the energy minima are deeper.

The most pronounced confinement was observed for the pure mAb sample for which no excipient matrix was present. This suggests that protein-protein interactions play a crucial role.

Ageing could result in more stable mAb conformations which would be in accordance with storage time as an influential factor for the confinement. High sucrose content might have

inhibited the confinement by suppressing conformational flexibility and protein-protein interactions. Without stability studies and conformational studies on the investigated formulations it is uncertain whether the confinement of the protein is increasing or decreasing its stability.

4.2.4 Conclusions

Mobility changes and stabilisation by sucrose in freeze-dried sucrose-mAb mixtures were investigated. Below 40% mAb content, the vibrational dynamics are similar to that of small molecular systems. At about 50% mAb content, the absorption changes the least with temperature, potentially indicating increased stability, whereas above 60% mAb, the sample behaviour is dominated by the mAb dynamics and the absorption plateaus or peaks at temperatures between 300 K and 320 K. This might be due to the protein being locked into a confined state with sucrose acting as void filler, and is substantiated by anharmonicity analysis. A mAb content of 75 % and more strongly suppresses the onset of anharmonic effects upon an increase in temperature.

State-of-the-art lyophilised protein formulations also contain surfactants, buffers, bulking agents, and tonicity modifiers. We have shown that drug-matrix and drug-drug interactions change depending on concentration and affect the sample's stability. This highlights the need to understand the underlying mechanisms of each formulation component.

5 The Influence of Salts on Protein Mobility in Solution

The majority of proteins cannot function without a solvation shell, but it is not currently clear what role the solvent plays in the misfolding and aggregation of proteins.

In a project with Dr. Amberley Stephens and Prof. Gabriele Kaminski from the University of Cambridge, we wanted to elucidate how the solvation shell contributes to the misfolding and aggregation of proteins. I performed THz-TDS measurements on solutions containing different salts and proteins and contributed these measurements and their analysis to the paper "Decreased water mobility increases amyloid protein misfolding",[187] which is currently under review. The paper combines simulations and a variety of experimental techniques focusing on the model intrinsically disordered protein α-synuclein (aSyn). The findings show that water mobility and aSyn mobility are inextricably linked and that enhancing water mobility reduces the propensity of aSyn to aggregate.

In this chapter, the influence of the two salts NaCl and CsI on the dynamics of three proteins (α-synuclein, bovine serum albumin, and β-lactoglobulin), as studied by THz-TDS, is analysed in detail. Complementary measurements, focusing on the effect of NaCl and CsI on the aggregation rate of aSyn in particular, were performed by co-authors Amberley Stephens, Rani Moons, Chyi Wei Chung, Michael Ruggiero, Najet Mahmoudi, Talia Shmool, Thomas McCoy, Daniel Nietlispach, Alexander Routh, and Frank Sobott. At the end of the chapter, their results are summarised briefly and can be found in detail in the pre-print "Decreased water mobility increases amyloid protein misfolding".[187]

5.1 Introduction

The misfolding of solvated proteins into insoluble β-sheet-rich structures has been linked to Parkinson's and Alzheimer's disease. Misfolding propensity and pathways to protein aggregation depend on the protein's local environment, which in turn is influenced by the solvent, water, as well as salts, metal ions, and lipids. Molecular crowding, including for example protein abundance, and pH also play a role.[188–193] Most intermolecular interactions that proteins form with their surrounding environment are hydrogen bonds with water. The molecules surrounding a protein constitute its solvation shell (sometimes also called hydration shell) and the mobility of this layer affects rates of conformational change, catalysis, and protein/DNA-protein

interactions.[194,195]

Water is essential for the structure and thereby function of proteins but its impact on misfolding and protein aggregation is not fully understood. Furthermore, the presence of salts in the solvation shell heavily influences protein stability and solubility.[196,197] For example, certain amyloid proteins aggregate when salt concentrations are increased, and others aggregate when they are decreased.[198,199] Molecular dynamics simulations have found that the charge density of the ion is one of the most important parameters influencing hydrogen bond dynamics: small ions with high charge density have tighter hydration shells than large ions with low charge density.[200]

If salt ions influence the hydrogen bond dynamics in a protein's hydration shell, it can be hypothesised that they subsequently also influence the hydrogen bond dynamics of the protein itself and thereby affect the misfolding propensity.

In order to study the effect of water dynamics in the presence of ions on the misfolding of proteins, the model intrinsically disordered protein (IDP) α-synuclein (aSyn) was used. IDPs have no fixed tertiary structure and are highly dynamic. In solution, they probe many conformations and are heavily influenced by interactions with the solvent due to their large solvent accessible surface area. Monomeric aSyn contains 140 amino acids and has a molecular weight of 14 kDa.[201,202]

In the current work, a range of MD simulations and in vitro experiments were performed to investigate how the aggregation rate of aSyn is altered by NaCl (comprised of two small, high charge density ions) and CsI (comprised of two large, low charge density ions). These different salt solutions were chosen as it was previously shown that NaCl significantly reduces the hydrogen bonds dynamics compared to CsI,[203] and as NaCl has been shown to increase the aggregation propensity of aSyn.[198]

Terahertz time-domain spectroscopy (THz-TDS) can be used to probe the complex interplay of molecular relaxation processes (dielectric relaxations and vibrational motions) that take place on timescales of picoseconds to hundreds of femtoseconds by coupling to the infrared-active dipoles of the molecular liquid. The changes in absorption measured by THz-TDS are in general the combined effect of changes in the concentration of the molecular dipoles as well as their mobility. Increased water mobility results in stronger absorption as does the increase in dipole concentration.

Intrinsically disordered proteins have a higher solvent-accessible surface area than globu-

lar proteins of the same size, increasing the importance of protein-solvent interactions. Many globular proteins contain hydrophobic parts which in the folded state are often found in their core.

Utilising THz-TDS, the effect of different salt ions on the protein dynamics is therefore also studied for the globular protein bovine serum albumin (BSA, molecular weight 66.5 kDa) and the hydrophobic, rigid protein β-lactoglobulin (BLG, forms dimer at the pH studied, dimer molecular weight 36.6 kDa). In solution, these three proteins take up a similar volume but their internal structure and interactions with the solvent are expected to be very different.

5.2 Materials and Methods

The proteins were dialysed extensively against H_2O to remove salts after purification. The samples were snap frozen in liquid nitrogen and lyophilised using a LyoQuest 85 freeze-dryer (Telstar, Spain). The samples were resuspended at a concentration of 10 mg/mL, i.e. 691.56 µM for aSyn, 150.46 µM for BSA, and 272 µM for BLG dimers. 10 mM Tris pH 7.2 was added to the samples to aid reconstitution. Samples were reconstituted in the salts and sonicated for 10 s on and 10 s off for three times before THz-TDS measurements. Salts were also measured in Tris solution for comparability with the protein solutions.

The liquid was injected into a liquid cell with a path length of 100 µm. Reference measurements of buffer were performed using the same liquid cell. THz-TDS spectra were acquired using a commercial TeraPulse 4000 instrument with a spectral range of 0.3 THz to 2.7 THz (TeraView, Cambridge, UK). The temperature was kept constant at 294 K. The absorption coefficient of the liquid samples was calculated in the same way as that of solid samples (described in Chapter 2).

A THz-TDS measurement of Tris buffer against water was performed as previous studies have shown that Tris can interact with peptides.[204] However, THz-TDS could not differentiate between water and Tris and we will hence refer to effects occurring in the buffer as affecting the water.

Buffer and salt solutions were measured in 0.25 M increments for NaCl concentrations of 0.5 M to 4 M, and for CsI concentrations of 0.25 M to 2.5 M. Measurements of pure salt solutions were repeated at least 5 times. aSyn in NaCl was measured at 2 M, as aSyn did not reconstitute successfully in concentrations below 2 M, and aSyn in CsI was measured at 1.25 M, 1.5 M, and

2 M. BSA was measured at 1.5 M in both NaCl and CsI, and BLG was measured at 1.0 M, 1.25 M, and 1.5 M in both NaCl and CsI. Each of these measurements was taken at least eight times.

5.3 Results and Discussion

Spectra of both salts in Tris solution were taken at different concentrations and are shown in Figure 5.1. In NaCl solutions, the absorption coefficient increased approximately linearly with frequency and was higher for higher salt concentrations. In samples containing CsI a spectral feature appeared at 0.7 THz.

Similar broad spectral features in ta similar frequency range have been reported in the terahertz spectra of ions in solution or in organic solvents. There is some evidence to support the hypothesis that such vibrational modes may originate from hydrate like structures.[205] Chen et al. probed a range of different salt hydrates with terahertz spectroscopy and some spectra are featureless whilst others exhibit features similar to the ones here seen for CsI. These features are due mostly to complex intermolecular interactions and depend strongly on the salts. The measurements by Chen et al. were carried out in the frozen state, but Schmidt et al.[206] already showed in 2009 the existence of such signatures in THz-TDS measurements in aqueous solution.

The shape of the terahertz spectra is not primarily influenced by the salts, but by the interaction of the salt with the surrounding water molecules, where absorption by water is dominant in the terahertz regime. A larger overall increase of the absorption coefficient was observed for water containing CsI than water containing NaCl. At 1 THz, the absorption coefficient of solutions containing CsI was approximately 2.7 times higher than that of solutions containing NaCl.

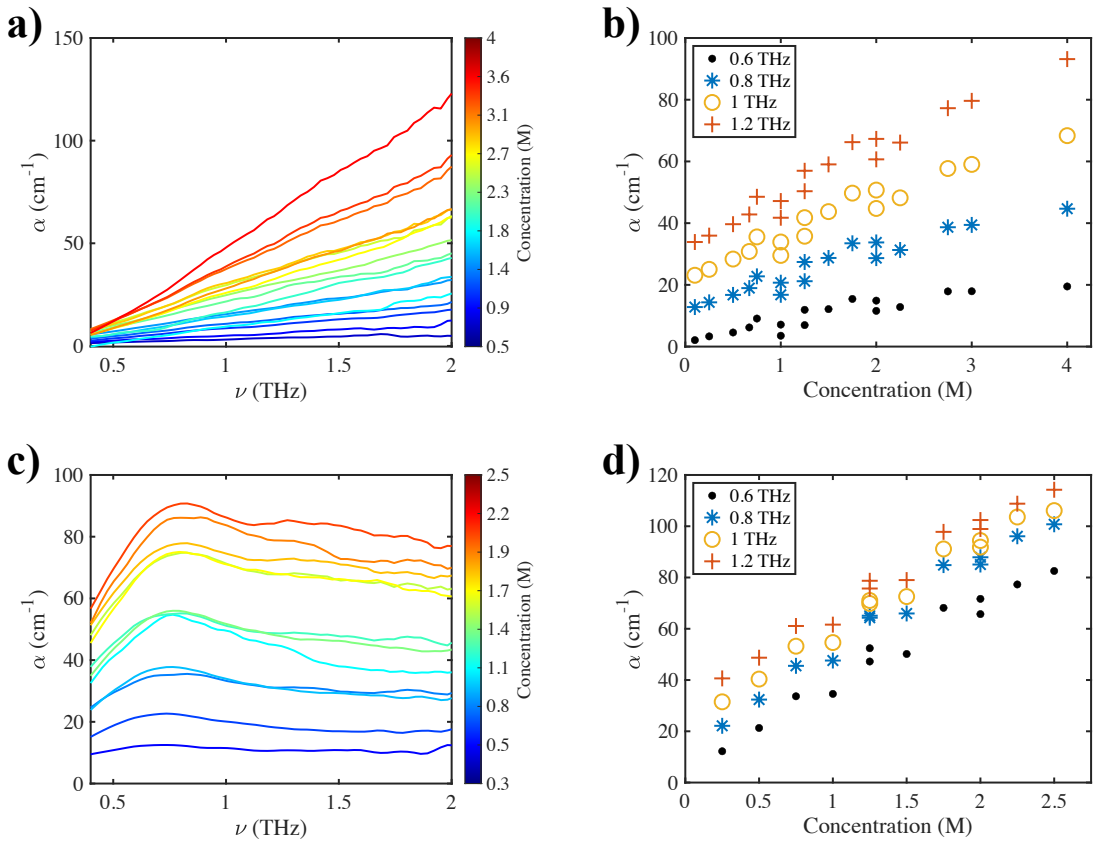

Figure 5.1. Top: NaCl solutions, bottom: CsI solutions.
(a) and (c) Absorption of solutions containing only the salt at different concentrations.
(b) and (d) Absorption coefficient at different frequencies. Offset by $0\,\mathrm{cm}^{-1}$ (0.6 THz), $10\,\mathrm{cm}^{-1}$ (0.8 THz), $20\,\mathrm{cm}^{-1}$ (1.0 THz), $30\,\mathrm{cm}^{-1}$ (1.2 THz) for clarity.

All spectra were subsequently divided by the salt concentration to obtain the molar absorption coefficient ϵ. ϵ was then fitted over frequencies with a linear function for samples containing NaCl and with the sum of a power law and a Lorentzian to incorporate the spectral features for samples containing CsI:

$$\epsilon = \frac{A}{1 + (\frac{f - x_1}{g})^2} + B \cdot f^a \tag{5.1}$$

Where A is the peak intensity, g the half width at half maximum, x_1 the centre frequency of the peak, f the frequency, and a and B are power law parameters. An offset was not observed in any measurement hence no absolute term is present.

The fits are shown in Figure 5.2 and the parameters describing the molar absorption coefficients are detailed in Table 5.1.

Once the absorption of the different salt solutions had been characterised, the three proteins

were each reconstituted in NaCl and CsI solutions. The concentrations were chosen to be as high as possible while ensuring the proteins did not aggregate.

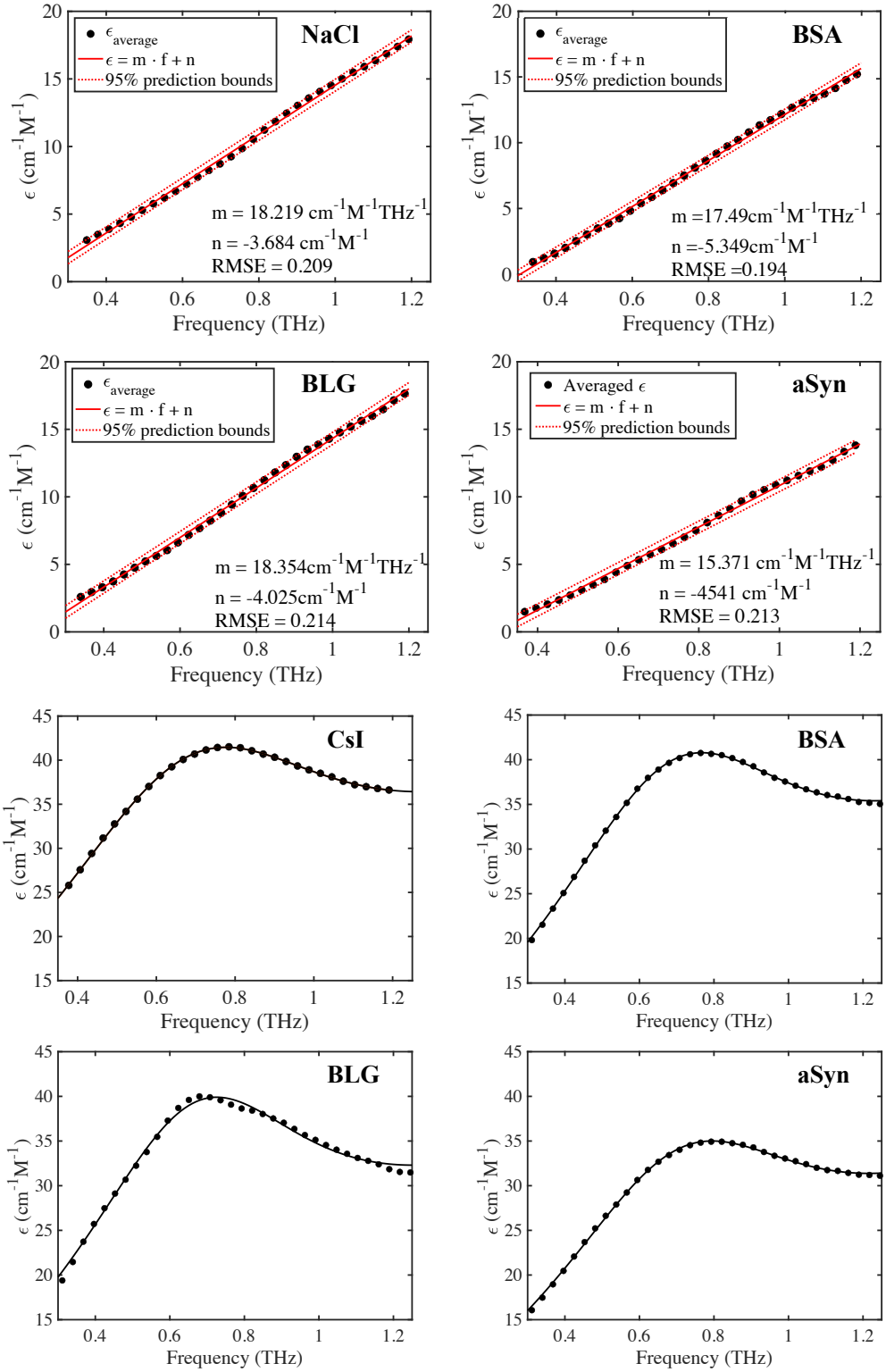

Figure 5.2. Molar absorption coefficient for salt solution and solutions with different proteins. Top: NaCl, bottom: CsI. Fit parameters for all spectra are also detailed in Table 5.1.

As can be seen in Figure 5.2 and Figure 5.3, addition of proteins did not change the spectral shape, but decreased the overall absorption. This is in line with previous results, as a protein displaces the ions and water molecules which have much stronger absorption than the protein due to the relative number of dipole oscillators.[207,208]

Table 5.1. Fit parameters for NaCl solutions (top) and CsI solutions (bottom).

Parameter	NaCl	NaCl and BSA	NaCl and BLG	NaCl and aSyn
m ($cm^{-1}M^{-1}THz^{-1}$)	18.2	17.5	18.5	15.4
n ($cm^{-1}M^{-1}$)	-3.7	-5.3	-4.0	-4.5

Parameter	CsI	CsI and BSA	CsI and BLG	CsI and aSyn
A ($cm^{-1}M^{-1}$)	27.83	27.5	26.6	23.2
x_1 (THz)	0.69	0.69	0.67	0.71
g (THz)	0.47	0.43	0.39	0.43
B ($cm^{-1}M^{-1}THz^{-a}$)	19.5	19.4	19.2	17.0
a (a.u.)	1.13	1.20	1.01	1.25

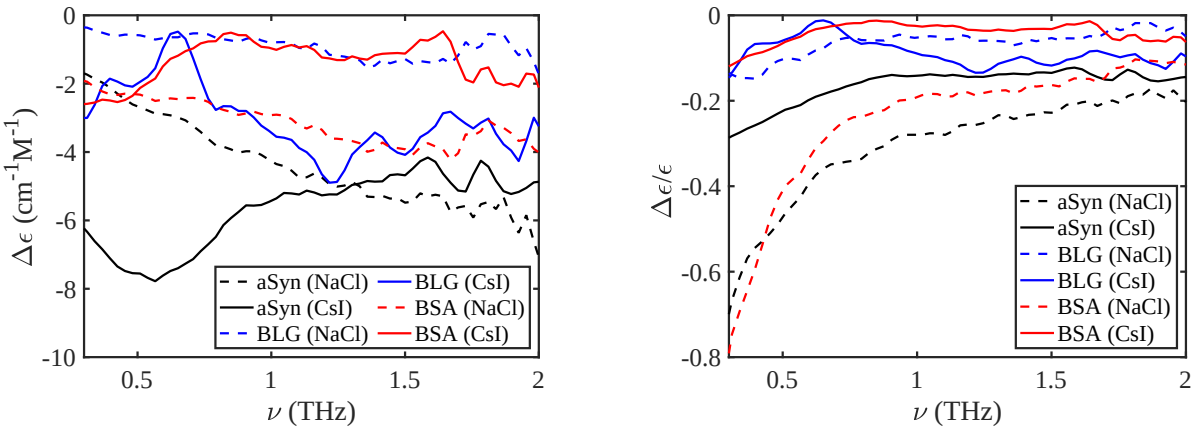

Figure 5.3. Absolute (left) and relative (right) change in the molar absorption coefficient when introducing proteins into salt solutions.

Despite the absorption of water in NaCl being lower than in CsI in the absence and presence of protein, upon addition of aSyn and BSA, the relative change in water absorption is greater in NaCl than CsI for aSyn and BSA. This shows that a greater perturbation to the water molecules is occurring in NaCl (Figure 5.3). In BLG, the relative change is similar for both salts. Above approximately 0.7 THz, the addition of NaCl results in a smaller change than the addition of CsI. Generally, the relative change in all three proteins is less frequency dependent at frequencies above the main feature in CsI solutions.

For further analysis, the THz-TDS spectra of protein-salt solutions were deconvoluted to investigate the effects of the salt ions on the solvation shell. The solvation shell size of the single ions was based on results obtained from *ab initio* molecular dynamics simulations performed by Michael Ruggiero and the radial pair distribution functions are shown in Figure 5.4. Due to the high computational cost, these simulations were performed on the solvated $aSyn_{72-78}$ peptide that is representative of the protein.

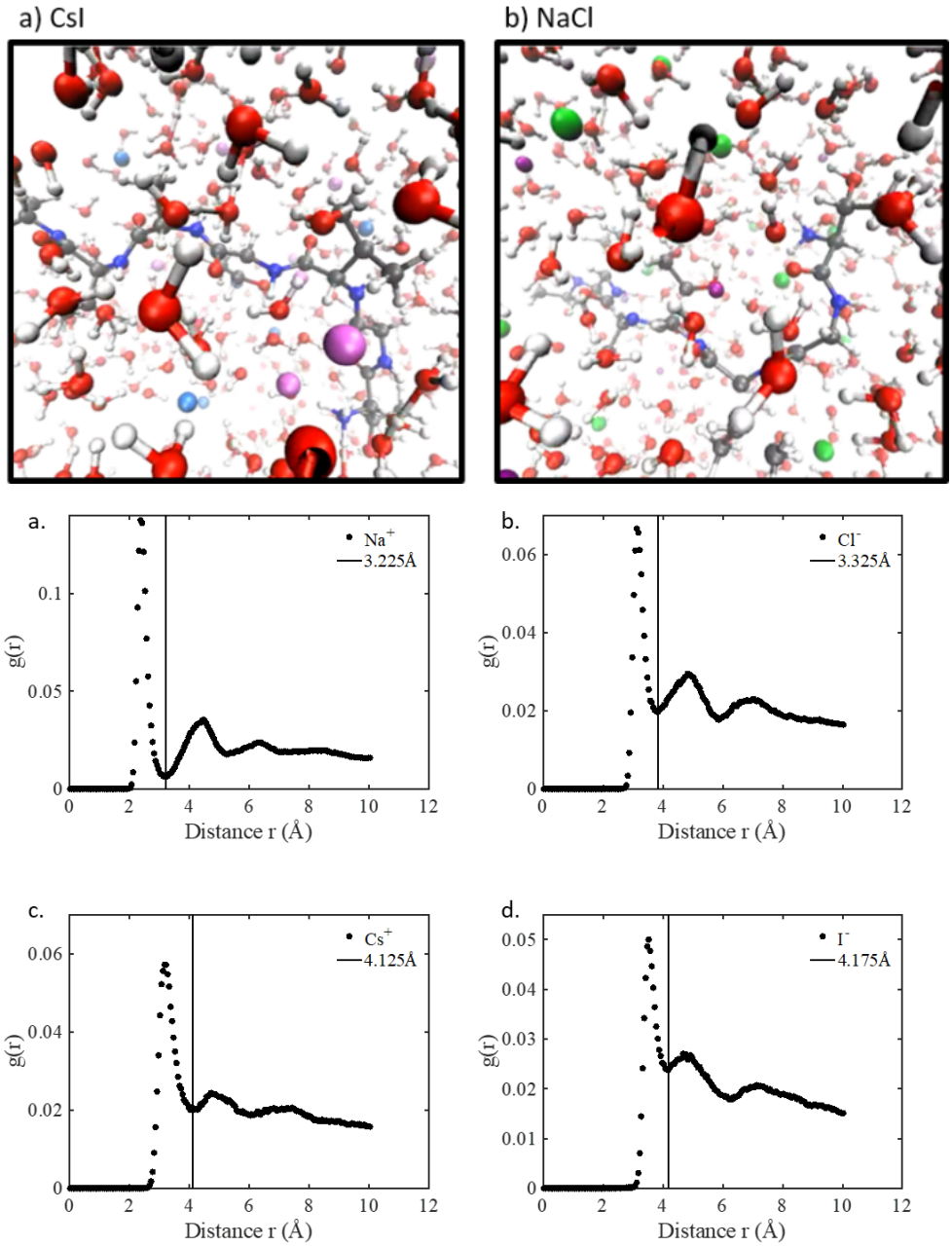

Figure 5.4. Top: Addition of NaCl and CsI alters water mobility in the bulk and in the aSyn solvation shell. A snapshot of the AIMD simulations of the solvated $aSyn_{72-78}$ peptide in a 125 nm^3 box after introduction and equilibration with 1.5 M salts. (a.i) $aSyn_{72-78}$ peptide in 1.5 M CsI and (a.ii) $aSyn_{72-78}$ peptide in 1.5 M NaCl, Cs^+ light purple, I^- light blue, Na^+ dark purple, Cl^- green, O red, H white, C grey, N dark blue.
Bottom: Radial pair distribution functions extracted from AIMD simulations. The first minima are used as a measure of the size of the solvation shell around different salt ions for THz data analysis (a) Na^+, (b) Cl^-, (c) Cs^+, (d) I^-. The horizontal line indicates the radius of the solvation shell around each ion.

Because the absorption coefficients of the salt solutions without protein present are known, absorption coefficients of the protein and its solvation shell can be calculated for different estimates of solvation shell sizes:

$$\epsilon = \epsilon_{\text{bulk}} \cdot \frac{V_{\text{bulk}}}{V_0} + \epsilon_{\text{ps}} \cdot \frac{V_{\text{ps}}}{V_0} = \epsilon_{\text{bulk}} \cdot \frac{V_{\text{bulk}}}{V_0} + \epsilon_{\text{p}} \cdot \frac{V_{\text{p}}}{V_0} + \epsilon_{\text{s}} \cdot \frac{V_{\text{s}}}{V_0} \tag{5.2}$$

As mentioned previously, the protein and shell absorb less terahertz radiation than the water-salt solution they replace (Figure 5.3). To investigate the absorption of the water in the solvation shell in the presence of the salts, we first defined the parameters for salt-independent absorption, where the protein molar absorption coefficient (ϵ_p) is not influenced by the hydration with different salts. As ϵ_p is not known, the salt-independent absorption coefficient of water in the solvation shell was calculated based upon different values for protein absorption. The lowest value was taken at $1\,\text{cm}^{-1}\text{M}^{-1}$, around the limit of detection. The highest value for aSyn was taken as $25\,\text{cm}^{-1}\text{M}^{-1}$, which is comparable to the absorption of aSyn in 1 M solid CsI at room temperature, as shown in Figure 5.5.

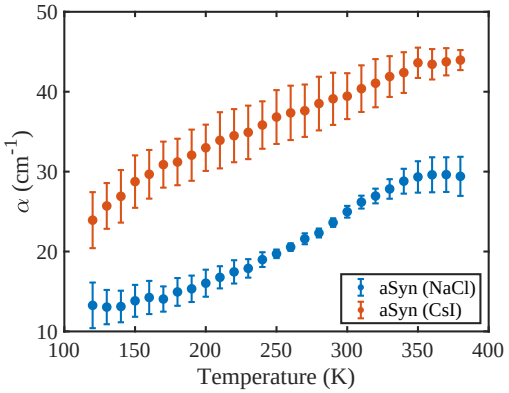

Figure 5.5. Absorption coefficient of aSyn at 1 THz with 1.5 M salt in the solid state. Error bars represent standard error of three measurements. Measurements taken by T. Shmool.

The same lower boundary was used for solutions containing BSA and BLG. As no solid-state measurements were performed for the other two proteins, the upper boundary was set to $35\,\text{cm}^{-1}\text{M}^{-1}$ for BLG and $45\,\text{cm}^{-1}\text{M}^{-1}$ for BSA (which is roughly its absorption coefficient that has previously been reported in the solid state[209]).

The resulting ratio of the absorption coefficient of the solvation shell compared to bulk salt solutions for the different scenarios are shown in Figure 5.6.

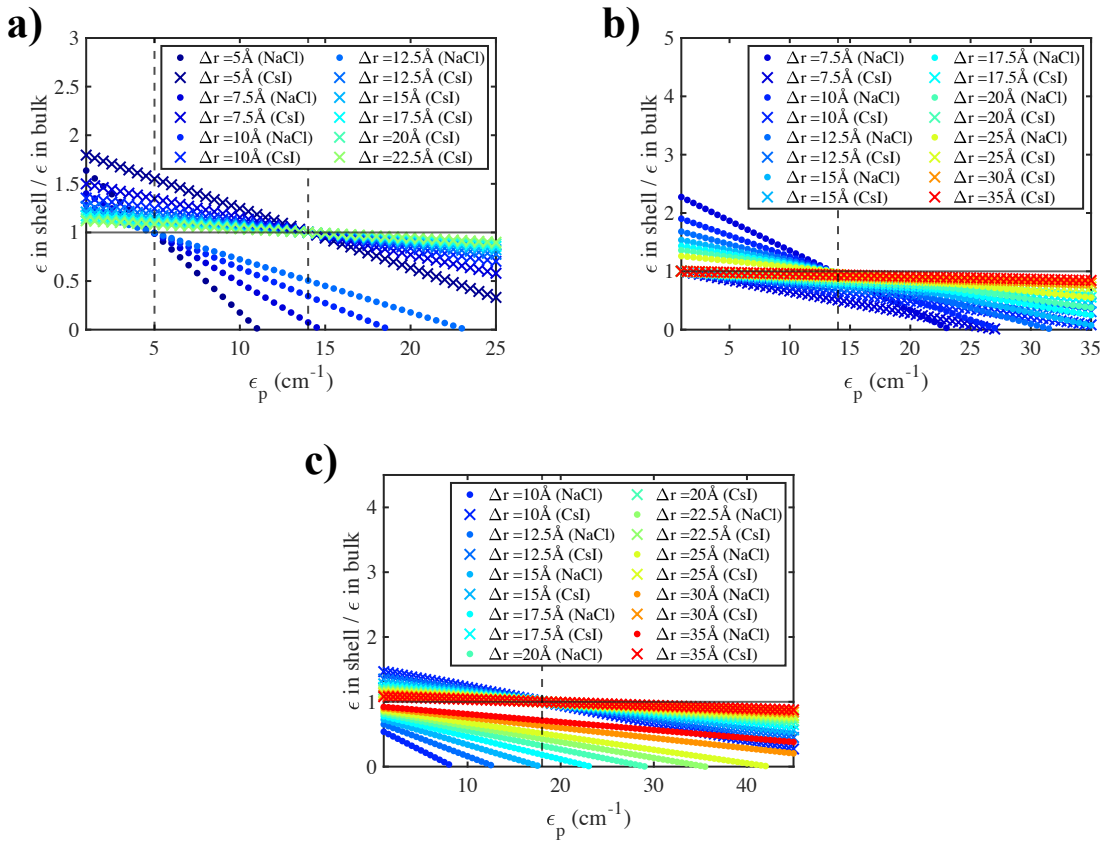

Figure 5.6. Absorption of water in the solvation shell excluding the protein itself is compared to bulk water absorption at 1 THz for solutions containing aSyn (a), BLG (b), and BSA (c). Vertical lines highlight the ϵ_p where the shell absorbs as much as the bulk for both NaCl and CsI. As the exact thickness of the solvation shell, Δr, is not known, different estimates are shown.

In aSyn, the water shell containing NaCl absorbs less than the bulk above $\epsilon_p = 5\,\mathrm{cm^{-1}M^{-1}}$, whereas the water shell containing CsI only absorbs less than the bulk above $\epsilon_p = 14\,\mathrm{cm^{-1}M^{-1}}$ (Figure 5.6a). If ϵ_p is higher than $14\,\mathrm{cm^{-1}M^{-1}}$, both shells absorb less than the bulk, but the one containing NaCl even less so than the one including CsI. This shows that across a physiological range of protein absorption, ion and water mobility in the vicinity of aSyn are increased in CsI compared to NaCl. This is clearly observed at $\epsilon_p = 10\,\mathrm{cm^{-1}M^{-1}}$, an intermediate protein absorption coefficient, where the water shell absorption in NaCl is reduced while increased in CsI.

A similar behaviour is observed for BSA. Until $\epsilon_p = 18\,\mathrm{cm^{-1}M^{-1}}$, shells containing CsI absorb more than the bulk solution, and less for a higher ϵ_p. For all considered scenarios, shells containing NaCl absorb less than pure salt solution.

BLG behaves differently. Apart from the fact that BLG was the only protein where the relative change in molar absorption coefficient at 1 THz was larger for solutions containing CsI,

the solvation shells surrounding BLG that contain CsI also absorb less than bulk solution for all scenarios considered. Conversely, the water shell containing NaCl only absorbs less than the bulk above $\epsilon_p = 14\,\mathrm{cm}^{-1}\mathrm{M}^{-1}$.

Intuitively, a larger hydration shell should result in the absorption coefficient being more similar to (but still lower than) that of bulk solution. This was investigated further by comparing the absorption of both the protein and its shell for solutions containing CsI and NaCl, as shown in Figure 5.7. The difference to bulk shows that the absorption of water in the solvation shell is directly influenced by the interaction of the protein and salts and cannot be explained by the different absorption of hydrated salt ions only.

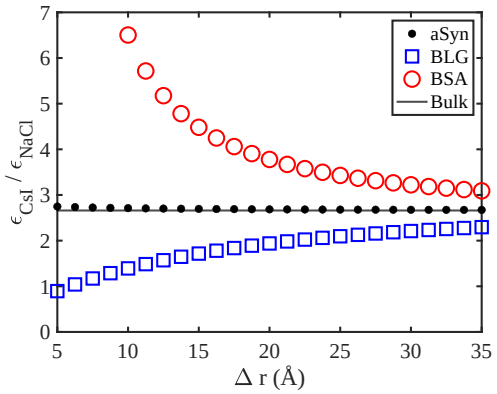

Figure 5.7. Absorption of protein and shell combined compared in solutions with NaCl and CsI for different thicknesses of the solvation shell. In aSyn and BSA, the ratio is larger than in bulk (2.7), and in BLG, it is smaller.

The ratio of the absorption coefficient of aSyn in CsI solution compared to in NaCl solution is slightly larger than without the protein present for relatively small values of solvation shell thickness. In BSA, the difference is more obvious, the absorption of BSA and its solvation shell is clearly enhanced in the presence of CsI compared to NaCl. The reverse is the case for BLG where NaCl increases the absorption of the solvated protein compared to CsI.

A protein's structural properties include intrinsic order, shape, charges, hydrophobicity, and surface roughness and influence their function in solution. Based on known properties, it can be hypothesised what the causes for the observed experimental differences are, but complementary measurements are needed for each individual protein to test these hypotheses.

α-synuclein is intrinsically disordered and while taking up a similar volume compared to BSA and BLG, the interactions with its environment on a shorter length scale are enhanced. aSyn

could hence be more tightly integrated into the water/salt network than the other two proteins that were investigated.

BSA is globular and much more compact. Most interactions with the solvent occur on the outer surface. The presence of CsI compared to NaCl led to increased water mobility in bulk and in the protein solvation shell, and a larger volume of water was affected compared to aSyn.

BLG has a lipocalin-type fold and represents a hydrophobic compartment for the solubilisation of otherwise physiologically insoluble molecules.[210] BLG affected a larger volume than aSyn, but probably due to the presence of exposed hydrophobic residues, the effects of NaCl and CsI were reversed. CsI ions are larger than NaCl ions and the results indicate that water molecules in the vicinity of both CsI and BLG are less mobile than in the presence of NaCl and BLG. Possibly, due to the specific fold of BLG, interactions with small charges could be enhanced compared to large charges.

Our THz-TDS measurements have shown that adding a protein disturbs the interaction between water molecules and salt ions, and depends on the salt ion as well as on the protein. The changes in absorption measured by THz-TDS are the combined effect of changes in the concentration of the molecular dipoles as well as their mobility. Complementary measurements can further investigate how the protein is specifically affected by the different salts.

5.4 Conclusions

The influence of ions on the mobility of water has been well studied, yet the effect of water mobility on the propensity of proteins to misfold is still not elucidated and in particular, not in connection with IDPs and amyloid fibril formation. Here, we show that ions can influence the mobility of bulk water and water in the solvation shell.

In the presence of α-synuclein, we directly observe that the presence of CsI leads to increased water mobility, both in bulk and in the protein solvation shell, in comparison to NaCl. An increase in absorption as measured with THz-TDS directly relates to an increased change in dipole moment and therefore ion and protein mobility which are inextricably linked to the mobility of surrounding water molecules.

Although solvent motions are on the fs to ps timescale and conformational changes in proteins occur on the ns-ms timescale, the solvent mobility still has a knock-on effect on the motions of the protein. For instance, methyl group rotations are fast, on the ps timescale, and facilitate protein

dynamics, yet amino acid motions and localised diffusion occur on ps-ns timescales and also are influenced by the surrounding solvent.[211] In combination with the complementary results discussed in the next section, we have shown that the presence of CsI reduced the likelihood of aSyn aggregation compared to the presence of NaCl.

The coupling of water motions, the presence of ions, and protein dynamics are likely to be protein specific due to differing charges, hydrophobicity and surface roughness.[212]

This was confirmed by also investigating the globular protein BSA and the hydrophobic protein BLG. The effects of the different salts observed for aSyn were also present for BSA: for a wide range of parameters, CsI also increased water mobility compared to NaCl. The solvation shell was probably wider than in aSyn. In BLG, however, the effects of the two salts were reversed, which can be traced back to protein-specific interactions with the solvent that could be investigated further in the future.

5.5 Outlook: Complementary Techniques

The mobility of aSyn in the presence of NaCl or CsI was further investigated with complementary techniques by various co-authors also contributing to the pre-print focusing on the aggregation propensity of aSyn. In the following, some of their results will be briefly discussed.

A fluorescence-based aggregation assay was used to measure the fluorescence of Thioflavin-T as it intercalated into the backbone of β-sheet containing fibrils.[191,213] Results showed that the aggregation rate of aSyn was increased upon addition of NaCl and decreased when adding CsI. Substituting H_2O for D_2O also increased the aggregation rate (shown in Figure 5.8).

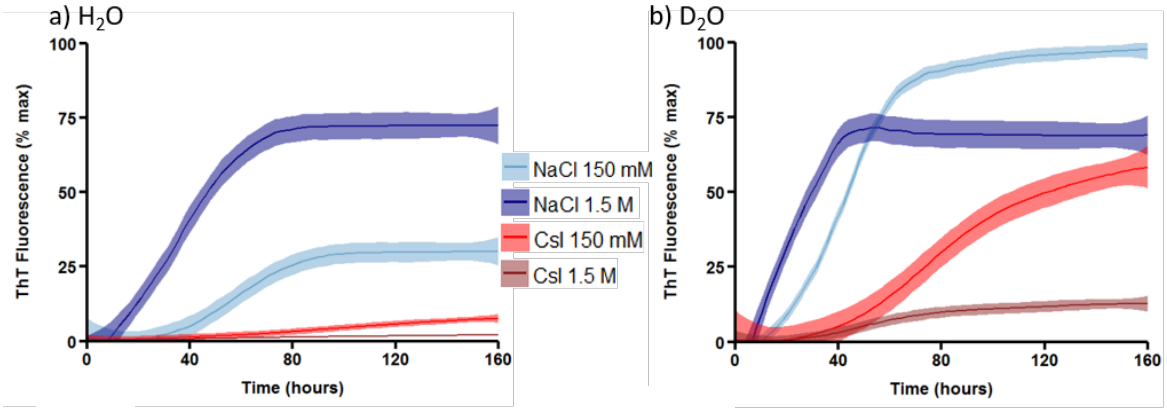

Figure 5.8. NaCl and CsI concentrations influence aSyn aggregation rate and morphology. aSyn aggregation kinetics were measured in the presence of (a) H_2O and (b) D_2O with 150 mM NaCl (red), 1.5 M NaCl (brown), 150 mM CsI (light blue), 1.5 M CsI (navy) and plotted as % maximum ThT fluorescence over time. Data represent three experiments with three or four wells per condition per experiment; error (shaded areas) represents rolling average of the SEM.

Ab initio molecular dynamics (AIMD) and classical molecular dynamics (MD) simulations were used to study the dynamics of the solvation shells, ions, and aSyn on fs to ps timescales.[214] Due to computational constraints, the simulations were performed on a heptapeptide (TGVTAVA, residues 72-78) from the central region of aSyn that is representative of the protein. The results showed that diffusion (i.e. further displacement from initial positions) was increased in the system containing CsI. This was mainly due to the Cs^+ cation disturbing the water geometries and leading to large-scale reorientation, also coupled to the $aSyn_{72-78}$ peptide.

Native nano-electrospray ionisation mass spectrometry (nano ESI-MS) showed that aSyn binds up to three Na^+ and five Cs^+ ions at a concentration of 20 µM aSyn : 1 mM salt while binding of the counter anions was not observed, as shown in Figure 5.9a.

The chemical shifts observed with nuclear magnetic resonance (NMR) spectroscopy, specifically 2D ^{15}N HSQC NMR spectroscopy, were found across all regions of aSyn, suggesting no specific binding regions for the ions. At very high unphysiological salt concentrations, binding may however induce structural changes (Figure 5.9b).

Nano-ESI-ion mobility MS (nano-ESI-IM-MS) was used to investigate changes of the distribution of aSyn conformations when bound to salt ions, and it was found that the aSyn conformational space did not extend or compact drastically.

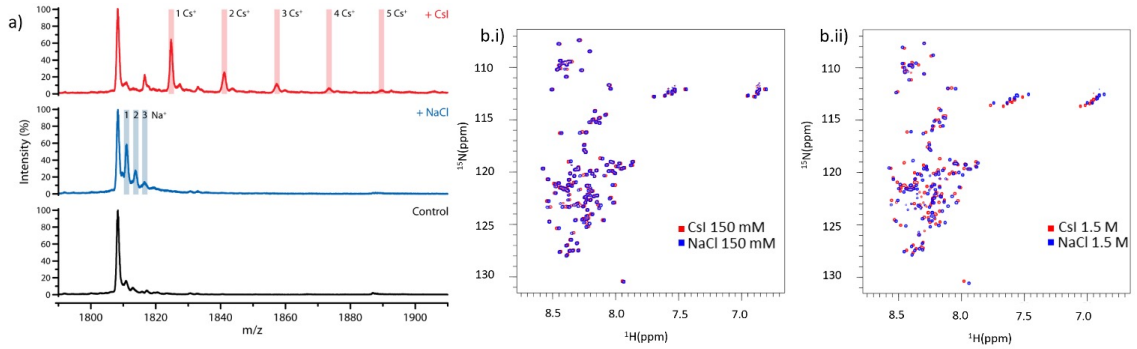

Figure 5.9. aSyn binds more Cs^+ than Na^+ which does not grossly affect aSyn conformation. The mass spectrum of (a) native aSyn (control, black) is shown in the 8+ charge state region, and in the presence of a 1:50 ratio (20 µM aSyn: 1 mM salt) we observe aSyn bound to three Na^+ (+NaCl, blue) and to five Cs^+ (+CsI, red). (b) 2D ^{1}H-^{15}N HSQC peak spectrum of aSyn containing (b, i) 150 mM CsI (red) in 5% D_2O, 95% H_2O (vol/vol) was overlaid with aSyn containing 150 mM NaCl (blue) in 5% D_2O, 95% H_2O (vol/vol). (b, ii) aSyn with 1.5 M NaCl (red) (vol/vol) was overlaid with aSyn containing 1.5 M CsI (blue). Gross shift perturbations are only observed across the protein sequence under very high (1.5 M) salt concentrations.

Further, the effect of conformational rearrangement of aSyn in the presence of the two salts was studied both with THz-TDS in the solid state (Figure 5.5) and with ^{15}N HSQC NMR spectroscopy in solution. Both techniques showed that the mobility of aSyn depended on the salt present and that aSyn is more mobile in the presence of CsI and also more able to reconfigure than in the presence of NaCl.

Finally, it was also shown that the aggregation of aSyn is affected by the presence of different ions in cells. *In vivo* experiments in E. coli showed that NaCl was more likely to cause aggregation than CsI.

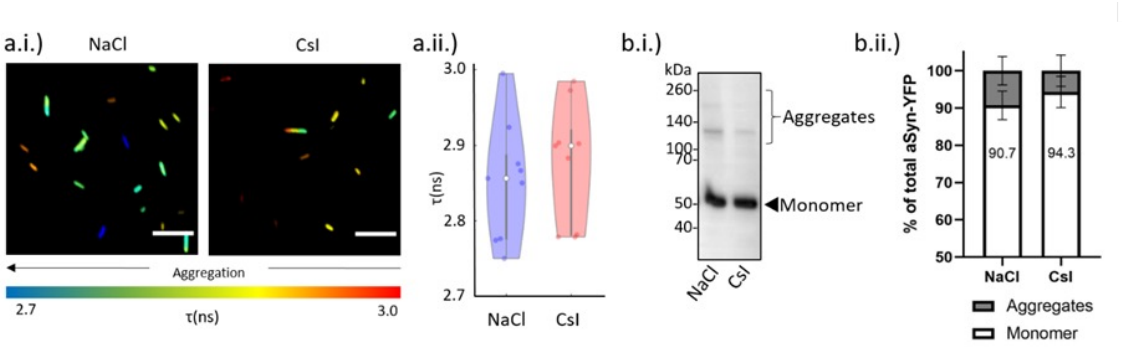

Figure 5.10. E. coli treated with NaCl have a higher content of aSyn aggregates compared to E.coli treated with CsI. (a.i.) Representative FLIM images of fixed E. coli expressing aSyn-YFP after heat shock with 150 mM NaCl or 150 mM CsI. Scale = 5 µm. (a.ii.) Fluorescence lifetimes (τ) were taken as an average of all E. coli from each field of view, $n = 9$ for each sample. (b.i) E. coli proteins were probed by Western blot with an antibody targeted at the aSyn-N-terminus, showing aSyn-YFP monomer and aggregates of higher molecular weights. (b.ii.) Densitometry analysis of the Western blots, normalised to Ponceau S staining for total protein content, shows E. coli treated with CsI contained less aggregates than those treated with NaCl, $n = 3$.

By combining different experimental and theoretical methods, it was shown that ions can influence the mobility of bulk water, water in the solvation shell, as well as protein mobility. Aggregation rates depend on the dynamics of the aqueous phase.

The difference in the aggregation rates in H_2O and D_2O suggests that the direct effect on aggregation is due to the solvent which is influenced by the ions. It has been proposed that direct ion binding to aSyn might influence aggregation rates, however, in the current observations, ion binding strength did not correlate with aggregation rates, suggesting that the Hofmeister series might not be the only explanation for why aSyn aggregation kinetics are either increased or decreased by ions.[215] Structural alterations cannot be ruled out: even though no gross structural differences in the presence of NaCl and CsI were observed, the applied NMR and MS techniques may not have been sensitive enough on the timescale needed to identify differences in transient dynamic interactions within the monomer structures in solution. These are the dynamics that govern whether a protein remains monomeric or misfolds into aggregation-prone conformations: The solubility and function of IDPs rely on their being able to probe different conformations and the mobility of IDPs is highly dependent on the surrounding solvent. Retardation of reconfiguration rates can lead to protein aggregation.[216–218] Slowing down the motions of the solvent can reduce the motion of the protein, thereby enhancing protein aggregation propensity. We have shown that the presence of ions modulates the mobility and intermolecular interactions of the water surrounding proteins. The data presented here support a mechanism whereby the pathway to oligomerisation and aggregation is determined by the intramolecular diffusion rate of the protein.

6 In-situ Observation of the Structure of Crystallising Magnesium Sulphate Solutions

When crystal nuclei form and grow in an undercooled amorphous system, the Gibbs free energy decreases and the system reaches a stable, crystalline state with a high level of order. In the following chapter, terahertz time-domain spectroscopy was used to study crystallisation, i.e. the transformation from a disordered into an ordered state, on the example of magnesium sulfate heptahydrate ($MgSO_4 \cdot 7H_2O$) that was chosen to simplify experimental procedures.

The chapter focuses on three key aspects:

- the experimental setup (Chapter 6.1, published in IEEE Transactions on Terahertz Science and Technology, 10.1109/TTHZ.2021.3132800),[219]
- a novel method to utilise THz-TDS to measure temperature-dependent solute concentration (Chapter 6.2, published in Analytical Chemistry, 10.1021/acs.analchem.1c04279),[220]
- and the investigation of the crystallisation process itself (Chapter 6.3, published in Crystal Growth and Design, 10.1021/acs.cgd.2c00352).[221]

The main experimental work was conducted jointly with Qi Li, a PhD student in our group. Prof. Timothy Korter and Margaret Davis from Syracuse University performed density functional theory (DFT) simulations to elucidate the origin of observed spectral features. Utilising powder X-ray diffraction measurements, Prof. Andrew Bond from Cambridge University confirmed the structure and presence of different hydrates that were also measured with THz-TDS. The entire project was a collaboration with Dr. Terrence Threlfall from the University of Southampton who first brought the intriguing magnesium sulfate heptahydrate system to our attention and we benefited from his extensive knowledge about crystallisation and $MgSO_4$ in particular.

6.1 Flow Cell to Study Crystallisation Processes In-Situ

6.1.1 Introduction

Crystallisation has been an intriguing topic in both crystallography and chemistry for decades, yet resolving its fundamental nature at the molecular level is still not straightforward. This is

due to the complexity of the seemingly simple process which can give the impression of a highly erratic process. Nucleation and crystal growth are widely understood to constitute the two main steps.[222,223]

A number of techniques have been applied to study the crystallisation process. X-ray techniques, such as small-angle and wide-angle X-ray scattering, X-ray spectroscopy, and X-ray diffraction, are of great importance in providing information on the molecular level. In addition, spectroscopic methods can be used to probe the chemical interactions in the system of interest, including NMR, FTIR, Raman, and UV/Vis spectroscopy.[223] Typically, a combination of selected techniques is necessary to fully characterise a system, and in recent years computational methods have been increasingly used to great effect to complement the experimental investigations.

In aqueous systems, the high absorption of water in the infrared results in a noisy background signal, which complicates FTIR measurements and limits their application largely to measurements near surfaces in attenuated total reflectance (ATR). Raman spectroscopy is therefore commonly used as an alternative to investigate the vibrational modes in the infrared given the lack of contribution from water molecules to the Raman spectra due to the different selection rules. In recent years, terahertz time-domain spectroscopy (THz-TDS), has emerged as a new tool that can be used, similar to FTIR, to probe the molecular vibrations due to permanent dipole changes but it has the advantage that it can also be applied in transmission when water is present in the sample, given the slightly lower absorption of water at terahertz frequencies compared with the mid-infrared. THz-TDS has been proved to be a useful technique to study both amorphous and crystalline materials in the solid state, as it is sensitive to inter- and intramolecular interactions within such systems.[224] It has been successfully applied to investigate the properties of pure amorphous materials and crystals, and also phase transitions of polymorphs and crystallisation from the amorphous to crystalline phase.[224–226] Additionally, the dielectric relaxation phenomena on picosecond time scales have been investigated with terahertz spectroscopy in polar liquids, such as alcohol, water, and their mixtures.[227]

However, there are not yet many studies utilising THz-TDS to investigate the crystallisation process in solutions. May and Taday employed terahertz spectroscopy in ATR configuration and monitored the crystallisation of sucrose in confectionary products.[228] The results clearly showed the transition from sugar solution to a solid glassy and then crystalline state. Soltani

et al. refined this method and successfully proved the existence of intermediate hydrate states in the crystallisation of L-(+)-tartaric acid during the evaporation of water from aqueous solutions of tartaric acid solutions.[229] Terahertz spectra were acquired over a period of 60 h while water evaporated and three stages of crystallisation were discernible. At the beginning of the measurement, the spectra of the solution phase were featureless. In the nucleation stage, the absorption decreased as a result of the reduction in water concentration due to evaporation. In some experiments discontinuous increases in absorption were observed which were attributed to water being released when the hydrated states transformed to the final crystals. A feature was spotted at approximately 750 GHz that was hypothesised to result from the vibration of water molecules surrounding the fragments of solvent molecules. The final observed stage was the crystalline phase displaying a dominant absorption feature at 1.1 THz. These three stages were assumed to be happening inhomogeneously throughout the probed volume.

Even though the absorption of terahertz radiation from water is approximately two orders of magnitude weaker than in the mid-infrared it is still around 200 cm^{-1} at 1 THz, which limits the path length of the cuvette that can be used for transmission measurements to around 100 µm in terms of trading off dynamic range and spectral bandwidth for the measurement. However, such a path length is sufficient for crystallisation experiments and terahertz spectroscopy combined with microfluidics offers the opportunity to measure samples containing water with high sensitivity and over a wide frequency range. Similar approaches using thin cuvettes in transmission were previously found to be useful to investigate biomaterials such as proteins and DNA.[230,231] While in the current set-up, a crystallisation cell with a fixed path length was used, it would be entirely feasible to replace this with a variable thickness cell, which opens up other avenues for data processing and extraction of optical constants as for example used by Venables et al.[87]

In the newly developed set up, a closed microfluidics platform made of z-cut quartz was utilised, enabling investigation of both the solvent and solute at frequencies from 0.35 THz to 2 THz whilst allowing for optical observations in the visible range of the spectrum during crystallisation and for cleaning of the cell between experiments. Magnesium sulphate hydrates were chosen as a model system, as different hydrates are known to form under specific conditions.[232] Between 2 °C to 47 °C, $MgSO_4 \cdot 7H_2O$ is the predominant form that can be crystallised at reasonable experimental time scales.[233] Therefore, $MgSO_4 \cdot 7H_2O$ is used as an example to demonstrate the setup designed based on transmission THz-TDS that can observe the crystallisation and

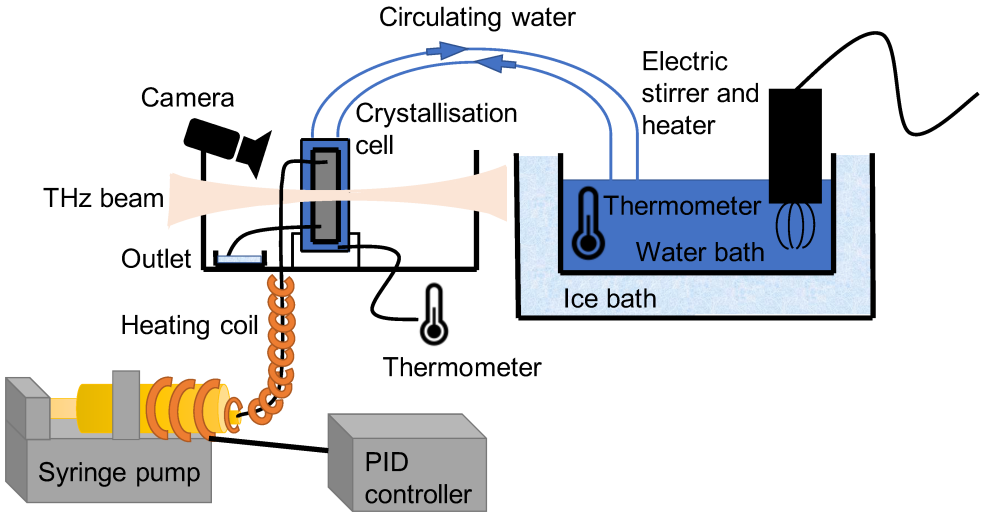

Figure 6.1. Schematic setup.

characterise the structure before, during, and after crystal formation *in situ*.

6.1.2 Methods

Up to now, all published studies using terahertz spectroscopy to study crystallisation from solution have relied on solvent evaporation to trigger nucleation. These studies were performed by ATR sampling, which restricts the observations to the evanescent field near the surface of the ATR crystal rather than in the bulk of the liquid.[228,229] The goal of this project was hence to build a versatile setup that would be capable to study crystallisation mechanisms from supersaturated solutions with THz-TDS in transmission geometry. Main design criteria were intended to cover operation over wide temperature and concentration ranges, assure stability at high temperature, control temperature gradients during crystallisation, and enable measurements under stagnant and flowing conditions.

Description of the Setup

The setup comprised a temperature controlled crystallisation cell that was designed such that it fits into a standard transmission chamber of a commercial THz-TDS setup (Figure 6.1). In parallel to the terahertz measurements it was possible to film the crystallisation process using a small camera that was integrated into the setup.

The central part of the setup was the crystallisation cell that held a cuvette containing the solution during the measurements. The cuvette was manufactured by Hellma (Southend-on-Sea, UK). It was made of two pieces of z-cut quartz (each 1.5 mm thick to avoid etalon reflections)

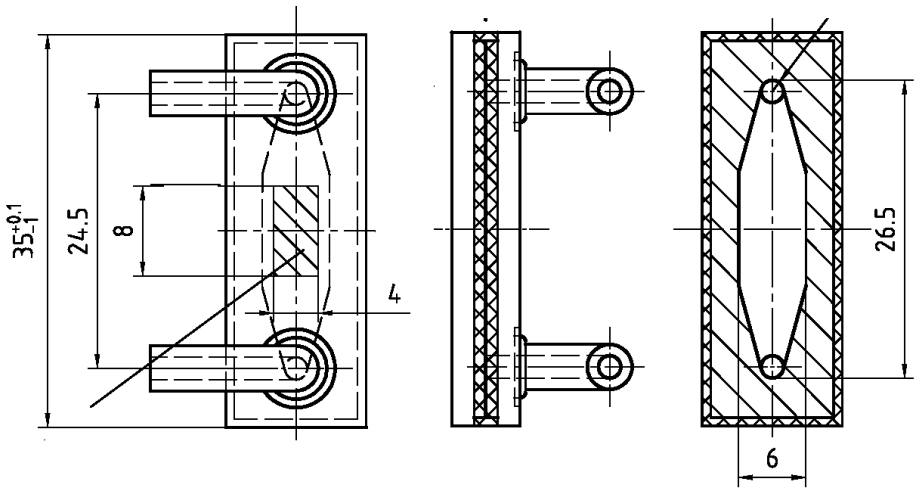

Figure 6.2. Three-view drawing of the cuvette. Left: view from the front, centre: view from the side, right: view from the bottom. Lengths are in mm.

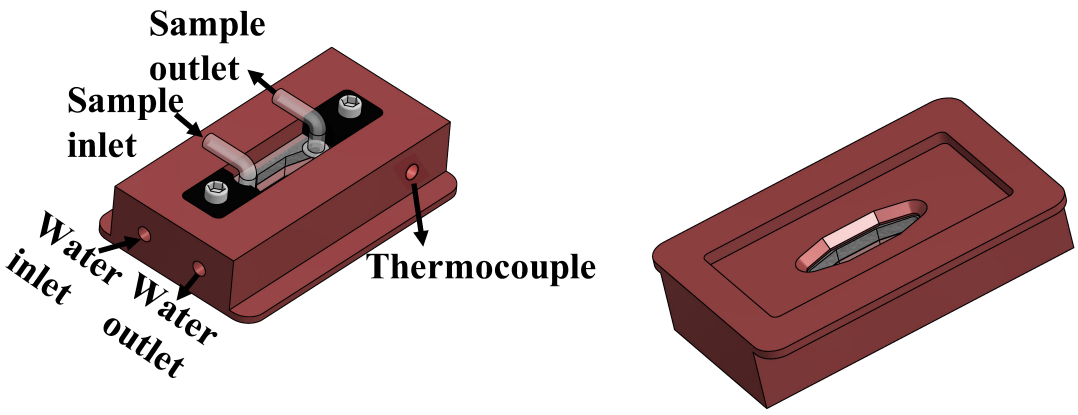

Figure 6.3. Renderings of the metal sample holder with cuvette inserted.

glued together using EP220 epoxy (Fiberdur, Aldenhoven, Germany) with an outlet on each side giving a pathway of solution. The channel was 24.5 mm long and 100 µm thick, and a schematic drawing is shown in Figure 6.2.

The quartz cuvette was held in a metal jacket which has been machined with channels to allow for water to circulate through the metal block in order to control the temperature of the quartz cuvette using a water bath and pump (Figure 6.3). A thermocouple was fitted to the block to allow for accurate temperature control. During the THz-TDS measurement, the assembled crystallisation cell was positioned at the focal position of the measurement chamber and the terahertz beam propagated through the centre of the cuvette with a beam width of about 2 mm.

The temperature of the crystallisation cell was controlled by an external recirculating water

bath that was connected to the inlet and outlet of the sample holder metal jacket. The pipes between water bath and crystallisation cell were insulated using foam pipe lagging, circulation of the coolant/ heating medium was performed using a pump (120s cased pump, Watson Marlow, Falmouth, UK), and the temperature was controlled by balancing variable heating with an in-built stirrer and PID controller (Anova Applied Electronics, San Francisco, CA, USA) against the near constant cooling from a surrounding ice bath.

Using this setup it was possible to vary the temperature setpoint by 0.1 °C intervals and it was possible to ramp the temperature over the course of a measurement. Using water and ice as the respective circulating and cooling media, the temperature of the crystallisation cell up could be equilibrated between 4 °C to 90 °C without further adjustments. Crystallisation was triggered by slowly decreasing the temperature of the crystallisation cell.

In order to investigate the effect of continuous sample flow, a syringe pump (Aladdin Syringe ONE Programmable Syringe Pump AL-1000, World Precision Instruments, Hitchin, UK) was used to provide a steady flow of solution. At its lowest setting, the flow was $0.375\,\mathrm{ml\,min^{-1}}$, which corresponded to a residence time of approximately 2.4 s within the sample cuvette when assuming plug flow. The syringe was contained by a metal tube which was wrapped with a heating coil (SRT051-040LSE, silicon rubber tape, Omega Engineering, Manchester, UK). This ensured that the heat provided by the heating coil was evenly distributed and single-use syringes could easily be replaced between measurements. Further heating coil was wrapped around the transfer tube all the way to the inlet of the crystallisation cell. This made it possible to control, and keep the temperature constant both inside the syringe and the transfer tube.

The temperature at the syringe was measured with a thermocouple and controlled via a PID controller (P6100, West Control Solutions, Brighton, UK). The syringe was kept at an elevated temperature to avoid supersaturation and to minimise the chance of nucleation and crystallisation occurring in the solution before reaching the cell. Over the course of the experiment, the solution was pumped into the crystallisation cell. The temperature at the inlet of the cell was again measured with a thermocouple to assure that the temperature was still high enough to avoid nucleation before the solution reaches the cell. This thermocouple was not connected to the PID controller and has been added only to monitor the system. Once the solution had passed through the cell, it flowed through the outlet at the bottom side to a beaker that was placed within the sample compartment of the terahertz spectrometer to collect the solution that

was purged out.

An optical camera (CF-25, CrazyFire, China) was attached to the cell and focused on the liquid layer in order to acquire images every 2 s of the crystallisation process in addition to the terahertz spectra.

The temperature was monitored continuously throughout the crystallisation experiments using thermocouples located in the water bath, at the heater, and inside the flow cell, as well as at the inlet as mentioned above. Temperature data was acquired once every second.

Sample Preparation and Operation

The $MgSO_4$ water solution was prepared by dissolving $MgSO_4 \cdot 7H_2O$ (Sigma-Aldrich, Gillingham, UK) in Milli-Q water (IQ 7000, Merck, Darmstadt, Germany, resistivity 18.2 MΩ cm) to the desired concentration in a beaker. The mixture was placed on a magnetic stirrer for constant stirring until the sample was fully dissolved. It was sometimes heated to a slightly higher temperature (in the range of 25 °C to 35 °C) when preparing solutions with high concentrations to facilitate dissolution. EDTA solution was used for cleaning and purging the crystallisation cell after each measurement. For the cleaning solution, commercial EDTA solution (pH = 8; Fisher Scientific, Loughborough, UK) was mixed with NaOH solution (Reagecon Diagnostics, Shannon, Ireland) to adjust the pH to 10, in which $MgSO_4 \cdot 7H_2O$ has a better solubility.

The temperature of the metal jacket around the crystallisation cell was equilibrated before injecting the solution. Once the sample was injected into the crystallisation cell the temperature was either kept stable and crystallisation was observed as a function of time or it was varied using the heater control in order to induce crystallisation or dissolution.

For static measurements, solution was injected outside the spectrometer to avoid spillage inside the sample chamber. Tubes were connected to the inlet and outlet of the cell and solution was injected with a syringe from one end. It was taken care that no air bubbles remained within the crystallisation cell. Surplus solution purged from the cell was collected in a beaker and disposed of.

Previously it had been observed that crystals tend to form either at the inlet or outlet of the cell, or, if connected, at the end of tubes. To ensure higher reproducibility, the inlet and outlet tubes were truncated at a length of 3 cm and the ends sealed with parafilm to avoid evaporation of the sample. It would also have been possible to do without tubes, however, due to the small size of the crystallisation cell and the need to seal the inlet and outlet, this often introduced air

bubbles so that it was decided to use tubes of a constant length instead.

Following injection, the sample holder was immediately placed into the chamber and measurement acquisition was initiated no longer than 30 s after injecting the sample.

For the continuous flow measurements, a suitably large syringe was first fully filled with the prepared $MgSO_4$ solution, then placed into the metal tube that was kept at the set-point temperature. The syringe within the temperature controlled metal jacket was then fixed to the syringe pump and connected to the inlet tube before starting the measurements.

In either case, static or continuous flow, once the sample was injected into the crystallisation cell the temperature was either kept stable or varied using the circulating water bath, depending on the type of experiment performed.

To clean the flow cell and to remove remaining crystals after an experiment was completed, the cell was purged with the cleaning solution several times before and after each measurement, additionally with Milli-Q water as well. The spectrometer was used to confirm the absence of crystals after purging.

Terahertz Time-domain Spectroscopy

A TeraPulse 4000 (Teraview, Cambridge, UK) spectrometer was used to perform the terahertz transmission measurements. The thickness of the z-cut quartz windows comprising the flow cell, as well as the need to use air as the reference, caused a relatively large optical delay between the reference pulse and the sample pulse for these measurements. Therefore, the high-resolution mode was chosen, which allowed for acquiring a time-domain waveform of 45 ps duration.

Each spectrum was calculated from the co-average of 15 individual waveforms, resulting in the acquisition of one spectrum per 20 s. The spectral resolution set in the software was $0.94\,cm^{-1}$. Given the dynamic range of the spectrometer and the absorption of water in the terahertz region, high quality spectroscopic data were acquired in the frequency range of 0.3 THz to 2 THz.

6.1.3 Results and Discussion

Data Processing

During a THz-TDS measurement, the waveforms of reference and sample were recorded. The ratio of the Fourier transforms of reference and sample (the so-called power spectrum) yielded the complex transmission coefficient of the sample as a function of frequency.

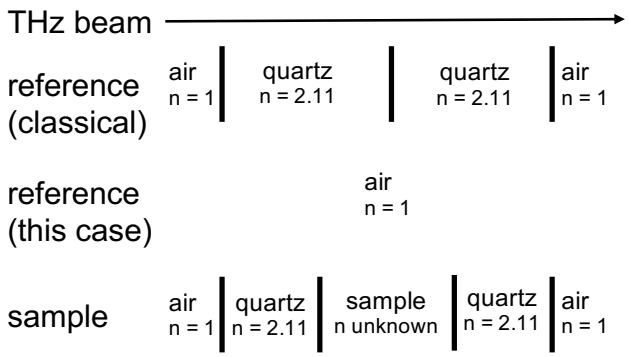

Figure 6.4. Schematic of the path of the terahertz beam in the sample chamber for different cases (quartz windows as reference, air as reference, and the sample sandwiched between windows). n denotes the real part of the refractive index.

In their paper from 1996 Duvillaret et al. described a reliable method to extract optical constants from THz-TDS measurements by taking the complex refractive indices of the surrounding media and sample into consideration, and solving the inverse problem of extracting the complex index of refraction iteratively from the measured transmission coefficient.[138]

In this case however, the analysis was complicated by the fact that the surrounding media were not the same for the reference and sample measurement, as is demonstrated in Figure 6.4. To avoid the Fabry-Pérot effect from internal reflections caused by the empty crystallisation cell, the reference measurements were performed in air without quartz windows.

This posed a challenge when attempting to calculate the complex optical constants using the method of Duvillaret et al. because their method assumed the surrounding media for the reference and sample measurement were the same.

The absorption of z-cut quartz windows in the terahertz region of interest is very low, with an extinction coefficient of approximately zero and the real part of the refractive index being approximately constant. Inserting windows into the beam path mostly lead to a longer time delay before detecting the pulse on the order of 20 ps for a window thickness of 3 mm. This could be utilised when calculating the absorption coefficient. While the spectral shape of the absorption was not influenced by the reference thickness, the absolute values were. By shifting the acquired reference waveform by about 20 ps and subsequently using the method of Duvillaret et al., the absorption coefficient was calculated. The absolute shift necessary depended on the thickness of the windows and sample. By comparing the absorption coefficient of pure water with literature values, introducing a time delay of 18.43 ps to the reference data recovered the absorption. This is illustrated in Figure 6.5a and 6.5b.

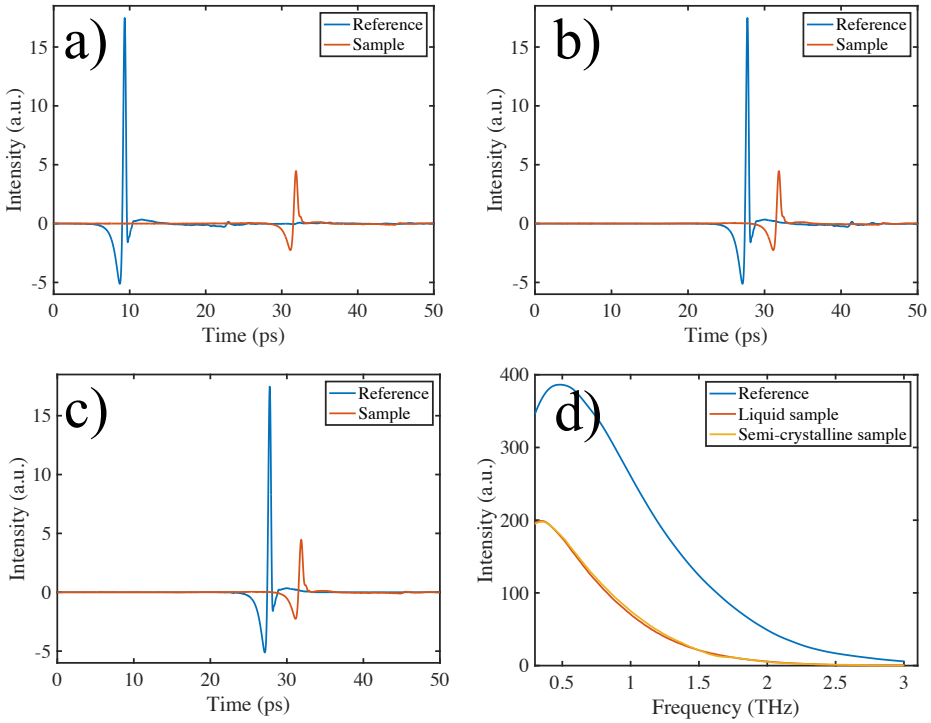

Figure 6.5. a)-c): Reference (blue) and sample (orange) waveforms. a): original case, b): after shifting the reference waveform, c): after shifting and zero-padding the reference waveform. d) Power spectra of reference (blue) and sample (red and yellow). In red, a liquid sample and in yellow after crystallisation.

Due to the optical design of the Terapulse 4000 instrument, a small feature was visible in the reference waveform at a time-delay of approximately 15 ps following the main peak. This introduced artefacts in the frequency domain unless temporal windowing was applied. The reference waveform was therefore zero-padded to remove those artefacts and Figure 6.5c shows both the reference and sample waveforms that were being used to calculate the absorption coefficient. Application of a Fourier transformation resulted in the power spectra shown in Figure 6.5d.

The different sets of data (time, THz-TDS, temperature, images) had to be linked together prior to further analysis. Temperature data was acquired each second, an image every 2 seconds, and THz-TDS data every 20 seconds. The temperature assigned to each terahertz spectrum was calculated as the average temperature during its acquisition. This way, terahertz data could be plotted as a function of time as well as temperature and linked to images via their time stamps for visual clarification.

Whilst the molar absorptivity ($1\,\mathrm{mol}^{-1}\,\mathrm{cm}^{-1}$) is commonly used as a unit of absorption intensity in chemistry we have continued the analysis in keeping with common practice in the

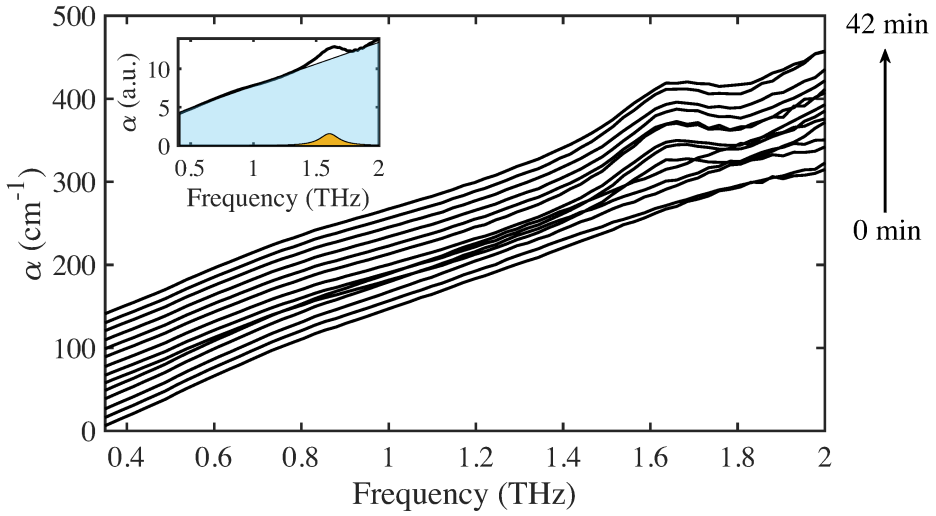

Figure 6.6. Spectra recorded at different times throughout the process. Each subsequent spectrum is offset by $10\,\mathrm{cm}^{-1}$. Inset: Typical spectrum of the crystalline system. It is depicted here as the sum of the amorphous background (blue) and the peak at 1.6 THz (orange).

terahertz literature in terms of the absorption coefficient (cm^{-1}) for consistency.

Results and Discussion

When operated under stagnant condition the concentration of $MgSO_4$ in the solution within the cuvette was constant and crystallisation could be observed as a function of time, depending on the chosen temperature and concentration. At concentrations of 25 wt% to 29 wt% $MgSO_4$ crystallised into its heptahydrate form within minutes at temperatures between 4 °C to 12 °C.

In Figure 6.6, the crystallisation of a supersaturated $MgSO_4$ solution over time is shown while the sample was being kept at approximately 4 °C. As expected, the spectrum of the $MgSO_4$ solution was completely featureless with a monotonously increasing baseline. Such spectral features are expected for aqueous solutions where no molecular order on the timescales of picoseconds is maintained and thus the molecules in solution are completely disordered in an amorphous phase. Over time the baseline dropped, and a peak emerged at 1.6 THz, evidencing the formation and existence of crystals.

Magnesium sulfate heptahydrate - water spectra containing crystalline features could hence be separated into the sum of the amorphous background and the peak at 1.6 THz, as shown in the inset in Figure 6.6.

Observed Clipping

When comparing the absorption of water with literature values,[234,235] it was observed that the terahertz beam was clipped somewhat by the sample holder, resulting in a typical reduction of the measured absorption at lower frequencies compared to literature values. However, the clipping only affects the spectrum below approximately 1 THz (Figure 6.7). Furthermore, we were not interested in absolute values as of yet and because the geometry was constant throughout the measurements, relative changes in absorption are still valid and useful for investigating sample properties.

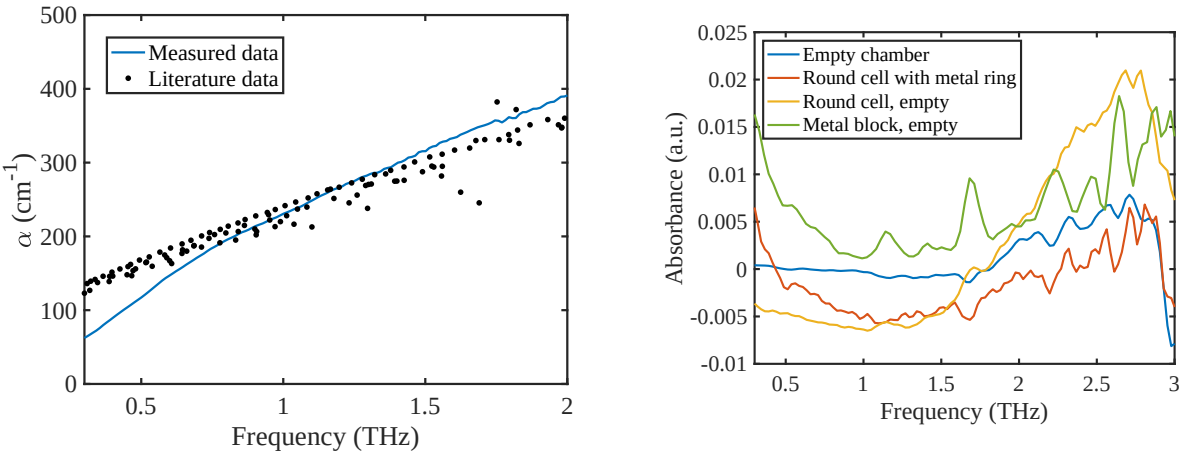

Figure 6.7. Left: Absorption coefficient of water from literature (black dots)[234,235] and measured in the crystallisation cell (blue line). Right: Different sample holders measured without sample to quantify possible beam clipping. Some water vapour was still present in the measurement of the metal crystallisation cell, because of tubes connected to the water bath sticking out of the measurement chamber, causing several spectral features due to imperfect sealing. In real experiments with samples, these features are too low to be noticeable.

To further investigate the beam clipping, different sample holders (the metal block from the crystallisation experiments as well as the round cell used in the study of different salt ions in Chapter 5) without windows were measured against the empty chamber as reference. Some clipping was observed below 0.5 THz in the round cell caused by the metal ring that is used to fix the windows in place. The beam was also found to be slightly clipped by the empty crystallisation cell block. However, the absorbance values in Figure 6.7b are about a factor of 100 lower than the absorbance of a typical sample. The traces of water vapour observed in the crystallisation cell are not visible in a sample measurement.

This leads to the conclusion that the differences in the spectra observed when the quartz crystallisation cell was used inside the metal block come from the fact that a) the beam is already slightly clipped by the metal (even though this is below the detection threshold when

a sample is measured) and b) further clipped/distorted by the channel that does not fill out the whole cell. In the future, when designing another crystallisation cell, it would therefore be beneficial to make the channel and opening wider, as well as finding an alternative to fixing the windows in place in the other liquid cell.

6.1.4 Conclusions

We developed a setup that can be used to observe crystallisation processes from aqueous and other organic solvents utilising terahertz time-domain spectroscopy in transmission geometry. Both static systems and systems under flow were investigated while either keeping the temperature constant or employing temperature ramping. Utilising the versatility of the setup, the magnesium sulfate heptahydrate system was studied at different temperatures before, during, and after crystals formed, thereby allowing the investigation of both crystals and the solvent at different levels of saturation.

The effects of temperature and concentration changes will be investigated further. The setup is designed for operating temperatures between 4 °C to 90 °C, which can be extended with minor adjustments. Therefore, it can be applied to a wide range of crystalline systems at various concentrations. Future work will focus on being able to trigger crystallisation within the cell, allowing the observation of initial crystal nucleation and growth.

6.2 Measuring Solute Concentration in Single and Multiphase Systems

6.2.1 Introduction

Terahertz time-domain spectroscopy (THz-TDS) is a useful far-infrared spectroscopy tool that is increasingly used in the field of solid state crystallography to complement x-ray diffraction methods to distinguish between polymorphs and other solid forms, as it probes collaborative motions in molecular systems that are largely influenced by the different crystalline packing.[236] Its use can be extended to study crystallisation itself and it has been shown that even low amounts of crystallinity can be detected in semi-crystalline systems,[126] and we recently developed a setup that allows for the in-situ investigation of crystallisation from the liquid phase over a range of concentrations and temperatures as described in Chapter 6.1.

Ultraviolet-visible (UV-Vis) spectroscopy has been widely applied for determining the concentration of a range of chemical species in a liquid, such as in the field of solution chemistry and water quality monitoring.[237] By measuring the absorption spectrum of the sample of interest, the identity of a known compound or molecule in solution can be confirmed and using a calibration curve, the concentration of the compound can be determined quantitatively.[238] However, despite its excellent sensitivity and ready availability some drawbacks of the method remain: the electronic transitions that give rise to the absorption in the UV-Vis are not very specific and often overlap; in addition, it is not always straightforward to utilise UV-Vis spectroscopy for measuring the concentration of chemicals in semi-crystalline systems, as the crystal particles will result to scattering losses and signal distortion.

In contrast, Raman spectroscopy can resolve the formation of crystals in the mid-infrared with much higher chemical specificity even in the presence of water, but it is inherently limited to study the properties of the crystals in solution rather than capturing much information about the liquid phase.[239] Other optical techniques such as second harmonic generation and polarized light microscopy can both detect the onset of the crystallisation, but are not ideally suited to infer detailed mechanistic insight into the nascent molecular structures.[240,241]

The method that is proposed in this study is using THz-TDS to determine the concentration of the solute prior and during crystallisation. In contrast to UV-Vis spectroscopy the method does not require the presence of a chromophore but rather exploits the differences in relaxation dynamics of the dipole moments of the solvent molecules that strongly affect the absorption measured at terahertz frequencies. In analogy to the quantification by UV-Vis a calibration curve over a range of concentrations is required but for the THz-TDS method the sample temperature needs to be taken into account as well.

Using this method, it is possible to measure the concentration of solute in the liquid phase not just in the neat liquid but throughout phase changes such as during crystallisation. In liquid systems, the coupling of photons to VDOS forms the so-called microscopical peak, which is responsible for an increasing absorption coefficient with frequency observed in the terahertz region. In crystalline systems, the VDOS is depleted and instead spectral peaks are formed at discrete frequencies, thereby decreasing the baseline. Hence, terahertz spectroscopy can probe liquid relaxation dynamics as well as vibrational transitions in crystals simultaneously, represented by the baseline and the peaks on a spectrum, respectively. The crystallisation of the model system

magnesium sulfate heptahydrate is discussed here to demonstrate the method.

6.2.2 Experimental Section

THz-TDS Measurements of Crystalline $MgSO_4 \cdot 7H_2O$ in the Solid State

A sample of $MgSO_4 \cdot 7H_2O$ (Sigma-Aldrich, Gillingham, UK) was ground using an agate mortar and a pestle, and then mixed with polyethylene (PE) powder to 2.5 w/w% by gentle mixing. The powder mixture was compressed into a pellet of 13 mm diameter using a hydraulic press (Specac Ltd., Kent, UK) at a load of 2 tons. A blank PE pellet was used as a reference. A terahertz time-domain spectrometer TeraPulse 4000 (Teraview, Cambridge, UK) was equipped with a cryostat (Janis, Massachusetts, USA) and an attached heater and controller (Lakeshore 330, Ohio, USA). The setup was capable of performing temperature-variant transmission measurements. For each measurement, 1000 waveforms were acquired and averaged and a spectral resolution of $0.94\,cm^{-1}$ was achieved per spectrum.

$MgSO_4$ Solution Measurements

Aqueous magnesium sulfate solutions were prepared to various defined concentrations from commercial $MgSO_4 \cdot 7H_2O$ (Sigma-Aldrich, Gillingham, UK). The experimental setup was described in detail in Chapter 6.1 and consisted of a liquid cell inserted into a hollow metal sample holder. The temperature was controlled by a recirculating water bath. The setup could be used either under stagnant conditions, i.e. the solution was inserted at the beginning of the measurement and the liquid cell was sealed, or in the continuous flow conformation, i.e. the solution was initially kept in a heated syringe that was fixed to a syringe pump, and was slowly injected into the cell.

Once the solution was injected into the liquid cell and the temperature had stabilised at the setpoint temperature (here $\sim 4\,°C$), the temperature of the cell was slowly increased at a rate of $1\,°C\,min^{-1}$ up to 25 °C. In the present study, calibration was therefore performed in the temperature range of 4 °C to 25 °C and the concentration region that was explored ranged from 0 (pure water) and 0.28 w/w %, corresponding to a maximum molar ratio of 0.054 ($MgSO_4$ to water). The weight ratio/concentration is denoted as c (w/w %), which represents the concentration of the solution.

Transmission spectra were acquired using a TeraPulse 4000 spectrometer (Teraview, Cam-

bridge, UK) and images were acquired with an attached camera (CF-25, CrazyFire, China). Utilising the high-resolution transmission geometry mode of the spectrometer, time-domain waveforms of 45 ps with a spectral resolution of 0.94 cm^{-1} were recorded. Before a sample solution was measured, a reference measurement of the empty chamber was performed. Subsequently, each sample spectrum was calculated from the average of 15 individual waveforms, resulting in the acquisition of one spectrum per 20 s and covering the frequency range from 0.35 THz to 2 THz. The absorption coefficient was calculated by shifting the acquired reference waveform by about 20 ps and subsequently using the method of Duvillaret et al.,[138,242] one of a number of transfer matrix approaches.[243]

Several thermocouples continuously monitored the temperature of the water bath, of the circulating water surrounding the crystallisation cell, of the syringe, and of the solution at the inlet of the cell.

6.2.3 Results and Discussion

Crystalline $MgSO_4 \cdot 7H_2O$

Reference terahertz spectra of crystalline $MgSO_4 \cdot 7H_2O$ in the solid state were acquired over a range of temperatures in order to characterise the vibrational features that are characteristic of the crystalline form. Three strong vibrational features were identified at 1.2, 1.6 and 2.8 THz in the spectral range that was accessible using the THz-TDS setup (Figure 6.8). The measurement at temperatures below room temperature confirmed the presence of sharp vibrational features that underly each of the features observed at room temperature. Given that the subsequent crystallisation experiments were performed in the temperature range of 4 °C to 25 °C, and that the presence of the liquid flow cell limits the spectral bandwidth of the spectrometer to the range of 0.35 THz to 2 THz, the more intense feature at 1.6 THz at 21 °C was used to represent the behaviour of the crystalline phase (Figure 6.8).

Concentration Calibration

The temperature-dependent behaviour of the liquid phase was characterised with terahertz spectroscopy for solutions over a range of concentrations, c. For the measurement of solution at each concentration, the absorption at selected frequencies was taken from the spectra and a linear fit was applied against temperature, as demonstrated in Figure 6.9.

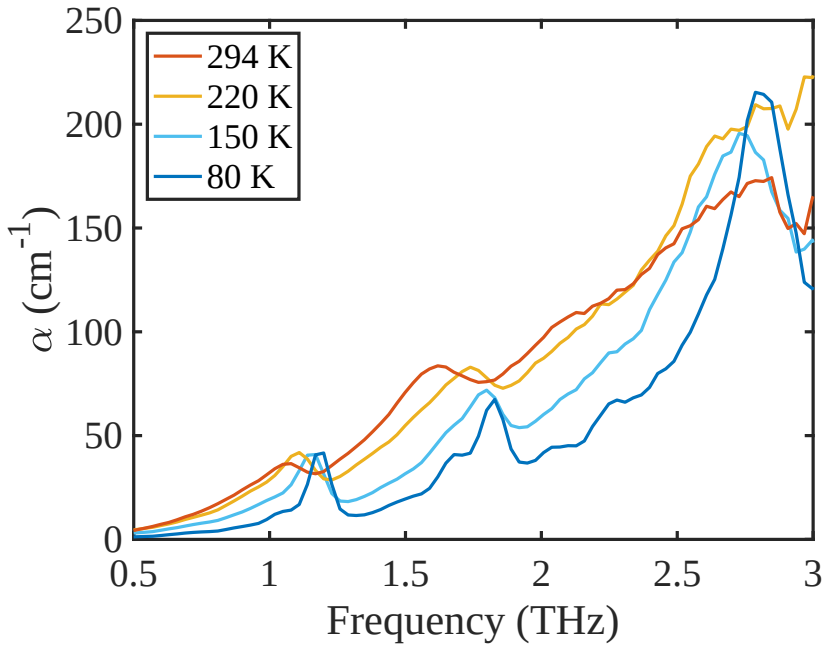

Figure 6.8. Solid-state terahertz spectra of crystalline $MgSO_4 \cdot 7H_2O$ at various temperatures from 80 K up to room temperature.

$$\alpha(c, T, \nu) = a_1 \cdot T[^{\circ}\mathrm{C}] + b_1 \tag{6.1}$$

where α is the absorption extracted from the terahertz spectra of solution at a certain concentration c acquired in the temperature (T) range of 4 °C to 25 °C at a chosen frequency ν. a_1 and b_1 are the least square linear fitting parameters. Using this methodology, the parameters a_1 and b_1 for a range of concentrations are determined.

Based on the calibration methodology outlined above it is then possible to fit the change in absorption with concentration at a given temperature and frequency with a_2 and b_2 as the linear fit parameters.

$$\alpha_{\nu,T}(c) = a_2 \cdot c[\mathrm{w/w\ \%}] + b_2 \tag{6.2}$$

Figure 6.10 shows the data that was derived for the case of $MgSO_4$ solution at the three chosen frequencies: 0.5 THz (lower bound), 1.0 THz (high signal to noise ratio), and 1.6 THz (centre of the crystalline peak) at a temperature of 5 °C. The measurements were performed under static as well as continuous flow, and no significant deviation was identified between the different conditions, as demonstrated by the red data points in Figure 6.11 which correspond to the

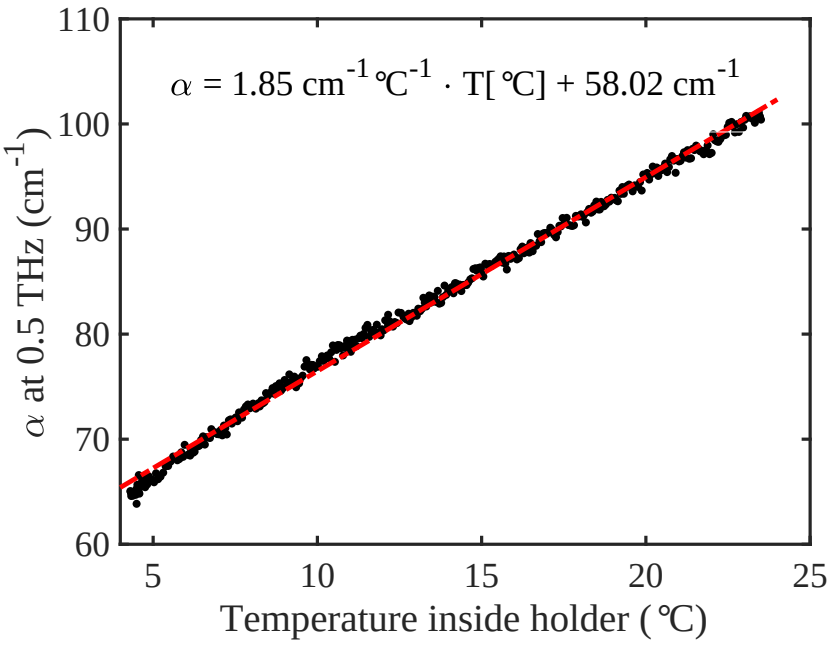

Figure 6.9. Linear fit of temperature (°C) and absorption for the example of a solution of $MgSO_4$ at a frequency of 0.5 THz and $c = 0.14$ w/w %.

continuous flow conditions.

The calibration procedure can thus be used to extract the concentration of the solute in the liquid phase based on the measured absorption at any given temperature within calibration range and for any frequency within the spectral bandwidth of the instrument.

Case Study of $MgSO_4$ Crystallisation

Applying the above method, it was possible to determine the local concentration of solute in the liquid phase during the crystallisation process. Compared to the case of measuring the solute concentration in the neat solution outlined above in the presence of a solid phase, i.e. the crystals, the total absorption (α) is the sum of the absorption from the liquid phase α_{liquid} and the solid phase α_{solid}, here crystalline $MgSO_4$ heptahydrate. To identify the local concentration in solution the contribution from α_{solid} can be minimised by measuring the absorption at the lower frequency end of the available bandwidth for the calibration curve. At a frequency of 0.5 THz the crystalline phase exhibits negligible absorption (Figure 6.8) and $\alpha \approx \alpha_{\text{liquid}}$. The vast majority of crystalline systems do not exhibit phonon modes at frequencies below a few hundred gigahertz and hence this method is not restricted to the $MgSO_4$ system but generally applicable as long as the spectral characteristics have been established by a simple transmission

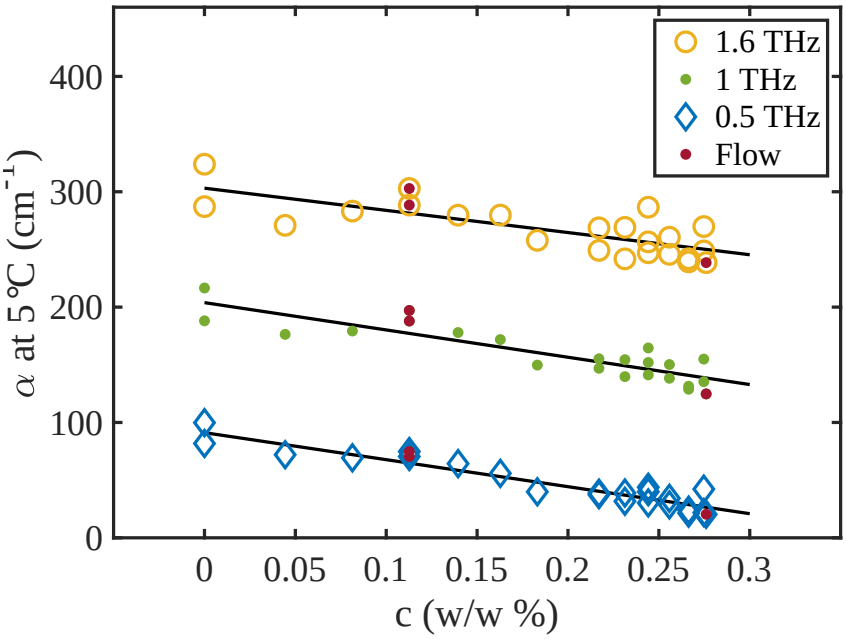

Figure 6.10. Calibration curve of $MgSO_4 \cdot 7H_2O$ at 5 °C. The absorption at 0.5, 1.0, and 1.6 THz is represented by the yellow, green, and blue markers, respectively, and the red data points are the measurements using continuous flow.

measurement of the crystalline phase. As a general rule it can be assumed that the higher the frequency that is chosen for the analysis the more likely it would be affected by the crystalline phase when calculating the equivalent concentration.

Figure 6.11(a) shows the absorption at 0.5 THz directly extracted from the terahertz spectra acquired throughout the crystallisation process, which was at the lower bound of the frequency window and no crystalline feature was expected. With the information of frequency, temperature, and absorption, the corresponding solute concentration was determined as shown in Figure 6.11(b) using the calibration curve in Figure 6.10. The concentration first decreased gradually due to the water depletion from the two ends of the flow cell. In the second region, the concentration increased drastically as crystals started to grow which resulted in relatively denser liquid in the area that was probed with THz-TDS. Afterwards, the concentration reduced again and slowly reached the same equilibrium point as in the beginning, which was assumed as the stable concentration at that temperature. In this way, the temperature-dependent absorption was converted to information that was independent of temperature.

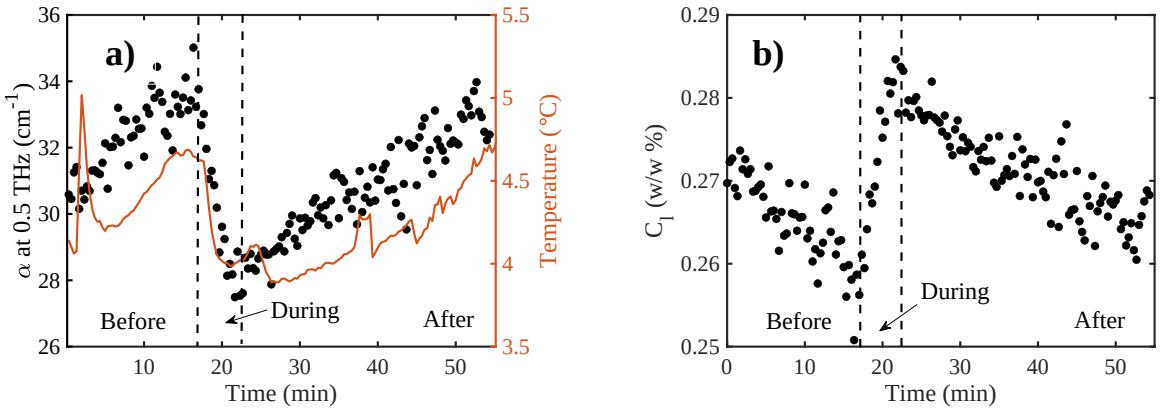

Figure 6.11. Absorption and calculated concentration of the solute in the liquid phase c_l at 0.5 THz. (a) The change of absorption over time at 0.5 THz along with the temperature profile. (b) The calculated c_l during the crystallisation process.

6.2.4 Conclusions

The newly established set up, based on microfludics and THz-TDS, has been applied to develop a method of measuring solute concentration. By acquiring terahertz spectra of liquid samples over a range of concentration and temperature, a calibration curve was determined for the extracted absorption at terahertz frequencies to calculate the concentration of solute in the liquid phase. The method can be applied to study the local solute concentration in multi-phase systems, e.g. during crystallisation. By using the absorption at lower frequencies, ideally below 1 THz, the complexity of convolved spectral features that originate from the liquid and crystalline phases at higher frequencies can be successfully avoided. THz-TDS can be used as a complementary method to other spectroscopic techniques for studying changes in concentration in the absence of a chromophore whilst at the same time providing insight into the solid state properties of the crystals forming during crystallisation. There is significant potential for this approach to study phase separation processes, and crystallisation in particular, and the behaviour of organic molecular crystals such as pharmaceutical drug molecules will be especially exciting to explore with this approach.

6.3 In-Situ Observation of the Structure of Crystallising Magnesium Sulphate Heptahydrate Solutions

6.3.1 Introduction

The crystallisation process has been used for centuries as a purification and separation step for various applications. Therefore, it is surprising that empirical models rather than fundamental understanding still govern the comprehension of crystallisation's underpinning mechanisms and kinetics. What is well established is that nucleation and crystal growth are the two main steps contributing to the crystallisation process. However, the microscopic mechanism of the formation of the nuclei and how they subsequently evolve into crystals is still unclear.[223,244–246] Two widely popular models are used to describe the crystallisation process: classical nucleation theory and non-classical theory. The former states that density and order fluctuations in the solution cause the formation of crystal-like clusters, which in turn result in nuclei that gradually grow into the crystal form defined by the packing of the cluster.[247] The non-classical theory proposes that the clusters first formed are liquid like, and crystalline order is only introduced later when they grow into nuclei.[248,249]

One widely used model system for investigating crystallisation is the $MgSO_4$-H_2O system. A variety of hydrate forms can crystallise depending on the temperature and concentrations in solution, but this system also recently received added attention because the presence of such sulfates and their hydrated forms are discussed as the origin of near-surface water content on Mars.[232] A comprehensive understanding of the crystallisation mechanism is highly desirable to support further research into this topic.

A range of techniques are widely used to investigate the crystallisation process: Traditional crystallographic methods to characterise crystalline structures, such as small-angle and wide-angle X-ray scattering, X-ray spectroscopy, and X-ray diffraction; spectroscopic techniques including nuclear magnetic resonance (NMR), Fourier-transform infrared spectroscopy (FTIR), and Raman spectroscopy provide insight into the chemical structure and the shape of the molecules during crystallisation; ultraviolet-visible (UV-Vis) spectroscopy can measure the solute concentration but are of limited use when nascent particles result in scattering losses that cannot be distinguished from absorption.[223,237] Turbidimetry is used to measure the loss of intensity of transmitted light due to the scattering effect of those particles. Second-harmonic

generation and polarised light microscopy are applied to detect the onset of crystallisation but are not very sensitive to the structure.[240,241]

When investigating crystallisation in aqueous solutions, the strong absorption due to the presence of water makes it difficult to perform FTIR measurements in transmission. Instead, observations are restricted to surface measurements using attenuated total reflection (ATR). While Raman spectroscopy does not suffer from this restriction, the lack of interaction means that only very little information, if any, of the solvent molecules during the crystallisation process can be extracted.[239]

Terahertz time-domain spectroscopy (THz-TDS) offers a unique perspective to characterise the crystallisation process both in terms of information from the solvent as well as the emerging crystals. By measuring the amplitude and phase of single-cycle pulses of far-infrared radiation, in solution, THz-TDS can probe large-amplitude inter-molecular vibrations as well as high-frequency dielectric relaxation processes that correspond to relaxation times of less than 10 ps.[224] In solids, the technique can distinguish between different polymorphic forms, cocrystals, hydrates and solvates, as well as provide an excellent measure for overall crystallinity and defect density crystallinity since the long-range order in crystals results in well-defined spectral features (fingerprints) in the terahertz region. In contrast, in amorphous materials, the lack of long-range order results in the collapse of the well-defined peaks into a vibrational density of states (VDOS), which starts at a few hundred gigahertz and exceeds the entire spectral bandwidth of many THz-TDS spectrometers (0.3 THz to 3 THz). It is characterised by a featureless, monotonously increasing absorption coefficient that typically peaks at frequencies beyond 3 THz.[73]

The contributions of individual atomic motions in experimental terahertz spectra are not discernible without additional information, which is usually gathered from theoretical simulations. Density functional theory (DFT) simulations provide normal mode vectors and force constants and can therefore be used to investigate and visualise vibrational modes.[30]

Studies of water and water/alcohol mixtures with THz-TDS suggested key concentration transition points that marked different stages of water and alcohol molecular interactions.[235] Other water mixtures and solutions also demonstrated the use of THz-TDS to probe water molecules based on their mobilities and the behaviour of the hydration shell.[250,251] As well as for characterising static structures, THz-TDS has also been found useful to probe reaction

dynamics, such as solid-solid phase transitions, amorphous-solid transformations, and crystallisation.[224,228,229,252]

Previously, terahertz spectroscopy has been applied to study the crystallisation of sugar and L-(+)-tartaric acid utilising attenuated total reflectance geometry and triggering the crystallisation process by the evaporation of water from the aqueous solution.[228,229] In a separate experiment terahertz narrow-band absorption and time-domain spectroscopy were combined to investigate the early stages of $CaCO_3$ nucleation. Experimental evidence for the nucleation to occur via the pre-nucleation pathway for aqueous systems was found.[253]

During crystallisation the VDOS is depleted, resulting in the emergence of peaks and a dropping of the overall baseline given its nature as the flank of the VDOS. It is important to emphasise that this change in the spectral response of the absorption baseline in the frequency range studied is not the result of a drift in the background signal but contains quantitative information regarding the depletion of the VDOS as well as the dielectric relaxation dynamics on picosecond to femtosecond timescales. THz-TDS can therefore simultaneously probe amorphous and crystalline phases represented by the behaviour of the baseline and peaks, respectively. In addition, this suggests that the behaviour of liquid phase can be extracted from the baseline while crystallising, hence the solute concentration can be measured even in semi-crystalline samples.[254]

$MgSO_4$ is chosen as a model system to demonstrate that THz-TDS is an option to complement the currently widely applied tools in the field of crystallisation. The versatile set-up based on THz-TDS in transmission geometry and the methodology described in detail in Chapter 6.1 and Chapter 6.2 are further used to observe the dissolution of crystals at elevated temperatures, calculate the equivalent local concentration, and can be extended to other systems of interest.

6.3.2 Materials and Methods

Solid-state samples measurements

Commercial samples of four different $MgSO_4$ hydrates were investigated as listed in Table 6.1.

Powder X-ray diffraction measurements were made on a Panalytical XPert Pro diffractometer in Bragg-Brentano geometry using non-monochromated CuKα radiation ($\lambda_{ave} = 1.5418\,\text{Å}$). Samples were prepared on glass flat-plate sample holders, and data were measured over the range $2\theta = 5°$ to $70°$ with an effective step size of $0.0167°$ and counting time of 60 s per step.

Table 6.1. Concentration overview for different solid-state samples.

Sample	Concentration (% w/w)
Anhydrous $MgSO_4$ 97 percent (AcrosOrganics)	7.5
Anhydrous $MgSO_4$ 99.5 percent (AlfaAesar)	7.5
$MgSO_4$ monohydrate 97 percent (Sigma-Aldrich)	6.3
$MgSO_4$ heptahydrate 98 percent (Sigma-Aldrich)	2.5
$MgSO_4$ heptahydrate crystallised at room temperature from solution	2.5

Measured data were compared to simulated patterns generated using Mercury[255] from available crystal structures of $MgSO_4$,[256] $MgSO_4 \cdot H_2O$,[257] and $MgSO_4 \cdot 7H_2O$.[258]

For terahertz measurements, the crystalline samples were ground gently in an agate mortar with a pestle, and the polycrystalline samples were then mixed with polyethylene (Induchem, Volketwil, Switzerland) to a defined concentration that varied for different hydrates, as detailed in Table 6.1.

The well-mixed powder was compressed into a pellet of 13 mm diameter with a thickness of 2 mm to 3 mm using a hydraulic press (Specac Ltd., Kent, UK) at a load of 2 ton, and a blank polyethylene pellet prepared in the same way was used as a reference. During the THz-TDS transmission measurement, 1000 waveforms were acquired and averaged, with a resolution of $0.94\,cm^{-1}$.

Additionally, a supersaturated solution of $MgSO_4$ was prepared from $MgSO_4$ heptahydrate 98 % (Sigma-Aldrich, Gillingham, UK) dissolved in Milli-Q water (IQ 7000, Merck, Darmstadt, Germany, resistivity $18.2\,M\Omega \cdot cm$), and filled into a well-sealed petri dish. The petri dish was left in a fume hood at 20 °C until crystals formed. This process was to mimic the crystallisation process in the crystallisation cell. Due to constraints of the set-up it was impossible to investigate crystals grown directly in the microfluidic cell at cryogenic temperatures. The crystals grown in the petri dish were made into pellets using the method described above and characterised at cryogenic temperatures with terahertz spectroscopy later to confirm their structure more accurately.

THz-TDS measurements were performed with a commercial spectrometer TeraPulse 4000 (TeraView Ltd., Cambridge, UK), and the measurement chamber was purged with nitrogen to eliminate the effect of water vapour. Variable-temperature measurements were facilitated by a cryostat (Janis, Massachusetts, USA) and the temperature was well-controlled with an attached temperature controller Lakeshore 330 (Ohio, USA). The sample pellets were first cooled down

to 80 K and then heated up in steps to 300 K to examine the temperature-dependent behaviour of the spectral features. Measuring commercial samples at room temperatures allows the direct comparison of their spectra with those acquired during crystallisation experiments. However, acquiring spectra for crystalline samples at lower temperatures improves their quality since absorption in the terahertz region is highly affected by the temperature background, reflected in effects such as peak broadening and peak shifting.

Computational Methods

The solid-state density functional theory (ss-DFT) program CRYSTAL17[259] was used to perform geometry optimisation and frequency analysis calculations on crystalline $MgSO_4$ heptahydrate using periodic boundary conditions. All calculations utilised the revised version of the Peintinger-Oliverira-Bredow split-valence triple-ζ basis set (pob-TZVP-rev2)[260] and the Becke-3-Lee-Yang-Parr (B3LYP)[261,262] hybrid density functional. The B3LYP density functional was supplemented with Grimme's noncovalent dispersion correction (D3) and the Becke-Johnson damping correction[263–265] with three-body Axilrod-Teller-Muto repulsion contributions (program keyword "ABC").[266–268] In all $MgSO_4$ heptahydrate calculations, 125 k-points were used in the irreducible Brillouin zone (keyword SHRINK=9) and 99 radial points and 1454 angular points were used for the pruned integration grid. The overlap-based truncation criteria for the bielectronic integrals (Coulomb and exchange) (program keyword "TOLINTEG") were set to 10^{-12}, 10^{-12}, 10^{-12}, 10^{-20} and 10^{-40} for all calculations and the maximum order of multipolar expansion was set to 6 (program keyword "POLEORDR"). The starting structure for $MgSO_4$ heptahydrate was published by Ferraris, Jones, and Yerkess in 1973[258] and the initial ionic charges were explicitly set to Mg^{2+} and $(SO_4)^{2-}$. In the geometry optimisation, the lattice dimensions and atomic positions were allowed to fully optimise within the $P2_12_12_1$ space group (Schoenflies symbol: D_2^4), and the energy convergence was set to $\Delta E < 10^{-8}\,E_h$. The optimised structure was used to calculate the vibrational frequency analysis and the energy convergence was set to $\Delta E < 10^{-10}\,E_h$. The vibrational frequency analysis determined that the optimised structure was a minimum on the potential energy surface (no negative frequencies). During the frequency analysis, each atom was displaced twice along each Cartesian axis and the numerical derivatives of the Hessian matrix were calculated using the central difference formula. The IR intensities were calculated using the Berry phase method.[269,270]

Crystallisation Measurements

To investigate crystallisation, magnesium sulfate solutions were prepared at various concentrations using commercial $MgSO_4$ heptahydrate 98 % (Sigma-Aldrich, Gillingham, UK). The sample was dissolved in Milli-Q water (IQ 7000, Merck, Darmstadt, Germany, resistivity 18.2 $M\Omega \cdot cm$) in a beaker, which was then left on a magnetic stirrer until the crystals were fully dissolved. After several rounds of preliminary experiments, three concentrations (mass ratio of $MgSO_4$ heptahydrate to water) were chosen for further repeats: 1.41:1, 1.29:1, and 1.20:1, corresponding to a molar ratio of 0.103:1, 0.094:1, and 0.088:1, respectively. This was based on the time and temperature observed for crystallisation.

A detailed description of the crystallisation set up was given in Chapter 6.1. The set up consisted of a liquid cell (thickness 100 µm) that was held by a hollow metal sample holder inside of which water was circulated. The temperature of the circulating water was controlled via an external water bath and its temperature was balanced between an electric heater and a surrounding ice bath with an accuracy of 0.1 °C. The operation temperature was in the range of 4 °C to 90 °C, and during the experiments described here it was operated between 4 °C to 25 °C.

The temperature during measurements was recorded independently at three different positions in the setup. It was not possible to measure the actual temperature inside the liquid between the spacers of the cell due to space constraints but one reading was taken in immediate proximity. The temperature measurement instrument had a resolution of 0.025 °C for the Type K thermocouples used. The thermal mass of the metal block that was attached to the quartz cell and that was used to circulate the water through was much larger than that of the crystallisation cell and any potential temperature difference would therefore be negligible in the context of this experiment.

Air was used as the reference, and the high-resolution mode of the spectrometer was utilised to extend the extent of acquired time-domain waveforms to 45 ps. Each spectrum was formed of the average of 15 individual waveforms with a spectral resolution of 0.94 cm^{-1}, resulting in an acquisition time of 20 s per spectrum. The valid frequency range was from 0.35 THz to 2 THz.

When monitoring the crystallisation process at a set temperature, the cell was first cooled down and kept constant at the target temperature until the system was stable. Afterwards, the $MgSO_4$ solution was injected into the flow cell with a syringe via a tube, and the outlets on both sides of the flow cell were sealed with parafilm. The sample holder including the cell

was promptly placed at the centre of the measurement chamber and terahertz spectra and images were acquired. The time from injecting the solution to the start of the measurement was minimised to no more than 30 s, in case of triggering undesired nucleation. The temperature was kept as constant as possible during the whole crystallisation process, until crystals formed across the cell in the view of the optical probe and the terahertz spectra did not exhibit further changes. The experiment was either terminated at this point, or the behaviour of the system during slow heating to room temperature was studied. In the latter case, the temperature was increased by 0.2 °C min^{-1} up to 25 °C in the flow cell. This was found to be an ideal heating rate to introduce a constant temperature change to the cell.

For all measurements, three thermocouples monitored the temperature at various positions: in the water bath, inside the metal sample holder, and at the inlet of the cell, and one data point was acquired per second. The optical probe used for image acquisition was set to acquire one photograph every two seconds. The time-stamped images of each measurement were further analysed using ImageJ. Edge detection was performed using a Sobel edge detector to highlight intensity changes.[271] The images were then binarised (using the same threshold settings for all images) and the background set to black. Crystalline features were then represented by white pixels which were counted using the "Measure" functionality of ImageJ. The area fraction of white pixels was normalised to 0 (at the beginning of the measurement) and 100 (once crystals had covered the whole cell) and was linked to the time of acquisition and hence terahertz measurements. It was observed that a sigmoid described the process well. After each crystallisation measurement, the liquid cell was thoroughly cleaned to remove grown crystals, contaminations, or seeds which could influence subsequent measurements. The cleaning solution was prepared from commercial EDTA solution (pH = 8; Fisher Scientific, Loughborough, UK) and NaOH solution (Reagecon Diagnostics, Shannon, Ireland) to adjust the pH to 10 in which $MgSO_4$ exhibits a higher solubility.

6.3.3 Results and Discussion

PXRD Analysis of $MgSO_4$ Hydrates

Commercially available samples of anhydrous $MgSO_4$ from two different suppliers and the $MgSO_4 \cdot 7H_2O$ sample were highly crystalline and agreed closely with the patterns simulated from the crystal structure.[256,258]

The $MgSO_4 \cdot H_2O$ sample showed much broader peaks, indicative of smaller particle/domain size. It largely agreed with the pattern simulated from the monohydrate crystal structure,[257] but additional peaks at $2\theta \approx 20°$, 32° and 40° (marked by an asterisk in Figure 6.12a) indicate the presence of an additional minor phase. Comparison to other known $MgSO_4/H_2O$ phases suggests the impurity was most likely to be hexahydrate:[272] its most prominent peak matched that seen at $2\theta \approx 20°$, plus groups of peaks just above 30 ° 2θ and just below 40 ° 2θ could match to the features seen in the monohydrate sample.

All measured and simulated PXRD patterns can be found in Figure 6.12.

Terahertz Spectra of $MgSO_4$ Hydrates

The terahertz spectra of $MgSO_4$ anhydrous, monohydrate, heptahydrate, and the crystal grown in the lab from solution were acquired at different temperatures (Figure 6.13). Comparing the spectra of the three different hydrates, neither the anhydrous nor monohydrate forms of $MgSO_4$ showed pronounced peaks in the region of interest (0.3 THz to 3.0 THz), and the only change that was observed upon cooling was a drop in the baseline.

For the commercial heptahydrate sample, three pronounced bands were observed at 80 K: at 1.2 THz, 1.7 THz (double features), and 2.8 THz. These vibrations probably resulted from the interactions between $MgSO_4$ and water because they were not present in the anhydrous and monohydrate samples. As expected, the spectra exhibited peak broadening and shifting as well as an increase of the baseline upon heating to room temperature. This is due to the significant population of excited vibrational states at room temperature, which is characteristic of the far-infrared where the energy gap between ground state and excited states is on the order of several meV and therefore slightly lower and close to k_bT at room temperature. In addition, the increased thermal vibration and emission contribute to this effect. At 294 K, which was close to the temperature of the crystallisation experiments, the high intensity peak at 2.8 THz diminished into the baseline and the two features at lower frequencies became weaker and broader while the double peak at 1.7 THz merged and shifted to a single feature at 1.6 THz.

The spectra of crystals grown under the conditions similar to the crystallisation in the flow cell exhibited less temperature-dependent behaviour. The feature at 1.2 THz was slightly more intense at low temperatures, while the peak at 1.7 THz was consistently observable in the whole temperature range. The latter shifted to 1.6 THz upon heating to room temperature, though as a single feature rather than a double one at temperatures above 80 K. The high similarity between

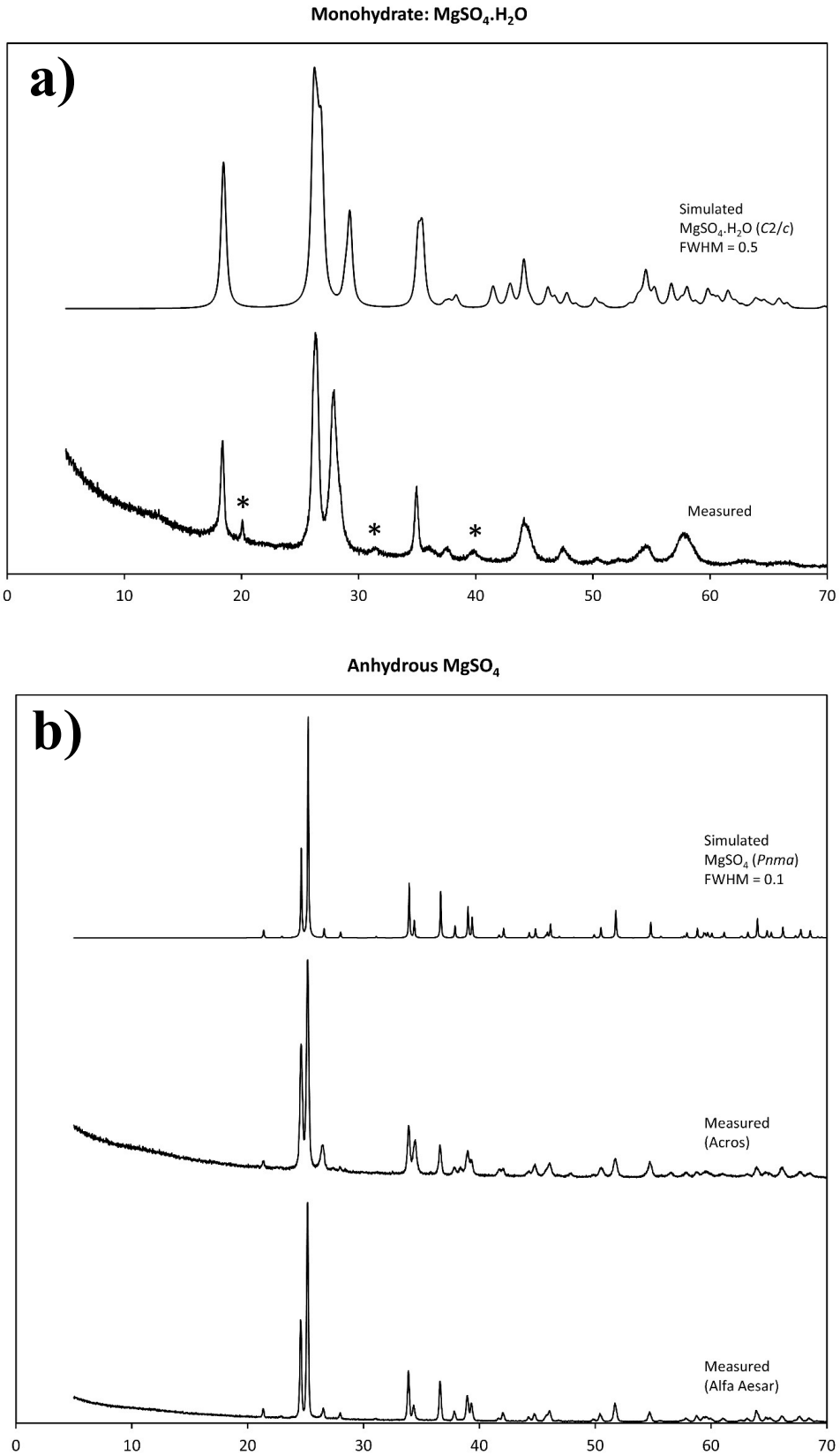

Figure 6.12. PXRD pattern of a) $MgSO_4$ monohydrate, b) anhydrous $MgSO_4$, c) $MgSO_4$ heptahydrate, and d) $MgSO_4$ hexahydrate. Additional peaks in a) are marked with * and indicate the presence of an additional minor phase. a), b), and c) are compared with respective simulated patterns.

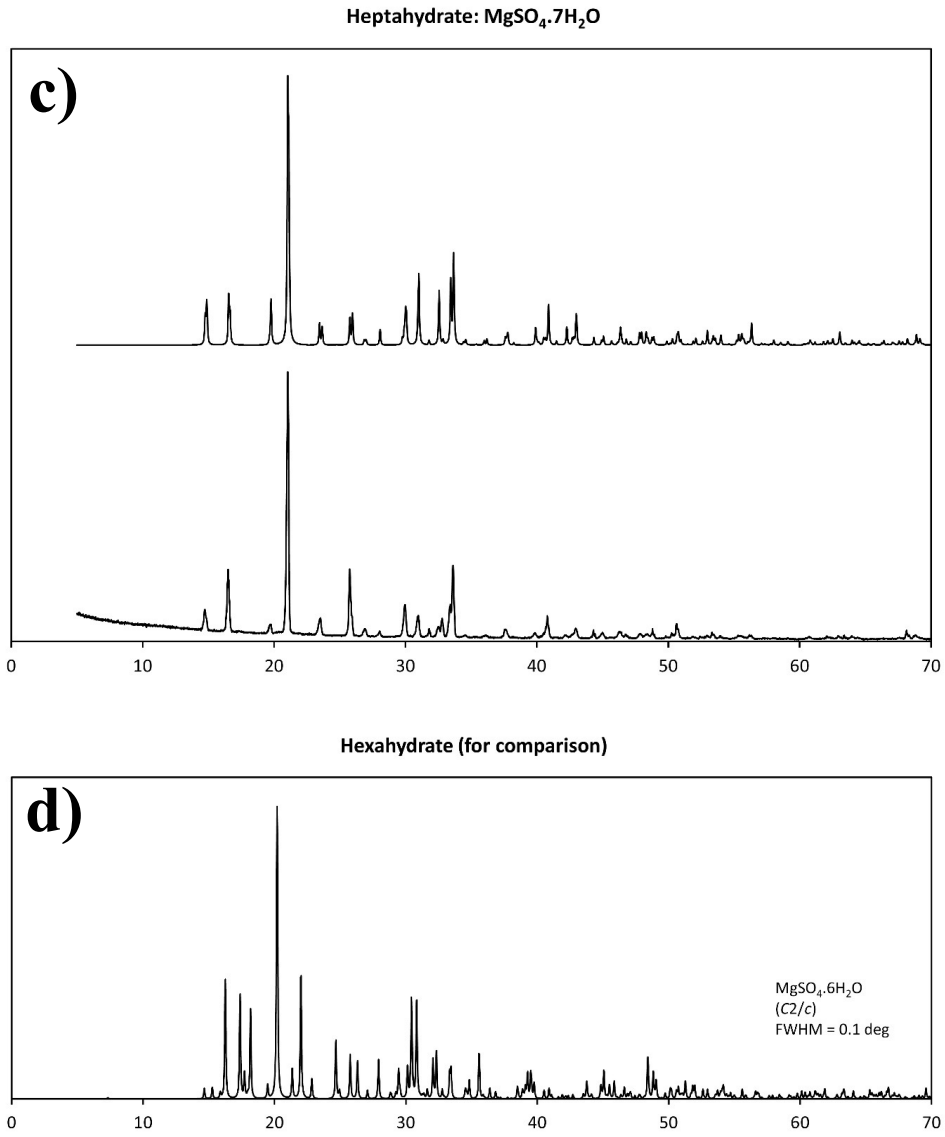

Figure 6.12. PXRD pattern of a) $MgSO_4$ monohydrate, b) anhydrous $MgSO_4$, c) $MgSO_4$ heptahydrate, and d) $MgSO_4$ hexahydrate. Additional peaks in a) are marked with * and indicate the presence of an additional minor phase. a), b), and c) are compared with respective simulated patterns.

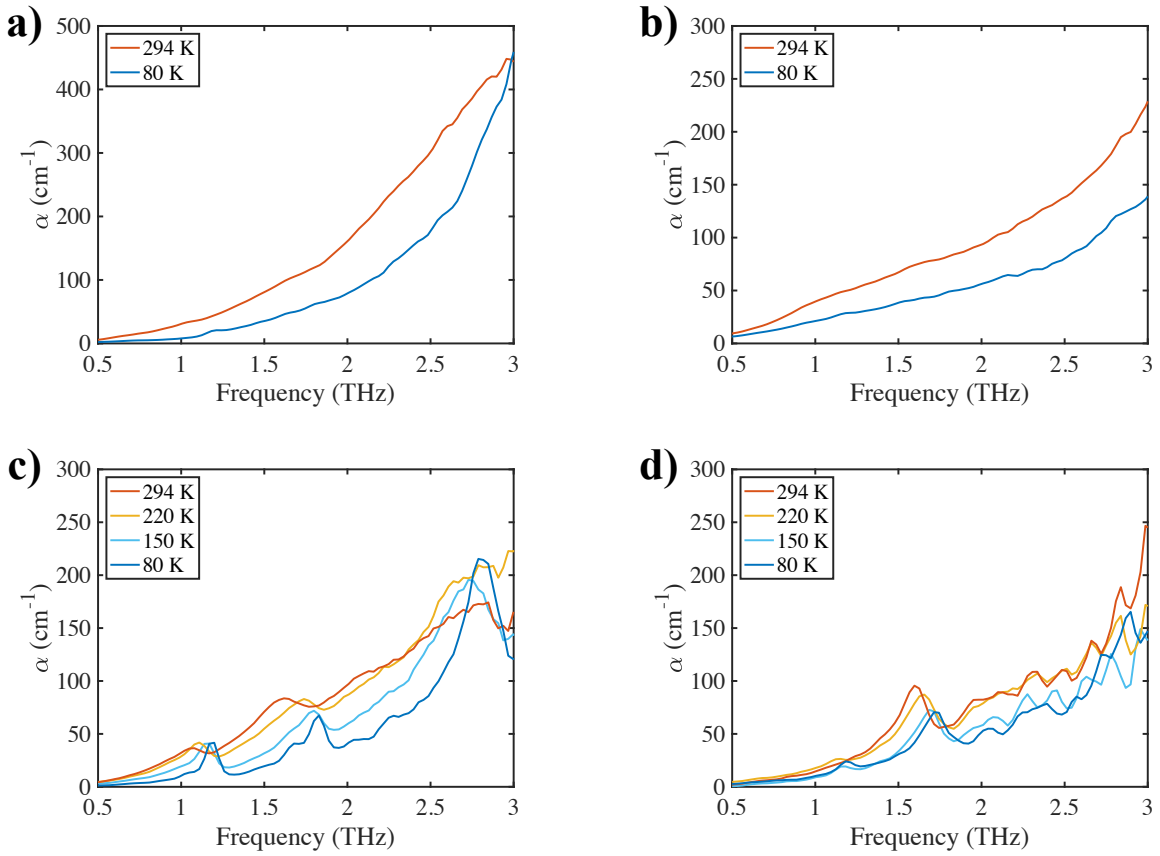

Figure 6.13. Crystalline $MgSO_4$ hydrates measured at different temperatures: (a) Anhydrous $MgSO_4$; (b) $MgSO_4$ monoydrate; (c) commercial $MgSO_4$ heptahydrate; and (d) $MgSO_4$ heptahydrate grown in the lab from solution.

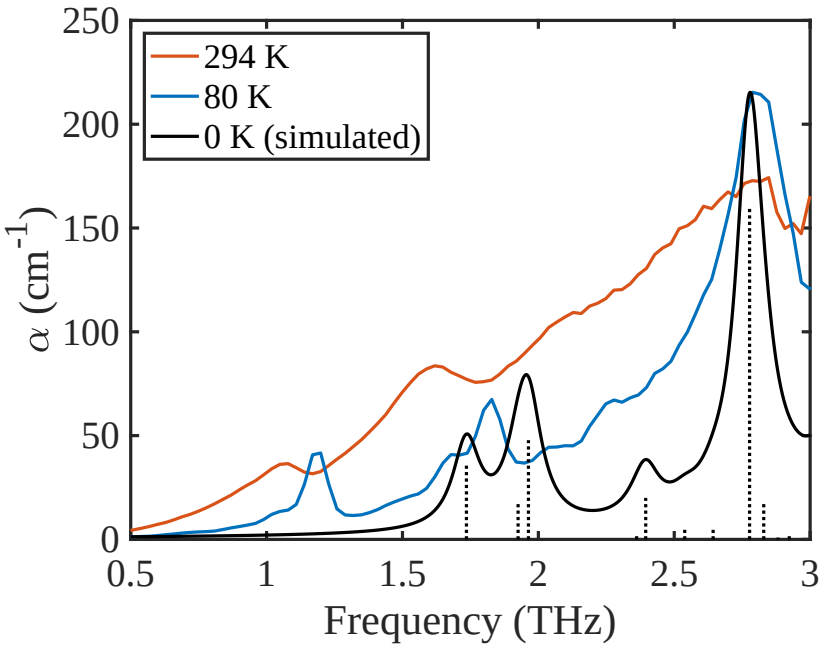

Figure 6.14. Comparison of simulated (black) and measured spectra of $MgSO_4$ heptahydrate. Simulated data have been scaled to the feature at 2.8 THz. Dotted lines denote positions and relative intensities of infrared-active modes.

the terahertz spectra of heptahydrate and grown crystals, especially at 294 K, confirmed that the crystals grown in the crystallisation cell were indeed $MgSO_4$ heptahydrate. The differences between the two could be accounted for by the different purity and defect density. In addition, the 1.1 THz peak became too weak to be observed at room temperature, so the feature at 1.6 THz was used in the following analysis to monitor the crystallisation process.

Within the inherent limitations of the computational methodology[56] the ss-DFT simulation produced a good correlation with the experimental results (see Figure 6.14). The relative shift in the frequencies of the features between calculation and experiment is expected due to the difference in temperature between calculation and the experimental data amongst other factors. No scaling was applied to the frequency of the calculated modes. The calculation revealed that the double features near 1.7 THz originate from three distinct lattice vibrational motions predicted to be at 1.74 THz, 1.93 THz and 1.96 THz. As outlined above, the slight overestimation of the vibrational frequencies is attributable to the simulation being performed at 0 K while the experimental data is acquired at temperatures $\geq$ 80 K. The predicted 1.74 THz vibration (B3 symmetry) involves primarily the rotational motions of the $[Mg(H_2O)_6]^{2+}$ and $(SO_4)^{2-}$ moieties about the *c*-axis of the crystallographic unit cell, with a smaller contribution of translational

motion along the a-axis. The atomic motions associated with the optical phonons observed in this work preserve the centre of mass of the unit cell. This is achieved by the different unit cell components moving in specific phase relationships to one another.The 1.93 THz vibration (B3 symmetry) is a translational vibration of the crystal components along the c-axis. The 1.96 THz mode (B2 symmetry) is largely rotational motion like the 1.74 THz mode but with rotation about the c-axis and some translational motion along the b-axis. The intense experimental peak near 2.8 THz is predicted at 2.78 THz (B3 symmetry) and is a rotational lattice vibration about the a-axis with a small component of translation along the c-axis. Noticeably missing from the simulation is a feature matching with the experimental peak at 1.2 THz, as the 1.74 THz vibration is the lowest frequency vibration (infrared or Raman) produced by ss-DFT. The reason behind this absence is not clear. The use of other basis sets and density functionals did not produce the lower feature, nor did the explicit calculation of transverse optical (TO) and longitudinal optical (LO) phonon splitting. One possible explanation is that the published space group of $P2_12_12_1$ is not an accurate representation of the symmetry of the crystal at reduced temperatures and is instead $P2_1$ (Schoenflies symbol: C_2^2) as suggested by others.[273] A reduction in crystal symmetry may yield new vibrations in the ss-DFT predicted spectra, but such simulations are not trivial given the high computational cost of the much larger asymmetric unit.

Crystallisation of $MgSO_4 \cdot 7H_2O$

As described in the method section, the flow cell was kept constant at the desired temperature for crystallisation, and the process was monitored with both terahertz spectroscopy and an optical probe. Confirmed by visual analysis, crystallisation was usually observed to start at either inlet or outlet (or both) of the crystallisation cell, followed by crystal growth across the cell to its other end. Acquired images were useful complementary information to track the progress of crystal growth throughout the cell. After performing image edge detection and binarisation, crystals were represented by white pixels, and the amount of crystals in the field of view of the camera was quantified as demonstrated in Figure 6.15. In most measurements, it took approximately 4 min to 10 min for crystals to grow from one end of the cell to the other once crystal growth had initiated.

The spot of terahertz radiation probing the centre of the cell was about 2 mm in diameter (as highlighted in Figure 6.15b). Before the crystals had grown into the centre of the cell, the sample volume probed with terahertz radiation was entirely filled with liquid, and the terahertz spectra

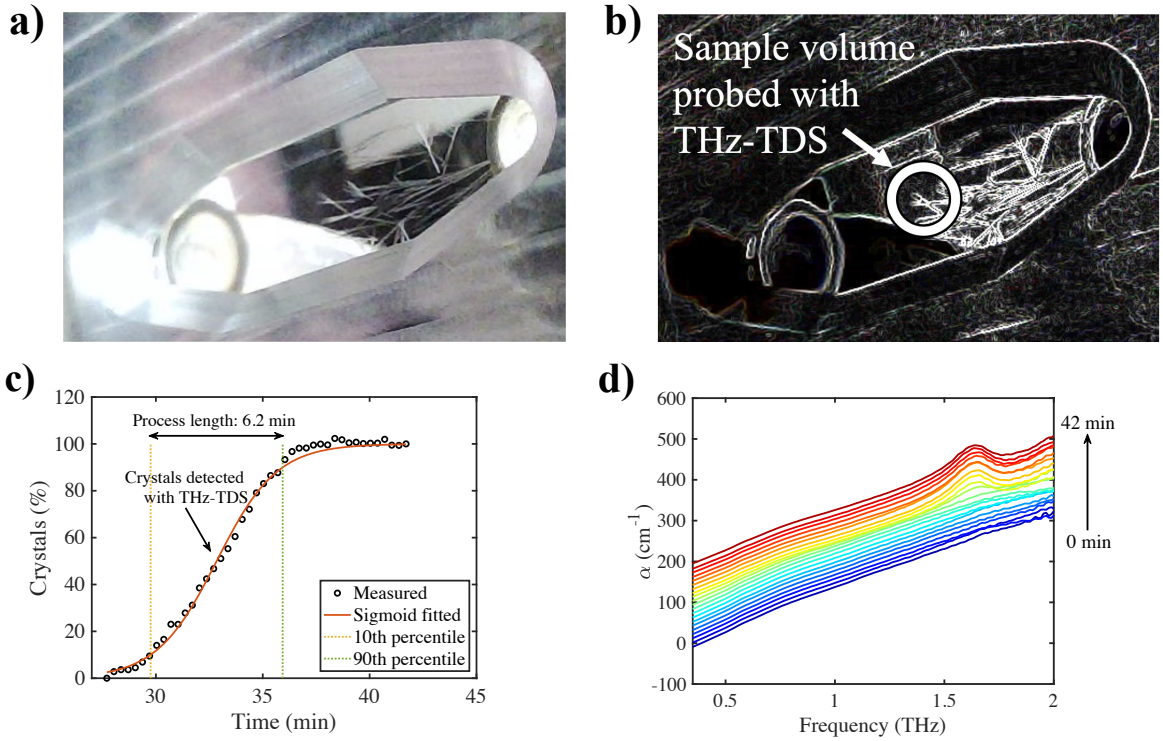

Figure 6.15. Visual analysis of crystal growth. (a) Raw image recorded when the crystals grew into the middle of the cell and were detected by THz-TDS. (b) The same image after edge detection. The approximate sample volume probed with THz-TDS is highlighted. (c) Percentage of area covered by crystals as observed with visual analysis plotted against time. In this case, the crystal growth through the cell occurred in about 6 min at around 4 °C. (d) Terahertz spectra acquired during crystallisation. Each subsequent spectrum is offset by 10 cm^{-1}.

were hence completely featureless. However, as crystal growth continued toward the centre of the cell, the absorption below 1.6 THz decreased and a peak emerged at 1.6 THz. This indicated the existence of crystals in the field of view of the spectrometer (see Figure 6.15d). The peak at 1.6 THz correlated with the peak in the solid state heptahydrate samples measured previously and shown in Figure 6.13. The time by which crystals were detected by THz-TDS coincided well with the time expected from image analysis (also shown in Figure 6.15c).

Three frequencies were chosen to illustrate the changes of the spectrum over the course of the experiment: 1.6 THz, i.e. the peak maximum, 1.0 THz, the frequency where the spectrometer has the highest signal to noise ratio, and 0.5 THz, which was a sufficiently low frequency that it should not directly be influenced by the crystalline spectral feature. At each of those three frequencies, the absorption coefficient was extracted and plotted as a function of time, as illustrated in Figure 6.16.

An algorithm was used to differentiate reliably and reproducibly between three regions (before, during, and after crystal growth) by fitting three linear functions to the data and selecting

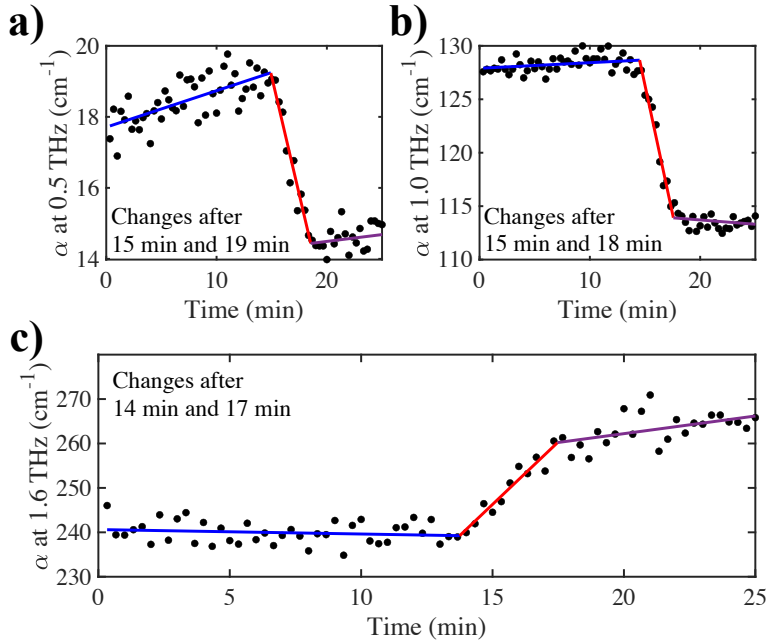

Figure 6.16. Absorption extracted at 0.5, 1, and 1.6 THz. This highlighted the different behaviour of the peak feature compared to the rest of the spectrum (i.e. the differences between crystalline and liquid phases). Whereas the absorption at 1.6 THz increased after 14 min, when crystallisation occurred, the absorption decreased at lower frequencies. Linear fits were performed before (first region, blue), during (second region, red), and after (third region, purple) crystal growth through the field of view.

the fits that minimised the sum of their root mean square error. The code is based on an algorithm previously used to identify glass transition temperatures from THz-TDS data.[101] The fits are in Figure 6.16. This allowed more information to be extracted at each stage of the crystallisation, and facilitated comparison between the subsequent measurements which were performed under a range of conditions. The variation in absorption coefficient between two subsequent points is on the order of 1 cm^{-1} to 2 cm^{-1} at 0.5 THz whereas the observed "step height" was about 5 cm^{-1} at 0.5 THz and larger at higher frequencies. Due to the time scale of the experiment, enough data points were available to perform a linear regression to observe clear trends. The random error in each measured data point was caused by a combination of power fluctuations, waveform averaging, and changes in the sample during the acquisition time (e.g., 20 s).

Crystallisation experiments and the analysis described above were performed for a range of different temperatures and concentrations. A measure for how fast the crystals covered the field of view was found by evaluating the time difference between the emergence of the peak and reaching the equilibrium afterward. This time period was denoted as "second region". The

"first region" corresponded to the time before crystals appeared in the field of view, and the "third region" referred to the last part of the experiment after crystals had fully covered the field of view.

During analysis, the slope of the linear fit to the data points in the second region was evaluated. In most experiments, the gradient of the linear fit was positive for 1.6 THz and negative at lower frequencies.

In Figure 6.17 a range of experiments are presented that systematically explore the important factors during crystallisation, such as temperature and concentration changes. Based on this, the dynamics in both liquid and crystalline phases will be discussed later. During analysis, the slope change in the second region (i.e., during the crystallisation process as measured by the terahertz beam) at different frequencies was extracted, as well as the corresponding time in the region. In general, the larger the gradient was, the faster the crystals grew, and the less time it spent in this stage of the process. In most experiments, the gradient of the linear fit was positive for a frequency of 1.6 THz and negative at lower frequencies, reflecting that, during crystallisation, the absorption at the frequency of the vibrational peak of the crystalline feature increased while that of liquid phase dropped.

Figure 6.17a clearly shows the different behaviour of the absorption for the peak at 1.6 THz compared to other frequencies. While the absorption at 1.6 THz (triangles) increased during crystallisation, it decreased for lower frequencies (dots and diamonds). The spread was higher at higher concentrations, meaning that a faster crystallisation was more likely to result from more supersaturated solutions of $MgSO_4$.

If less time was spent in the second region, i.e. the crystal growth rate was increased, the higher was the absolute gradient in that region at all frequencies. This is shown in Figure 6.17b. For better clarity, the slope during the phase at which the crystals grew into the field of view of the THz-TDS system is shown at only 1 THz, where the signal to noise ratio is largest. The slope in the second region of the data at 1 THz is plotted against the time the crystals took to fully cover the field of view of the spectrometer. The shown slope is negative because the absorption decreased at 1 THz when crystals appeared.

Figure 6.17c shows the relationship between the duration of the middle region with the temperature at which the experiments were performed. While crystal growth through the field of view of the spectrometer seemed to take around 4 min at temperatures between 3.5 °C to 5 °C,

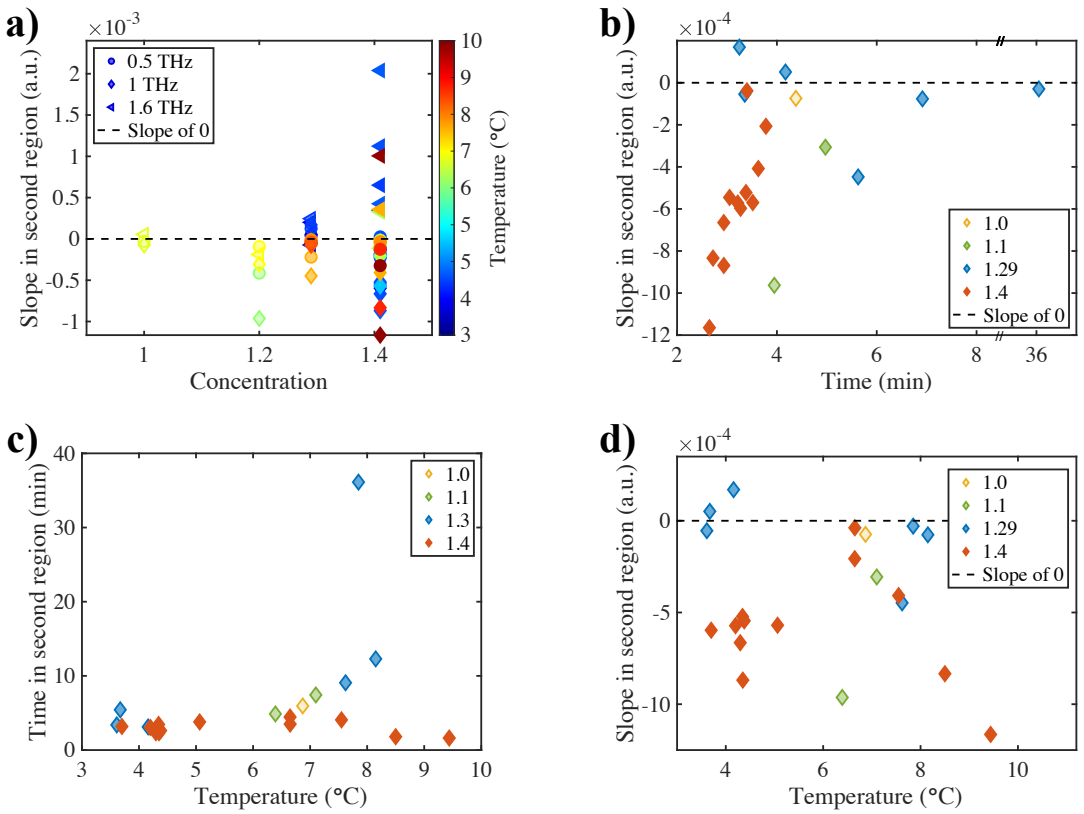

Figure 6.17. Analysis parameters during crystal growth plotted against concentration, time, and temperature. The concentrations were represented by the mass ratio of $MgSO_4$ heptahydrate to water. (a) Slope in the second region plotted against concentration, shown at 0.5 THz (dots), 1.0 THz (diamonds), and 1.6 THz (triangles). The colour denotes the temperature at which the system was kept during crystallisation. (b) Gradient of the linear fit to the absorption at 1.0 THz in the second region plotted against time. The colour denoted the different initial concentrations. (c) Time spent in the second region plotted against temperature. The data was extracted at 1.0 THz and different colours denoted different initial concentrations. (d) Slope in the second region plotted against the temperature at which the experiments were performed, shown at 1.0 THz and different colours denoted different initial concentrations.

the spread was larger at temperatures above 6 °C. In one extreme case it took almost 40 min for the crystals to fully cover the field of view. In most other cases, it took between 2 min to 12 min, independent of concentration. Finally, Figure 6.17d shows how much the absorption at 1.0 THz changed with time at different temperatures and concentrations.

Combining Figure 6.17a and Figure 6.17c it was concluded that, based on the results from our experiments presented here, both a higher initial concentration and elevated temperature above 6 °C made the crystal growth more erratic indicated by a wider spread of the data.

Calibrated Local Concentration and Hydration Shell

Terahertz spectra are inherently temperature dependent. As discussed above, both a decrease in $MgSO_4$ concentration and an increase in temperature yield a higher absorption coefficient.

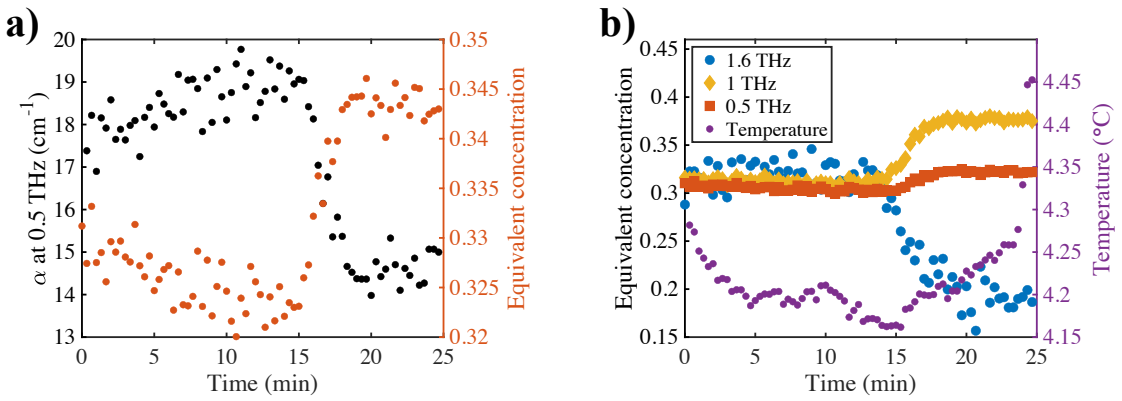

Figure 6.18. Illustration of using the calibration method to calculate liquid phase solute concentration based on measured absorption at various frequencies. (a) Absorption α at 0.5 THz (black) and corresponding calculated liquid phase solute concentration over time (red). (b) Liquid phase solute concentration calculated at 0.5 THz (red squares), 1.0 THz (orange diamonds), and 1.6 THz (blue dots). Right: The temperature throughout the measurement. It was stable and stayed within 0.1 °C of the setpoint until the temperature control was turned off after crystallisation.

Therefore, if the data are corrected for temperature variations, all changes that are observed in the absorption coefficient are directly linked to structural changes of the probed sample volume.

To eliminate temperature effects, a calibration procedure described in Chapter 6.2 was followed. By measuring the absorption of liquid mixtures of varying concentrations at different temperatures, a calibration curve had previously been determined. This allowed the calculation of the concentration of a solution of unknown concentration at arbitrary temperatures. In purely liquid samples, the calibration procedure resulted in the actual concentration for solutions. However, the emergence of crystalline features affected the spectra and in this case, the liquid phase absorption was calculated at frequencies furthest away from the peak of the crystalline feature at 1.6 THz.

An example of converting temperature-dependent data into the temperature-independent equivalent concentration is shown in Figure 6.18. Instead of the slowly rising absorption before crystals reached the field of view that was observed in Figure 6.16, the concentration decreased. This complemented the information gained only by analysing the absorption coefficient and yielded an explanation of the changes in the spectra during crystallisation as follows.

At the beginning of the experiment, both the terahertz spectra and visual analysis confirmed the absence of $MgSO_4$ crystals located in the centre of the cell. Once nucleation occurred, typically not in the centre of the cuvette but near one end of the cell, a local increase in water concentration was observed in the terahertz spectra due to the increase in water concentration

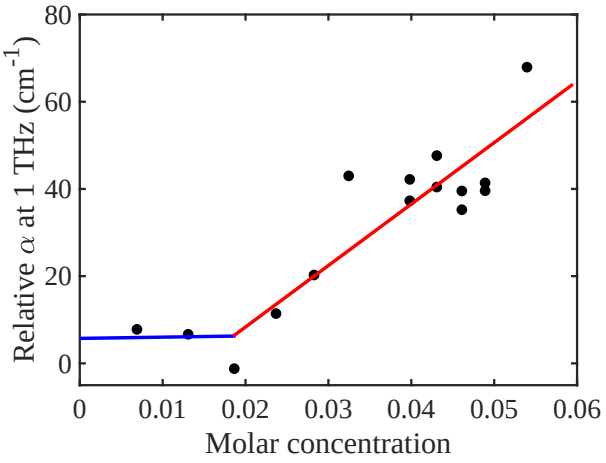

Figure 6.19. Relative absorption calculated and plotted against molar concentration of $MgSO_4$. The experimental error is on the order of $4\,cm^{-1}$ because the absolute absorption coefficient between different measurements and concentrations is compared. Within one measurement, the absolute error is lower (e.g.,$1\,cm^{-1}$ to $2\,cm^{-1}$). The lines are drawn to guide the eye and are not intended to be indicative of a physical model.

immediately adjacent to the growing crystals as magnesium and sulphate ions crystallised into the $MgSO_4$ heptahydrate form. This caused a slight increase of the absorption coefficient, corresponding to a lower $MgSO_4$ concentration measured in the centre of the cell.

$MgSO_4$ in solution is surrounded by a hydration shell whose absorption is markedly different from that of bulk water.[274] This was demonstrated by calculating a theoretical absorption coefficient based on the known absorption coefficient of pure water (α_{water}) and that of anhydrous $MgSO_4$ and that of $MgSO_4{\cdot}7H_2O$ (α_{crystal}), neglecting the effect of a larger hydration shell. A series of $MgSO_4$ aqueous solution with a range of concentrations were measured, and a difference between the measured (α_{solution}) and the calculated ($\alpha_{\text{ideal mixture}}$) absorption was consistently observed.

$$\alpha_{\text{ideal mixture}} = \alpha_{\text{crystal}} \cdot c_{MgSO_4} + \alpha_{\text{water}} \cdot c_{\text{water}} > \alpha_{\text{solution}} \tag{6.3}$$

This difference was calculated with Eqn. 6.3 for a number of measurements and is shown in Figure 6.19 for anhydrous $MgSO_4$, where c_{MgSO_4} represents the molar concentration of anhydrous $MgSO_4$ or $MgSO_4{\cdot}7H_2O$ of the solutions in the corresponding case. Changes were subtle below 0.02 molar concentration and increased steadily above for in both the case of anhydrous $MgSO_4$ and $MgSO_4$ heptahydrate.

The calculated theoretical absorption excluding the effect of the hydration shell was larger than that of the measured absorption, indicating that the hydration shell surrounding $MgSO_4$

had a lower absorption coefficient than the bulk water that it replaced which is in line with expectation as the dipoles in the hydration shell tend to exhibit slower relaxation behaviour.[275–277] The results also inferred that the hydration shell encompassed more than the 7 water molecules that form part of the $MgSO_4$ heptahydrate crystal because of the observed difference between the measured and calculated absorption. This is in line with other observations that also found extended hydration shells when probing samples with THz-TDS.[274]

An increase of the overall absorption coefficient at 0.5 THz and 1.0 THz as seen in experiments when crystals grew hence corresponded to water being expelled from the hydration shells into the bulk phase when the crystals formed. The bulk aqueous phase is pushed toward the field of view sampled by THz-TDS during the growth of the crystals before the crystals themselves enter the field of view of the terahertz beam. Therefore, the growth of $MgSO_4$ heptahydrate, that started at one end of the cell, increased the local concentration of bulk water in the centre of the cell, where it was probed with THz-TDS. This explained the initial slight increase in absorption that was observed at both 0.5 THz and 1.0 THz, given that the absorption coefficient of bulk water is much higher than that of the solution mixed with $MgSO_4$ or the heptahydrate.

Once the crystals reached the centre of the cell, the absorption at 0.5 THz and 1 THz decreased (see Figure 6.16) as the probed sample became more ordered and thereby the VDOS was depleted, while the absorption at 1.6 THz increased as the peak emerged. On the other hand, the liquid phase concentration seemed to increase at 0.5 THz and 1.0 THz when crystals started to grow in the field of view of THz-TDS. This was in line with a decrease of the hydration shell size, and a potentially denser liquid in the area of forming crystals that was probed with THz-TDS.[223] The absorption coefficient at the peak at 1.6 THz clearly increased, and this effect was accompanied by a decrease in $MgSO_4$ concentration. Once the crystals covered the centre of the cell and the system reached an equilibrium state, the changes at all frequencies became subtle again.

However, the calculated liquid phase concentration was not quantitatively valid at frequencies close to crystal features, as no rigorous method has yet been developed within the framework presented[254] to systematically account for peak effects to the baseline, and the calibration curve was determined from the experimental data of a series of samples in the liquid phase only. Others have used a multi features model[278] that could be used in future to explore this further, but in the present work we were not relying on the modelling of peaks and wanted to avoid making

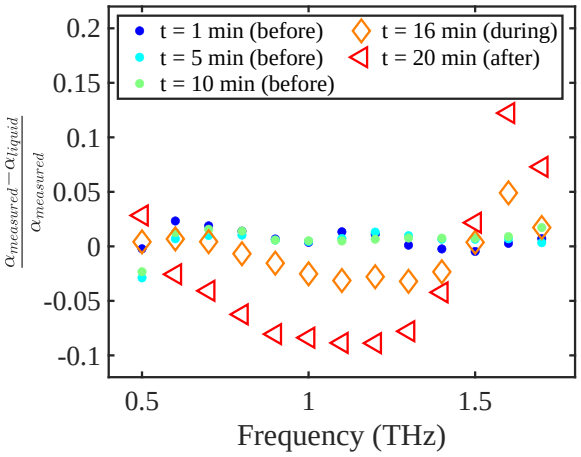

Figure 6.20. Relative changes in α when comparing the measured to the calculated purely liquid absorption before, during, and after crystallisation.

further assumptions.

To examine further the influence of the crystalline feature to the data collected at other frequencies, the previous procedure for calculating concentration was applied inversely, i.e. the known and frequency-independent calculated concentration was used to calculate the equivalent absorption if it was fully liquid (α_{liquid}). Of the three frequencies described here, the data at 0.5 THz were the least affected by the crystalline feature, since that frequency was the furthest away from the feature at 1.6 THz. Therefore, the concentration calculated from it was being used as the basis to calculate α_{liquid}.

The relative difference compared to the measured absorption is plotted in Figure 6.20 for different experimental stages. Before crystals were observed in the field of view, the relative difference was close to zero for all frequencies. During crystal growth into the field of view however, the relative difference increased between 1.5 THz to 1.7 THz, and decreased between 0.6 THz to 1.4 THz. This effect became even stronger once crystallisation was complete. Maxima of the relative difference were found at 1 THz and 1.6 THz while the difference decreased toward lower frequencies. This showed that while the peak only seemed to impact a relatively narrow frequency range between 1.5 THz and 1.7 THz, the effects of crystallisation are still strongly observed at 1.0 THz. The spectral change was directly visible: depletion of the VDOS below 1.5 THz and appearance of a peak above. It should be noted that while current results focus on crystal growth into field of view of the spectrometer, nucleation itself has not yet been observed directly. This will be the focus of future work, possibly by observing very subtle spectral changes.

Dissolution Observed

All the crystallisation experiments were performed and monitored at a constant temperature, and once both visual and spectral analysis confirmed that the crystallisation was completed, the system was slowly heated up. Meanwhile, it was also observed that crystals started to dissolve at elevated temperatures. Therefore, further measurements were carried out to study this phenomenon systematically.

With the well-controlled heating component, an experimental heating rate of $0.2\,^{\circ}\mathrm{C\,min^{-1}}$ was determined to ensure a constant temperature change in the crystallisation cell. Faster heating might have led to a temperature difference between the circulating water and the inside of the cell, while slower heating rates (although possible) prolonged the experiment. With the chosen heating rate, crystal dissolution was observed within a reasonable experimental time frame. However, an accurate dissolution temperature was not measured because hysteresis effects related to kinetics of crystallisation and dissolution have to be taken into account.

The temperature profile over time is shown in Figure 6.21a, and the times when characteristic changes occurred in the spectra are highlighted with vertical lines. These agreed well with the times extracted from the images acquired by the camera. When the temperature was increased steadily once crystals grew completely, crystal dissolution was observed both visually as the percentage of crystals decreased drastically in the cell (Figure 6.21c), as well as with THz-TDS resulting in the disappearance of the crystalline feature at higher temperatures (Figure 6.21b). This was also investigated by utilising the calculation of liquid phase concentrations to remove the temperature effect from the spectra (Figure 6.21d).

The calculated concentration stayed mostly constant once crystals had formed until around 130 min after the beginning of the experiment, which coincided with the first observation of crystal dissolution in the camera images. Because heat was constantly being added to the system by the heat of dissolution of magnesium sulfate and the temperature increased steadily, the equilibrium concentration of $MgSO_4$ in the vicinity of the crystal features varied because the saturation point changed with temperature. Therefore, the crystals dissolved slowly while the surrounding liquid was approaching the point of local saturation upon increasing the temperature. Opposite to crystal growth, dissolution resulted in an enlargement of the hydration shells accompanied by an increase of the absorption at 0.5 THz and 1.0 THz and a decrease at 1.6 THz. The calculated concentration however decreased at 0.5 THz.

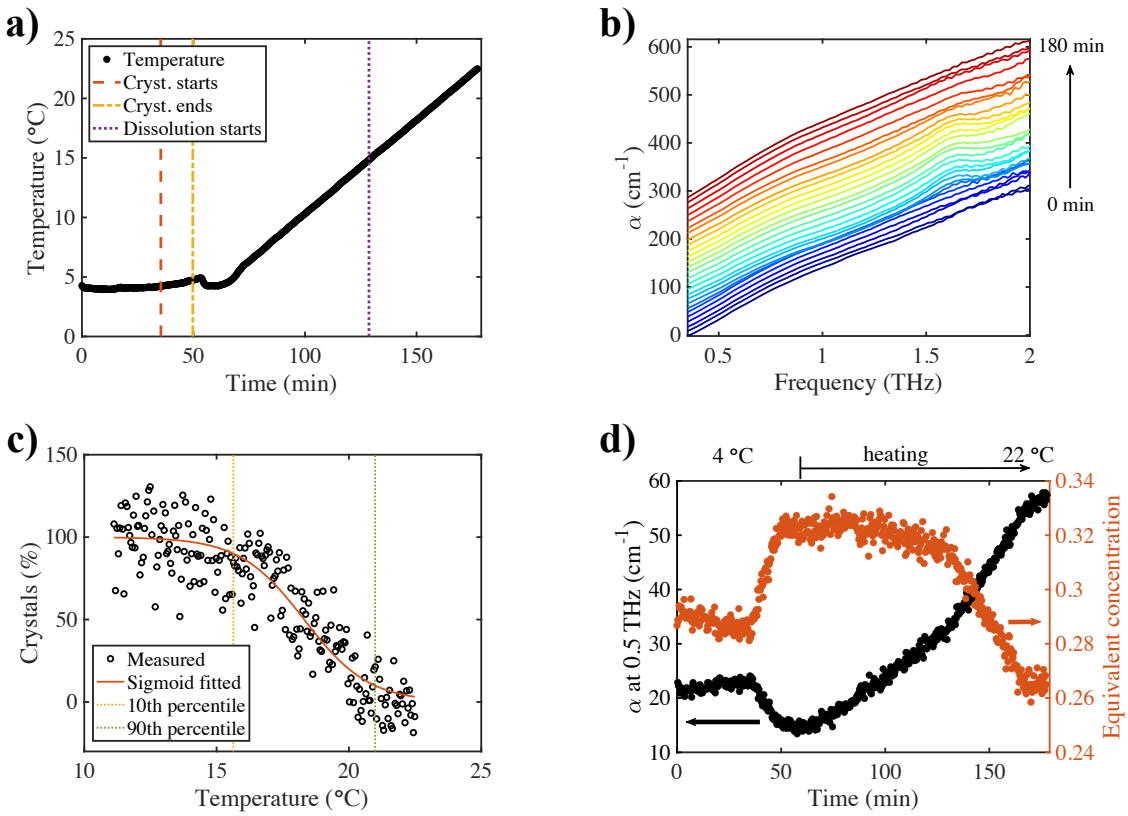

Figure 6.21. Crystal dissolution analysis. (a) Temperature profile during the experiment. Vertical lines denote changes in the spectra. (b) Terahertz spectra acquired throughout the experiment (liquid - semi-crystalline - liquid). Subsequent spectra are offset by $10\,\mathrm{cm}^{-1}$. (c) Dissolution of crystals observed with visual analysis. Dissolving started at a temperature shortly below 16 °C and was completed just above 20 °C. At a heating rate of $0.2\,^{\circ}\mathrm{C\,min}^{-1}$, this process took about 34 min to complete. (d) α at 0.5 THz and corresponding calculated concentration over time. After initial crystallisation, the temperature was steadily increased up to room temperature.

6.3.4 Conclusion

THz-TDS was used to study the crystallisation process of $MgSO_4 \cdot 7H_2O$. The emergence and disappearance of the spectral feature at 1.6 THz indicated the growth or dissolving of crystals in the field of view of the spectrometer (validated by image analysis), while the change of the baseline reflected the behaviour of solvent. This is useful for investigating solvation dynamics and the behaviour of molecular species at phase boundaries.

The absorption at three frequencies was investigated in particular, and the process clearly showed three stages. Experiments at three concentrations and in the temperature range of 4 °C to 9 °C suggested that both a higher initial concentration and elevated temperature above 6 °C were likely to result in a more erratic crystal growth. The faster the crystals grew through the field of view of the spectrometer, the higher was the change in absorption at all frequencies. The temperature effect on terahertz spectra was addressed as outlined previously in Chapter 6.2, leading to the calculation of an equivalent liquid phase concentration. In addition, changes in the absorption coefficient were correlated with the composition and size of the hydration shell surrounding the salt ions.

The results covered here are from experiments where the crystals grew into an area probed by terahertz radiation. Therefore, the onset of nucleation was not observed directly. The focus of future work can be to trigger nucleation at desired locations (e.g. in the centre of the cell) so that the investigation can be extended from that of crystal growth to that of nucleation. The current setup is designed for operating temperatures between 4 °C to 9 °C, and this range can be extended further with simple adjustments. Therefore, this technique can be applied to investigate a wide range of crystalline and semi-crystalline systems, thereby offering an interesting perspective of low-frequency motions of multiphase systems.

7 Conclusion and Future Work

THz-TDS was utilised to study systems with varying levels of disorder, including disordered and supercooled liquids, macromolecules in the solid and solvated state, as well as crystallising solutions. Insights into the effect of anharmonicity and the importance of the local environment in disordered and crystallising materials were gained.

Glycerol-Water System

The behaviour of the model glass-former glycerol and its aqueous mixtures was investigated in the harmonic (below the glass transition temperature T_g), anharmonic (above T_g), and liquid regime. The onset temperature of the molecular mobility as measured by the infrared active dipoles, T_g, was found to correlate with anharmonic effects, leading to an apparent shift of the boson peak and obscuring it at elevated temperatures. The influence of clustered and unclustered water on the dynamics, the boson peak, and the vibrational dynamics was also investigated. A change in structural dynamics was observed at a water concentration of approximately 5 wt % water, corresponding to a transition from isolated water molecules distributed homogeneously throughout the sample to the presence of small water clusters and an increased number of water-water hydrogen bonds which lower the barriers on the PES.

Future work could focus more on establishing a theoretical frame work to relate the density of states measured with different techniques. In particular, the infrared absorption coefficient measured with THz-TDS will be theoretically related to the reduced Raman intensity ($\propto \alpha/\omega^2$) and the reduced density of states ($\propto \alpha/\omega^3$). This will allow to use THz-TDS instead of the more time- and resource-intensive neutron scattering in a range of experiments and aid the interpretation of results immensely. The developed methodology can be applied to other systems of interest.

Additional density measurements of glycerol-water mixtures could give further insights into cluster sizes. The intriguing high-temperature transition found in the mixtures is situated at temperatures close to the melting point of the glue used in the liquid cell which restricted the temperature interval available for the investigation. A change to the experimental setup would allow to acquire data in a broader temperature range and investigate the high-temperature behaviour more closely. The initial measurements investigating hygroscopicity could be extended to also study mixing and diffusion,for example by utilising a humidity-controlled chamber.

Lyophilised Protein Formulations

The temperature-dependent mobility of freeze-dried proteins and antibody-sucrose matrices was measured and linked to anharmonic motions potentially leading to partial unfolding and molecular jamming when high concentrations of macromolecules were present.

Future work can focus on binary mixtures of sucrose with the other macromolecules already investigated, for example HSA. Preliminary measurements have already been prepared and some examples are shown in Figure 7.1. Another interesting topic is the influence of a small amount of water in these systems. At very low concentrations, water could increase a lyophilised protein's stability. Samples with small amounts of water added during lyophilisation have already been prepared and can be measured next. Further work could also be done to explore the exact origin of the decrease/plateau in the absorption coefficient, possibly utilising complementary experimental techniques.

These results have been acquired in the solid state, and can give important insights into terahertz dynamics during storage of biopharmaceuticals. More studies can also focus on how differences observed in the solid state influence reconstitution, which is of importance for the design of pharmaceuticals.

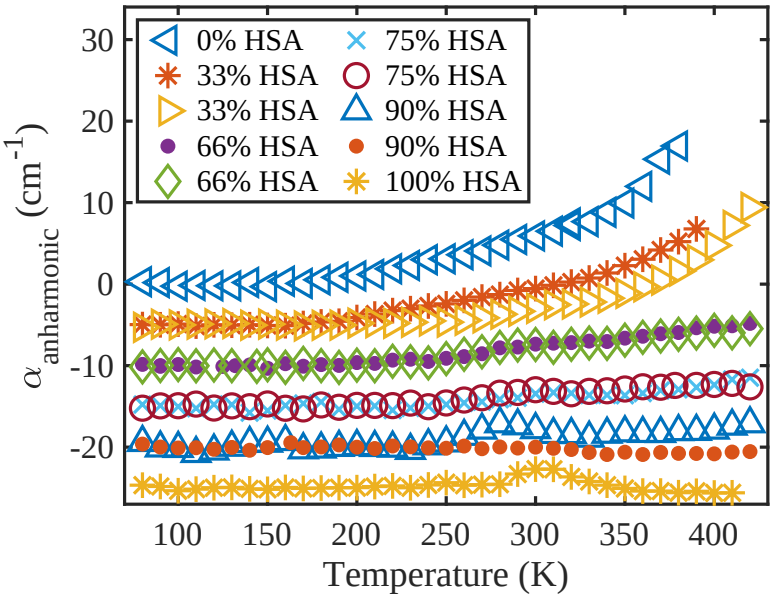

Figure 7.1. Anharmonic absorption coefficient of HSA-sucrose mixtures. Subsequent concentrations are offset by −5 /cm for clarity. Repeats are shown for samples containing 33, 66, 75, and 90 % HSA.

Proteins in Solution

The influence of CsI and NaCl on the mobility of solvated proteins (aSyn, BLG, and BSA) was studied and the interactions were found to be highly protein- and ion-specific. If more protein was available, a higher number of intermediate concentrations and repeats would increase the data quality. aSyn was also investigated with a range of complementary methods that could also be applied to BLG and BSA in order to explain the differences in the measured terahertz response of the samples.

These results are very promising and the setup can be utilised to investigate a wider range of solvated proteins. Further controlling the temperature of the sample cell will enable the study of protein and solvent dynamics under different conditions.

Crystallisation

A novel setup was built that allows to study the terahertz dynamics of stagnant and flowing liquid samples over a wide temperature range. The data analysis procedure could be simplified if a reference measurement of the liquid cell windows became possible without the interference of internal reflections.

The setup was utilised to develop a method to measure local solute concentration in multi-phase systems which was applied to crystallising magnesium sulfate heptahydrate. While the initial calibration is time-consuming, it would be interesting to apply this method to a wider range of systems, for example for studying liquid-liquid phase separations. The setup can further be integrated into a new THz-TDS spectrometer recently acquired by the research group that will allow the beam to pass vertically through a sample. This will aid the study of phase separations in particular, as both the dense and less dense phase can be probed simultaneously.

The emergence and disappearance of a spectral feature corresponding to $MgSO_4 \cdot 7H_2O$ indicated crystal growth and dissolution and simultaneous measurements of local concentrations were linked to the expulsion of water from the hydration shell upon crystal growth.

However, the onset of nucleation in the field of view of the terahertz spectrometer was not yet detected directly. Future work can focus on triggering nucleation at a desired location. One avenue is utilising intense terahertz pulses (for example generated with a tilted-pulse front setup) to induce crystallisation or polymorph changes.

Experimental Setup and Data Analysis

The experimental setup to perform measurements of samples that are liquid at room temperatures has been improved by utilising different liquid cells that entailed differing data analysis procedures. However, one straightforward improvement to the data acquisition during THz-TDS measurements at variable temperatures is to calculate the temperature average during or just before sample acquisition which is then utilised for further analysis instead of the fixed setpoint. This would allow to account for small temperature variations in a reproducible way.

The performance of THz-TDS measurements at variable temperatures can also be further automated by including a remotely controlled valve into the nitrogen feedline to change the nitrogen flow automatically. Preliminary measurements of the flow rate that is needed to keep the temperature well controlled have already been performed and the temperatures at which the flow rate was adjusted were recorded. This is shown in Figure 7.2 and it is apparent that instead of constant regulation, targeted reducing of the flow at certain temperatures (including an appropriate feedback) could succeed in furthering measurement automation.

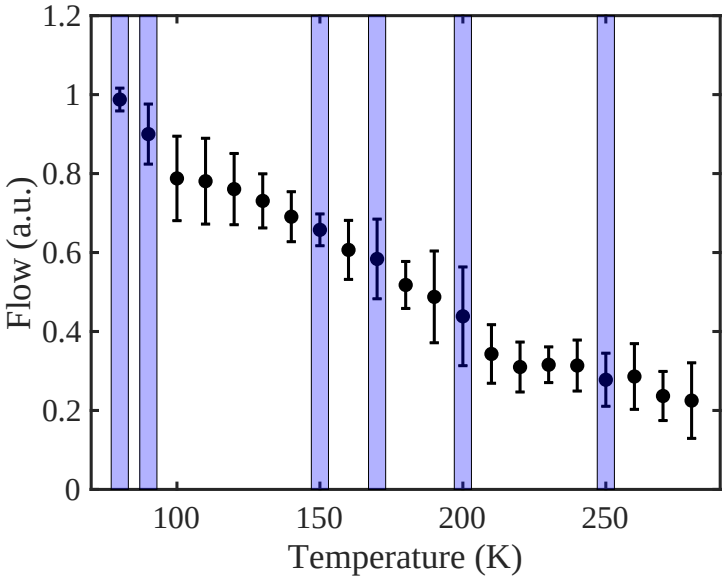

Figure 7.2. Nitrogen flow measured during various measurements. Shaded areas denote the temperatures where the flow was reduced most commonly. Error bars denote the standard error.

8 References

[1] M. Descamps. *Disordered pharmaceutical materials*. John Wiley & Sons, 2016.

[2] S. Elliott. *The physics and chemistry of solids*. Wiley, 1998.

[3] V. Novikov, Y. Ding, and A. Sokolov. Correlation of fragility of supercooled liquids with elastic properties of glasses. *Physical Review E*, 71(6):061501, 2005.

[4] A. Cavagna. Supercooled liquids for pedestrians. *Physics Reports*, 476(4-6):51–124, 2009.

[5] M. S. Thayyil, S. Capaccioli, D. Prevosto, and K. L. Ngai. Is the Johari-Goldstein β-relaxation universal? *Philosophical Magazine*, 88(33-35):4007–4013, 2008.

[6] G. P. Johari. Intrinsic mobility of molecular glasses. *The Journal of Chemical Physics*, 58(4):1766–1770, 1973.

[7] G. Johari. Source of JG-relaxation in the entropy of glass. *The Journal of Physical Chemistry B*, 123(13):3010–3023, 2019.

[8] K. Ngai, M. S. Thayyil, and L.-M. Wang. Quasielastic neutron scattering evidence of coupling of caged molecule dynamics to JG β-relaxation. *Journal of Molecular Liquids*, 247:300–303, 2017.

[9] K. Ngai. Why the fast relaxation in the picosecond to nanosecond time range can sense the glass transition. *Philosophical Magazine*, 84(13-16):1341–1353, 2004.

[10] K. Ngai. Relation between some secondary relaxations and the α-relaxations in glass-forming materials according to the coupling model. *The Journal of Chemical Physics*, 109(16):6982–6994, 1998.

[11] S. Capaccioli, K. Ngai, M. S. Thayyil, and D. Prevosto. Coupling of caged molecule dynamics to JG β-relaxation: I. *The Journal of Physical Chemistry B*, 119(28):8800–8808, 2015.

[12] K. Grzybowska, S. Capaccioli, and M. Paluch. Recent developments in the experimental investigations of relaxations in pharmaceuticals by dielectric techniques at ambient and elevated pressure. *Advanced Drug Delivery Reviews*, 100:158–182, 2016.

[13] E. O. Kissi, H. Grohganz, K. Loebmann, M. T. Ruggiero, J. A. Zeitler, and T. Rades. Glass-transition temperature of the β-relaxation as the major predictive parameter for recrystallization of neat amorphous drugs. *The Journal of Physical Chemistry B*, 122(10):2803–2808, 2018.

[14] S. Vyazovkin and I. Dranca. Probing β-relaxation in pharmaceutically relevant glasses by using DSC. *Pharmaceutical Research*, 23(2):422–428, 2006.

[15] J. Sibik and J. A. Zeitler. Direct measurement of molecular mobility and crystallisation of amorphous pharmaceuticals using terahertz spectroscopy. *Advanced Drug Delivery Reviews*, 100:147–157, 2016.

[16] M. T. Ruggiero, M. Krynski, E. O. Kissi, J. Sibik, D. Markl, N. Y. Tan, D. Arslanov, W. Van Der Zande, B. Redlich, T. M. Korter, et al. The significance of the amorphous potential energy landscape for dictating

glassy dynamics and driving solid-state crystallisation. *Physical Chemistry Chemical Physics*, 19(44):30039–30047, 2017.

[17] G. Adam and J. H. Gibbs. On the temperature dependence of cooperative relaxation properties in glass-forming liquids. *The Journal of Chemical Physics*, 43(1):139–146, 1965.

[18] J. Cavaille, J. Perez, and G. Johari. Molecular theory for the rheology of glasses and polymers. *Physical Review B*, 39(4):2411, 1989.

[19] M. Goldstein. Viscous liquids and the glass transition: a potential energy barrier picture. *The Journal of Chemical Physics*, 51(9):3728–3739, 1969.

[20] M. Goldstein. Viscous liquids and the glass transition: a potential energy barrier picture. *The Journal of Chemical Physics*, 51(9):3728–3739, 1969.

[21] W. Goetze. *Complex dynamics of glass-forming liquids: A mode-coupling theory*, volume 143. OUP Oxford, 2008.

[22] L. Janssen. Mode-coupling theory of the glass transition: a primer. *arXiv preprint arXiv:1806.01369*, 2018.

[23] J. Sibik, E. Y. Shalaev, and J. A. Zeitler. Glassy dynamics of sorbitol solutions at terahertz frequencies. *Physical Chemistry Chemical Physics*, 15(28):11931–11942, 2013.

[24] J. Wuttke, J. Hernandez, G. Li, G. Coddens, H. Cummins, F. Fujara, W. Petry, and H. Sillescu. Neutron and light scattering study of supercooled glycerol. *Physical Review Letters*, 72(19):3052, 1994.

[25] T. Franosch, W. Goetze, M. Mayr, and A. Singh. Evolution of structural relaxation spectra of glycerol within the gigahertz band. *Physical Review E*, 55(3):3183, 1997.

[26] P. Lunkenheimer, U. Schneider, R. Brand, and A. Loidl. Glassy dynamics. *Contemporary Physics*, 41(1):15–36, 2000.

[27] E. P. Parrott and J. A. Zeitler. Terahertz time-domain and low-frequency Raman spectroscopy of organic materials. *Applied Spectroscopy*, 69(1):1–25, 2015.

[28] W. Demtroeder. *Molecular physics: theoretical principles and experimental methods*. John Wiley & Sons, 2008.

[29] E. B. Wilson, J. C. Decius, and P. C. Cross. *Molecular vibrations: the theory of infrared and Raman vibrational spectra*. Courier Corporation, 1980.

[30] M. T. Ruggiero and J. A. Zeitler. Resolving the origins of crystalline anharmonicity using terahertz time-domain spectroscopy and ab initio simulations. *The Journal of Physical Chemistry B*, 120(45):11733–11739, 2016.

[31] H.-J. Song and T. Nagatsuma. *Handbook of terahertz technologies: devices and applications*. CRC press, 2015.

[32] J. Chamberlain. Where optics meets electronics: recent progress in decreasing the terahertz gap. *Philosophical Transactions of the Royal Society of London. Series A: Mathematical, Physical and Engineering Sciences*, 362(1815):199–213, 2004.

[33] M. Parker. Photonic devices help reach terahertz frequencies. *Nature Electronics*, 4(12):859–859, 2021.

[34] D. H. Auston, K. P. Cheung, and P. R. Smith. Picosecond photoconducting Hertzian dipoles. *Applied physics letters*, 45(3):284–286, 1984.

[35] C. Fattinger and D. Grischkowsky. Point source terahertz optics. *Applied Physics Letters*, 53(16):1480–1482, 1988.

[36] P. R. Smith, D. H. Auston, and M. C. Nuss. Subpicosecond photoconducting dipole antennas. *IEEE Journal of Quantum Electronics*, 24(2):255–260, 1988.

[37] J. Neu and C. A. Schmuttenmaer. Tutorial: An introduction to terahertz time domain spectroscopy (THz-TDS). *Journal of Applied Physics*, 124:231101, 2018.

[38] C. A. Schmuttenmaer. Exploring dynamics in the far-infrared with terahertz spectroscopy. *Chemical Reviews*, 104(4):1759–1780, 2004.

[39] Q. Wu, M. Litz, and X.-C. Zhang. Broadband detection capability of ZnTe electro-optic field detectors. *Applied Physics Letters*, 68(21):2924–2926, 1996.

[40] M. T. Ruggiero. *Elucidating the electronic origins of intermolecular forces in crystalline solids*. PhD thesis, Syracuse University, 2016.

[41] Y.-S. Lee, T. Meade, V. Perlin, H. Winful, T. B. Norris, and A. Galvanauskas. Generation of narrow-band terahertz radiation via optical rectification of femtosecond pulses in periodically poled lithium niobate. *Applied Physics Letters*, 76(18):2505–2507, 2000.

[42] A. Rice, Y. Jin, X. Ma, X.-C. Zhang, D. Bliss, J. Larkin, and M. Alexander. Terahertz optical rectification from ¡110¿ zinc-blende crystals. *Applied physics letters*, 64(11):1324–1326, 1994.

[43] Y. Cai, I. Brener, J. Lopata, J. Wynn, L. Pfeiffer, J. Stark, Q. Wu, X. Zhang, and J. Federici. Coherent terahertz radiation detection: Direct comparison between free-space electro-optic sampling and antenna detection. *Applied Physics Letters*, 73(4):444–446, 1998.

[44] H. Tuononen, E. Gornov, J. A. Zeitler, J. Aaltonen, and K. E. Peiponen. Using modified Kramers–Kronig relations to test transmission spectra of porous media in THz-TDS. *Optics Letters*, 35(5):631–633, 2010.

[45] P. Bawuah and J. A. Zeitler. Advances in terahertz time-domain spectroscopy of pharmaceutical solids: A review. *TrAC Trends in Analytical Chemistry*, 139:116272, 2021.

[46] P. Jepsen, D. Cooke, and M. Koch. Terahertz spectroscopy and imaging – Modern techniques and applications. *Laser and Photonics Reviews*, 5:124–166, 2011.

[47] A. Ren, A. Zahid, D. Fan, X. Yang, M. A. Imran, A. Alomainy, and Q. H. Abbasi. State-of-the-art in terahertz sensing for food and water security – a comprehensive review. *Trends in Food Science & Technology*, 85:241–251, 2019.

[48] M. Al-Sharabi, D. Markl, T. Mudley, P. Bawuah, A.-P. Karttunen, C. Ridgway, P. Gane, J. Ketolainen, K.-E. Peiponen, T. Rades, et al. Simultaneous investigation of the liquid transport and swelling performance during tablet disintegration. *International Journal of Pharmaceutics*, 584:119380, 2020.

[49] H. Hirori, M. Nagai, and K. Tanaka. Destructive interference effect on surface plasmon resonance in terahertz attenuated total reflection. *Optics Express*, 13(26):10801–10814, 2005.

[50] S. K. Mathanker, P. R. Weckler, and N. Wang. Terahertz (THz) applications in food and agriculture: A review. *Transactions of the ASABE*, 56(3):1213–1226, 2013.

[51] M. Hangyo, M. Tani, and T. Nagashima. Terahertz time-domain spectroscopy of solids: a review. *International Journal of Infrared and Millimeter Waves*, 26(12):1661–1690, 2005.

[52] J. Sibik, K. Loebmann, T. Rades, and J. A. Zeitler. Predicting crystallization of amorphous drugs with terahertz spectroscopy. *Molecular Pharmaceutics*, 12(8):3062–3068, 2015.

[53] E. M. Paiva, Q. Li, A. J. Zaczek, C. F. Pereira, J. J. R. Rohwedder, and J. A. Zeitler. Understanding the metastability of theophylline FIII by means of low-frequency vibrational spectroscopy. *Molecular Pharmaceutics*, 18(9):3578–3587, 2021.

[54] M. T. Ruggiero and J. A. Zeitler. Resolving the origins of crystalline anharmonicity using terahertz time-domain spectroscopy and ab initio simulations. *The Journal of Physical Chemistry B*, 120(45):11733–11739, 2016.

[55] G. J. O. Beran. Modeling polymorphic molecular crystals with electronic structure theory. *Chemical Reviews*, 116(9):5567–5613, 2016.

[56] M. T. Ruggiero. Invited review: Modern methods for accurately simulating the terahertz spectra of solids. *Journal of Infrared, Millimeter, and Terahertz Waves*, 41(5):491–528, 2020.

[57] A. G. Markelz, J. R. Knab, J. Y. Chen, and Y. He. Protein dynamical transition in terahertz dielectric response. *Chemical Physics Letters*, 442(4-6):413–417, 2007.

[58] P. Carbonniere, A. Erba, F. Richter, R. Dovesi, and M. Rerat. Calculation of anharmonic IR and Raman intensities for periodic systems from DFT calculations: Implementation and validation. *Journal of Chemical Theory and Computation*, 16(5):3343–3351, 2020.

[59] R. Schireman, J. Maul, A. Erba, and M. Ruggiero. Anharmonic coupling of stretching vibrations in ice: A periodic VSCF and VCI description. 2022.

[60] S. J. Dampf and T. M. Korter. Anomalous temperature dependence of the lowest-frequency lattice vibration in crystalline γ-aminobutyric acid. *The Journal of Physical Chemistry A*, 123(10):2058–2064, 2019.

[61] R. Dovesi, V. Saunders, C. Roetti, R. Orlando, C. Zicovich-Wilson, F. Pascale, B. Civalleri, K. Doll, N. Harrison, I. Bush, et al. Crystal17. 2017.

[62] C. J. Strachan, P. F. Taday, D. A. Newnham, K. C. Gordon, J. A. Zeitler, M. Pepper, and T. Rades. Using terahertz pulsed spectroscopy to quantify pharmaceutical polymorphism and crystallinity. *Journal of Pharmaceutical Sciences*, 94(4):837–846, 2005.

[63] S. Taraskin, S. Simdyankin, S. Elliott, J. Neilson, and T. Lo. Universal features of terahertz absorption in disordered materials. *Physical Review Letters*, 97(5):055504, 2006.

[64] D. V. Nickel, M. T. Ruggiero, T. M. Korter, and D. M. Mittleman. Terahertz disorder-localized rotational modes and lattice vibrational modes in the orientationally-disordered and ordered phases of camphor. *Physical Chemistry Chemical Physics*, 17(10):6734–6740, 2015.

[65] M. T. Ruggiero, J. Sibik, and J. A. Zeitler. The influence of intermolecular forces on the terahertz response of amorphous materials. In *2016 41st International Conference on Infrared, Millimeter, and Terahertz Waves (IRMMW-THz)*, pages 1–2. IEEE, 2016.

[66] W. Schirmacher, G. Diezemann, and C. Ganter. Harmonic vibrational excitations in disordered solids and the "boson peak". *Physical Review Letters*, 81(1):136, 1998.

[67] A. Marruzzo, S. Koehler, A. Fratalocchi, G. Ruocco, and W. Schirmacher. Vibrational anomalies and marginal stability of glasses. *The European Physical Journal Special Topics*, 216(1):83–93, 2013.

[68] A. Chumakov, I. Sergueev, U. Van Buerck, W. Schirmacher, T. Asthalter, R. Rueffer, O. Leupold, and W. Petry. Collective nature of the boson peak and universal transboson dynamics of glasses. *Physical Review Letters*, 92(24):245508, 2004.

[69] W. Schirmacher, T. Scopigno, and G. Ruocco. Theory of vibrational anomalies in glasses. *Journal of Non-Crystalline Solids*, 407:133–140, 2015.

[70] J. Wuttke, W. Petry, G. Coddens, and F. Fujara. Fast dynamics of glass-forming glycerol. *Physical Review E*, 52(4):4026, 1995.

[71] W. Schirmacher, G. Ruocco, and V. Mazzone. Heterogeneous viscoelasticity: A combined theory of dynamic and elastic heterogeneity. *Physical Review Letters*, 115(1):015901, 2015.

[72] W. Schirmacher, G. Ruocco, and V. Mazzone. Theory of heterogeneous viscoelasticity. *Philosophical Magazine*, 96(7-9):620–635, 2016.

[73] J. Sibik, E. Y. Shalaev, and J. A. Zeitler. Glassy dynamics of sorbitol solutions at terahertz frequencies. *Physical Chemistry Chemical Physics*, 15(28):11931–11942, 2013.

[74] S. Wietzke, C. Jansen, T. Jung, M. Reuter, B. Baudrit, M. Bastian, S. Chatterjee, and M. Koch. Terahertz time-domain spectroscopy as a tool to monitor the glass transition in polymers. *Optics Express*, 17(21):19006–19014, 2009.

[75] M. Walther, B. Fischer, M. Schall, H. Helm, and P. U. Jepsen. Far-infrared vibrational spectra of all-trans, 9-cis and 13-cis retinal measured by THz time-domain spectroscopy. *Chemical Physics Letters*, 332(3-4):389–395, 2000.

[76] S. Kojima, H. Kitahara, S. Nishizawa, Y. Yang, and M. W. Takeda. Terahertz time-domain spectroscopy of low-energy excitations in glasses. *Journal of Molecular Structure*, 744:243–246, 2005.

[77] J. Barthel, K. Bachhuber, R. Buchner, and H. Hetzenauer. Dielectric spectra of some common solvents in the microwave region. Water and lower alcohols. *Chemical Physics Letters*, 165(4):369–373, 1990.

[78] J. Barthel and R. Buchner. High frequency permittivity and its use in the investigation of solution properties. *Pure and Applied Chemistry*, 63(10):1473–1482, 1991.

[79] F. N. Keutsch and R. J. Saykally. Water clusters: Untangling the mysteries of the liquid, one molecule at a time. *Proceedings of the National Academy of Sciences*, 98(19):10533–10540, 2001.

[80] H. Yada, M. Nagai, and K. Tanaka. Origin of the fast relaxation component of water and heavy water revealed by terahertz time-domain attenuated total reflection spectroscopy. *Chemical Physics Letters*, 464(4-6):166–170, 2008.

[81] J. Kindt and C. Schmuttenmaer. Far-infrared dielectric properties of polar liquids probed by femtosecond terahertz pulse spectroscopy. *The Journal of Physical Chemistry*, 100(24):10373–10379, 1996.

[82] U. Moeller, D. G. Cooke, K. Tanaka, and P. U. Jepsen. Terahertz reflection spectroscopy of Debye relaxation in polar liquids. *JOSA B*, 26(9):A113–A125, 2009.

[83] P. U. Jepsen, U. Møller, and H. Merbold. Investigation of aqueous alcohol and sugar solutions with reflection terahertz time-domain spectroscopy. *Optics Express*, 15(22):14717–14737, 2007.

[84] M. Asaki, A. Redondo, T. Zawodzinski, and A. Taylor. Dielectric relaxation and underlying dynamics of acetonitrile and 1-ethyl-3-methylimidazolium triflate mixtures using THz transmission spectroscopy. *The Journal of Chemical Physics*, 116(23):10377–10385, 2002.

[85] M. Koeberg, C.-C. Wu, D. Kim, and M. Bonn. THz dielectric relaxation of ionic liquid: water mixtures. *Chemical Physics Letters*, 439(1-3):60–64, 2007.

[86] K. Tielrooij, R. Timmer, H. Bakker, and M. Bonn. Structure dynamics of the proton in liquid water probed with terahertz time-domain spectroscopy. *Physical Review Letters*, 102(19):198303, 2009.

[87] D. Venables and C. Schmuttenmaer. Far-infrared spectra and associated dynamics in acetonitrile–water mixtures measured with femtosecond THz pulse spectroscopy. *The Journal of Chemical Physics*, 108(12):4935–4944, 1998.

[88] D. S. Venables and C. A. Schmuttenmaer. Spectroscopy and dynamics of mixtures of water with acetone, acetonitrile, and methanol. *The Journal of Chemical Physics*, 113(24):11222–11236, 2000.

[89] P. Dutta and K. Tominaga. Dependence of low frequency spectra on solute and solvent in solutions studied by terahertz time-domain spectroscopy. *Molecular Physics*, 107(18):1845–1854, 2009.

[90] P. Dutta and K. Tominaga. Obtaining low-frequency spectra of acetone dissolved in cyclohexane by terahertz time-domain spectroscopy. *The Journal of Physical Chemistry A*, 113(29):8235–8242, 2009.

[91] P. Dutta and K. Tominaga. Terahertz time-domain spectroscopic study of the low-frequency spectra of nitrobenzene in alkanes. *Journal of Molecular Liquids*, 147(1-2):45–51, 2009.

[92] Y. Yomogida, Y. Sato, R. Nozaki, T. Mishina, and J. Nakahara. Comparative dielectric study of monohydric alcohols with terahertz time-domain spectroscopy. *Journal of Molecular Structure*, 981(1-3):173–178, 2010.

[93] Y. Yomogida, Y. Sato, R. Nozaki, T. Mishina, and J. Nakahara. Comparative study of boson peak in normal and secondary alcohols with terahertz time-domain spectroscopy. *Physica B: Condensed Matter*, 405(9):2208–2212, 2010.

[94] Y. Yomogida, Y. Sato, K. Yamakawa, R. Nozaki, T. Mishina, and J. Nakahara. Comparative dielectric study of pentanol isomers with terahertz time-domain spectroscopy. *Journal of Molecular Structure*, 970(1-3):171–176, 2010.

[95] J. Sibik, S. R. Elliott, and J. A. Zeitler. Thermal decoupling of molecular-relaxation processes from the vibrational density of states at terahertz frequencies in supercooled hydrogen-bonded liquids. *The Journal of Physical Chemistry Letters*, 5(11):1968–1972, 2014.

[96] A. Alegria and J. Colmenero. Dielectric relaxation of polymers: segmental dynamics under structural constraints. *Soft Matter*, 12(37):7709–7725, 2016.

[97] S. Murthy and M. Shahin. A note on 'sub-Tg relaxation processes in poly (cyclohexylmethacrylate)'. *European Polymer Journal*, 42(3):715–720, 2006.

[98] T. G. Fox Jr and P. J. Flory. Second-order transition temperatures and related properties of polystyrene. I. Influence of molecular weight. *Journal of Applied Physics*, 21(6):581–591, 1950.

[99] R. P. White and J. E. Lipson. Polymer free volume and its connection to the glass transition. *Macromolecules*, 49(11):3987–4007, 2016.

[100] L. Zhang, J. A. Marsiglio, T. Lan, and J. M. Torkelson. Dramatic tunability of the glass transition temperature and fragility of low molecular weight polystyrene by initiator fragments located at chain ends. *Macromolecules*, 49(6):2387–2398, 2016.

[101] T. A. Shmool and J. A. Zeitler. Insights into the structural dynamics of poly lactic-co-glycolic acid at terahertz frequencies. *Polymer Chemistry*, 10(3):351–361, 2019.

[102] T. A. Shmool, P. J. Hooper, G. S. Kaminski Schierle, C. F. van der Walle, and J. A. Zeitler. Terahertz spectroscopy: an investigation of the structural dynamics of freeze-dried poly lactic-co-glycolic acid microspheres. *Pharmaceutics*, 11(6):291, 2019.

[103] T. Shmool, M. Batens, J. Massant, G. Van den Mooter, and J. Axel Zeitler. Tracking solid state dynamics in spray-dried protein powders at infrared and terahertz frequencies. 2019.

[104] T. A. Shmool, P. Woodhams, M. Leutzsch, A. D. Stephens, M. U. Gaimann, M. D. Mantle, G. S. K. Schierle, C. F. van der Walle, and J. A. Zeitler. Observation of high-temperature macromolecular confinement in lyophilised protein formulations using terahertz spectroscopy. *International Journal of Pharmaceutics: X*, 1:100022, 2019.

[105] T. Shmool. Structural dynamics of amorphous solid-state macromolecular materials at terahertz frequencies, 2020.

[106] M. Batens, T. A. Shmool, J. Massant, J. A. Zeitler, and G. Van den Mooter. Advancing predictions of protein stability in the solid state. *Physical Chemistry Chemical Physics*, 22(30):17247–17254, 2020.

[107] M. T. Cicerone, M. J. Pikal, and K. K. Qian. Stabilization of proteins in solid form. *Advanced Drug Delivery Reviews*, 93:14–24, 2015.

[108] M. Mizuno and M. J. Pikal. Is the pre-Tg DSC endotherm observed with solid state proteins associated with the protein internal dynamics? Investigation of bovine serum albumin by solid state hydrogen/deuterium exchange. *European Journal of Pharmaceutics and Biopharmaceutics*, 85(2):170–176, 2013.

[109] S. Khodadadi and A. P. Sokolov. Atomistic details of protein dynamics and the role of hydration water. *Biochimica et Biophysica Acta (BBA)-General Subjects*, 1861(1):3546–3552, 2017.

[110] Y. He, P. I. Ku, J. Knab, J. Chen, and A. Markelz. Protein dynamical transition does not require protein structure. *Physical Review Letters*, 101(17):178103, 2008.

[111] W. Doster. The protein-solvent glass transition. *Biochimica et Biophysica Acta (BBA)-Proteins and Proteomics*, 1804(1):3–14, 2010.

[112] J. Roh, R. Briber, A. Damjanovic, D. Thirumalai, S. Woodson, and A. Sokolov. Dynamics of tRNA at different levels of hydration. *Biophysical Journal*, 96(7):2755–2762, 2009.

[113] J. Roh, J. Curtis, S. Azzam, V. Novikov, I. Peral, Z. Chowdhuri, R. Gregory, and A. Sokolov. Influence of hydration on the dynamics of lysozyme. *Biophysical Journal*, 91(7):2573–2588, 2006.

[114] F. Fujara, W. Petry, R. Diehl, W. Schnauss, and H. Sillescu. Localized motion in supercooled glycerol as measured by 2H-NMR spin-lattice relaxation and incoherent neutron scattering. *EPL (Europhysics Letters)*, 14(6):563, 1991.

[115] E. Cornicchi, S. Cinelli, F. Natali, G. Onori, and A. Paciaroni. Elastic neutron scattering study of proton dynamics in glycerol. *Physica B: Condensed Matter*, 350(1-3):E951–E954, 2004.

[116] K. Niss, C. Dalle-Ferrier, B. Frick, D. Russo, J. Dyre, and C. Alba-Simionesco. Connection between slow and fast dynamics of molecular liquids around the glass transition. *Physical Review E*, 82(2):021508, 2010.

[117] U. Buchenau, R. Zorn, and M. Ramos. Probing cooperative liquid dynamics with the mean square displacement. *Physical Review E*, 90(4):042312, 2014.

[118] F. Lipps, S. Levy, and A. Markelz. Hydration and temperature interdependence of protein picosecond dynamics. *Physical Chemistry Chemical Physics*, 14(18):6375–6381, 2012.

[119] M. Katava, G. Stirnemann, M. Zanatta, S. Capaccioli, M. Pachetti, K. Ngai, F. Sterpone, and A. Paciaroni. Critical structural fluctuations of proteins upon thermal unfolding challenge the Lindemann criterion. *Proceedings of the National Academy of Sciences*, 114(35):9361–9366, 2017.

[120] D. Laage, T. Elsaesser, and J. T. Hynes. Perspective: Structure and ultrafast dynamics of biomolecular hydration shells. *Structural Dynamics*, 4(4):044018, 2017.

[121] V. Conti Nibali and M. Havenith. New insights into the role of water in biological function: Studying solvated biomolecules using terahertz absorption spectroscopy in conjunction with molecular dynamics simulations. *Journal of the American Chemical Society*, 136(37):12800–12807, 2014.

[122] M. Heyden and D. J. Tobias. Spatial dependence of protein-water collective hydrogen-bond dynamics. *Physical Review Letters*, 111(21):218101, 2013.

[123] P. Schienbein, G. Schwaab, H. Forbert, M. Havenith, and D. Marx. Correlations in the solute–solvent dynamics reach beyond the first hydration shell of ions. *The Journal of Physical Chemistry Letters*, 8(11):2373–2380, 2017.

[124] D. Russo, J. Teixeira, and J. Ollivier. The impact of hydration water on the dynamics of side chains of hydrophobic peptides: From dry powder to highly concentrated solutions. *The Journal of Chemical Physics*, 130(23):06B614, 2009.

[125] S. Dellerue, A.-J. Petrescu, J. C. Smith, and M.-C. Bellissent-Funel. Radially softening diffusive motions in a globular protein. *Biophysical Journal*, 81(3):1666–1676, 2001.

[126] J. Sibik, M. J. Sargent, M. Franklin, and J. A. Zeitler. Crystallization and phase changes in paracetamol from the amorphous solid to the liquid phase. *Molecular Pharmaceutics*, 11(4):1326–1334, 2014.

[127] J. A. Zeitler, D. A. Newnham, P. F. Taday, T. L. Threlfall, R. W. Lancaster, R. W. Berg, C. J. Strachan, M. Pepper, K. C. Gordon, and T. Rades. Characterization of temperature-induced phase transitions in five polymorphic forms of sulfathiazole by terahertz pulsed spectroscopy and differential scanning calorimetry. *Journal of Pharmaceutical Sciences*, 95:2486–2498, 2006.

[128] J. A. Zeitler, K. Kogermann, J. Rantanen, T. Rades, P. F. Taday, M. Pepper, J. Aaltonen, and C. J. Strachan. Drug hydrate systems and dehydration processes studied by terahertz pulsed spectroscopy. *International Journal of Pharmaceutics*, 334(1-2):78–84, 2007.

[129] H.-B. Liu, Y. Chen, and X.-C. Zhang. Characterization of anhydrous and hydrated pharmaceutical materials with THz time-domain spectroscopy. *Journal of Pharmaceutical Sciences*, 96(4):927–934, 2007.

[130] E. P. Parrott, J. A. Zeitler, T. Friščić, M. Pepper, W. Jones, G. M. Day, and L. F. Gladden. Testing the sensitivity of terahertz spectroscopy to changes in molecular and supramolecular structure: a study of structurally similar cocrystals. *Crystal Growth and Design*, 9(3):1452–1460, 2009.

[131] K. Lien Nguyen, T. Friščić, G. M. Day, L. F. Gladden, and W. Jones. Terahertz time-domain spectroscopy and the quantitative monitoring of mechanochemical cocrystal formation. *Nature Materials*, 6(3):206–209, 2007.

[132] G. Takebe, Y. Kawada, K. Akiyama, H. Takahashi, H. Takamoto, and M. Hiramatsu. Evaluation of drug crystallinity in aqueous suspension using terahertz time-domain attenuated total reflection spectroscopy. *Journal of Pharmaceutical Sciences*, 102(11):4065–4071, 2013.

[133] J. Sibik, K. Loebmann, T. Rades, and J. A. Zeitler. Predicting crystallization of amorphous drugs with terahertz spectroscopy. *Molecular Pharmaceutics*, 12(8):3062–3068, 2015.

[134] J. A. Zeitler, P. F. Taday, M. Pepper, and T. Rades. Relaxation and crystallization of amorphous carbamazepine studied by terahertz pulsed spectroscopy. *Journal of Pharmaceutical Sciences*, 96(10):2703–2709, 2007.

[135] A. I. McIntosh, B. Yang, S. M. Goldup, M. Watkinson, and R. S. Donnan. Crystallization of amorphous lactose at high humidity studied by terahertz time domain spectroscopy. *Chemical Physics Letters*, 558:104–108, 2013.

[136] M. S. Bradley. Lineshapes in ir and raman spectroscopy: A primer. *Spectroscopy*, 30(11):42–+, 2015.

[137] U. Strom, J. Hendrickson, R. Wagner, and P. Taylor. Disorder-induced far infrared absorption in amorphous materials. *Solid State Communications*, 15(11-12):1871–1875, 1974.

[138] L. Duvillaret, F. Garet, and J.-L. Coutaz. A reliable method for extraction of material parameters in terahertz time-domain spectroscopy. *IEEE Journal of Selected Topics in Quantum Electronics*, 2(3):739–746, 1996.

[139] C. Corsaro, E. Fazio, and D. Mallamace. The Stokes-Einstein relation in water/methanol solutions. *The Journal of Chemical Physics*, 150(23):234506, 2019.

[140] B. C. Hancock and G. Zografi. Characteristics and significance of the amorphous state in pharmaceutical systems. *Journal of Pharmaceutical Sciences*, 86(1):1–12, 1997.

[141] M. T. Ruggiero, M. Krynski, E. O. Kissi, J. Sibik, D. Markl, N. Y. Tan, D. Arslanov, W. Van Der Zande, B. Redlich, T. M. Korter, et al. The significance of the amorphous potential energy landscape for dictating glassy dynamics and driving solid-state crystallisation. *Physical Chemistry Chemical Physics*, 19(44):30039–30047, 2017.

[142] J. Wuttke, J. Hernandez, G. Li, G. Coddens, H. Cummins, F. Fujara, W. Petry, and H. Sillescu. Neutron and light scattering study of supercooled glycerol. *Physical Review Letters*, 72(19):3052, 1994.

[143] C. Wang and R. Wright. Raman scattering studies of liquids and glasses. I. Liquid and supercooled liquid glycerol. *The Journal of Chemical Physics*, 55(4):1617–1624, 1971.

[144] C. Wang and R. Wright. Raman scattering studies in liquids and glasses. II. Liquid and supercooled liquid glycerol. *The Journal of Chemical Physics*, 55(7):3300–3307, 1971.

[145] J. L. Dashnau, N. V. Nucci, K. A. Sharp, and J. M. Vanderkooi. Hydrogen bonding and the cryoprotective properties of glycerol/water mixtures. *The Journal of Physical Chemistry B*, 110(27):13670–13677, 2006.

[146] T. Perova, D. Christensen, U. Rasmussen, J. Vij, and O. Nielsen. Far-infrared spectra of highly viscous liquids: glycerol and triacetin (glycerol triacetate). *Vibrational Spectroscopy*, 18(2):149–156, 1998.

[147] S. Murthy. Experimental study of the dynamics of water and the phase behavior of the supercooled aqueous solutions of propylene glycol, glycerol, poly (ethylene glycol) s, and poly (vinylpyrrolidone). *The Journal of Physical Chemistry B*, 104(29):6955–6962, 2000.

[148] J. Huck, G. Noyel, and L. Jorat. Dielectric properties of supercooled glycerol-water solutions. *IEEE Transactions on Electrical Insulation*, 23(4):627–638, 1988.

[149] T. E. Dirama, G. A. Carri, and A. P. Sokolov. Role of hydrogen bonds in the fast dynamics of binary glasses of trehalose and glycerol: A molecular dynamics simulation study. *The Journal of Chemical Physics*, 122(11):114505, 2005.

[150] C. Angell and D. Smith. Test of the entropy basis of the Vogel-Tammann-Fulcher equation. Dielectric relaxation of polyalcohols near Tg. *The Journal of Physical Chemistry*, 86(19):3845–3852, 1982.

[151] J. Sibik and J. A. Zeitler. Terahertz spectroscopy of hydrogen-bonded glass-forming liquids. In *2013 38th International Conference on Infrared, Millimeter, and Terahertz Waves (IRMMW-THz)*, pages 1–3. IEEE, 2013.

[152] R. Busselez, R. Lefort, M. Guendouz, B. Frick, O. Merdrignac-Conanec, and D. Morineau. Molecular dynamics of glycerol and glycerol-trehalose bioprotectant solutions nanoconfined in porous silicon. *The Journal of Chemical Physics*, 130(21):214502, 2009.

[153] U. Schneider, P. Lunkenheimer, R. Brand, and A. Loidl. Dielectric and far-infrared spectroscopy of glycerol. *Journal of Non-Crystalline Solids*, 235:173–179, 1998.

[154] Y. E. Ryabov, Y. Hayashi, A. Gutina, and Y. Feldman. Features of supercooled glycerol dynamics. *Physical Review B*, 67(13):132202, 2003.

[155] S. Capaccioli, K. Ngai, M. S. Thayyil, and D. Prevosto. Coupling of caged molecule dynamics to JG β-relaxation: I. *The Journal of Physical Chemistry B*, 119(28):8800–8808, 2015.

[156] J. M. Sztein, T. Takeo, and N. Nakagata. History of cryobiology, with special emphasis in evolution of mouse sperm cryopreservation. *Cryobiology*, 82:57–63, 2018.

[157] E. Y. Shalaev and G. Zografi. How does residual water affect the solid-state degradation of drugs in the amorphous state? *Journal of Pharmaceutical Sciences*, 85(11):1137–1141, 1996.

[158] T. Starciuc, Y. Guinet, A. Hedoux, and E. Shalaev. Water content thresholds in glycerol/water system: Low-and high-wavenumber Raman spectroscopy study. *Journal of Molecular Liquids*, 321:114678, 2021.

[159] K. Murata and H. Tanaka. Liquid-liquid transition without macroscopic phase separation in a water-glycerol mixture. *Nature Materials*, 11(5):436–443, 2012.

[160] J. Towey and L. Dougan. Structural examination of the impact of glycerol on water structure. *The Journal of Physical Chemistry B*, 116(5):1633–1641, 2012.

[161] J. Towey, A. Soper, and L. Dougan. The structure of glycerol in the liquid state: a neutron diffraction study. *Physical Chemistry Chemical Physics*, 13(20):9397–9406, 2011.

[162] J. Towey, A. Soper, and L. Dougan. Molecular insight into the hydrogen bonding and micro-segregation of a cryoprotectant molecule. *The Journal of Physical Chemistry B*, 116(47):13898–13904, 2012.

[163] T. Uchino and T. Yoko. Low-frequency Raman scattering and the fast relaxation process in glycerol. *Science*, 273(5274):480–483, 1996.

[164] J. Wuttke, W. Petry, and S. Pouget. Structural relaxation in viscous glycerol: Coherent neutron scattering. *The Journal of Chemical Physics*, 105(12):5177–5182, 1996.

[165] S. Ewing, A. Hussain, G. Collins, C. Roberts, and E. Shalaev. Low-temperature mobility of water in sugar glasses: insights from thermally stimulated current study. In *Water stress in biological, chemical, pharmaceutical and food systems*, pages 75–87. Springer, 2015.

[166] Y. Hayashi, A. Puzenko, and Y. Feldman. Slow and fast dynamics in glycerol–water mixtures. *Journal of Non-Crystalline Solids*, 352(42-49):4696–4703, 2006.

[167] S. Sudo, M. Shimomura, N. Shinyashiki, and S. Yagihara. Broadband dielectric study of α–β separation for supercooled glycerol–water mixtures. *Journal of Non-Crystalline Colids*, 307:356–363, 2002.

[168] P. U. Jepsen and B. M. Fischer. Dynamic range in terahertz time-domain transmission and reflection spectroscopy. *Optics Letters*, 30(1):29–31, 2005.

[169] L. B. Lane. Freezing points of glycerol and its aqueous solutions. *Industrial & Engineering Chemistry*, 17(9):924–924, 1925.

[170] C. A. Angell. Entropy and fragility in supercooling liquids. *Journal of Research of the National Institute of Standards and Technology*, 102(2):171, 1997.

[171] M. L. Sheely. Glycerol viscosity tables. *Industrial & Engineering Chemistry*, 24(9):1060–1064, 1932.

[172] J. Kölbel, M. L. Anuschek, I. Seifert, W. Frieß, and J. A. Zeitler. Stability of protein-sugar lyophilizates investigated with terahertz spectroscopy. In *2020 45th International Conference on Infrared, Millimeter, and Terahertz Waves (IRMMW-THz)*, pages 1–1, 2020.

[173] J. Kölbel, M. L. Anuschek, I. Seifert, W. Frieß, and J. A. Zeitler. Conformational jamming of protein molecules in the solid state measured by terahertz dynamics.

[174] X. C. Tang and M. J. Pikal. Design of freeze-drying processes for pharmaceuticals: practical advice. *Pharmaceutical Research*, 21(2):191–200, 2004.

[175] K. Grzybowska, S. Capaccioli, and M. Paluch. Recent developments in the experimental investigations of relaxations in pharmaceuticals by dielectric techniques at ambient and elevated pressure. *Advanced Drug Delivery Reviews*, 100:158–182, 2016.

[176] E. O. Kissi, H. Grohganz, K. Loebmann, M. T. Ruggiero, J. A. Zeitler, and T. Rades. Glass-transition temperature of the β-relaxation as the major predictive parameter for recrystallization of neat amorphous drugs. *The Journal of Physical Chemistry B*, 122(10):2803–2808, 2018.

[177] S. Vyazovkin and I. Dranca. Probing β-relaxation in pharmaceutically relevant glasses by using DSC. *Pharmaceutical Research*, 23(2):422–428, 2006.

[178] J. Allen, T. Sanders, J. Horvat, and R. Lewis. Anharmonicity-driven redshift and broadening of sharp terahertz features of α-glycine single crystal from 20 K to 300 K: Theory and experiment. *Spectrochimica Acta Part A: Molecular and Biomolecular Spectroscopy*, 244:118635, 2021.

[179] L. L. Chang and M. J. Pikal. Mechanisms of protein stabilization in the solid state. *Journal of Pharmaceutical Sciences*, 98(9):2886–2908, 2009.

[180] K. Roe and T. Labuza. Glass transition and crystallization of amorphous trehalose-sucrose mixtures. *International Journal of Food Properties*, 8(3):559–574, 2005.

[181] E. Paci and M. Karplus. Unfolding proteins by external forces and temperature: the importance of topology and energetics. *Proceedings of the National Academy of Sciences*, 97(12):6521–6526, 2000.

[182] D. Verrall, L. Gladden, and S. Elliott. The structure of phosphorus selenide glasses. *Journal of Non-Crystalline Solids*, 106(1-3):47–49, 1988.

[183] M. T. Cicerone, M. J. Pikal, and K. K. Qian. Stabilization of proteins in solid form. *Advanced Drug Delivery Reviews*, 93:14–24, 2015.

[184] T. A. Shmool, P. Woodhams, M. Leutzsch, A. D. Stephens, M. U. Gaimann, M. D. Mantle, G. S. K. Schierle, C. F. van der Walle, and J. A. Zeitler. Observation of high-temperature macromolecular confinement in lyophilised protein formulations using terahertz spectroscopy. *International Journal of Pharmaceutics: X*, 1:100022, 2019.

[185] K. Roe and T. Labuza. Glass transition and crystallization of amorphous trehalose-sucrose mixtures. *International Journal of Food Properties*, 8(3):559–574, 2005.

[186] M. Batens, T. A. Shmool, J. Massant, J. A. Zeitler, and G. Van den Mooter. Advancing predictions of protein stability in the solid state. *Physical Chemistry Chemical Physics*, 22(30):17247–17254, 2020.

[187] A. D. Stephens, J. Kölbel, R. Moons, M. T. Ruggerio, N. Mahmoudi, T. A. Shmool, T. M. McCoy, D. Nietlispach, A. F. Routh, F. Sobott, et al. The role of water mobility in protein misfolding. *bioRxiv*, 2021.

[188] S. J. Roeters, A. Iyer, G. Pletikapić, V. Kogan, V. Subramaniam, and S. Woutersen. Evidence for intramolecular antiparallel beta-sheet structure in alpha-synuclein fibrils from a combination of two-dimensional infrared spectroscopy and atomic force microscopy. *Scientific Reports*, 7(1):1–11, 2017.

[189] C. Galvagnion, A. K. Buell, G. Meisl, T. C. Michaels, M. Vendruscolo, T. P. Knowles, and C. M. Dobson. Lipid vesicles trigger α-synuclein aggregation by stimulating primary nucleation. *Nature Chemical Biology*, 11(3):229–234, 2015.

[190] L. A. Munishkina, A. L. Fink, and V. N. Uversky. Concerted action of metals and macromolecular crowding on the fibrillation of α-synuclein. *Protein and Peptide Letters*, 15(10):1079–1085, 2008.

[191] A. Binolfi, R. M. Rasia, C. W. Bertoncini, M. Ceolin, M. Zweckstetter, C. Griesinger, T. M. Jovin, and C. O. Fernández. Interaction of α-synuclein with divalent metal ions reveals key differences: A link between structure, binding specificity and fibrillation enhancement. *Journal of the American Chemical Society*, 128(30):9893–9901, 2006.

[192] V. N. Uversky, J. Li, and A. L. Fink. Evidence for a partially folded intermediate in α-synuclein fibril formation. *Journal of Biological Chemistry*, 276(14):10737–10744, 2001.

[193] L. Giehm and D. E. Otzen. Strategies to increase the reproducibility of protein fibrillization in plate reader assays. *Analytical Biochemistry*, 400(2):270–281, 2010.

[194] K. Aoki, K. Shiraki, and T. Hattori. Salt effects on the picosecond dynamics of lysozyme hydration water investigated by terahertz time-domain spectroscopy and an insight into the Hofmeister series for protein stability and solubility. *Physical Chemistry Chemical Physics*, 18(22):15060–15069, 2016.

[195] J. N. Dahanayake and K. R. Mitchell-Koch. How does solvation layer mobility affect protein structural dynamics? *Frontiers in Molecular Biosciences*, 5:65, 2018.

[196] P. Lo Nostro and B. W. Ninham. Hofmeister phenomena: an update on ion specificity in biology. *Chemical Reviews*, 112(4):2286–2322, 2012.

[197] W. Kunz. Specific ion effects in colloidal and biological systems. *Current Opinion in Colloid & Interface Science*, 15(1-2):34–39, 2010.

[198] A. K. Buell, C. Galvagnion, R. Gaspar, E. Sparr, M. Vendruscolo, T. P. Knowles, S. Linse, and C. M. Dobson. Solution conditions determine the relative importance of nucleation and growth processes in α-synuclein aggregation. *Proceedings of the National Academy of Sciences*, 111(21):7671–7676, 2014.

[199] S. Qamar, G. Wang, S. J. Randle, F. S. Ruggeri, J. A. Varela, J. Q. Lin, E. C. Phillips, A. Miyashita, D. Williams, F. Stroehl, et al. Fus phase separation is modulated by a molecular chaperone and methylation of arginine cation-π interactions. *Cell*, 173(3):720–734, 2018.

[200] F. Sobott, A. Wattenberg, H.-D. Barth, and B. Brutschy. Ionic clathrates from aqueous solutions detected with laser induced liquid beam ionization/desorption mass spectrometry. *International Journal of Mass Spectrometry*, 185:271–279, 1999.

[201] A. D. Stephens, N. Nespovitaya, M. Zacharopoulou, C. F. Kaminski, J. J. Phillips, and G. S. Kaminski Schierle. Different structural conformers of monomeric α-synuclein identified after lyophilizing and freezing. *Analytical Chemistry*, 90(11):6975–6983, 2018.

[202] L. Stefanis. α-Synuclein in Parkinson's disease. *Cold Spring Harbor perspectives in medicine*, 2(2):a009399, 2012.

[203] Y. Ding, A. A. Hassanali, and M. Parrinello. Anomalous water diffusion in salt solutions. *Proceedings of the National Academy of Sciences*, 111(9):3310–3315, 2014.

[204] M. Taha and M.-J. Lee. Interactions of tris [tris (hydroxymethyl) aminomethane] and related buffers with peptide backbone: thermodynamic characterization. *Physical Chemistry Chemical Physics*, 12(39):12840–12850, 2010.

[205] L. Chen, G. Ren, L. Liu, P. Guo, E. Wang, L. Zhou, Z. Zhu, J. Zhang, B. Yang, W. Zhang, et al. Terahertz signatures of hydrate formation in alkali halide solutions. *The Journal of Physical Chemistry Letters*, 11(17):7146–7152, 2020.

[206] D. A. Schmidt, O. Birer, S. Funkner, B. P. Born, R. Gnanasekaran, G. W. Schwaab, D. M. Leitner, and M. Havenith. Rattling in the cage: Ions as probes of sub-picosecond water network dynamics. *Journal of the American Chemical Society*, 131(51):18512–18517, 2009.

[207] B. Born, H. Weingaertner, E. Bruendermann, and M. Havenith. Solvation dynamics of model peptides probed by terahertz spectroscopy. observation of the onset of collective network motions. *Journal of the American Chemical Society*, 131(10):3752–3755, 2009.

[208] S. Ebbinghaus, S. J. Kim, M. Heyden, X. Yu, U. Heugen, M. Gruebele, D. M. Leitner, and M. Havenith. An extended dynamical hydration shell around proteins. *Proceedings of the National Academy of Sciences*, 104(52):20749–20752, 2007.

[209] X. Li, X. Fu, J. Liu, Y. Du, and Z. Hong. Investigation of thermal denaturation of solid bovine serum albumin by terahertz dielectric spectroscopy. *Journal of Molecular Structure*, 1049:441–445, 2013.

[210] H. Vondracek, J. Dielmann-Gessner, W. Lubitz, M. Knipp, and M. Havenith. THz absorption spectroscopy of solvated β-lactoglobulin. *The Journal of Chemical Physics*, 141(22):12B639_1, 2014.

[211] S. Khodadadi and A. Sokolov. Protein dynamics: from rattling in a cage to structural relaxation. *Soft Matter*, 11(25):4984–4998, 2015.

[212] T. Janc, M. Lukšič, V. Vlachy, B. Rigaud, A.-L. Rollet, J.-P. Korb, G. Mériguet, and N. Malikova. Ion-specificity and surface water dynamics in protein solutions. *Physical Chemistry Chemical Physics*, 20(48):30340–30350, 2018.

[213] W. Hoyer, T. Antony, D. Cherny, G. Heim, T. M. Jovin, and V. Subramaniam. Dependence of α-synuclein aggregate morphology on solution conditions. *Journal of Molecular Biology*, 322(2):383–393, 2002.

[214] D. Li, E. M. Jones, M. R. Sawaya, H. Furukawa, F. Luo, M. Ivanova, S. A. Sievers, W. Wang, O. M. Yaghi, C. Liu, et al. Structure-based design of functional amyloid materials. *Journal of the American Chemical Society*, 136(52):18044–18051, 2014.

[215] L. A. Munishkina, J. Henriques, V. N. Uversky, and A. L. Fink. Role of protein- water interactions and electrostatics in α-synuclein fibril formation. *Biochemistry*, 43(11):3289–3300, 2004.

[216] B. Ahmad, Y. Chen, and L. J. Lapidus. Aggregation of α-synuclein is kinetically controlled by intramolecular diffusion. *Proceedings of the National Academy of Sciences*, 109(7):2336–2341, 2012.

[217] M.-K. Cho, G. Nodet, H.-Y. Kim, M. R. Jensen, P. Bernado, C. O. Fernandez, S. Becker, M. Blackledge, and M. Zweckstetter. Structural characterization of α-synuclein in an aggregation prone state. *Protein Science*, 18(9):1840–1846, 2009.

[218] K. R. Srivastava, K. C. French, F. O. Tzul, G. I. Makhatadze, and L. J. Lapidus. Intramolecular diffusion controls aggregation of the PAPf39 peptide. *Biophysical Chemistry*, 216:37–43, 2016.

[219] Q. Li, J. Kölbel, T. Threlfall, and J. A. Zeitler. Flow cell to study crystallization processes in situ using terahertz time-domain spectroscopy. *IEEE Transactions on Terahertz Science and Technology*, 12(2):193–198, 2021.

[220] J. Kölbel, Q. Li, T. L. Threlfall, and J. A. Zeitler. Measuring solute concentration with terahertz time-domain spectroscopy in single and multiphase systems. *Analytical Chemistry*, 94(3):1713–1716, 2022.

[221] Q. Li, J. Kölbel, M. P. Davis, T. M. Korter, A. D. Bond, T. Threlfall, and J. A. Zeitler. In situ observation of the structure of crystallizing magnesium sulfate heptahydrate solutions with terahertz transmission spectroscopy. *Crystal Growth & Design*, 2022.

[222] J. Hulliger. Chemistry and crystal growth. *Angewandte Chemie International Edition*, 33(2):143–162, 1994.

[223] R. J. Davey, S. L. M. Schroeder, and J. H. ter Horst. Nucleation of organic crystals—a molecular perspective. *Angewandte Chemie International Edition*, 52(8):2166–2179, 2013.

[224] J. Sibik, M. J. Sargent, M. Franklin, and J. A. Zeitler. Crystallization and phase changes in paracetamol from the amorphous solid to the liquid phase. *Molecular Pharmaceutics*, 11(4):1326–1334, 2014.

[225] J. A. Zeitler, D. A. Newnham, P. F. Taday, T. L. Threlfall, R. W. Lancaster, R. W. Berg, C. J. Strachan, M. Pepper, K. C. Gordon, and T. Rades. Characterization of temperature-induced phase transitions in five polymorphic forms of sulfathiazole by terahertz pulsed spectroscopy and differential scanning calorimetry. *Journal of Pharmaceutical Sciences*, 95(11):2486–2498, November 2006.

[226] E. P. Parrott and J. A. Zeitler. Terahertz time-domain and low-frequency Raman spectroscopy of organic materials. *Applied Spectroscopy*, 69:1–25, Jan 2015.

[227] R. Li, C. D'Agostino, J. McGregor, M. D. Mantle, J. A. Zeitler, and L. F. Gladden. Mesoscopic structuring and dynamics of alcohol/water solutions probed by terahertz time-domain spectroscopy and pulsed field gradient nuclear magnetic resonance. *The Journal of Physical Chemistry B*, 118(34):10156–10166, 2014.

[228] R. May and P. F. Taday. Crystallization of sucrose monitored by terahertz pulsed spectroscopy. In *2013 38th International Conference on Infrared, Millimeter, and Terahertz Waves (IRMMW-THz)*, pages 1–1. IEEE, 2013.

[229] A. Soltani, D. Gebauer, L. Duscheck, B. M. Fischer, H. Coelfen, and M. Koch. Crystallization caught in the act with terahertz spectroscopy: Non-classical pathway for l-(+)-tartaric acid. *Chemistry*, 23(57):14128–14132, 2017.

[230] S. Alfihed, J. F. Holzman, and I. G. Foulds. Developments in the integration and application of terahertz spectroscopy with microfluidics. *Biosensors and Bioelectronics*, page 112393, 2020.

[231] M. Nagel, P. Haring Boilvar, M. Brucherseifer, H. Kurz, A. Bosserhoff, and R. Buettner. Integrated THz technology for label-free genetic diagnostics. *Applied Physics Letters*, 80(1):154–156, 2002.

[232] D. T. Vaniman, D. L. Bish, S. J. Chipera, C. I. Fialips, J. William Carey, and W. C. Feldman. Magnesium sulphate salts and the history of water on Mars. *Nature*, 431(7009):663–665, 2004.

[233] T. M. Duncan and J. A. Reimer. *Chemical Engineering Design and Analysis: An Introduction*. Cambridge University Press, Cambridge, 2019.

[234] J. Xu, K. W. Plaxco, and S. J. Allen. Absorption spectra of liquid water and aqueous buffers between 0.3 and 3.72 THz. *The Journal of Chemical Physics*, 124(3):036101, 2006.

[235] R. Li, C. D'Agostino, J. McGregor, M. D. Mantle, J. A. Zeitler, and L. F. Gladden. Mesoscopic structuring and dynamics of alcohol/water solutions probed by terahertz time-domain spectroscopy and pulsed field gradient nuclear magnetic resonance. *The Journal of Physical Chemistry B*, 118(34):10156–10166, 2014.

[236] M. T. Ruggiero, J. Sibik, J. A. Zeitler, and T. M. Korter. Examination of L-glutamic acid polymorphs by solid-state density functional theory and terahertz spectroscopy. *The Journal of Physical Chemistry A*, 120(38):7490–7495, 2016.

[237] C. B. Ojeda and F. S. Rojas. Process analytical chemistry: applications of ultraviolet/visible spectrometry in environmental analysis: an overview. *Applied Spectroscopy Reviews*, 44(3):245–265, 2009.

[238] G. D. Brabson. *Ultraviolet/Visible Absorption Spectroscopy in: ASM Handbook, Volume 10:.: Materials Characterization*. ASM International, 1986.

[239] N. Rodríguez-Hornedo, S. J. Nehm, K. F. Seefeldt, Y. Pagan-Torres, and C. J. Falkiewicz. Reaction crystallization of pharmaceutical molecular complexes. *Molecular Pharmaceutics*, 3(3):362–367, 2006.

[240] C. Correa-Soto, N. S. Trasi, P. D. Schmitt, Y. Su, Z. Liu, E. Miller, N. Variankaval, P. J. Marsac, G. J. Simpson, and L. S. Taylor. Second harmonic generation microscopy as a tool for the early detection of crystallization in spray dried dispersions. *Journal of Pharmaceutical and Biomedical Analysis*, 146:86–95, 2017.

[241] R. C. Basso, A. P. B. Ribeiro, M. H. Masuchi, L. A. Gioielli, L. A. G. Gonçalves, A. O. dos Santos, L. P. Cardoso, and R. Grimaldi. Tripalmitin and monoacylglycerols as modifiers in the crystallisation of palm oil. *Food Chemistry*, 122(4):1185–1192, 2010.

[242] Q. Li, J. Kölbel, T. Threlfall, and J. A. Zeitler. Flow cell to study crystallisation processes in-situ using terahertz time-domain spectroscopy. *IEEE Transactions on Terahertz Science and Technology*, pages 1–1, 2021.

[243] U. Tayvah, J. A. Spies, J. Neu, and C. A. Schmuttenmaer. Nelly: A user-friendly and open-source implementation of tree-based complex refractive index analysis for terahertz spectroscopy. *Analytical Chemistry*, 93(32):11243–11250, 2021.

[244] J. J. De Yoreo, P. U. Gilbert, N. A. Sommerdijk, R. L. Penn, S. Whitelam, D. Joester, H. Zhang, J. D. Rimer, A. Navrotsky, J. F. Banfield, et al. Crystallization by particle attachment in synthetic, biogenic, and geologic environments. *Science*, 349(6247):aaa6760, 2015.

[245] G. R. Desiraju. Crystal engineering: from molecule to crystal. *Journal of the American Chemical Society*, 135(27):9952–9967, 2013.

[246] M. Svaerd, K. R. Devi, D. Khamar, D. Mealey, D. Cheuk, J. Zeglinski, and Å. C. Rasmuson. Solute clustering in undersaturated solutions – systematic dependence on time, temperature and concentration. *Physical Chemistry Chemical Physics*, 20(22):15550–15559, 2018.

[247] M. Volmer. *Kinetics of phase formation*. K. F. Bonhoeffer, 1939.

[248] P. G. Vekilov. Nucleation. *Crystal Growth Design*, 10(12):5007–5019, 2010.

[249] D. Gebauer and H. Coelfen. Prenucleation clusters and non-classical nucleation. *Nano Today*, 6(6):564–584, 2011.

[250] K. Tielrooij, D. Paparo, L. Piatkowski, H. Bakker, and M. Bonn. Dielectric relaxation dynamics of water in model membranes probed by terahertz spectroscopy. *Biophysical Journal*, 97(9):2484–2492, 2009.

[251] K.-J. Tielrooij, J. Hunger, R. Buchner, M. Bonn, and H. J. Bakker. Influence of concentration and temperature on the dynamics of water in the hydrophobic hydration shell of tetramethylurea. *Journal of the American Chemical Society*, 132(44):15671–15678, 2010.

[252] J. A. Zeitler, D. A. Newnham, P. F. Taday, C. J. Strachan, M. Pepper, K. C. Gordon, and T. Rades. Temperature dependent terahertz pulsed spectroscopy of carbamazepine. *Thermochimica Acta*, 436(1):71–77, 2005.

[253] F. Sebastiani, S. L. Wolf, B. Born, T. Q. Luong, H. Coelfen, D. Gebauer, and M. Havenith. Water dynamics from THz spectroscopy reveal the locus of a liquid–liquid binodal limit in aqueous CaCO3 solutions. *Angewandte Chemie International Edition*, 56(2):490–495, 2017.

[254] J. Kölbel, Q. Li, T. Threlfall, and J. A. Zeitler. Measuring the local concentration of semi-crystalline systems with terahertz spectroscopy. *Analytical Chemistry*, 94(3):1713–1716, 2021.

[255] C. F. Macrae, I. Sovago, S. J. Cottrell, P. T. Galek, P. McCabe, E. Pidcock, M. Platings, G. P. Shields, J. S. Stevens, M. Towler, et al. Mercury 4.0: From visualization to analysis, design and prediction. *Journal of Applied Crystallography*, 53(1):226–235, 2020.

[256] M. Weil. The high-temperature modification of magnesium sulfate (β-MgSO4) from single-crystal data. *Acta Crystallographica Section E: Structure Reports Online*, 63(8):i172–i172, 2007.

[257] F. Hawthorne, L. Groat, M. Raudsepp, and T. Ercit. Kieserite, $Mg(SO_4)(H_2O)$, a titanite-group mineral. *Neues Jahrbuch für Mineralogie Abhandlungen*, 157:121–132, 1987.

[258] G. Ferraris, D. W. Jones, and J. Yerkess. Refinement of the crystal structure of magnesium sulphate heptahydrate (epsomite) by neutron diffraction. *Journal of the Chemical Society, Dalton Transactions*, (8):816–821, 1973.

[259] R. Dovesi, A. Erba, R. Orlando, C. M. Zicovich-Wilson, B. Civalleri, L. Maschio, M. Rérat, S. Casassa, J. Baima, S. Salustro, et al. Quantum-mechanical condensed matter simulations with CRYSTAL. *Wiley Interdisciplinary Reviews: Computational Molecular Science*, 8(4):e1360, 2018.

[260] D. Vilela Oliveira, J. Laun, M. F. Peintinger, and T. Bredow. BSSE-correction scheme for consistent Gaussian basis sets of double-and triple-zeta valence with polarization quality for solid-state calculations. *Journal of Computational Chemistry*, 40(27):2364–2376, 2019.

[261] A. D. Becke. A new mixing of Hartree–Fock and local density-functional theories. *The Journal of Chemical Physics*, 98(2):1372–1377, 1993.

[262] C. Lee, W. Yang, and R. G. Parr. Development of the Colle-Salvetti correlation-energy formula into a functional of the electron density. *Physical Review B*, 37(2):785, 1988.

[263] S. Grimme, J. Antony, S. Ehrlich, and H. Krieg. A consistent and accurate ab initio parametrization of density functional dispersion correction (DFT-D) for the 94 elements H-Pu. *The Journal of Chemical Physics*, 132(15):154104, 2010.

[264] S. Grimme, S. Ehrlich, and L. Goerigk. Effect of the damping function in dispersion corrected density functional theory. *Journal of Computational Chemistry*, 32(7):1456–1465, 2011.

[265] S. Grimme, A. Hansen, J. G. Brandenburg, and C. Bannwarth. Dispersion-corrected mean-field electronic structure methods. *Chemical Reviews*, 116(9):5105–5154, 2016.

[266] B. Axilrod and E. Teller. Interaction of the van der Waals type between three atoms. *The Journal of Chemical Physics*, 11(6):299–300, 1943.

[267] Y. Muto. Force between nonpolar molecules. *Proceedings of the Physico-Mathematical Society of Japan*, 17:629–631, 1943.

[268] L. Donà, J. Brandenburg, I. Bush, and B. Civalleri. Cost-effective composite methods for large-scale solid-state calculations. *Faraday Discussions*, 224:292–308, 2020.

[269] F. Pascale, C. M. Zicovich-Wilson, F. López Gejo, B. Civalleri, R. Orlando, and R. Dovesi. The calculation of the vibrational frequencies of crystalline compounds and its implementation in the CRYSTAL code. *Journal of Computational Chemistry*, 25(6):888–897, 2004.

[270] C. Zicovich-Wilson, F. Pascale, C. Roetti, V. Saunders, R. Orlando, and R. Dovesi. Calculation of the vibration frequencies of α-quartz: The effect of Hamiltonian and basis set. *Journal of Computational Chemistry*, 25(15):1873–1881, 2004.

[271] C. A. Schneider, W. S. Rasband, and K. W. Eliceiri. NIH Image to ImageJ: 25 years of image analysis. *Nature Methods*, 9(7):671–675, 2012.

[272] A. Zalkin, H. Ruben, and D. Templeton. The crystal structure of cobalt sulfate hexahydrate. *Acta Crystallographica*, 15(12):1219–1224, 1962.

[273] A. D. Fortes, I. G. Wood, M. Alfredsson, L. Vocadlo, and K. S. Knight. The thermoelastic properties of $MgSO_4 \cdot 7D_2O$ (epsomite) from powder neutron diffraction and ab initio calculation. *European Journal of Mineralogy*, 18(4):449–462, 2006.

[274] D. M. Leitner, M. Gruebele, and M. Havenith. Solvation dynamics of biomolecules: modeling and terahertz experiments. *HFSP Journal*, 2(6):314–323, 2008.

[275] M. Heyden and M. Havenith. Combining THz spectroscopy and MD simulations to study protein-hydration coupling. *Methods*, 52(1):74–83, 2010.

[276] V. Matvejev, M. Zizi, and J. Stiens. Hydration shell parameters of aqueous alcohols: THz excess absorption and packing density. *The Journal of Physical Chemistry B*, 116(48):14071–14077, 2012.

[277] U. Heugen, G. Schwaab, E. Bruendermann, M. Heyden, X. Yu, D. Leitner, and M. Havenith. Solute-induced retardation of water dynamics probed directly by terahertz spectroscopy. *Proceedings of the National Academy of Sciences*, 103(33):12301–12306, 2006.

[278] S. Mitryukovskiy, D. E. Vanpoucke, Y. Bai, T. Hannotte, M. Lavancier, D. Hourlier, G. Roos, and R. Peretti. On the influence of water on THz vibrational spectral features of molecular crystals. *Physical Chemistry Chemical Physics*, 24(10):6107–6125, 2022.

Appendix

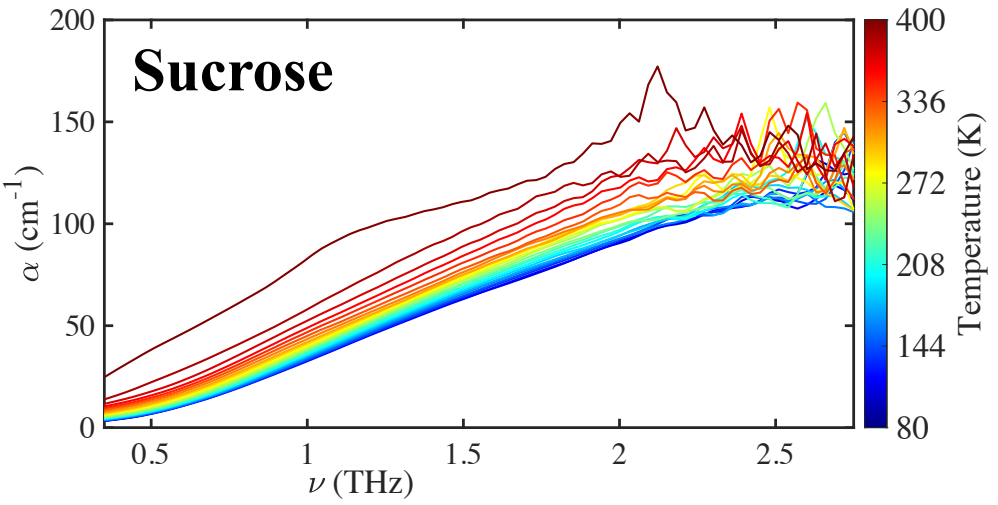
Sucrose
α (cm-1)
ν (THz)
Temperature (K)
0
50
100
150
200
0.5
1
1.5
2
2.5
80
144
208
272
336
400

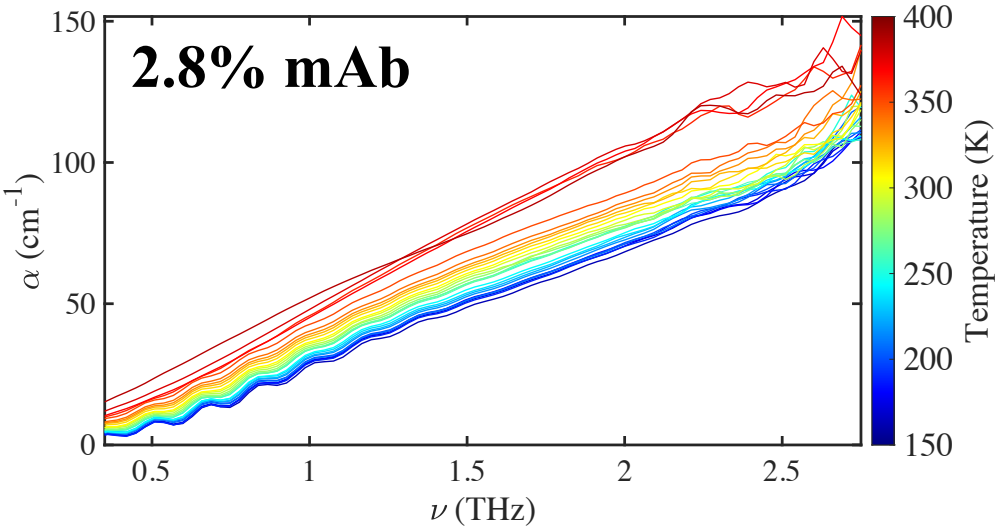
2.8% mAb
α (cm-1)
ν (THz)
Temperature (K)
0
50
100
150
0.5
1
1.5
2
2.5
150
200
250
300
350
400

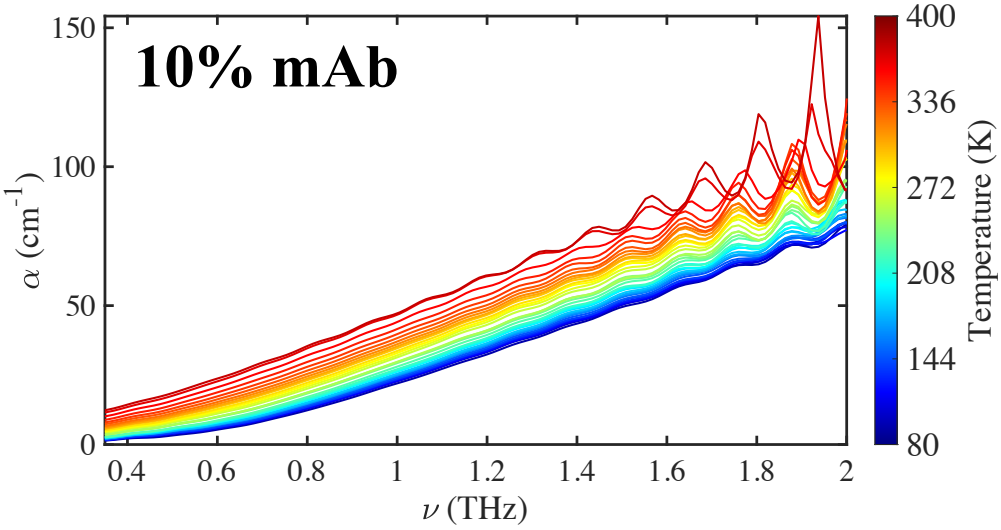
10% mAb
α (cm-1)
ν (THz)
Temperature (K)
0
50
100
150
0.4
0.6
0.8
1
1.2
1.4
1.6
1.8
2
80
144
208
272
336
400

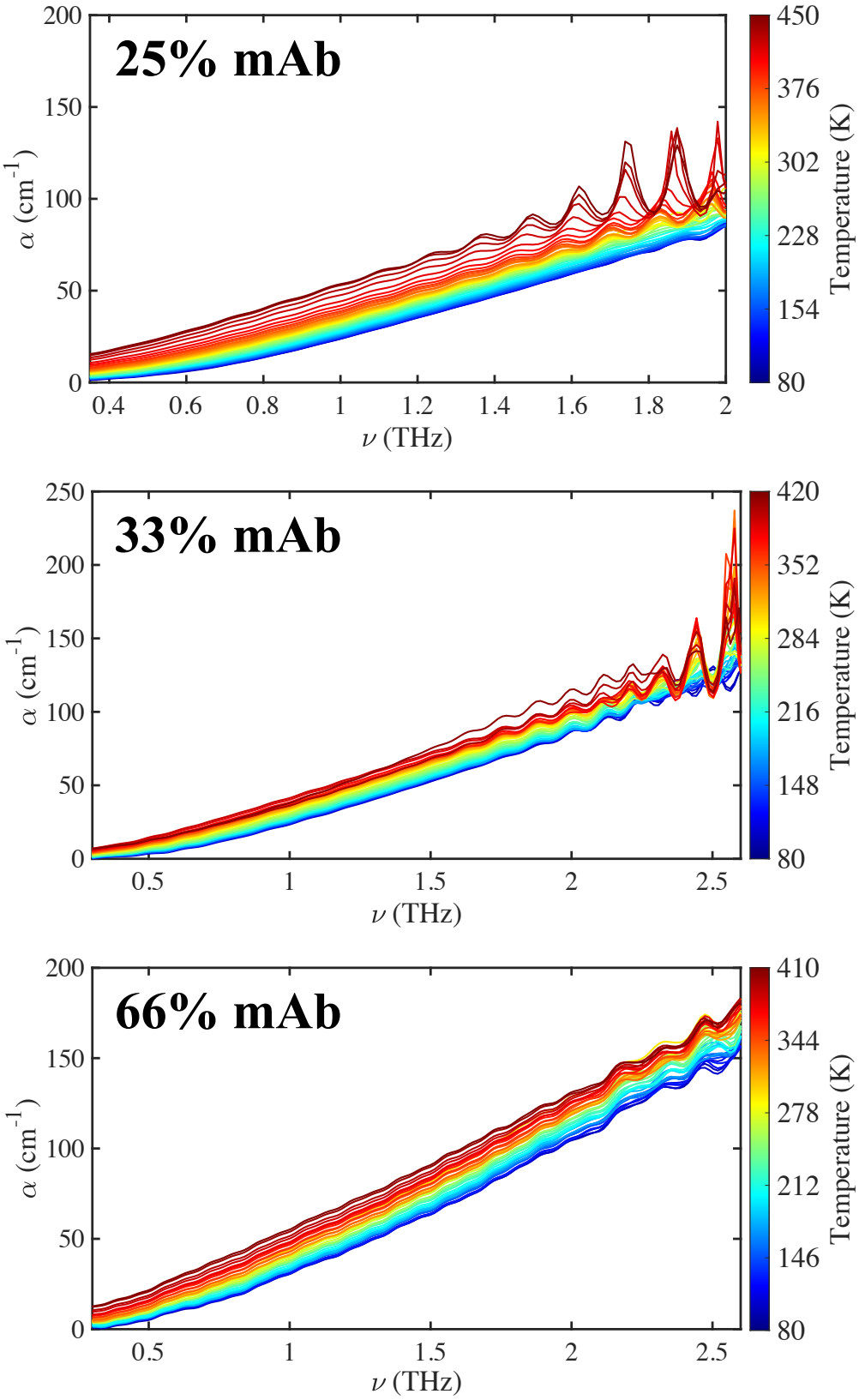
25% mAb
33% mAb
66% mAb
α (cm-1)
ν (THz)
Temperature (K)
0
50
100
150
200
250
0.4
0.6
0.8
1
1.2
1.4
1.6
1.8
2
0.5
1.5
2.5
80
154
228
302
376
450
148
216
284
352
420
146
212
278
344
410

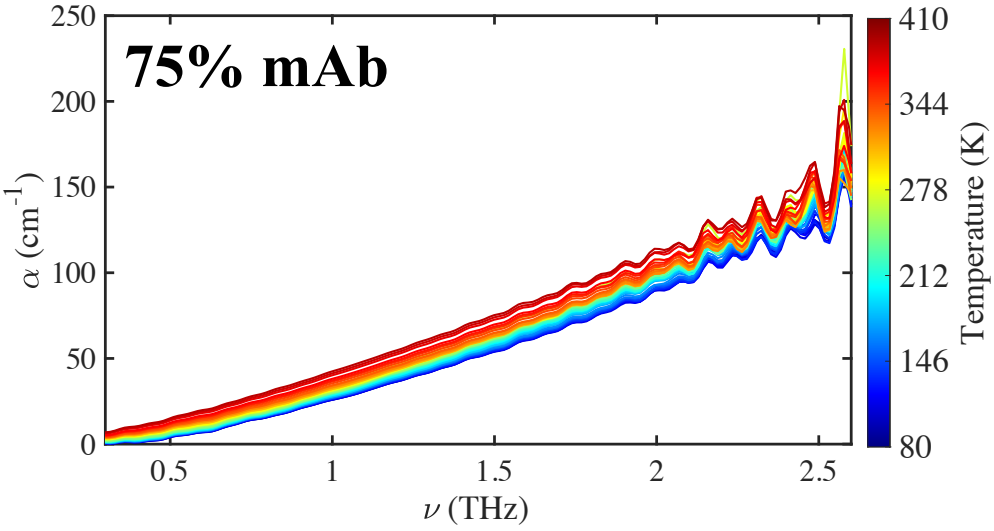
75% mAb
α (cm-1)
ν (THz)
Temperature (K)
250
200
150
100
50
0
0.5
1
1.5
2
2.5
410
344
278
212
146
80

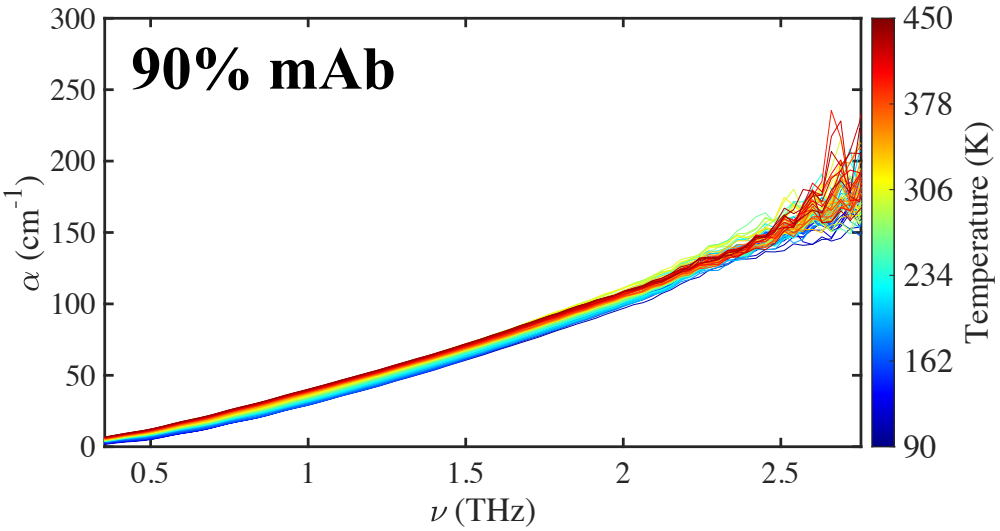
90% mAb
α (cm-1)
ν (THz)
Temperature (K)
300
250
200
150
100
50
0
0.5
1
1.5
2
2.5
450
378
306
234
162
90

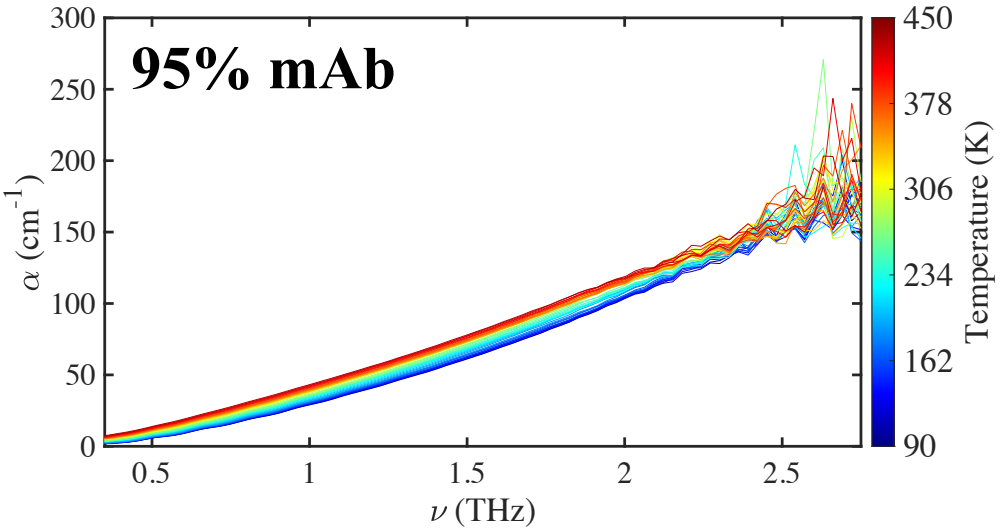
95% mAb
α (cm-1)
ν (THz)
Temperature (K)
300
250
200
150
100
50
0
0.5
1
1.5
2
2.5
450
378
306
234
162
90

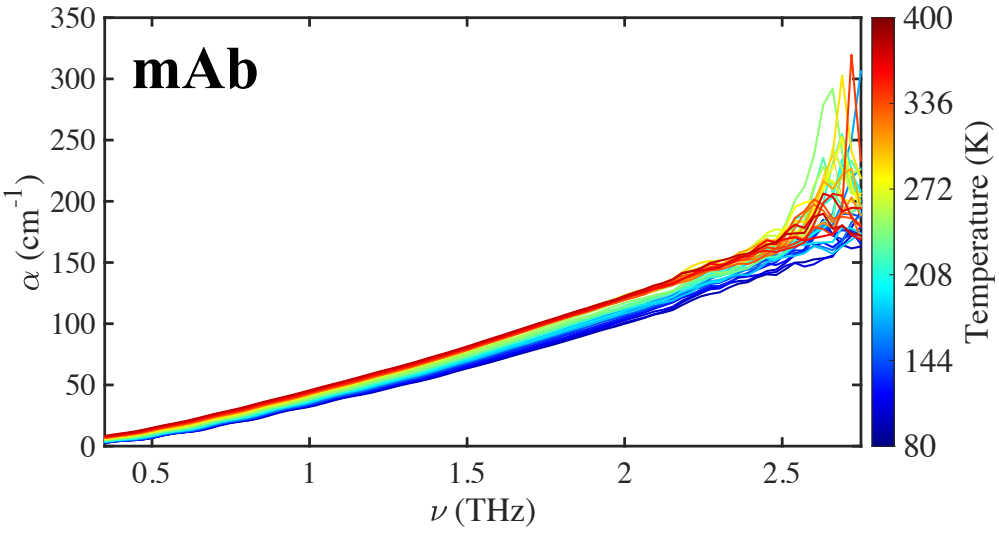
mAb
350
300
250
200
150
100
50
0
α (cm-1)
0.5
1
1.5
2
2.5
ν (THz)
400
336
272
208
144
80
Temperature (K)